Terahertz Spectroscopy and Modelling of Biotissue

by

Gretel Markris Png

Bachelor of Engineering (Electrical and Electronics Engineering, First Class Honours),
The University of Edinburgh, Scotland, UK, 1997

Master of Science (Electrical Engineering and Computer Science),
University of California at Irvine, USA, 2003

Thesis submitted for the degree of

Doctor of Philosophy

in

School of Electrical and Electronic Engineering,
Faculty of Engineering, Computer and Mathematical Sciences
The University of Adelaide, Australia

June, 2010

Appendix A

Preliminary Studies

RECOMMENDATIONS for extending the work in Chapters 5–9 are provided in Section 10.3. In addition, four smaller studies are summarised in Section 10.3. These smaller pieces of work are in various stages of development; some are more developed with preliminary results, whereas others are literature reviews only. This Appendix describes the studies in greater detail.

A.1 Preliminary Study 1: Pseudo-Phase Contrast

In order to encourage a rapid adoption of THz imaging in industry and medicine, it is necessary to present THz data in ways that are useful and familiar to professionals in these fields. Established image processing methods can be applied to THz data to enhance its representation. Figure A.1(a) shows an example of a THz time domain image captured by a conventional charge-coupled device (CCD) camera after optical upconversion. This image of an insect on a leaf consists of $N \times P$ pixels, and is at one time instance along a discretized time domain with M points. By stacking many of these $N \times P$ arrays over time, a 3D time domain array as shown in Fig. A.1(b) is generated.

The time domain response of one pixel can be extracted for analysis. In Fig. A.1(c), the time response of three pixels from the leaf/insect specimen mentioned above is presented: one pixel is that of the insect, another of the vein of the leaf, and the last is of free-space. When compared to the free-space plot (black line-dot plot), the THz profiles after exiting the insect (red solid line plot) and leaf (blue dashed plot) are attenuated in amplitude. Since the insect and leaf contain water, which strongly attenuates THz radiation, this attenuation is expected. The THz profile for the insect is phase shifted more than the leaf's profile, implying that the insect is thicker than the leaf and/or has a higher refractive index, therefore slowing down the propagating THz radiation. These time profiles can be Fourier transformed to obtain the broadband frequency response.

A.1.1 Preliminary Results

Figure A.2(a) shows THz data after application of common image processing techniques, such as edge detection, Laplacian filtering, and smoothing. Instead of separate amplitude and phase plots, this enhanced image more closely resembles 3D images generated using medical visualisation tools, thus allowing medical professionals to analyse and compare results easily.

An open question is can we implement a new form of THz data representation inspired by established image enhancement techniques used in the scientific field, such as Zernike's optical phase contrast method? Zernike's optical phase contrast method is based on the effect of light passing through a phase[79] object. When light passes

[79] An object that is not observable (transparent, invisible) because it does not provide contrast with the background. It does, however, cause phase modulations in the irradiated light wave, whereby these

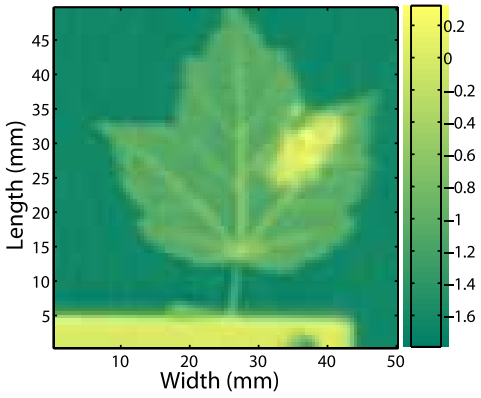

(a) One slice of the 3D dataset with $N \times P$ pixels, containing spatial information

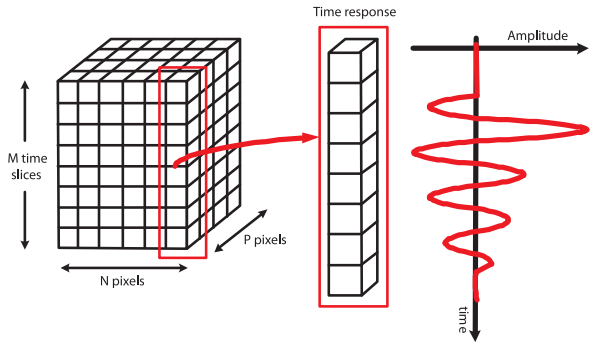

(b) 3D dataset contains both time and spatial information

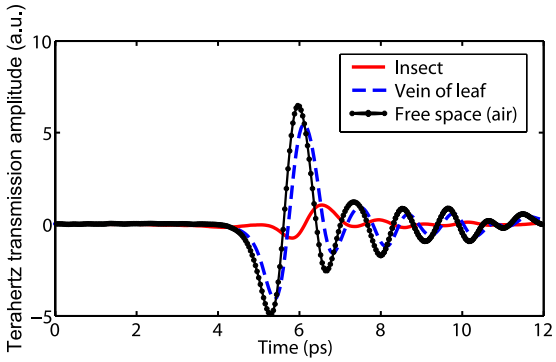

(c) Time response of 3 locations in the 3D dataset: insect, vein of leaf, and free-space (air)

Figure A.1: Extracting the time response from various pixels in the 3D dataset. (a–b) The 3D dataset contains time and spatial information of the sample space under investigation. Spatial information from one time slice is pseudo-coloured in various shades of green to highlight the different objects in the sample space. Data courtesy of X.-C. Zhang at RPI. (c) The time responses of 3 different pixels: insect, vein of leaf and free-space.

through free-space/air (*surround path*), the phase and amplitude information in the light wave is unaltered. When light passes through a phase object (*particle path*), the amplitude of the light wave is slightly attenuated due to energy loss. The light wave also slows down due to the refractive index of the phase object; the amount of delay introduced will also depend on the object's thickness. The difference in phase between the surround and particle paths is approximately a quarter of the wavelength of optical light. The human eye, however, can only sense amplitude and colour differences when both the surround and particle paths are in phase. The eye however fails to sense

phase modulations are due to either the different refractive index of the object from air, the thickness of the object, or both (Hecht 2002).

the contrast between the surround and particle paths due to their being out of phase by a quarter wavelength (Bennett *et al.* 1951). Phase objects therefore appear invisible under a conventional light microscope. In optical phase contrast, the surround path is manipulated to bring it back in phase with the particle path, resulting in the visibility of the phase object due to constructive interference.

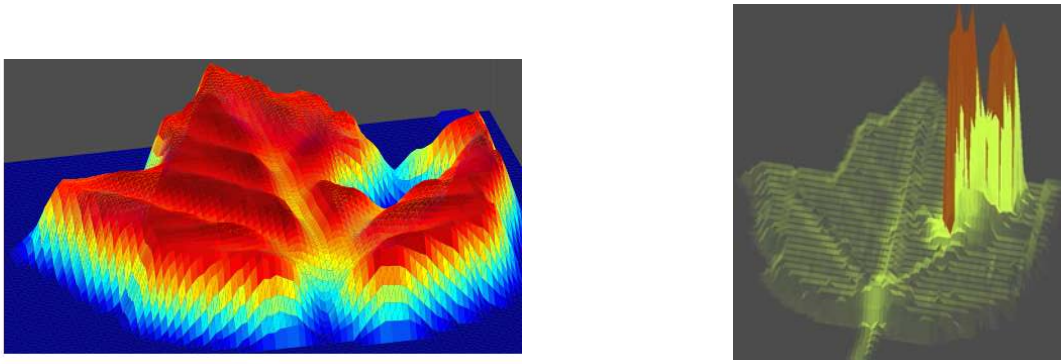

(a) After application of image processing techniques (b) Pseudo-phase contrast imaging

Figure A.2: Alternative representations of THz data. (a) Improvements made to THz image after application of common image processing techniques. The third dimension, intensity, is used to pseudo-colour this image. (b) With THz pseudo-phase contrast imaging. The third dimension in this case is thickness.

Considering one pixel from the leaf/insect sample in this study, the path length of the sample can be obtained indirectly by first calculating the relative time delay between the peak of the sample's (e.g. at position i) and the peak of a reference signal. Repeating for the whole $N \times P$ matrix, the relative propagation times τ_i with respect to τ_{ref} is given by:

$$\tau_i = |(\text{time occurrence of peak } i) - \tau_{ref}| , \quad \text{for} \quad i \epsilon [1, \cdots, N \times P] , \tag{A.1}$$

and the optical path length is then given by:

$$d_i = \text{speed of light } c \times \tau_i , \quad \text{for} \quad i \epsilon [1, \cdots, N \times P] . \tag{A.2}$$

The optical path lengths can now be converted to sample thickness. Figure A.2(b) shows an image of the various sample thicknesses. There are strong contrasts between the different parts of the leaf, and between the two halves of the insect. This is a novel form of phase contrast because the various path lengths are translated into an image with high contrast.

The relative amplitude I_{i} tells us how absorptive the medium is to THz radiation. If I_{i} is large, then large THz levels have been absorbed by the medium, hence low THz levels are captured by the detector. If I_{i} is small, then the THz radiation propagates through the medium without being absorbed. Therefore I_{i} can be used to set the opacity of a pixel in Fig. A.2(b) such that $I_{\text{i}} = I_{\text{ref}}$ implies zero opacity (I_{ref} is the free-space amplitude where free-space is transparent) and $I_{\text{i}} = \max\{I_{i\,\epsilon\,[1,\ldots,N\times P\}}\}$ implies unity opacity (opaque). The sample's opacity is calculated using:

$$I_{\text{i}} = |I_{\text{ref}} - (\text{peak amplitude at pixel } i)| \,, \quad \text{for} \quad i\,\epsilon\,[1,\cdots,N\times P] \,. \tag{A.3}$$

The low signal-to-noise ratio (SNR) however makes it difficult to pin-point a particular pixel as the reference. To overcome this, peak detection was performed on every pixel in the time domain, i.e. the peak of each $M \times 1$ array was found. The peak detection extracted from each pixel the time occurrence and value of the peak amplitude, thus generating two $N \times P$ matrices. From each matrix, 15 neighbouring pixels that correspond to the top left corner of Fig. A.1(a) were selected and used to average I_{ref} and propagation time τ_{ref}.

In this investigation, it is assumed that the peaks of the leaf's time profiles do not suffer from changes in polarity, and that pulse broadening does not adversely affect the shape of the profile. These assumptions are adopted because the leaf has a higher refractive index than air, so the THz radiation have propagated through three media (air-leaf-air) and the polarity of their time profiles are unaltered upon exiting the leaf. The leaf used in this analysis is dry, thus it has minimal water content; strong water absorption that causes deformation of the profile is not expected. Internal reflection is ignored. The insect, being thicker and/or denser than the leaf, causes some pulse broadening in the THz profile as seen by the solid line plot in Fig. A.1(c). The polarity of the peak is expected to be inverted (a trough) because the THz radiation have propagated through four media (air-insect-leaf-air). Referring to Fig. A.1(c), the trough at around 6 picoseconds seems to be the one of interest. This trough, however, occurs before the peak of the free-space profile (solid-circle plot), which gives a false impression of negative group velocity. The trough is therefore ignored in this initial analysis. The positive peak (after the peak of the free-space profile) is chosen instead, and the insect and the portion of leaf beneath it are treated as one object.

Note that Zernike's original phase contrast method is based on interference between two beam paths. By altering the path length of one path, the phase difference between

the two paths is revealed proportionally as amplitude variations in the observed image. This is akin to heterodyne detection. However, with functional THz imaging, the full phase information is recovered and so interference effects are not exploited. This method of rendering sample thickness on the z-axis, as shown in Fig. A.2(b), is therefore dubbed 'pseudo-phase contrast'.

A.1.2 Future Work

Future work could consider signal processing techniques that transform the full phase information from THz imaging to produce the actual appearance of Zernike phase contrast images. Given that THz functional imaging recovers the full phase information, this should be possible in principle.

A.2 Preliminary Study 2: Polymer Hole Arrays

An array of holes spaced periodically apart can function as a notch filter, allowing only specific frequencies from a wideband electromagnetic signal to pass through. This idea is not novel—-doors of microwave ovens are affixed with such filters to minimise leakage of microwave radiation. The shape of holes, size of holes, pitch of holes (distance from the centres of adjacent holes), arrangement of holes (e.g. triangular lattice), type of material, and thickness of the material all play a part in determining the notch frequency/frequencies of the hole array.

In the submillimeter and THz frequency regions, metal structures containing arrays of subwavelength holes have been observed to pass frequencies in the low THz frequency range (Drysdale *et al.* 2003, Qu *et al.* 2004, Qu and Grischkowsky 2004, Miyamaru and Hangyo 2004, Biber *et al.* 2004a, Biber *et al.* 2004b, Azad and Zhang 2005, Tanaka *et al.* 2005, Lo *et al.* 2005, Biber *et al.* 2006). Such structures, which are called metal hole arrays (MHAs) or Frequency Selective Surfaces (FSSs), are usually made from a very thin sheet of metal (e.g. aluminium with thickness between a few hundred nanometers to a few hundred micrometers) mounted on a thicker substrate (e.g. silicon) for mechanical support. Figure A.3 presents examples of MHAs.

The aim of several reported THz MHA studies has primarily been on characterising the frequency resonant behaviours of these structures. Enhancement of THz transmission was also proposed (Lo *et al.* 2005). However, a practical purpose for these filters has

NOTE:
These figures are included on page 301 of the print copy of the thesis held in the University of Adelaide Library.

(a) MHA with slot-shaped holes, passband at 0.6 THz

(b) MHA with dogbone-shaped holes, passband also at 0.6 THz

Figure A.3: Examples of metal hole arrays. (a–b) Photographs of metal hole array (MHAs) with differently shaped holes, but with the same passband frequency. Close-up view of a hole is shown on the right of each subfigure. After Biber *et al.* (2006).

not been explicitly identified. The small size of MHAs, together with their sensitivities to the low THz frequency range, which is less affected by water absorption, raises the question as to whether MHAs would be suitable for detecting minute quantities of liquids. This proposal is encouraged by the work done in Yoshida *et al.* (2007), where protein detection was demonstrated on a thin metallic mesh.

A.2.1 Preliminary Evaluation

The case study presented henceforth explores the ease of designing a MHA, and investigates if alternative materials can be used. Figure A.4 shows an HFSS model of a MHA. Recalling that in Chapter 8, in order to model the array of cylinders along the y-axis, a pair of master-slave boundaries are used in HFSS. In Fig. A.4, two master-slave boundaries are used to create periodicity along two-dimensions, the x and y axes. Outcomes from varying in the hole configurations are shown in Fig. A.5. Recalling Section 8.7.2, the S_{11} plot describes backscattering in a two-port network, with port 1 being the input and port 2 being the output. If $S_{11} = 0$ dB, then there is 100% backscattering, i.e. stopband of a filter; if $S_{11} < 0$ dB, then there is forward transmission from port 1 to port 2, i.e. passband of a filter.

Based on the size and material descriptions provided in existing literature, a plan was made to manufacture a MHA similar to that shown in Fig. A.4, with a passband below 0.2 THz. This frequency range is desired because THz is more strongly attenuated by liquid water at higher frequencies. The MHA manufacturing process would involved

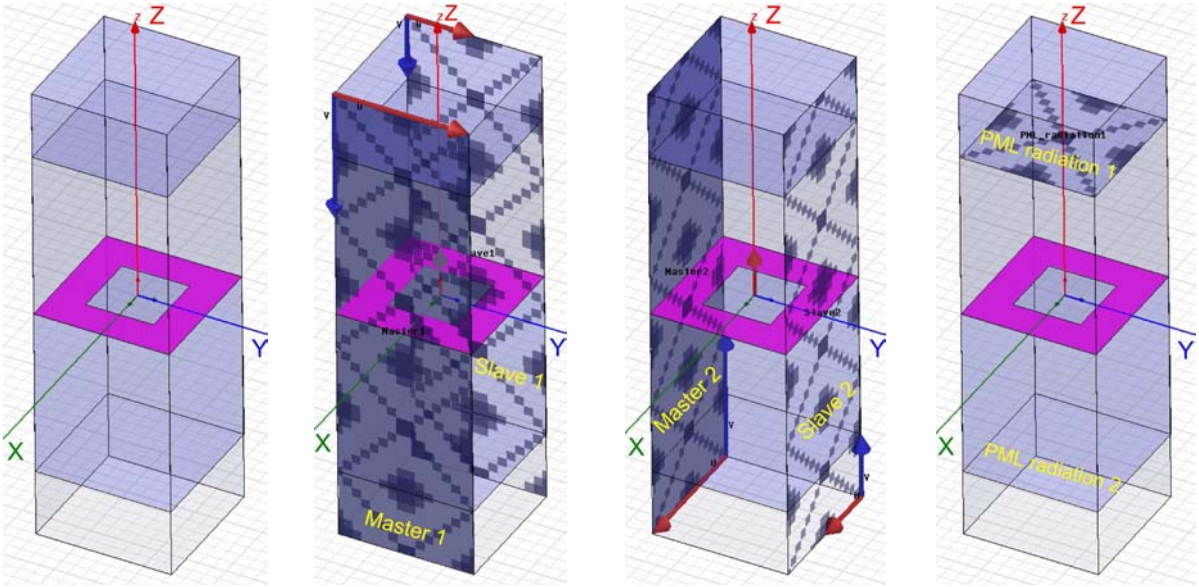

(a) Basic cell (b) First master-slave boundaries (c) Second master-slave boundaries (d) PML boundaries

Figure A.4: Modelling periodic hole arrays in HFSS. (a) Basic cell with the array highlighted. (b) The first set of master-slave boundaries models periodicity along the x-axis. (c) The second set of master-slave boundaries models periodicity along the y-axis. (d) The PML boundaries reduce the problem space.

those utilised in the fabrication of printed circuit boards (PCBs). However, the thickness of the metal (a few hundred micrometers to achieve a passband below 0.2 THz) was considered too thick for current modern etching methods; an older etching machine is required. One such machine was found at the University of Cardiff in Wales, UK, whereby the cost of the etching process was quoted at £500.

Although this cost is not prohibitively high, the question of finding alternative materials was raised. Additionally, being able to manufacture a FSS locally at a lower cost would be most desirable so that an assortment of filters with different passbands are available for use. One possible material was found after lengthy discussions with the authors of Gallant *et al.* (2007b). Polydimethylsiloxane (PDMS, or silicone rubber) is a flexible polymer, which can be manufactured following a recipe involving photoresists, solvents, and standard spin coating and ultraviolet curing techniques (Gallant *et al.* 2007a). Figure A.6 shows an example of a PDMS hole array. The PDMS hole array has been verbally reported[80] by Gallant to be effective for detection of chemicals; the

[80] From an oral presentation at the Joint 32nd International Conference on Infrared and Millimeter Waves, and the 15th International Conference in Terahertz Electronics (IRMMW-THz) in 2007.

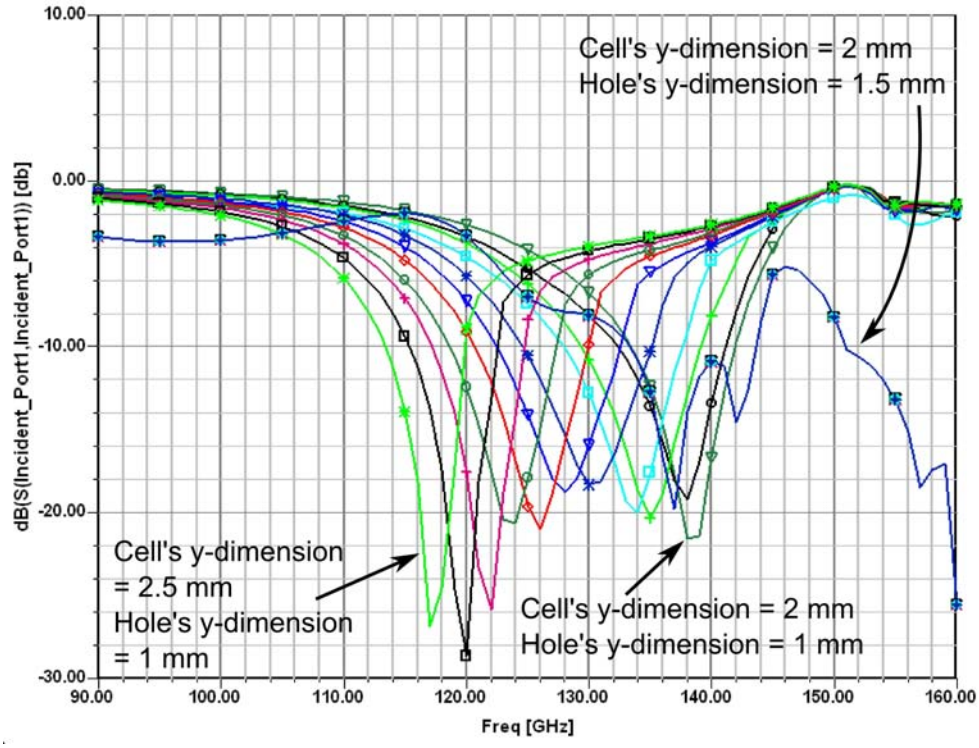

Figure A.5: Effect of modifying cell and hole dimensions. Annotated screen shot of S_{11} plots from HFSS. The tunability of the structure is evident from the varying locations of the passband as the cell and hole dimensions are altered. In the first instance, only the cell's y-dimension is altered from 2.5 mm to 2 mm in steps of 0.05 mm. Then the hole's y-dimension is altered from 1 mm to 1.5 mm in a single step of 0.5 mm, resulting in the generation of a less defined passband.

array was measured with and without biotin, resulting in different transmitted THz signals.

A.2.2 Future Work

If the PDMS' optical properties are known, then various PDMS configurations can be modelled using HFSS. The presence of a thin layer of sample on the PDMS array (e.g. protein solution, biological fluid such as blood) may also be modelled with HFSS as a thin second layer on the array structure. The optimal thickness, if any, of the protein sample on the array can also be explored. Furthermore, an optimal array passband may also exist for a specific type of sample. The results from HFSS can then be verified experimentally using a customised PDMS array.

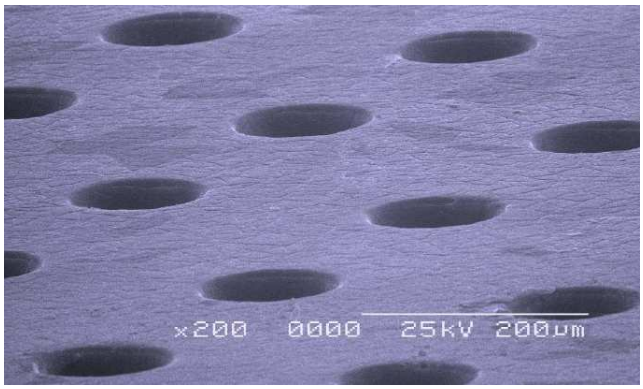

Figure A.6: PDMS hole array. This specific array has a strong passband at $\approx$ 0.8 THz, but it also passes frequencies above 0.8 THz but at attenuated signal strengths, therefore behaving like a non-ideal high pass filter. By changing the size of holes, pitch of holes, and arrangement of holes, the filter characteristics of the array is expected to change. Photograph courtesy of A.J. Gallant from Durham University, UK.

A.3 Preliminary Study 3: Etalon Removal

In Chapter 7, polystyrene culture dishes (BD Falcon 353001) are required in the manufacturing process of gels. Since polystyrene is transparent to THz radiation, these dishes are assumed to not interfere with the THz measurements of the gels. This assumption is valid with regards to quantitative measurements of a sample's optical properties. Referring to Fig. 7.8 of the extinction coefficients of gels measured in dishes, the slope of the plots provide quantitative distinction between the three types of samples (pH 2, 4 and 7). However, each plot has an oscillatory artefact caused by Fabry-Pérot etalon effects (multiple reflections) inside the lids and bases of the dishes. The absence of these oscillatory artefacts is clearly apparent in the plots of samples measured without dishes, such as Fig. 7.12.

Fabry-Pérot etalon effects exist as either undesired embedded reflections within a THz pulsed signal, or as reflections that appear shortly after the THz pulsed signal. Algorithms have been proposed to remove both types of reflections (Duvillaret *et al.* 1996, Naftaly and Miles 2007a). In Duvillaret *et al.* (1996), removal of reflections from a single layer are demonstrated; reflections from multiple layers are reported but not demonstrated. In the study presented below, an algorithm for removing undesired embedded reflections from multiple layers is demonstrated.

The algorithm models embedded reflections from multiple layers as a train of weighted delta functions in the time domain. The embedded reflections are either entirely removed or significantly reduced when the measured THz signal is divided by the delta train in the frequency domain. The algorithm is applied to measured data from multilayered samples with estimated *a priori* knowledge of the optical properties of the layers.

A.3.1 Proposed Algorithm

Transmission and reflection pathways of a THz wave in a sample can be described by the Fresnel equations (Hecht 2002). These pathways are provided in detail in (Dorney *et al.* 2001). In this study, the angles of incidence and transmission of the THz signal are assumed to be normal to the sample. In the time domain, the measured THz signal $E(t)$ is the sum of the primary signal $E_{\mathrm{p}}(t)$ and multiple weighted, delayed copies (reflections) of the primary signal with time delay τ_x:

$$\begin{aligned} E(t) &= a_0\, E_{\mathrm{p}}(t) + \overbrace{a_1\, E_{\mathrm{p}}(t-\tau_1) + a_2\, E_{\mathrm{p}}(t-\tau_2) + \cdots}^{\text{unwanted}}, \\ \text{where } \tau_x &= \tau_{x-1} + \frac{2(\text{thickness of layer } x)(n_{\text{layer } x})}{\text{speed of light in vacuum}}, \end{aligned} \tag{A.4}$$

and the normalised Fresnel coefficients, $a_0 = 1$ and $\cdots < a_2 < a_1 < 1$, are dependent on the refractive indices n_x of the layers under investigation. For example, the first four normalised coefficients of a one-layered sample suspended in air are:

$$\begin{aligned} a_0 &= T_{12} = \frac{2\,n_{\text{air}}}{n_{\text{air}} + n_{\text{layer 1}}} = 1 \quad (\text{normalised}), \\ a_1 &= \frac{R_{21}^2\, T_{12}}{T_{12}} = \left(\frac{n_{\text{layer 1}} - n_{\text{air}}}{n_{\text{layer 1}} + n_{\text{air}}}\right)^2, \\ a_2 &= \frac{R_{21}^4\, T_{12}}{T_{12}}, \quad a_3 = \frac{R_{21}^6\, T_{12}}{T_{12}}. \end{aligned}$$

Recalling that the unwanted reflections cause oscillatory artefacts in the frequency domain, this technique matches the oscillation by first treating the primary signal as a Dirac delta function at zero time, and the reflections as weighted, delayed Dirac delta functions:

$$E(t) = a_0\,\delta(t) + \overbrace{a_1\,\delta(t-\tau_1) + a_2\,\delta(t-\tau_2) + \cdots}^{\text{unwanted}}. \tag{A.5}$$

In the frequency domain, Equation (A.5) transforms to Equation (A.6), which now contains a sum of exponential functions that match the oscillatory artefact:

$$E(\omega) = 1 + \overbrace{a_1 e^{-i(\omega-\omega_1)\tau_1} + a_2 e^{-i(\omega-\omega_1)\tau_2} + \cdots}^{\text{unwanted oscillation}}, \tag{A.6}$$

where ω is the angular frequency, and ω_1 is a variable to allow minor adjustments in frequency to best match Equation (A.6) with the oscillation. Here, ω_1 is a fitting parameter that selects the case with minimum deviation from the oscillation; it helps account for slight inaccuracies in the measurement of thickness or optical properties. Equation (A.6) can be extended to include multiple layers by adding more exponential terms and recalculating the normalised Fresnel coefficients accordingly.

A.3.2 Preliminary Results

The algorithm is first applied to a scenario with two layers: α-lactose monohydrate (BDH reagent grade, mixed with polyethylene powder) stored in a polystyrene culture dish (BD Falcon 353001). The α-lactose is measured *in situ*. The culture dish has a 1 mm thick base and is the reference signal in this scenario. To ensure that any oscillatory artefact in the frequency domain is solely due to embedded reflections, the time domain signals are truncated before the arrival of secondary reflections that are generated by mirrors or lenses. The time domain signals are then padded with zeros. The dashed line plots in Figs. A.7(a)–A.7(c) show the optical properties of α-lactose without any correction. The inset plots clearly illustrate the oscillatory artefact, particularly at the lower frequency range.

The oscillation is matched by calculating the variables in Equation (A.6) based on the estimated optical and physical properties of α-lactose and polystyrene, and using $\omega_1 = 13\Delta\omega$ (where $\Delta\omega$ is the known frequency step in the frequency domain). This value of ω_1 is obtained by first running the algorithm with $\omega_1 = 0$ to check if Equation (A.6) requires a slight frequency shift to match the oscillation. If required, the best ω_1 value is then selected to align Equation (A.6) with the oscillation. By dividing the original uncorrected sample frequency response by Equation (A.6), the oscillation in the resulting sample frequency response is significantly smoothed. More importantly, a recalculation of the optical properties of α-lactose shows that the spectral peaks are preserved. This is visible by the solid line plots in both the inset and main plots of Figs. A.7(a) and A.7(b).

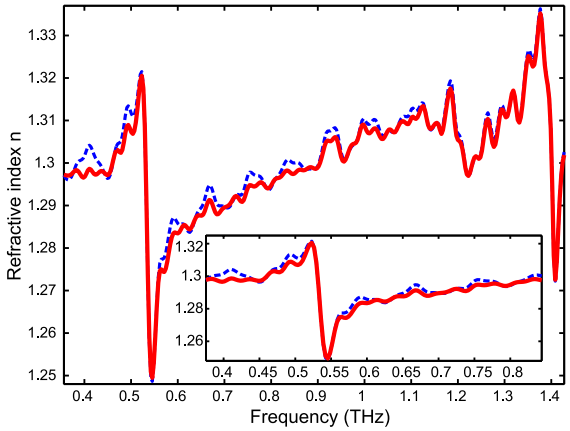

(a) Refractive index without (dashed line) and with (solid line) correction using the algorithm proposed in this Section

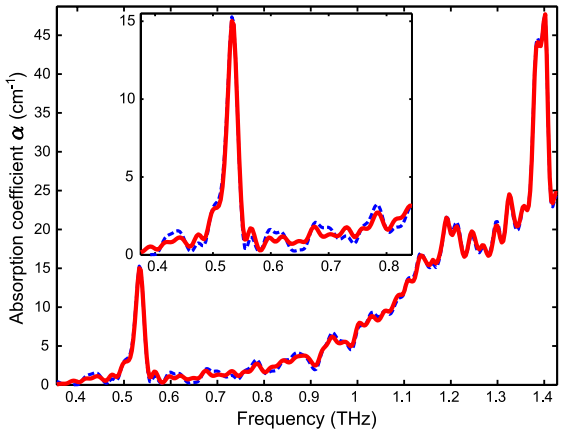

(b) Absorption coefficient without (dashed line) and with (solid line) correction using the algorithm proposed in this Section

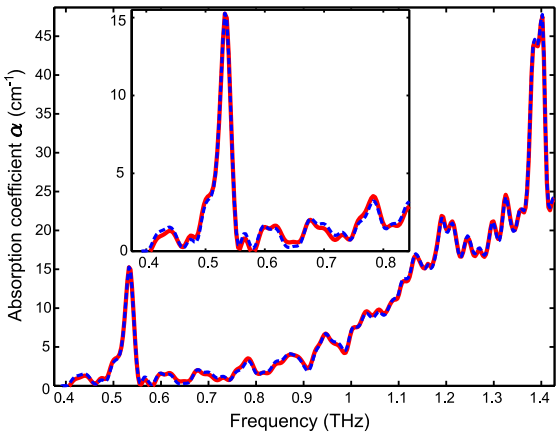

(c) Absorption coefficient without (dashed line) and with (solid line) correction using Duvillaret's algorithm

Figure A.7: Performance comparison of algorithms for a multilayered test scenario. α-lactose is mixed with polyethylene powder, and measured inside a polystyrene culture dish with a 1 mm thick base (with no lid). (a) Refractive index without (dashed line) and with (solid line) correction using the algorithm proposed in this Section. (b) Absorption coefficient without (dashed line) and with (solid line) correction using the algorithm proposed in this Section. (c) Absorption coefficient without (dashed line) and with (solid line) correction using Duvillaret's algorithm.

The same two-layered scenario as described above (α-lactose and polystyrene) is used in a comparison of the performance of the algorithm in Duvillaret *et al.* (1996) and the one proposed in this Section. It is evident from the solid line plot in Fig. A.7(c)

that application of Duvillaret's algorithm provides some smoothing but exacerbates the oscillation at certain frequencies (e.g. 0.75–0.8 THz).

In order to compare the performance of the two algorithms for a single-layered case, the next test scenario utilises a 1 mm thick polyethylene slab. Although both algorithms allow multiple iterations, only one pass of each algorithm was required as no significant improvements were observed from additional passes. The time domain signals were truncated and padded as described above. It is evident from the dashed line plot in Fig. A.8 that the oscillation in this example is pronounced, and application of either algorithm provides considerable smoothing. The extent of smoothing from this algorithm is comparable to that of Duvillaret's.

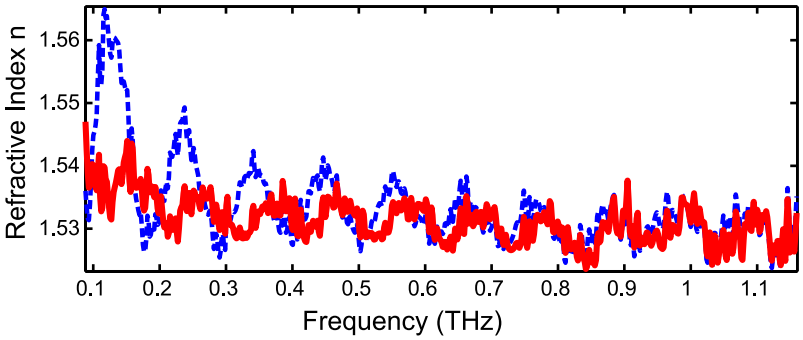

(a) Refractive index without correction (dashed line) and with correction (solid line) using Duvillaret's algorithm

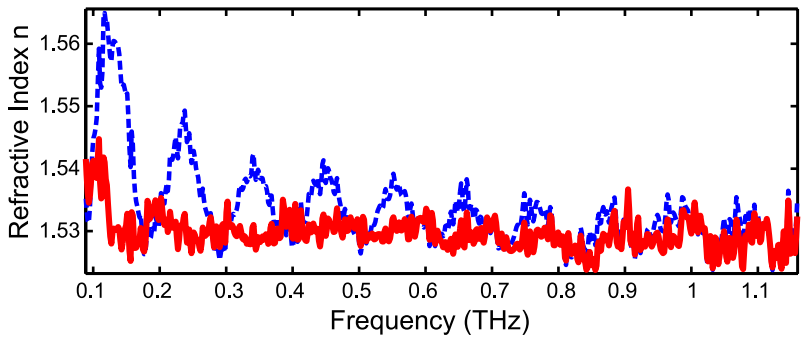

(b) Refractive index without correction (dashed line) and with correction (solid line) using the algorithm proposed in this Section

Figure A.8: Performance comparison of algorithms for a single layered test scenario. A 1 mm thick polyethylene slab is used as the single layered sample. (a) Refractive index without correction (dashed line) and with correction (solid line) using Duvillaret's algorithm. After Duvillaret *et al.* (1996). (b) Refractive index without correction (dashed line) and with correction (solid line) using the algorithm proposed in this Section, where $\omega_1 = 4\Delta\omega$ in Equation (A.6).

A.3.3 Future Work

One shortcoming of the proposed algorithm is the use of the fitting parameter ω_1. The chosen value of ω_1 in the algorithm is presently decided manually by trial and error. A search algorithm can be introduced to optimise the chosen ω_1. More fitting parameters may also be needed to remove oscillations at the higher frequencies.

A.4 Preliminary Study 4: Inverse Problems

In Chapters 5–8, the THz optical properties of samples are determined from the THz time domain measurements of electric field. Extracting the optical properties from the time domain measurements requires the application of a series of transforms and equations as described in Chapter 5; the THz optical properties cannot, at present, be probed directly. The extraction of THz optical properties is considered an *inverse problem* because the measured parameters (electric field) differs from the desired quantities (optical properties).

Many real-world problems can be considered inverse problems. For example, the use of seismic waves to probe the earth's crust, or the use of ground penetrating radar to study vegetation. In an ideal measurement, the inverse problem is *well-posed*: a unique solution (e.g. THz optical property) exists for any measurement (e.g. THz time domain measurement), and the reverse mapping (the measurement produces a unique solution) also exists. However, in non-ideal measurements, issues such as scattering and dispersion can result in there being many possible solutions, making it impossible to perform a unique reverse mapping. When this happens, the inverse problem is considered *ill-posed* in the sense of Hadamard (Hadamard 1923). Formal mathematical definitions of well-posed, ill-posed, and *ill-conditioned* inverse problems can be found in literature (Vasin and Ageev 1995, Kirsch 1996, Bukhgeim 2000); the definition of well-posedness is reproduced below from Kirsch (1996).

Definition for well-posedness: Let X and Y be normed spaces, $K : X \mapsto Y$, where K is a linear or non-linear mapping. The equation $Kx = y$ is called well-posed if the following holds:

1. Existence: For every $y \in Y$, $\exists$ (at least one) $x \in X$ such that $Kx = y$.
2. Uniqueness: For every $y \in Y$, $\exists$ at most one $x \in X$ with $Kx = y$.

3. Stability: The solution x depends continuously on y.

If any one of the above three properties does not hold, then the problem is called ill-posed.

In the context of THz spectroscopy, x is the sample's property of interest that cannot be measured directly (e.g. optical property), y is the time domain THz measurement, K is the mapping from x to y. In practice, y is most likely corrupted by noise, such as multipath reflections and scattering. This corruption may cause ill-posedness of the inverse problem, resulting in the poor reconstruction of x denoted by $\hat{x}$. To improve the quality of $\hat{x}$, a *regularisation* scheme, such as the Tikhonov regularisation scheme (Tikhonov and Samarskii 1963), is required. Details of regularisation can be found in Kirsch (1996).

Inverse scattering is the term used to refer to the study of inverse problems involving scattering (Tijhuis 1987, Popović and Taflove 2004). Since scattering is one concern in this Thesis, a proposed future direction is to utilise Tikhonov regularisation to solve inverse ill-posed THz scattering problems from biotissue, protein microstructures, stratified layers, and rough surfaces (Ogilvy 1991). Inverse scattering from stratified layers and rough surfaces would be of particular interest to the THz community researching security applications of THz, such as detection of hidden explosives (Oliveira *et al.* 2003, Oliveira *et al.* 2004), and land mines (Osiander *et al.* 2003, Bosq *et al.* 2005).

A.5 Appendix Summary

Four novel short case studies are presented to extend the novel work presented in this Thesis. Preliminary results and reviews from these studies aim to improve the extraction of information from THz measurements, and to improve the modelling of THz propagation and scattering from biotissue.

Appendix B

Nonlinearity in Materials

NONLINEAR materials were introduced in Chapter 3. This Appendix provides a brief overview of the terms and conventions used to describe nonlinearity. It also gives an overview of THz-related crystals that have nonlinear properties. The dependence of THz electro-optic (EO) generation on the geometries and orientations of nonlinear crystals is highlighted.

B.1 Susceptibility χ

This Section elaborates on the electric susceptibility χ introduced in Section 3.2.

When an electric field $\mathbf{E}$ is incident on a dielectric medium, a polarisation density vector $\mathbf{P}$ is emitted as shown in Fig. B.1. In a linear medium, the relationship between $\mathbf{E}$ and $\mathbf{P}$ is as follows:

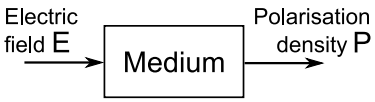

Figure B.1: Relationship between applied electric field strength and emitted polarisation density. The polarisation density vector $\mathbf{P}$ is emitted due to an applied electric field $\mathbf{E}$. After Saleh and Teich (1991).

$$\mathbf{P} = \epsilon_0 \chi^{(1)} \mathbf{E}, \tag{B.1}$$

where $\chi^{(1)}$ is the unitless scalar *electric susceptibility*. If the constant ϵ_0 is ignored, then $\chi^{(1)}$ is the transfer function describing the linear medium in Fig. B.1, and $\chi^{(1)}$ can be thought of as a parameter that describes the extent to which a medium produces a polarised output in response to the incident electric field. If $\chi^{(1)} = 0$ in a linear medium, then polarisation is not achievable. In Equation (3.1), $\mathbf{E}$ and $\mathbf{P}$ are expressed as $\tilde{\mathbf{E}}$ and $\tilde{\mathbf{P}}$ that vary rapidly over time: $\tilde{\mathbf{P}}(t) = \chi^{(1)}\, \tilde{\mathbf{E}}(t)$.

For a nonlinear medium, the transfer function describing the medium is also nonlinear. As expressed in Equation (3.3), the relationship between $\tilde{\mathbf{E}}$ and $\tilde{\mathbf{P}}$ is as follows:

$$\tilde{P}(t) = \chi^{(1)}\, \tilde{E}(t) + \chi^{(2)}\, \tilde{E}^2(t) + \chi^{(3)}\, \tilde{E}^3(t) + \chi^{(4)}\, \tilde{E}^4(t) + \cdots, \quad \text{[Equation (3.3)]}$$

where the scalar quantities of $\tilde{\mathbf{E}}$ and $\tilde{\mathbf{P}}$ are used in Equation (3.3) for simplicity (Yariv 1989, Boyd 2003).

B.1.1 Sample Values of $\chi^{(2)}$

Thus far, the electric susceptibilities $\chi^{(1)}$, $\chi^{(2)}$, and $\chi^{(3)}$ have been defined as a scalar property independent of geometry and frequency. By incorporating Cartesian components of the incident electric field into the electric susceptibilities, the following electric susceptibility tensors are obtained:

$$\begin{aligned} \chi^{(1)} &\rightarrow \chi^{(1)}_{ij} \\ \chi^{(2)} &\rightarrow \chi^{(2)}_{ijk} \\ \chi^{(3)} &\rightarrow \chi^{(3)}_{ijkl}, \end{aligned}$$

where the indices i, j, k, and l refer to the Cartesian indices.

If frequency components are included in the electric susceptibility tensors, the equations relating the scalar components of **P** to **E** become:

$$P_i^1(\omega_m) = \sum_j \chi_{ij}^{(1)}(\omega_m)\, E_j(\omega_m) \tag{B.2}$$

$$P_i^2(\omega_m + \omega_n) = \sum_{jk}\sum_{mn} \chi_{ijk}^{(2)'}(-\omega_m - \omega_n, \omega_m, \omega_n)\, E_j(\omega_m) E_k(\omega_n) \tag{B.3}$$

$$P_i^3(\omega_m + \omega_n + \omega_o) = \sum_{jkl}\sum_{mno} \chi_{ijkl}^{(3)'}(-\omega_m - \omega_n - \omega_o, \omega_m, \omega_n, \omega_o) \ldots E_j(\omega_m) E_k(\omega_n) E_k(\omega_o)\,, \tag{B.4}$$

where $\chi_{ijk}^{(2)'}$ and $\chi_{ijkl}^{(3)'}$ are the conjugates of $\chi_{ijk}^{(2)}$ and $\chi_{ijkl}^{(3)}$ respectively. The number of electric susceptibility tensors $\chi_{ijk}^{(2)}$ and $\chi_{ijkl}^{(3)}$ increase significantly considering the different permutations of the Cartesian indices, and the frequencies ω_m , ω_n , and ω_o . The *contracted notation* is one way to reduce the number of electric susceptibility tensors, whereby:

$$d_{ijk} = \frac{1}{2}\chi_{ijk}^{(2)} \tag{B.5}$$

$$d_{ijkl} = \frac{1}{2}\chi_{ijkl}^{(2)}\,, \tag{B.6}$$

provided the Kleinman symmetry condition is fulfilled as follows:

$$\begin{aligned}\chi_{ijk}^{(2)}(\omega_3 = \omega_1 + \omega_2) &= \chi_{jki}^{(2)}(\omega_3 = \omega_1 + \omega_2) = \chi_{kij}^{(2)}(\omega_3 = \omega_1 + \omega_2) = \chi_{ikj}^{(2)}(\omega_3 = \omega_1 + \omega_2) \\ &= \chi_{jik}^{(2)}(\omega_3 = \omega_1 + \omega_2) = \chi_{kji}^{(2)}(\omega_3 = \omega_1 + \omega_2)\,.\end{aligned} \tag{B.7}$$

Details of $\chi_{ij}^{(1)}$, $\chi_{ijk}^{(2)}$, $\chi_{ijkl}^{(3)}$, the contracted notation, and the Kleinman symmetry condition are found in Boyd (2003) and Kaminow (1974). As described in Equation (3.5), $\chi^{(2)}$ and other even harmonics are of interest in optical rectification. Therefore, sample values of $\chi^{(2)}$ in contracted notation are listed in Table B.1.

B.2 Noncentrosymmetrical Crystals

This Section provides a summary of commonly used nonlinear, THz-related crystals alluded to in Sections 3.2.1 and 3.10. As shown in Table B.2, a variety of semiconductor crystals available for THz applications exceeds those of organic and inorganic ones. A brief explanation of crystal structure and point group will be given in Section B.3.

Material	d_{il} ($\times 10^{-9}$cm/statvolt)
lithium niobate ($LiNbO_3$)	d_{22} = 7.4, d_{31} = 14, d_{33} = -98
gallium arsenide (GaAs)	d_{36} = 406
beta barium borate (BBO)	d_{11} = 4.6
quartz	d_{11} = 0.96, d_{14} = 0.02

Table B.1: Examples of $\chi^{(2)}$ of several THz-related crystals. Second order nonlinear optical susceptibilities in contracted notation, where $\chi^{(2)} = 2d_{il}$. Note that in the gaussian system of units, 1 statvolt = 299.8 volts. If assuming $P = dE^2$, then multiply d_{il} by $4\pi\epsilon_0/(3 \times 10^4)$ to convert d_{il} to MKS units of C/V^2. After Boyd (2003).

Semiconductor Crystal	Crystal Structure	Point Group
zinc telluride (ZnTe)	cubic (zincblende)	$\bar{4}$3m
gallium arsenide (GaAs)	cubic (zincblende)	$\bar{4}$3m
gallium phosphide (GaP)	cubic (zincblende)	$\bar{4}$3m
indium antimonide (InSb)	cubic (zincblende)	$\bar{4}$3m
indium phosphide (InP)	cubic (zincblende)	$\bar{4}$3m
indium arsenide (InAs)	cubic (zincblende)	$\bar{4}$3m
cadmium telluride (CdTe)	cubic (zincblende)	$\bar{4}$3m
zinc cadmium telluride (ZnCdTe)	cubic (zincblende)	$\bar{4}$3m
gallium selenide (GaSe)	hexagonal	$\bar{6}$2m
silicon-on-sapphire (SOS)	hexagonal	–
Inorganic Crystal	**Crystal Structure**	**Point Group**
lithium niobate ($LiNbO_3$)	trigonal	3m
lithium tantalate ($LiTaO_3$)	trigonal	3m
beta barium borate (BBO)	trigonal	3m
Organic Crystal	**Crystal Structure**	**Point Group**
4-N-methylstilbazolium tosylate (DAST)	monoclinic	m

Table B.2: Examples of nonlinear THz-related crystals. The dashed lines indicate that the relevant information was not found from literature. After Dmitriev *et al.* (1999), Liu *et al.* (2004), Schneider *et al.* (2006), Wilke and Sengupta (2008), and Ruiz *et al.* (2008).

The popularity of a crystal for THz emission and detection usually depends on the crystal's figure-of-merit, its group velocity mismatch (GVM), and its phonon resonances; a high figure-of-merit and low GVM is desired (Wu and Zhang 1996b). For example, DAST has a figure-of-merit of 633 pm/V and a GVM of 1.22 ps/mm. By contrast, $LiTaO_3$ has a figure-of-merit of 87.2 pm/V and a GVM of 14.1 ps/mm. Although DAST has the best electro-optic properties among the crystals listed in Table B.2, it has two phonon resonances between 0.1–3.1 THz (Schneider *et al.* 2006), therefore making it less desirable as a THz emitter than other crystals listed above that have phonon resonances at higher THz frequencies. For example, ZnCdTe has a phonon resonance at 5.3 THz (Liu *et al.* 2002).

B.3 Introduction to Nonlinear Crystal Geometry

In Section 3.9, both electro-optic (EO) THz generation and detection are described as being dependent on the physical orientation of the nonlinear crystal. This Section briefly introduces the conventions used in crystallography to describe the geometries and orientations of crystals. These conventions are then used in Section B.3.4 to briefly highlight the dependence of THz EO generation on crystal type and orientation.

B.3.1 Miller Index

In crystallography, the Miller index is a notational system that describes planes in crystals, and directions orthogonal to the surface of planes. The Miller index comprises of set of coordinates (e.g. 110) enclosed between one of four types of brackets, e.g. (110), {110}, [110], or <110>. The parentheses denote a specific plane, such as the 110 plane shown in Fig. B.2; the curly braces denote a set of planes; the square brackets denote a direction orthogonal to the plane as shown in shown in Fig. B.3; and the angled brackets denote a set of symmetrically equivalent directions.

In Fig. B.3(a), the directions [100], [010], and [001] are illustrated. The respective reverse directions $[\bar{1}00]$, $[0\bar{1}0]$, and $[00\bar{1}]$ are not illustrated for brevity. All six directions are symmetrically equivalent, hence they can be categorised by one Miller index <100>. In Fig. B.3(b), only 3 directions are illustrated in this figure although several others exist. A collection of directions are symmetrically equivalent, and are categorised by Miller index <110>. In Fig. B.3(c), Miller index <111> represents the symmetrically equivalent directions as listed.

NOTE:
This figure is included on page 316 of the print copy of the thesis held in the University of Adelaide Library.

Figure B.2: Miller indices for planes. Adapted from Wikipedia (2009).

NOTE:
This figure is included on page 316 of the print copy of the thesis held in the University of Adelaide Library.

Figure B.3: Miller indices for directions. Reverse directions are denoted by a negative sign in this Figure (e.g. -1); in the Miller index notation, reverse directions are denoted by a bar above the number (e.g. $\bar{1}$). Adapted from Brigham Young University (2009).

B.3.2 Bravais Lattice

The lattice of a crystal consists of a periodic array of atoms. The Bravais lattice is used to describe how the atoms in a lattice are arranged. As illustrated in Fig. B.4, there are 14 Bravais lattices. In the context of THz generation, zinc telluride (ZnTe) has a cubic face-centred crystal structure. The 14 Bravais lattices can be further categorised into 7 crystal systems as listed in Table B.3. The crystal system is used in the next Subsection to define the point group of a crystal.

NOTE:
This figure is included on page 317 of the print copy of the thesis held in the University of Adelaide Library.

Figure B.4: Schematic of the 14 Bravais lattices. After Pietrovito and Davies (2007).

Bravais Lattice	Crystal System	Bravais Lattice	Crystal System
triclinic	triclinic	hexagonal	hexagonal
simple monoclinic base-centred monoclinic	monoclinic	simple tetragonal body-centred tetragonal	tetragonal
simple orthorhombic body-centred orthorhombic base-centred orthorhombic face-centred orthorhombic	orthorhombic	simple cubic face-centred cubic body-centred cubic	cubic
rhombohedral	trigonal	–	–

Table B.3: Bravais lattices. The 14 Bravais lattices can be categorised into 7 crystal systems. After Kaminow (1974).

B.3.3 Point Groups

By knowing the crystal system of a crystal, the point group (or *crystal class*) can then be defined in order to describe the symmetry of a crystal. There are 32 point groups as listed in Table B.4 below. The symbols used to define the point groups follow the Hermann-Mauguin convention. In this convention, the numbers 1,2,3,4,6 denote rotational axes; $\bar{1}$,$\bar{2}$,$\bar{3}$,$\bar{4}$,$\bar{6}$ denote rotoinversion axes; the alphabet 'i' denotes inversion; and the alphabet 'm' denotes mirror planes.

Crystal System	Point Group	Crystal System	Point Group	Crystal System	Point Group
triclinic	1	–	–	–	–
	$\bar{1}$				
monoclinic	m	orthorhombic	2mm	trigonal	3
	2		222		$\bar{3}$
	2/m		mmm		3m
	–		–		32
	–		–		$\bar{3}$m
tetragonal	4	hexagonal	6	cubic	23
	$\bar{4}$		$\bar{6}$		m3
	4/m		6/m		$\bar{4}$3m
	4mm		$\bar{6}$m2		432
	$\bar{4}$2m		6mm		m3m
	422		622		–
	4/mmm		6/mmm		–

Table B.4: Point groups using the Hermann-Mauguin convention. The numbers 1,2,3,4,6 denote rotational axes; $\bar{1}$,$\bar{2}$,$\bar{3}$,$\bar{4}$,$\bar{6}$ denote rotoinversion axes; the alphabet 'i' denotes inversion; and the alphabet 'm' denotes mirror planes. After Kaminow (1974).

B.3.4 Dependence of THz Generation on Crystal Properties

As summarised in Wilke and Sengupta (2008), electro-optic (EO) THz generation has been reported from <100>, <110>, and <111> zincblende crystals that have cubic Bravais lattice, and $\bar{4}$3m point group. The extent of THz generation varies between the different symmetry directions of each type of crystal. Furthermore, the angles of incidence and polarisation of the incident laser pulse, with respect to the surface of the crystal, also influence the extent of EO rectification in the different types of crystal.

In <110> and <111> zincblende crystals, a three-fold rotational symmetry exists as the crystal is rotated through 360°. This means that there are three rotational angles where the THz peaks are strongest. Two-fold and four-fold symmetry can exist depending on the polarisation angle of the incident laser pulse (Zhang *et al.* 1992a).

Appendix C

Main and Auxiliary Equipment for Terahertz Measurements

SEVERAL THz-TDS systems are used to conduct experiments reported in Chapters 5–8. This Appendix lists the equipment used in the various THz-TDS systems. It also lists the auxiliary laboratory equipment highlighted in Chapters 3 and 5.

C.1 Components of THz-TDS Systems Used

Tables C.1–C.4 list the THz-related laboratory equipment used to conduct experiments reported in this Thesis. Since the experiments are conducted in several locations globally, the Tables include references to the locations of the equipment, and the appropriate Chapters in this Thesis.

C.2 Hank's Buffer

In Section 5.3.1, Hank's buffer is used to preserve the freshly excised biotissue samples. Hank's buffer is a salt solution that is balanced at around pH 7, and contains glucose. Glucose is important for sustaining the freshly excised biotissue samples in Chapter 5. Phenol red is often added into Hank's buffer as a pH indicator. The type of Hank's buffer used in the experiment in Chapter 5 does not contain phenol red.

The main ingredients in Hank's buffer are:

sodium chloride (NaCl)	glucose
potassium chloride (KCl)	magnesium sulfate ($MgSO_4$)
sodium phosphate dibasic (Na_2HPO_4)	calcium chloride (CaCl)
potassium phosphate monobasic (KH_2PO_4)	sodium bicarbonate

University of Adelaide (Picometrix)			
Purpose	**Equipment Type**	**Manufacturer**	**Model**
Femtosecond laser pulse generation	Ultrafast laser	Spectra Physics	Mai Tai
THz generation	Fibre-coupled	Picometrix	T-ray 2000
THz detection	Fibre-coupled	Picometrix	T-ray 2000

Table C.1: List of equipment used at the University of Adelaide for experiments reported in this Thesis. The experiments described in Chapters 6 and 7, and Appendix Sections A.1 and A.3 are conducted on this system. The Spectra Physics Mai Tai ultrafast laser has a built-in pump laser.

University of Adelaide (PCA)			
Purpose	**Equipment Type**	**Manufacturer**	**Model**
Femtosecond laser pulse generation	Ultrafast laser	Coherent	Mira Seed
Pump laser for femtosecond laser	Green laser	Coherent	Verdi V6 DPSS
THz generation	PCA	Zomega	PCA-GAAS-BT40
THz detection	PCA	Zomega	PCA-GAAS-BT40
High voltage power supply	DC bias to PCA	Zomega	HVM-500
Delay stage	Motorised translation stage	Newport	ILS250CC
Motion controller for delay stage	Universal motion controller	Newport	ESP300
Optical modulation	Chopper	Thor Labs	MC1000A
Phase sensitive detection	Lock-in amplifier	Stanford Research Systems	SR830

Table C.2: List of equipment used at the University of Adelaide for experiments reported in this Thesis. The experiments described in Chapters 7 and 8 are conducted on this system. The green pump laser is the diode-pumped solid state (DPSS) type.

Rensselaer Polytechnic Institute (RPI)			
Purpose	**Equipment Type**	**Manufacturer**	**Model**
Femtosecond laser pulse generation	Ultrafast laser	Coherent	Mira 900
Pump laser for femtosecond laser	Green laser	Coherent	Verdi V18 DPSS
THz generation	ZnTe	Zomega	2 mm thick
THz detection	ZnTe	Zomega	1 mm thick
Delay stage and motor	Translation stage and stepper motor	Newport	850G
Motion controller for delay stage	Universal motion controller	Newport	ESP300
Optical modulation	Chopper	Stanford Research Systems	SR540
Phase sensitive detection	Lock-in amplifier	Stanford Research Systems	SR830
Intensity detection	Photodetectors	Manufactured in-house	–

Table C.3: List of equipment used at Rensselaer Polytechnic Institute (RPI) for experiments reported in this Thesis. The experiments described in Chapter 5 are conducted on this system. The green pump laser is the diode-pumped solid state (DPSS) type.

University of Leeds			
Purpose	**Equipment Type**	**Manufacturer**	**Model**
Femtosecond laser pulse generation	Ultrafast laser	Spectra Physics	Tsunami
Pump laser for femtosecond laser	Green laser	Spectra Physics	Millenia Xs DPSS
THz generation	GaAs PCA	Manufactured in-house	–
THz detection	ZnTe	–	2 mm thick
High voltage power supply	DC bias to PCA	Kikusui	PMC350
Delay stage	Motorised translation stage	Melles Griot	NST
Motor on translation stage	Stepper motor	Melles Griot	EAS
Motion controller for delay stage	Stepper motor controller	Melles Griot	EAS
Phase sensitive detection	Lock-in amplifier	Perkin Elmer/Signal Recovery	7265
Intensity detection	Photodetectors	New Focus	Nirvana 2007

Table C.4: List of equipment used at the University of Leeds for experiments reported in this Thesis. The experiments described in Chapter 8 are conducted on this system. The green pump laser is the diode-pumped solid state (DPSS) type.

Appendix D

Mathematical Derivation of the Complex Refractive Index

THE complex refractive index, containing the real and imaginary components, were introduced in Chapter 5. This Appendix presents the mathematical derivation of the complex refractive index in the context of polar molecules, which were defined in Section 4.2.

D.1 Derivation of the Complex Refractive Index $\hat{n}(\omega)$

The formal derivation of Equation (5.11) in the context of polar molecules is given in this Section. Explanations of the variables used in Equation (5.16) are also given. The mathematics and explanations presented are extracted from Jackson (1975), Born and Wolf (1999), and Hecht (2002).

D.1.1 Complex Refractive Index $\hat{n}(\omega)$

In Born and Wolf (1999), Maxwell's equation for an electric field $\mathbf{E}$ in the form of the three-dimensional wave equation is given by Equation (D.1) as follows:

$$\nabla^2\mathbf{E} = \frac{\mu\epsilon}{c^2}\frac{\partial^2\mathbf{E}}{\partial t^2} + \frac{4\pi\mu\sigma}{c^2}\frac{\partial\mathbf{E}}{\partial t}, \tag{D.1}$$

where μ, ϵ and σ are the magnetic permeability, electric permittivity, and electric conductivity of a non free-space medium respectively; c is the speed of light *in vacuo*.

The Fourier transforms of $\frac{\partial}{\partial t}$ and $\frac{\partial^2}{\partial t^2}$ are $i\omega$ and $(i\omega)^2$ respectively, where ω is the angular frequency. The Fourier transform of Equation (D.1) yields:

$$\begin{aligned} \nabla^2\mathbf{E} &= \frac{-\mu\epsilon\omega^2}{c^2}\mathbf{E} + \frac{4\pi\mu\sigma i\omega}{c^2}\mathbf{E} \\ &= \left(\frac{-\mu\epsilon\omega^2}{c^2} + \frac{4\pi\mu\sigma i\omega}{c^2}\right)\mathbf{E}, \end{aligned} \tag{D.2}$$

$$\nabla^2\mathbf{E} + \left(\frac{\mu\epsilon\omega^2}{c^2} - \frac{4\pi\mu\sigma i\omega}{c^2}\right)\mathbf{E} = 0$$

$$\begin{aligned} \text{where} \quad \hat{k}^2 &= \frac{\mu\epsilon\omega^2}{c^2} - \frac{4\pi\mu\sigma i\omega}{c^2} \\ &= \frac{\mu\omega^2}{c^2}\left(\epsilon - i\frac{4\pi\sigma}{\omega}\right). \end{aligned} \tag{D.3}$$

From Equation (D.3), the electric permittivity ϵ is now a complex number. Therefore, ϵ is now expressed as:

$$\hat{\epsilon} = \epsilon - i\frac{4\pi\sigma}{\omega}. \tag{D.4}$$

Substituting Equation (D.4) into the equation of velocity $v = 1/\sqrt{\mu\epsilon}$ results in:

$$\hat{v} = \frac{1}{\sqrt{\mu\hat{\epsilon}}} \tag{D.5}$$

$$\text{and} \quad \hat{n} = \frac{c}{\hat{v}} = \sqrt{\mu\hat{\epsilon}} = \frac{c\hat{k}^2}{\omega}. \tag{D.6}$$

This means that the refractive index is now a complex number, which can be expressed as shown in Equation (5.11): $\hat{n}(\omega) = n(\omega) - i\kappa(\omega)$.

D.1.2 Explanation of Variables Used in Equation (5.16)

Polar molecules were defined in Section 4.2 as being molecules that have a permanent dipole moment[81] $P(t)$ due to an equal sharing of valence electrons. In the absence of any electric field, thermal agitation keeps a polar molecule's dipoles randomly oriented. In the presence of a static electric field $\mathbf{E}$, the polar molecule's internal charge distribution is distorted due to the generation of electric dipole moments. The resultant dipole moment per unit volume is called the *electric polarisation* $\mathbf{P}$, whereby:

$$(\hat{\epsilon} - \epsilon_0)\mathbf{E} = \mathbf{P}, \tag{D.7}$$

where ϵ_0 is the permittivity of free-space *in vacuo*, and $\hat{\epsilon}$ is the permittivity of a non free-space medium. $\mathbf{P}$ is in the same direction as $\mathbf{E}$. This means that the dipoles align themselves with the applied $\mathbf{E}$ so that the medium now has an *orientation polarisation*.

In the presence of a time varying (harmonic) electric field $\mathbf{E}(t)$, the polar molecules undergo rapid rotations and align themselves with the $\mathbf{E}(t)$ field. If $\mathbf{E}(t)$ varies too quickly (e.g. at high driving angular frequencies ω), then the polar molecules are unable to align themselves fast enough with the alternating $\mathbf{E}(t)$. This reduces the polar molecules' electric polarisation $\mathbf{P}$. However, the electrons of a polar molecule, each with charge q_e and mass m_e, are small and have little inertia when compared to the whole polar molecule. These electrons can follow the changing $\mathbf{E}(t)$, i.e. the electrons can align themselves fast enough at different frequencies ω. Since the electrons are bound to the nucleus of the atom, the electrons behave like *forced oscillators* as they move in response to $\mathbf{E}(t)$, with each electron experiencing a force $F_e = q_e E(t)$.

In the presence of $\mathbf{E}(t)$, the relative displacement $x(t)$ of the electrons with respect to the atom's nucleus is expressed as follows:

$$x(t) = \frac{q_e}{m_e\left(\omega_0^2 - \omega^2\right)} E(t), \tag{D.8}$$

where ω_0 is the resonant frequency of the oscillator, and ω is the frequency of $\mathbf{E}(t)$. The dipole moment $P(t)$ of N oscillators can therefore be expressed as:

$$P(t) = q_e\, x(t)\, N = \frac{N q_e^2 E(t)}{m_e\left(\omega_0^2 - \omega^2\right)}. \tag{D.9}$$

Substituting Equation (D.9) into Equation (D.7) gives:

$$\hat{\epsilon} = \epsilon_0 + \frac{P(t)}{E(t)} = \epsilon_0 + \frac{q_e^2 N}{m_e\left(\omega_0^2 - \omega^2\right)}. \tag{D.10}$$

[81] A dipole moment is a vector quantity $\mathbf{P}$ that points from the negative to the positive charge, or from the south to the north pole (magnetic dipole moment $\boldsymbol{\mu}$).

Since $\hat{n}^2(\omega) = \hat{\epsilon}/\epsilon_0$, then

$$\hat{n}^2(\omega) = 1 + \frac{q_e^2 N}{\epsilon_0 m_e}\left(\frac{1}{\omega_0^2 - \omega^2}\right). \tag{D.11}$$

Referring to Equation (D.8), if $\omega > \omega_0$, then $(\omega_0^2 - \omega^2) < 0$. This means that $x(t) \propto -E(t)$, implying that the displacement is 180° out-of-phase to the excitation $E(t)$. If $\omega < \omega_0$, then $(\omega_0^2 - \omega^2) > 0$. This means that $x(t) \propto E(t)$, implying that the displacement is in-phase with the excitation $E(t)$. To account for more than one resonant frequency, Equation (D.11) is modified as follows:

$$\hat{n}^2(\omega) = 1 + \frac{q_e^2 N}{\epsilon_0 m_e}\sum_k\left(\frac{f_k}{\omega_{0k}^2 - \omega^2}\right), \tag{D.12}$$

where f_k are transitional probabilities (or oscillator strengths), such that $\sum_k f_k = 1$.

To account for damping in the oscillator model describing the electrons, a damping factor proportional to the speed of the oscillators' motion is included in Equation (D.12) to give:

$$\hat{n}^2(\omega) = 1 + \frac{N q_e^2}{\epsilon_0 m_e}\sum_k \frac{f_k}{\omega_{0k}^2 - \omega^2 + i\gamma_k\omega}, \qquad \text{[Equation (5.16)]}$$

where γ_k is the damping force experienced by an atom in a dense material due to the induced field set up by neighbouring atoms.

D.2 Derivation of the Real Refractive Index $n(\omega)$

The formal derivation of Equation (5.22) is given in this Section. The derivation utilises the Fresnel equations, thus the Fresnel equations are defined first in the next Subsection. The derivation of Equation (5.22) then follows.

D.2.1 The Fresnel Equations

Assume an electric field with amplitude E_{0i} travels in a medium with refractive index n_i. If the field is incident at angle θ onto a linear, isotropic and homogeneous medium with refractive index n_t, then the Fresnel equations describe the relationship between E_{0i} and the transmitted and reflected electric field amplitudes E_{0t} and E_{0r} respectively.

The Fresnel equations consist of the amplitude transmission coefficients $T_\perp$ and $T_\parallel$, and the reflection coefficients $R_\perp$ and $R_\parallel$:

$$T_\perp = \left(\frac{E_{0t}}{E_{0i}}\right)_\perp = \frac{2n_i\cos\theta_i}{n_i\cos\theta_i + n_t\cos\theta_t} = +\frac{2\sin\theta_t\cos\theta_i}{\sin(\theta_i + \theta_t)} \tag{D.13}$$

$$T_{\parallel} = \left(\frac{E_{0t}}{E_{0i}}\right)_{\parallel} = \frac{2n_i\cos\theta_i}{n_i\cos\theta_t + n_t\cos\theta_i} = +\frac{2\sin\theta_t\cos\theta_i}{\sin(\theta_i+\theta_t)\cos(\theta_i-\theta_t)} \tag{D.14}$$

$$R_{\perp} = \left(\frac{E_{0r}}{E_{0i}}\right)_{\perp} = \frac{n_i\cos\theta_i - n_t\cos\theta_t}{n_i\cos\theta_i + n_t\cos\theta_t} = -\frac{\sin(\theta_i-\theta_t)}{\sin(\theta_i+\theta_t)} \tag{D.15}$$

$$R_{\parallel} = \left(\frac{E_{0r}}{E_{0i}}\right)_{\parallel} = \frac{n_t\cos\theta_i - n_i\cos\theta_t}{n_i\cos\theta_t + n_t\cos\theta_i} = +\frac{\tan(\theta_i-\theta_t)}{\tan(\theta_i+\theta_t)}, \tag{D.16}$$

where $\perp$ implies the incident electric field $\mathbf{E}_i$ is perpendicular to the plane of incidence (in other words, the incident $\mathbf{E}_i$ is parallel to the tangent plane of the interface), while $\parallel$ implies the incident electric field $\mathbf{E}_i$ is parallel to the plane of incidence.

If the incident and transmitted fields are orthogonal to the plane of incidence, then Equation (D.13) and Equation (D.14) simplify to:

$$T_{\perp} = T_{\parallel} = T_{i\to t} = \frac{E_{0t}}{E_{0i}} = \frac{2n_i}{n_i+n_t} \tag{D.17}$$

$$T_{t\to i} = \frac{E_{0i}}{E_{0t}} = \frac{2n_t}{n_i+n_t}. \tag{D.18}$$

D.2.2 Real Refractive Index $n(\omega)$

Let $E_{ref}(z,t)$ be the one dimensional wave equation of an electric field propagating along the z axis in a medium (called the reference medium) with complex refractive index $\hat{n}_r(\omega)$. The complex one dimensional wave equation is expressed as:

$$E_{ref}(z,t) = E\,e^{-i(\omega t - kz)}, \tag{D.19}$$

where the wavenumber k is equal to:

$$k = \frac{2\pi}{\lambda} = \frac{2\pi\nu}{\text{speed } v \text{ in medium}} = \frac{\omega\hat{n}_r(\omega)}{c}. \tag{D.20}$$

Substituting Equation (D.20) into Equation (D.19) gives:

$$\begin{aligned} E_{ref}(z,t) &= E\,e^{-i[\omega t - \frac{\omega\hat{n}_r(\omega)z}{c}]} = E\,e^{-i\omega t}\,e^{\frac{i\omega\hat{n}_r(\omega)z}{c}} = E\,e^{-i\omega t}\,e^{\frac{i\omega[n_r(\omega)+i\kappa_r(\omega)]z}{c}} \\ &= E\,e^{-i\omega t}\,e^{\frac{i\omega n_r(\omega)z}{c}}\,e^{\frac{-\omega\kappa_r(\omega)z}{c}} = E(t)\underbrace{e^{\frac{i\omega n_r(\omega)z}{c}}\,e^{\frac{-\omega\kappa_r(\omega)z}{c}}}_{E_{ref}(z,\omega)}. \end{aligned} \tag{D.21}$$

If $E_{ref}(z,t)$ is incident on a sample (called the sample medium) with complex refractive index $\hat{n}_s(\omega)$ and thickness d, whereby the sample is surrounded by the reference medium, then the transmitted electric field emerging from the sample can be expressed

in terms of the Fresnel amplitude transmission coefficients T (either $T_\parallel$ or $T_\perp$) defined in Equation (D.17) and Equation (D.18):

$$\begin{aligned} E_{\text{sample}}(z,t) &= E_{\text{ref}}(z,t)\, T_{\text{ref}\to\text{sample}}\, T_{\text{sample}\to\text{ref}} \\ &= \left[E(t)\, e^{\frac{i\omega n_s(\omega)d}{c}}\, e^{\frac{-\omega\kappa_s(\omega)d}{c}}\right] \frac{2\hat{n}_r(\omega)}{\hat{n}_r(\omega)+\hat{n}_s(\omega)} \frac{2\hat{n}_s(\omega)}{\hat{n}_r(\omega)+\hat{n}_s(\omega)}\,. \end{aligned} \tag{D.22}$$

If the reference medium is vacuum, then $\hat{n}_r(\omega) = 1 - i0$, so Equation (D.22) simplifies to:

$$E_{\text{sample}}(z,t) = E(t) \underbrace{e^{\frac{i\omega n_s(\omega)d}{c}}\, e^{\frac{-\omega\kappa_s(\omega)d}{c}} \frac{4\hat{n}_s(\omega)}{\left[1+\hat{n}_s(\omega)\right]^2}}_{E_{\text{sample}}(z,\omega)}\,. \tag{D.23}$$

Dividing only the frequency dependent terms in Equations (D.23) and (D.21) for the case when $\hat{n}_r(\omega) = 1 - i0$ gives:

$$\begin{aligned} \frac{E_{\text{sample}}(z,\omega)}{E_{\text{ref}}(z,\omega)} &= \frac{A_s\, e^{i\phi_s(\omega)}}{A_r\, e^{i\phi_r(\omega)}} = \frac{4\hat{n}_s(\omega)}{\left[1+\hat{n}_s(\omega)\right]^2} \frac{e^{\frac{i\omega n_s(\omega)d}{c}}\, e^{\frac{-\omega\kappa_s(\omega)d}{c}}}{e^{\frac{i\omega d}{c}}} \\ &= \frac{4\hat{n}_s(\omega)}{\left[1+\hat{n}_s(\omega)\right]^2} e^{\frac{i\omega[n_s(\omega)-1]d}{c}}\, e^{\frac{-\omega\kappa_s(\omega)d}{c}}\,. \end{aligned} \tag{D.24}$$

If $\kappa_s(\omega) \ll n_s(\omega)$, then Equation (D.24) can be approximated by:

$$\left[\frac{E_{\text{sample}}(z,\omega)}{E_{\text{ref}}(z,\omega)} = \frac{A_s\, e^{i\phi_s(\omega)}}{A_r\, e^{i\phi_r(\omega)}}\right] \equiv \underbrace{\frac{4n_s(\omega)}{\left[1+n_s(\omega)\right]^2} e^{\frac{-\omega\kappa_s(\omega)d}{c}}}_{\text{magnitude}} \underbrace{e^{\frac{i\omega[n_s(\omega)-1]d}{c}}}_{\text{phase}}$$

$$\begin{aligned} \Rightarrow \phi_s(\omega) - \phi_r(\omega) &= \frac{\omega[n_s(\omega)-1]d}{c} \\ n_s(\omega) &= \frac{[\phi_s(\omega)-\phi_r(\omega)]c}{\omega d} + 1\,, \qquad \text{[Equation (5.22)]} \\ \text{and}\quad \frac{A_s}{A_r} &= \frac{4n_s(\omega)}{\left[1+n_s(\omega)\right]^2}\; e^{\frac{-\omega\kappa(\omega)d}{c}} \\ \text{so}\quad \kappa(\omega) &= -\frac{c}{\omega d}\ln\left(\frac{A_s\left[1+n_s(\omega)\right]^2}{4A_r n_s(\omega)}\right) \\ \alpha(\omega) = \frac{2\omega\kappa(\omega)}{c} &= \frac{-2}{d}\ln\left(\frac{A_s\left[1+n_s(\omega)\right]^2}{4A_r n_s(\omega)}\right)\,. \quad \text{[Equation (5.21)]} \end{aligned} \tag{D.25}$$

If $\kappa_s(\omega) \not\ll n_s(\omega)$, then Equation (D.24) is solved iteratively (Duvillaret *et al.* 1996, Duvillaret *et al.* 1999).

Appendix E

Neuropsychological Assessment of Alzheimer's Disease

ASSESSMENT of dementia currently involves a battery of physical and neuropsychological tests. Oral questionnaires are often used to compare a patient's psychological performance against a benchmark. This Appendix reproduces one popular neuropsychological test, the Modified Mini Mental State (3MS) Examination, to highlight some of the difficulties in catering to all demographics. Examples of dementia types are also provided.

E.1 The Modified Mini Mental State (3MS) Examination

The Modified Mini Mental State (3MS) Examination introduced in Section 6.2.2 is reproduced in Table E.1. More details of this examination, including a more comprehensive explanation of the scoring system utilised, is given in Teng and Chui (1987).

As can be seen in the 3MS questionnaire, the questions may not cater to all demographics. A patient's level of education, life experiences, proficiency in language, and state of mind (e.g. nervousness on the day of test) may skew the results of the test, resulting in inaccurate diagnosis. As a result, oral questionnaires are usually used in conjunction with other types of examinations (such as blood tests, MRI scans, and behavioural observations) to more confidently identify the type of dementia.

E.2 Types of Dementia

The following list presents examples of dementias (Hannay *et al.* 2004).

Cortical Dementias

Alzheimer's Disease (AD)
Dementia with Lewy Bodies (DLB)
Frontal lobe dementia
Other cortical atrophies

Subcortical Dementias

Parkinson's disease/Parkinsonism (PD)
Progressive Supranuclear Palsy (PSP)
Huntington's disease (HD)

Vascular Disorders

Stroke
Hypertension
Migraine
Vascular dementia
Multi-infarct dementia

Other progressive disorders of the Central Nervous System where neuropsychological effects may be prominent

Normal Pressure Hydrocephalus (NPH)
Multiple Sclerosis (MS)

NOTE:
This table is included on page 333
of the print copy of the thesis held in
the University of Adelaide Library.

Table E.1: Modified Mini-Mental State (3MS) Examination. (Continued overleaf) After Teng and Chui (1987).

NOTE:
This table is included on page 334
of the print copy of the thesis held in
the University of Adelaide Library.

Table E.1: Modified Mini-Mental State (3MS) Examination (continued). After Teng and Chui (1987).

Appendix F

The Mathematics of Scattering-Related Theories

THIS Appendix presents the derivations of scattering-related equations used in Chapters 7 and 8. Other scattering models highlighted in Section 8.3 are also discussed briefly. In addition, an example of the use of one such model to study the impact of skin surface roughness in the THz regime is presented.

F.1 Introduction

Mie and Rayleigh scattering models for cylinders were introduced in Sections 7.5.1 and 8.3, and then utilised in Sections 7.5.1 and 8.6 to validate experimental results. Derivations of the equations utilised in Sections 7.5.1 and 8.6 are presented in the next Section. The derivations begin with exploring spherical scatterers because the equations for cylindrical scatterers are based on them. The Appendix concludes with brief discussions of the Rayleigh-Gans model, geometrical optics, and the Beckmann distribution function, where a THz application of the Beckmann distribution function is given (Png *et al.* 2007). The bulk of mathematics presented in this Appendix follows Bohren and Huffman (1983).

F.2 Spherical Scatterers

The Mie scattering model for a sphere is introduced in this Section as a precursor to the Mie scattering model for a cylinder.

F.2.1 Plane Wave Equation in Cartesian Coordinates

In a linear, isotropic, homogeneous medium, a physically realisable time-harmonic electromagnetic field $(\mathbf{E}, \mathbf{H})$ must satisfy the wave equation:

$$\frac{\partial^2 \mathbf{E}}{\partial x^2} + \frac{\partial^2 \mathbf{E}}{\partial y^2} + \frac{\partial^2 \mathbf{E}}{\partial z^2} + k^2 \mathbf{E} = \nabla^2 \mathbf{E} + k^2 \mathbf{E} = 0, \tag{F.1}$$

$$\frac{\partial^2 \mathbf{H}}{\partial x^2} + \frac{\partial^2 \mathbf{H}}{\partial y^2} + \frac{\partial^2 \mathbf{H}}{\partial z^2} + k^2 \mathbf{E} = \nabla^2 \mathbf{H} + k^2 \mathbf{H} = 0, \tag{F.2}$$

where $k^2 = \omega^2 \epsilon \mu$, and $(\mathbf{E}, \mathbf{H})$ must be divergence free:

$$(\mathbf{i}\frac{\partial}{\partial x} + \mathbf{j}\frac{\partial}{\partial y} + \mathbf{k}\frac{\partial}{\partial z}) \cdot \mathbf{E} = \nabla \cdot \mathbf{E} = 0, \tag{F.3}$$

$$(\mathbf{i}\frac{\partial}{\partial x} + \mathbf{j}\frac{\partial}{\partial y} + \mathbf{k}\frac{\partial}{\partial z}) \cdot \mathbf{H} = \nabla \cdot \mathbf{H} = 0. \tag{F.4}$$

Note $\mathbf{E}$ and $\mathbf{H}$ are not independent because

$$\nabla \times \mathbf{E} = i\omega\mu\mathbf{H}, \qquad \nabla \times \mathbf{H} = -i\omega\mu\mathbf{E}.$$

F.2.2 Plane Wave Equation of a Sphere

In spherical coordinate, the scalar wave equation Equation (F.1) becomes:

$$\frac{1}{r^2}\frac{\partial}{\partial r}\left(r^2\frac{\partial\psi}{\partial r}\right)+\frac{1}{r^2\sin\theta}\frac{\partial}{\partial\theta}\left(\sin\theta\frac{\partial\psi}{\partial\theta}\right)+\frac{1}{r^2\sin\theta}\frac{\partial^2\psi}{\partial\phi^2}+k^2\psi \;=\; 0\,. \tag{F.5}$$

The solution to $\psi(r,\theta,\phi)$ in Equation (F.5) can be found using separable variables as follows:

$$\begin{aligned}\psi(r,\theta,\phi) \;&=\; R(r)\Theta(\theta)\Phi(\phi)\,, \qquad (F.6)\\ \text{where}\qquad \frac{\partial^2\Phi(\phi)}{\partial\phi^2}+m^2\Phi(\phi) \;&=\; 0\,,\\ \frac{1}{\sin\theta}\frac{\partial}{\partial\theta}\left(\sin\theta\frac{\partial\Theta(\theta)}{\partial\theta}\right)+\left[s(s+1)-\frac{m^2}{(\sin\theta)^2}\right]\Theta(\theta) \;&=\; 0,\\ \frac{\partial}{\partial r}\left(r^2\frac{\partial R(r)}{\partial r}\right)+\left[k^2r^2-s(s+1)\right]R(r) \;&=\; 0\,.\end{aligned}$$

The solutions of $\Phi(\phi)$, $\Theta(\theta)$, $R(r)$, and $\psi(r,\theta,\phi)$ are expressed in the following four Subsections.

F.2.3 Solution of $\Phi(\phi)$

The solution of $\Phi(\phi)$ in Equation (F.6) consists of even (e) and odd (o) terms as follows:

$$\Phi_{\rm e}(\phi) \;=\; \cos(m\phi), \qquad \Phi_{\rm o}(\phi) \;=\; \sin(m\phi)\,.$$

F.2.4 Solution of $\Theta(\theta)$

The solutions of $\Theta(\theta)$ are the associated Legendre functions of the first kind $P_s^m(\cos\theta)$ of order m, and degree $s = m, m+1, \cdots$. These solutions are orthogonal.

F.2.5 Solution of $R(r)$

There are four possible linearly independent solutions of $R(r)$. The first two are the spherical Bessel functions:

$$j_s(kr) \;=\; \sqrt{\frac{\pi}{2kr}}\,J_{s+\frac{1}{2}}(kr), \tag{F.7}$$

$$y_s(kr) = \sqrt{\frac{\pi}{2kr}}\, Y_{s+\frac{1}{2}}(kr)\,, \tag{F.8}$$

where $J_{s+\frac{1}{2}}(kr)$ and $Y_{s+\frac{1}{2}}(kr)$ are the Bessel functions of the first and second kind respectively.

Since any linear combination of $j_n(kr)$ and $y_n(kr)$ is also a solution to $R(r)$, a simpler way of expressing the solutions of $R(r)$ can be written. This takes the form of the spherical Bessel functions of the third kind (also known as spherical Hankel functions):

$$h_s^{(1)}(kr) = j_s(kr) + iy_s(kr) \tag{F.9}$$
$$h_s^{(2)}(kr) = j_s(kr) - iy_s(kr)\,. \tag{F.10}$$

Therefore, Equations (F.7–F.10) are all solutions of $R(r)$.

F.2.6 Solution of $\psi(r,\theta,\phi)$

From the discussion in Sections F.2.3, F.2.4 and F.2.5, the solution of Equation (F.6) can finally be expressed as:

$$\psi(r,\theta,\phi) = R(r)\Theta(\theta)\Phi(\phi)\,, \qquad \text{[Equation (F.6)]}$$
$$\psi_{ems} = R(r)\Theta(\theta)\Phi_{\mathrm{e}}(\phi) = \cos(m\phi)\, P_s^m(\cos\theta)\, z_s(kr) \tag{F.11}$$
$$\psi_{oms} = R(r)\Theta(\theta)\Phi_{\mathrm{o}}(\phi) = \sin(m\phi)\, P_s^m(\cos\theta)\, z_s(kr)\,, \tag{F.12}$$

where $z_s(kr)$ is any of the four solutions given by Equations (F.7–F.10) in Section F.2.5. The e and o notations denote the even and odd terms as highlighted in Section F.2.3, and the variables m and s are as defined in Section F.2.4.

F.2.7 Vector Spherical Harmonics

With knowledge of the solution of $\psi(r,\theta,\phi)$ from Section F.2.6, it is now possible to construct the vector spherical harmonics that are generated by Equations (F.11–F.12). These vector spherical harmonics are the electromagnetic *normal modes* of the spherical particle, and can be used to construct the electric and magnetic fields as follows:

$$\mathbf{E} = \mathbf{M}_{oms} + i\,\mathbf{N}_{ems}$$
$$\mathbf{H} = m\left(-\mathbf{M}_{ems} + i\,\mathbf{N}_{oms}\right)\,,$$

where

$$\begin{aligned}
\mathbf{M}_{ems} &= \nabla \times (\mathbf{r}\psi_{ems}) \\
&= \frac{-m}{\sin\theta}\sin(m\phi)P_s^m(\cos\theta)z_s(kr)\boldsymbol{\theta} - \cos(m\phi)\frac{dP_s^m(\cos\theta)}{d\theta}z_s(kr)\boldsymbol{\phi}, \qquad \text{(F.13)} \\
\mathbf{M}_{oms} &= \nabla \times (\mathbf{r}\psi_{oms}) \\
&= \frac{m}{\sin\theta}\sin(m\phi)P_s^m(\cos\theta)z_s(kr)\boldsymbol{\theta} - \sin(m\phi)\frac{dP_s^m(\cos\theta)}{d\theta}z_s(kr)\boldsymbol{\phi}, \qquad \text{(F.14)} \\
\mathbf{N}_{ems} &= \frac{\nabla \times \mathbf{M}_{ems}}{k} \\
&= \frac{z_s(kr)}{kr}\cos(m\phi)s(s+1)P_s^m(\cos\theta)\mathbf{r} + \cos(m\phi)\frac{dP_s^m(\cos\theta)}{d\theta}\frac{1}{kr}\frac{d\left[krz_s(kr)\right]}{d\,kr}\boldsymbol{\theta} \\
&\quad -m\sin(m\phi)\frac{P_s^m(\cos\theta)}{\sin\theta}\frac{1}{kr}\frac{d\left[krz_s(kr)\right]}{d\,kr}\boldsymbol{\phi}, \qquad \text{(F.15)} \\
\mathbf{N}_{oms} &= \frac{\nabla \times \mathbf{M}_{oms}}{k} \\
&= \frac{z_s(kr)}{kr}\sin(m\phi)s(s+1)P_s^m(\cos\theta)\mathbf{r} + \sin(m\phi)\frac{dP_s^m(\cos\theta)}{d\theta}\frac{1}{kr}\frac{d\left[krz_s(kr)\right]}{d\,kr}\boldsymbol{\theta} \\
&\quad +m\cos(m\phi)\frac{P_s^m(\cos\theta)}{\sin\theta}\frac{1}{kr}\frac{d\left[krz_s(kr)\right]}{d\,kr}\boldsymbol{\phi}. \qquad \text{(F.16)}
\end{aligned}$$

F.2.8 Equation of a Plane Wave in Vector Spherical Harmonics

The incident electric wave with amplitude E_0 can be expressed in terms of the vector spherical harmonics derived in Section F.2.7:

$$\begin{aligned}
\mathbf{E}_{\text{inc}} &= E_0\, e^{ikr\cos\theta}\left[\sin(\theta)\cos(\phi)\mathbf{r} + \cos(\theta)\cos(\phi)\boldsymbol{\theta} - \sin(\phi)\boldsymbol{\phi}\right] \\
&= E_0\sum_{s=1}^{\infty} i^s\,\frac{2s+1}{s(s+1)}\left(\mathbf{M}_{\text{o1s}}^{(1)} - i\mathbf{N}_{\text{e1s}}^{(1)}\right), \qquad \text{(F.17)}
\end{aligned}$$

where as defined in Equation (F.14), the term $\mathbf{M}_{\text{o1s}}^{(1)}$ means that the associated Legendre functions of the first kind have order $m = 1$, and degree $s = m, m+1, \cdots$. The superscript (1) implies that $z_s(kr) = j_s(kr)$. As defined in Equation (F.15), the subscripts $1s$ and superscript (1) in $\mathbf{N}_{\text{e1s}}^{(1)}$ have the same meaning as in $\mathbf{M}_{\text{o1s}}^{(1)}$.

The incident magnetic wave can also be expressed in terms of the vector spherical harmonics:

$$\mathbf{H}_{\text{inc}} = \frac{-k}{\omega\mu}E_0\sum_{s=1}^{\infty} i^s\,\frac{2s+1}{s(s+1)}\left(\mathbf{M}_{e1s}^{(1)} + i\mathbf{N}_{o1s}^{(1)}\right). \qquad \text{(F.18)}$$

F.3 Cylindrical Scatterers

The Mie scattering model for a cylinder, which was utilised in Sections 7.5.1 and 8.6, is now derived in this Section.

F.3.1 Plane Wave Equation of a Cylinder

In Section F.2.2, the scalar wave equation in spherical polar coordinates r, ϕ, θ was presented in Equation (F.5) as:

$$\frac{1}{r^2}\frac{\partial}{\partial r}\left(r^2\frac{\partial \psi}{\partial r}\right) + \frac{1}{r^2\sin\theta}\frac{\partial}{\partial \theta}\left(\sin\theta\frac{\partial \psi}{\partial \theta}\right) + \frac{1}{r^2\sin\theta}\frac{\partial^2 \psi}{\partial \phi^2} + k^2\psi \;=\; 0\,. \quad \text{[Equation (F.5)]}$$

The scalar wave equation in cylindrical polar coordinates r, ϕ, z is expressed as:

$$\frac{1}{r}\frac{\partial}{\partial r}\left(r\frac{\partial \psi}{\partial r}\right) + \frac{1}{r^2}\frac{\partial^2 \psi}{\partial \phi^2} + \frac{\partial^2 \psi}{\partial z^2} + k^2\psi \;=\; 0\,. \tag{F.19}$$

The solution to $\psi(r, \phi, z)$ in Equation (F.19) can be found using separable variables as follows:

$$\begin{aligned} \psi(r,\phi,z) &= R(r)\Phi(\phi)Z(z) \qquad (F.20)\\ \text{where } \Phi(\phi) &= e^{is\phi}, \quad s = 0, \pm 1, \ldots \\ Z(z) &= e^{ihz}, \end{aligned}$$

where the separation constant h depends on the polarisation of the incident field; $R(r)$ is now $R\left(r\sqrt{k^2-h^2}\right)$, which is a solution to the Bessel equation below:

$$\left[r\sqrt{k^2-h^2}\right]\frac{d}{d\left[r\sqrt{k^2-h^2}\right]}\left(\left[r\sqrt{k^2-h^2}\right]\frac{d\,R\left(r\sqrt{k^2-h^2}\right)}{d\left[r\sqrt{k^2-h^2}\right]}\right) + \cdots \tag{F.21}$$

$$\left(\left[r\sqrt{k^2-h^2}\right]^2 - s^2\right) \;=\; 0\,. \tag{F.22}$$

The two independent solutions of $R\left(r\sqrt{k^2-h^2}\right)$ are the Bessel functions of the first and second kind $J_s(r\sqrt{k^2-h^2})$ and $Y_s(r\sqrt{k^2-h^2})$ of integral order s. Alternative solutions of $R\left(r\sqrt{k^2-h^2}\right)$ are any linear combination of the above Bessel functions of the first and second kind, e.g. the Hankel functions. Therefore, the solution to $\psi(r, \phi, z)$ in Equation (F.19) can be expressed as:

$$\psi(r,\phi,z) \;=\; R(r)\Phi(\phi)Z(z) \quad \text{Equation (F.20)}$$

$$
\begin{aligned}
&= R\left(r\sqrt{k^2-h^2}\right) e^{is\phi}\, e^{ihz}, \quad s=0,\pm1,\ldots \qquad \text{(F.23)}\\
&= \psi_s\,.
\end{aligned}
$$

Note that Equation (F.23) has two possible solutions because $R\left(r\sqrt{k^2-h^2}\right)$ has two independent solutions. This means that Equation (F.23) can be denoted as ψ_s^e and ψ_s^o, where the e and o notations denote the even and odd terms.

F.3.2 Vector Cylindrical Harmonics

As in Section F.2.7, it is possible to construct the vector cylindrical harmonics that are generated by Equation (F.23). These vector cylindrical harmonics are the electromagnetic *normal modes* of the cylinder and can be used to construct the electric and magnetic fields as follows:

$$
\begin{aligned}
\mathbf{E} &= \mathbf{M}_s + i\,\mathbf{N}_s\\
\mathbf{H} &= m\left(-\mathbf{M}_s + i\,\mathbf{N}_s\right) \quad s=0,\pm1,\ldots, \qquad \text{(F.24)}
\end{aligned}
$$

where

$$
\begin{aligned}
\mathbf{M}_s &= \nabla\times(\mathbf{z}\psi_s)\\
&= \sqrt{k^2-h^2}\left(is\frac{\psi_s}{r\sqrt{k^2-h^2}}\mathbf{r}-\frac{\partial\psi_s}{\partial r}\boldsymbol{\phi}\right) = \sqrt{k^2-h^2}\left(is\frac{\psi_s}{r\sqrt{k^2-h^2}}\mathbf{r}-\psi_s'\boldsymbol{\phi}\right)\\
&= \sqrt{k^2-h^2}\left(is\frac{R\left(r\sqrt{k^2-h^2}\right)}{r\sqrt{k^2-h^2}}\mathbf{r}-R'\left(r\sqrt{k^2-h^2}\right)\boldsymbol{\phi}\right) e^{i(s\phi+hz)} \qquad \text{(F.25)}
\end{aligned}
$$

$$
\begin{aligned}
\mathbf{N}_s &= \frac{\nabla\times\mathbf{M}_s}{k}\\
&= \frac{\sqrt{k^2-h^2}}{k}\left(ih\frac{\partial\psi_s}{\partial r}\mathbf{r}-hs\frac{\psi_s}{r\sqrt{k^2-h^2}}\boldsymbol{\phi}+\sqrt{k^2-h^2}\,\psi_s\mathbf{z}\right)\\
&= \frac{\sqrt{k^2-h^2}}{k}\left(ih\,R'\left(r\sqrt{k^2-h^2}\right)\mathbf{r}-hs\frac{R\left(r\sqrt{k^2-h^2}\right)}{r\sqrt{k^2-h^2}}\boldsymbol{\phi}+\cdots\right.\\
&\qquad \left.\sqrt{k^2-h^2}\,R\left(r\sqrt{k^2-h^2}\right)\mathbf{z}\right) e^{i(s\phi+hz)}\,. \qquad \text{(F.26)}
\end{aligned}
$$

Note that $\mathbf{z}$ is a unit vector parallel to the cylinder's axis, and $R\left(r\sqrt{k^2-h^2}\right)$ is either $J_s(r\sqrt{k^2-h^2})$ or $Y_s(r\sqrt{k^2-h^2})$ or the Hankel function $H_s^{(1)}(r\sqrt{k^2-h^2})$.

F.3.3 Case I: Incident E Parallel to xz Plane, H Perpendicular to xz Plane

The incident electric wave with amplitude E_0 can now be expressed in terms of the vector cylindrical harmonics derived in Section F.3.2. However, the expression depends on the polarisation of the incident wave.

Let the propagation vector $\mathbf{k}$ of the incident wave plane be in the xz plane. The angle between $\mathbf{k}$ and the z axis is θ. When angle $\theta = 90°$, the incoming plane wave is perpendicular to the xz plane. Therefore $\mathbf{k} = -\sin(\theta)\mathbf{x} - \cos(\theta)\mathbf{z}$.

The equation of the plane wave is $\mathbf{E}_{\text{inc}} = E_{0,\text{inc}}\, e^{i\mathbf{k}\cdot x}$, where $E_{0,\text{inc}}$ is the amplitude of the incident wave.

$E_{0,\text{inc}}$ has both parallel and perpendicular components: $E_{0,\text{inc}} = E_{0,\text{inc},\parallel}\,\mathbf{e}_\parallel + E_{0,\text{inc},\perp}\,\mathbf{e}_\perp$, where $\mathbf{e}_\parallel = \sin(\theta)\,\mathbf{z} - \cos(\theta)\mathbf{x}$ is a vector parallel to the xz plane, and $\mathbf{e}_\perp = -\mathbf{y}$ a vector perpendicular to the xz plane.

Let us assume the electric field vector $E_{0,\text{inc}}$ is strictly parallel to xz plane, therefore the incident electric field is:

$$\begin{aligned}\mathbf{E}_{\text{inc}} &= E_{0,\text{inc},\parallel}\,\mathbf{e}_\parallel\, e^{i\mathbf{k}\cdot x} \\ &= E_0\left(\sin(\theta)\,\mathbf{z} - \cos(\theta)\,\mathbf{x}\right) e^{-ik(r\sin\theta\cos\phi + z\cos\theta)}\,. \end{aligned} \tag{F.27}$$

Only the $\mathbf{z}$ terms in Equations (F.26) and (F.27) can be compared, therefore the $\mathbf{z}$ term in Equation (F.27) can be expanded to:

$$\begin{aligned}\mathbf{E}_{\text{inc}} &= E_0\,\sin\theta\, e^{-ik(r\sin\theta\cos\phi + z\cos\theta)}\mathbf{z} \\ &= E_0\,\sin\theta\, e^{-ikr\sin\theta\cos\phi}\, e^{-ik\cos\theta z}\,\mathbf{z} \\ &= E_0\,\sin\theta\,\sum_{s=-\infty}^{\infty}(-i)^s\, J_s(kr\sin\theta)\, e^{is\phi}\, e^{ihz}\,\mathbf{z}\,, \end{aligned} \tag{F.28}$$

where $h = -k\cos\theta$, and the identity term is:

$$e^{-i[kr\sin\theta]\cos\phi} = \sum_{s=-\infty}^{\infty}(-i)^s\, J_s(kr\sin\theta)\, e^{is\phi}\,\mathbf{z}\,.$$

The $\mathbf{z}$ term in Equation (F.26) can be expanded to:

$$\frac{\sqrt{k^2-h^2}}{k}\sqrt{k^2-h^2}R(r)\, e^{i(s\phi+hz)}\mathbf{z} \;=\; \frac{k^2-h^2}{k}R(r)\, e^{is\phi}\, e^{ihz}\,\mathbf{z}$$

$$
\begin{aligned}
&= \frac{k^2 - k^2\cos^2\theta}{k} R(r)\, e^{is\phi}\, e^{ihz}\, \mathbf{z} \\
&= k(1-\cos^2\theta) R(r)\, e^{is\phi}\, e^{ihz}\, \mathbf{z} \\
&= k\,\sin^2\theta R(r)\, e^{is\phi}\, e^{ihz}\, \mathbf{z} \qquad \text{(F.29)} \\
&= k\,\sin^2\theta\, J_s(kr\sin\theta)\, e^{is\phi}\, e^{ihz}\, \mathbf{z} \qquad \text{(F.30)} \\
&= \mathbf{N}_s^{(1)}, \qquad \text{(F.31)}
\end{aligned}
$$

where $R(r)$ in Equation (F.29) is set to $J_s(kr\sin\theta)$ of integral order s in Equation (F.30). This is to allow direct substitution of Equation (F.30) into Equation (F.28). The superscript (1) in $\mathbf{N}_s^{(1)}$ implies that $R(r) = J_s(kr\sin\theta)$.

Comparing Equations (F.28) and (F.30), the incident electric field can now be expressed in terms of the vector cylindrical harmonics:

$$
\begin{aligned}
\mathbf{E}_{\text{inc}} &= E_0\,\sin\theta \sum_{s=-\infty}^{\infty} (-i)^s\, J_s(kr\sin\theta)\, e^{is\phi}\, e^{ihz}\, \mathbf{z} \\
&= \sum_{s=-\infty}^{\infty} E_0\,(-i)^s \frac{\mathbf{N}_s^{(1)}}{k\,\sin\theta}. \qquad \text{(F.32)}
\end{aligned}
$$

Since $\mathbf{E}_{\text{inc}}$ in Equation (F.32) is only dependent on $J_s(kr\sin\theta)$, then $\mathbf{H}_{\text{inc}}$ is also only dependent on $J_s(kr\sin\theta)$. In addition, because $\mathbf{E}_{\text{inc}}$ in Equation (F.32) contains the $\mathbf{N}_s^{(1)}$ term, then $\mathbf{H}_{\text{inc}}$ must contain the $\mathbf{M}_s^{(1)}$ term as shown by the relationship in Equation (F.24). However $\mathbf{M}_s^{(1)}$ must be scaled by i. Therefore, the incident magnetic wave expressed in terms of the vector cylindrical harmonics is:

$$
\mathbf{H}_{\text{inc}} = \frac{-ik}{\omega\mu} \sum_{s=-\infty}^{\infty} E_0\,(-i)^s \frac{\mathbf{M}_s^{(1)}}{k\,\sin\theta}, \qquad \text{(F.33)}
$$

where like Equation (F.31), the superscript (1) implies that $R(r)$ in Equation (F.25) is the Bessel function of the first kind $J_s(kr\sin\theta)$ of integral order s.

Internal Field in Vector Cylindrical Harmonics for Case I

The boundary conditions are:

- The tangential components of $\mathbf{E}$ and $\mathbf{H}$ are continuous at the surface of the cylinder, and
- h must be the same for all waves (i.e. incident, scattered and internal).

Therefore, h in the case of the internal wave is also equal to $-k\cos\theta$, and $R(r)$ in Equation (F.26) is also the Bessel function of the first kind $J_s(r)$ of integral order s, but differs from that in Equations (F.32) and (F.33) such that:

$$R(r) = J_s(kr\sqrt{m^2 - \cos^2\theta})\,. \tag{F.34}$$

Consequently,

$$\mathbf{E}_{\text{tx}} = \sum_{s=-\infty}^{\infty} \frac{E_0\,(-i)^s}{k\,\sin\theta}\,\left[g_s\,\mathbf{M}_s^{(1)} + f_s\,\mathbf{N}_s^{(1)}\right], \tag{F.35}$$

$$\mathbf{H}_{\text{tx}} = \frac{-ik_1}{\omega\mu_1}\sum_{s=-\infty}^{\infty} \frac{E_0\,(-i)^s}{k\,\sin\theta}\,\left[g_s\,\mathbf{N}_s^{(1)} + f_s\,\mathbf{M}_s^{(1)}\right], \tag{F.36}$$

where μ_1 is the permeability of the cylinder, and k_1 is the wavenumber in the cylinder. Like Equation (F.32), the superscript (1) implies that $R(r)$ in Equation (F.25) is $J_s(r)$ of integral order s.

Scattered Field in Vector Cylindrical Harmonics for Case I

For the scattered field,

$$\mathbf{E}_{\text{sca}} = -\sum_{s=-\infty}^{\infty} \frac{E_0\,(-i)^s}{k\,\sin\theta}\,\left[b_{s,\text{I}}\,\mathbf{N}_s^{(3)} + ia_{s,\text{I}}\,\mathbf{M}_s^{(3)}\right] \tag{F.37}$$

$$\mathbf{H}_{\text{sca}} = \frac{-ik}{\omega\mu}\sum_{s=-\infty}^{\infty} \frac{E_0\,(-i)^s}{k\,\sin\theta}\,\left[b_{s,\text{I}}\,\mathbf{M}_s^{(3)} + ia_{s,\text{I}}\,\mathbf{N}_s^{(3)}\right], \tag{F.38}$$

where the superscript (3) implies that $R(r)$ in Equation (F.26) is the Hankel function $H_s^{(1)} = J_s(\cdot) + iY_s(\cdot)$. Therefore,

$$\begin{aligned} R(r) &= H_s^{(1)}(kr\,\sin\theta)e^{is\phi}\,e^{-ikz\,\cos\theta} \\ &= \left(J_s(kr\,\sin\theta) + iY_s(kr\,\sin\theta)\right)\,e^{is\phi}\,e^{-ikz\,\cos\theta}\,. \end{aligned} \tag{F.39}$$

If $\mu = \mu_1$, and letting $\xi = kr\,\sin\theta$, and $\eta = kr\sqrt{m^2 - \cos^2\theta}$, then the scattering coefficients $a_{s,\text{I}}$ and $b_{s,\text{I}}$ in Equations (F.37) and (F.38) are:

$$a_{s,\text{I}} = \frac{C_s\,V_s - B_s\,D_s}{W_s\,V_s + i\,D_s^2} \tag{F.40}$$

$$b_{s,\text{I}} = \frac{W_s\,B_s + i\,D_s\,C_s}{W_s\,V_s + i\,D_s^2} \tag{F.41}$$

$$B_s = \xi\,[m^2\,\xi\,J_s'(\eta)\,J_s(\xi) - \eta\,J_s(\eta)\,J_s'(\xi)] \tag{F.42}$$

$$C_s = s\,(\cos\theta)\,\eta\,J_s(\eta)\,J_s(\xi)\left(\frac{\xi^2}{\eta^2} - 1\right) \tag{F.43}$$

$$D_s = s(\cos\theta)\,\eta\,J_s(\eta)\,H_s^{(1)}(\xi)\left(\frac{\xi^2}{\eta^2}-1\right) \tag{F.44}$$

$$V_s = \xi\left[m^2\,\xi\,J_s'(\eta)\,H_s^{(1)}(\xi) - \eta\,J_s(\eta)\,H_s^{(1)\prime}(\xi)\right] \tag{F.45}$$

$$W_s = i\xi\left(\eta\,J_s(\eta)\,H_s^{(1)\prime}(\xi) - \xi\,J_s'(\eta)\,H_s^{(1)}(\xi)\right), \tag{F.46}$$

where

$$\begin{aligned} J_s'(\eta) &= \frac{1}{2}\left[J_{s-1}(\eta) - J_{s+1}(\eta)\right] \\ H_s^{(1)\prime}(\xi) &= \frac{1}{2}\left[H_{s-1}^{(1)}(\xi) - H_{s+1}^{(1)}(\xi)\right] \\ a_{-s,\mathrm{I}} &= -a_{s,\mathrm{I}} \\ a_{0,\mathrm{I}} &= 0 \\ b_{-s,\mathrm{I}} &= b_{s,\mathrm{I}}\,. \end{aligned}$$

When $\theta = 90°$, $a_{s,I} = 0$ and

$$b_{s,\mathrm{I},90°} = \frac{J_s(mkr)\,J_s'(kr) - mJ_s'(mkr)\,J_s(kr)}{J_s(mkr)\,H_s^{(1)\prime}(kr) - mJ_s'(mkr)\,H_s^{(1)}(kr)}\,. \tag{F.47}$$

Large distances from cylinder for Case I (asymptotic scattered field)

If the observation distance from the cylinder is large ($kr\sin\theta >> 1$), then Equation (F.37) becomes:

$$\begin{aligned} \mathbf{E}_{\mathrm{sca}} \approx\; & -E_0\,e^{-i\pi/4}\sqrt{\frac{2}{\pi kr\sin\theta}}\;e^{ik(r\sin\theta - z\cos\theta)}\ldots \\ & \sum_s (-1)^s\,e^{is\phi}\left[a_{s,\mathrm{I}}\,\boldsymbol{\phi} + b_{s,\mathrm{I}}\left(\cos\theta\;\mathbf{r} + \sin\theta\;\mathbf{z}\right)\right]. \end{aligned} \tag{F.48}$$

The wavefronts of the scattered field map the shape of a cone. At any point on the cone, the unit propagation direction vector **s** of the scattered wave (i.e. *wave normal*) is

$$\mathbf{s} = \sin\theta\;\mathbf{r} - \cos\theta\;\mathbf{z}\,. \tag{F.49}$$

Note that the Poynting vector has direction **s**.

F.3.4 Case II: Incident E Perpendicular to xz Plane, H Parallel to xz Plane

As described in Section F.3.3, the incident electric wave with amplitude E_0 can be expressed in terms of the vector cylindrical harmonics derived in Section F.3.2. However, the expression depends on the polarisation of the incident wave.

Recall that in Section F.3.3, $\mathbf{z}$ was described as a unit vector parallel to the cylinder's axis. The propagation vector $\mathbf{k}$ of the incident wave plane is in the xz plane. θ is the angle between $\mathbf{k}$ and the z axis. When angle $\theta = 90°$, the incoming plane wave is perpendicular to the xz plane. Therefore, $\mathbf{k} = -\sin(\theta)\mathbf{x} - \cos(\theta)\mathbf{z}$.

Like in Section F.3.3, the equation of the plane wave is $\mathbf{E}_{\text{inc}} = E_{0,\text{inc}}\, e^{i\mathbf{k}\cdot x}$, where $E_{0,\text{inc}}$ is the amplitude of the incident wave. $E_{0,\text{inc}}$ has both parallel and perpendicular components: $E_{0,\text{inc}} = E_{0,\text{inc},\parallel}\, \mathbf{e}_\parallel + E_{0,\text{inc},\perp}\, \mathbf{e}_\perp$, where $\mathbf{e}_\parallel = \sin(\theta)\, \mathbf{z} - \cos(\theta)\mathbf{x}$ is a vector parallel to the xz plane, and $\mathbf{e}_\perp = -\mathbf{y}$ a vector perpendicular to the xz plane.

Let us assume the electric field vector $E_{0,\text{inc}}$ is strictly perpendicular to xz plane. Utilising the vector cylindrical harmonics derived in Section F.3.2:

$$\begin{aligned}
\mathbf{E}_{\text{inc}} &= -E_{0,\text{inc},\perp}\, \mathbf{e}_\perp\, e^{i\mathbf{k}\dot{x}} \\
&= E_0 \mathbf{y}\, e^{-ik(r\sin\theta\cos\phi + z\cos\theta)} \\
&= -i \sum_{s=-\infty}^{\infty} \frac{E_0\,(-i)^s}{k\,\sin\theta}\, \mathbf{M}_s^{(1)}\,.
\end{aligned} \tag{F.50}$$

Case II: Scattered Field in Vector Cylindrical Harmonics

For the scattered field,

$$\mathbf{E}_{\text{sca}} = -\sum_{s=-\infty}^{\infty} \frac{E_0\,(-i)^s}{k\,\sin\theta}\, \left[a_{s,\text{II}}\, \mathbf{M}_s^{(3)} + b_{s,\text{II}}\, \mathbf{N}_s^{(3)}\right]\,, \tag{F.51}$$

where as explained in Section F.3.3, the superscript (3) implies that $R(r)$ in Equation (F.26) is the Hankel function $H_s^{(1)} = J_s(\cdot) + iY_s(\cdot)$.

If $\mu = \mu_1$, and letting $\xi = kr\,\sin\theta$, and $\eta = kr\sqrt{m^2 - \cos^2\theta}$, then the scattering coefficients $a_{s,\text{II}}$ and $b_{s,\text{II}}$ in Equation (F.51) are

$$a_{s,\text{II}} = -\frac{A_s\, V_s - i\, C_s\, D_s}{W_s\, V_s + i\, D_s^2} \tag{F.52}$$

$$b_{s,\text{II}} = -i\,\frac{C_s\, W_s + A_s\, D_s}{W_s\, V_s + i\, D_s^2} \tag{F.53}$$

$$A_s = i\,\xi\,\left[\xi\, J_s'(\eta)\, J_s(\xi) - \eta\, J_s(\eta)\, J_s'(\xi)\right]\,, \tag{F.54}$$

where C_s, D_s, V_s, W_s, and $J_s'(\cdot)$ are defined in Section F.3.3, and

$$\begin{aligned}
a_{-s,\text{II}} &= a_{s,\text{II}} \\
b_{-s,\text{II}} &= -b_{s,\text{II}} \\
b_{0,\text{II}} &= 0
\end{aligned}$$

$$a_{s,\text{II}} = -b_{s,\text{II}}\,.$$

When $\theta = 90°$, $b_{s,\text{II}} = 0$, so

$$a_{s,\text{II},90°} = \frac{m\,J_s'(kr)\,J_s(mkr) - J_s(kr)\,J_s'(mkr)}{m\,J_s(mkr)\,H_s^{(1)\prime}(kr) - J_s'(mkr)\,H_s^{(1)\prime}(kr)}\,. \tag{F.55}$$

Large distances from cylinder for Case II (asymptotic scattered field)

If the observation distance from the cylinder is large ($kr\,\sin\theta >> 1$), then Equation (F.51) becomes:

$$\begin{aligned}\mathbf{E}_{\text{sca}} \approx\; & -E_0\,e^{-i\,\pi/4}\sqrt{\frac{2}{\pi kr\,\sin\theta}}\;e^{ik(r\,\sin\theta - z\,\cos\theta)}\,\ldots \\ & \sum_s (-1)^s\;e^{is\phi}\;\left[-a_{s,\text{II}}\,\boldsymbol{\phi} - b_{s,\text{II}}\,(\cos\theta\;\mathbf{r} + \sin\theta\;\mathbf{z})\right]\,.\end{aligned} \tag{F.56}$$

The wavefronts of the scattered filed are as described in Section F.3.3.

F.4 Scattering Matrix of a Cylinder

Recall that in Sections F.3.3 and F.3.4, the equation of the plane wave is $\mathbf{E}_{\text{inc}} = E_{0,\text{inc}}\,e^{i\mathbf{k}\cdot x}$. $E_{0,\text{inc}}$ can be resolved into its parallel and perpendicular components: $E_{0,\text{inc}} = E_{0,\text{inc},\parallel}\,\mathbf{e}_\parallel + E_{0,\text{inc},\perp}\,\mathbf{e}_\perp$, where $\mathbf{e}_\parallel = \sin(\theta)\,\mathbf{z} - \cos(\theta)\mathbf{x}$ is a vector parallel to the xz plane, $\mathbf{e}_\perp = -\mathbf{y}$ is a vector perpendicular to the xz plane, and $\mathbf{e}_\perp \times \mathbf{e}_\parallel = \mathbf{k}$.

In Section F.3.3, $E_{0,\text{inc}}$ was assumed to be strictly parallel to the xz plane. In Section F.3.4, $E_{0,\text{inc}}$ was assumed to be strictly perpendicular to the xz plane. If $E_{0,\text{inc}}$ has both the parallel and perpendicular components, then the equation of a plane wave becomes:

$$\mathbf{E}_{\text{inc}} = (E_{0,\text{inc},\parallel}\,\mathbf{e}_\parallel + E_{0,\text{inc},\perp}\,\mathbf{e}_\perp)\,e^{i\mathbf{k}\cdot x}\,.$$

The scattered field $\mathbf{E}_{\text{sca}}$ can also be resolved similarly. Let $\mathbf{s}$ be the direction of scattering. The perpendicular component of $\mathbf{s}$ is $\mathbf{e}_{\text{sca},\perp} = \boldsymbol{\phi}$; the parallel component of $\mathbf{s}$ is $\mathbf{e}_{\text{sca},\parallel} = \cos(\theta)\,\mathbf{r} + \sin(\theta)\,\mathbf{z}$. $\mathbf{e}_{\text{sca},\perp} \times \mathbf{e}_{\text{sca},\parallel} = \mathbf{s}$.

Note that $\mathbf{r} = \sin(\phi)\,\mathbf{y} + \cos(\phi)\,\mathbf{x}$, and $\boldsymbol{\phi} = -\sin(\phi)\,\mathbf{x} + \cos(\phi)\,\mathbf{y}$.

Now the equation of the scattered electric field can be resolved into its parallel and perpendicular components:

$$\begin{aligned}\mathbf{E}_{\text{sca}} &= E_{\text{sca},\parallel}\,\mathbf{e}_{\text{sca},\parallel} + E_{\text{sca},\perp}\,\mathbf{e}_{\text{sca},\perp} \\ &= E_{\text{sca},\parallel}\,(\cos\theta\,\mathbf{r} + \sin\theta\,\mathbf{z}) + E_{\text{sca},\perp}\,\boldsymbol{\phi} \\ &= E_{\text{sca},\parallel}\,(\cos\theta\,[\sin(\phi)\,\mathbf{y} + \cos(\phi)\,\mathbf{x}] + \sin\theta\;\mathbf{z}) + E_{\text{sca},\perp}\,(-\sin(\phi)\,\mathbf{x} + \cos(\phi)\,\mathbf{y})\,.\end{aligned}$$

F.4.1 Relationship Between Amplitudes of Incident and Scattered Fields for a Cylinder

The relationship between the amplitudes of the incident and scattered electromagnetic waves is as follows:

$$\begin{bmatrix} E_{\parallel\,\mathrm{sca}} \\ E_{\perp\,\mathrm{sca}} \end{bmatrix} = e^{\frac{i3\pi}{4}} \sqrt{\frac{2}{\pi kr\,\sin\theta}}\, e^{ik(r\,\sin\theta - z\,\cos\theta)} \underbrace{\begin{bmatrix} T_1 & T_4 \\ T_3 & T_2 \end{bmatrix}}_{\text{amplitude scattering matrix}} \begin{bmatrix} E_{\parallel\,\mathrm{inc}} \\ E_{\perp\,\mathrm{inc}} \end{bmatrix}, \tag{F.57}$$

where if ϕ is replaced with $\Theta = \pi - \phi$, then

$$T_1 = \sum_{-\infty}^{\infty} b_{s,\mathrm{I}}\, e^{-is\Theta} = b_{0,\mathrm{I}} + 2\sum_{s=1}^{\infty} b_{s,\mathrm{I}}\,\cos(s\Theta) \tag{F.58}$$

$$T_2 = \sum_{-\infty}^{\infty} a_{s,\mathrm{II}}\, e^{-is\Theta} = a_{0,\mathrm{II}} + 2\sum_{s=1}^{\infty} a_{s,\mathrm{II}}\,\cos(s\Theta) \tag{F.59}$$

$$T_3 = \sum_{-\infty}^{\infty} a_{s,\mathrm{I}}\, e^{-is\Theta} = -2i\sum_{s=1}^{\infty} a_{s,\mathrm{I}}\,\sin(s\Theta) \tag{F.60}$$

$$T_4 = \sum_{-\infty}^{\infty} b_{s,\mathrm{II}}\, e^{-is\Theta} = -2i\sum_{s=1}^{\infty} b_{s,\mathrm{II}}\,\sin(s\Theta) = -T_3\,. \tag{F.61}$$

The scattering coefficients a and b are given in Equations (F.40) and (F.41) and Equations (F.52) and (F.53).

Scattered Field in Forward or Backward Scattering Plane

If $\mathbf{s}$ lies in the forward scattering plane ($\Theta = 0°$), or if $\mathbf{s}$ lies in the backward scattering plane ($\Theta = 180°$), then

$$\begin{bmatrix} E_{\parallel\,\mathrm{sca}} \\ E_{\perp\,\mathrm{sca}} \end{bmatrix} = e^{\frac{i3\pi}{4}} \sqrt{\frac{2}{\pi kr\,\sin\theta}}\, e^{ik(r\,\sin\theta - z\,\cos\theta)} \begin{bmatrix} T_1 & 0 \\ 0 & T_2 \end{bmatrix} \begin{bmatrix} E_{\parallel\,\mathrm{inc}} \\ E_{\perp\,\mathrm{inc}} \end{bmatrix}. \tag{F.62}$$

Incident Wave Normal to z Axis ($\theta = 90°$)

If the incident wave is normal to the z axis (i.e. $\theta = 90°$), then

$$\begin{bmatrix} E_{\parallel\,\mathrm{sca}} \\ E_{\perp\,\mathrm{sca}} \end{bmatrix} = e^{\frac{i3\pi}{4}} \sqrt{\frac{2}{\pi kr}}\, e^{ikr} \begin{bmatrix} T_1 & 0 \\ 0 & T_2 \end{bmatrix} \begin{bmatrix} E_{\parallel\,\mathrm{inc}} \\ E_{\perp\,\mathrm{inc}} \end{bmatrix}, \quad \forall\,\Theta\,. \tag{F.63}$$

The scattering coefficients from Equations (F.47) and (F.55) can be expressed more simply by utilising the logarithmic derivative $D_s(\cdot)$ below:

$$D_s(\cdot) = \frac{J_s'(\cdot)}{J_s(\cdot)},$$

$$\text{where} \qquad D_{s-1}(a) = \frac{s-1}{a} - \frac{1}{\frac{s}{a} + D_s(a)} \tag{F.64}$$

is the recurrence relation.

Therefore, Equations (F.47) and (F.55) become:

$$a_{s,\text{II},90^\circ} = \frac{\left[\frac{D_s(mkr)}{m} + \frac{s}{kr}\right] J_s(kr) - J_{s-1}(kr)}{\left[\frac{D_s(mkr)}{m} + \frac{s}{kr}\right] H_s^{(1)}(kr) - H_{s-1}^{(1)}(kr)} \qquad \text{[Equation (8.3)]}$$

$$b_{s,\text{I},90^\circ} = \frac{\left[mD_s(mkr) + \frac{s}{kr}\right] J_s(kr) - J_{s-1}(kr)}{\left[mD_s(mkr) + \frac{s}{kr}\right] H_s^{(1)}(kr) - H_{s-1}^{(1)}(kr)}. \qquad \text{[Equation (8.4)]}$$

F.5 Efficiencies for a Cylinder

Let W_{inc} be the net rate at which electromagnetic energy is incident on the surface of a cylinder of length l, and radius r. The geometric cross sectional area of the cylinder is that of a rectangle, with area $2rl$. Let W_{sca} be the net rate at which electromagnetic energy scatters from the surface of this cylinder. The scattering cross section C_{sca} is the imaginary cross sectional area on the cylinder that interacts with and scatters the incident radiation. This imaginary cross sectional area can be larger or smaller than the actual geometric cross sectional area of the cylinder.

When the cross section C_{sca} (or C_{ext}) is normalised by the geometric cross section, the dimensionless term efficiency Q_{sca} (or Q_{ext}) is generated.

F.5.1 Efficiencies of a Cylinder for Case I: Parallel Incident Electric Field

For case I as described in Section F.3.3, the scattering efficiency of a cylinder is defined as:

$$Q_{\text{sca,I}} = \frac{W_{\text{sca,I}}}{2rlI_{\text{inc}}} = \frac{2}{kr}\left[|b_{0,\text{I}}|^2 + 2\sum_{s=1}^{\infty}\left(|a_{s,\text{I}}|^2 + |b_{s,\text{I}}|^2\right)\right]. \tag{F.65}$$

Multiplying Equation (F.65) by $2rl$ gives the scattering cross section $C_{\text{sca},\parallel}$ expressed in Equation (8.1).

If W_{abs} is the net rate at which electromagnetic energy is absorbed in the cylinder, then $W_{\text{ext}} = W_{\text{abs}} + W_{\text{sca}}$. Therefore the extinction efficiency is defined as:

$$Q_{\text{ext,I}} = \frac{W_{\text{ext,I}}}{2rlI_{\text{inc}}} = \frac{2}{kr}\Re\left\{b_{0,\text{I}} + 2\sum_{s=1}^{\infty} b_{s,\text{I}}\right\} = \frac{2}{kr}\Re\left\{T_1\left(\Theta = 0^\circ\right)\right\}. \tag{F.66}$$

Note that efficiency is usually plotted against $1/\lambda$, the reciprocal of wavelength.

F.5.2 Efficiencies of a Cylinder for Case II: Perpendicular Incident Electric Field

For case II as described in Section F.3.4, the scattering efficiency of a cylinder is defined as:

$$Q_{\text{sca, II}} = \frac{W_{\text{sca, II}}}{2rlI_{\text{inc}}} = \frac{2}{kr}\left[|a_{0,\text{II}}|^2 + 2\sum_{s=1}^{\infty}\left(|a_{s\,\text{II}}|^2 + |b_{s,\text{II}}|^2\right)\right]. \tag{F.67}$$

Multiplying Equation (F.65) by $2rl$ gives the scattering cross section $C_{\text{sca},\parallel}$ expressed in Equation (8.2).

The extinction efficiency is defined as:

$$Q_{\text{ext, II}} = \frac{W_{\text{ext, II}}}{2rlI_{\text{inc}}} = \frac{2}{kr}\,\Re\left\{a_{0,\text{II}} + 2\sum_{s=1}^{\infty}a_{s,\text{II}}\right\} = \frac{2}{kr}\,\Re\left\{T_2\left(\Theta = 0^\circ\right)\right\}. \tag{F.68}$$

F.5.3 Small Particle Limit

If kr and $|m|kr$ are small, then the scattering coefficients in Equations (F.65) and (F.67) can be approximated by:

$$\begin{aligned} b_0(\omega) &\approx \frac{-i\pi x^2(m^2-1)}{4} && \text{[Equation (7.8)]} \\ b_1(\omega) &\approx \frac{-i\pi x^4(m^2-1)}{32}. && \text{[Equation (7.9)]} \end{aligned}$$

For case I, this approximation results in Equation (F.65) being simplified to:

$$Q_{\text{sca, I}}(\omega) = \frac{2}{x}\left[\,|b_0(\omega)|^2 + 2\,|b_1(\omega)|^2\,\right]. \qquad \text{[Equation (7.7)]}$$

F.6 Rayleigh-Gans Scattering

In Section F.4.1, the relationship between the amplitudes of the incident and scattered fields for a cylinder is provided in Equation (F.57). If the scatterer has an irregular geometric shape (e.g. neither cylindrical nor spherical), and is either homogeneous or heterogeneous, then the Rayleigh-Gans theory can be used to approximate the relationship between the amplitudes of the incident and scattered fields as follows:

$$\begin{bmatrix} E_{\parallel\,\text{sca}} \\ E_{\perp\,\text{sca}} \end{bmatrix} = e^{\frac{ik(r-z)}{-ikr}} \begin{bmatrix} T_2 & 0 \\ 0 & T_1 \end{bmatrix} \begin{bmatrix} E_{\parallel\,\text{inc}} \\ E_{\perp\,\text{inc}} \end{bmatrix}, \tag{F.69}$$

where, in the homogeneous case:

$$T_1 = \frac{-ik^3}{2\pi}(m-1)\,V\,f(\theta,\phi) \tag{F.70}$$

$$T_2 = \frac{-ik^3}{2\pi}(m-1)\,V\,f(\theta,\phi)\,\cos(\theta) \tag{F.71}$$

$$f(\theta,\phi) = \frac{1}{V}\int_V e^{i\delta}\,dV\,, \tag{F.72}$$

and in the heterogeneous case:

$$T_1 = \frac{-ik^3}{2\pi}\sum_j (m_j-1)\,V_j\,f_j(\theta,\phi) \tag{F.73}$$

$$T_2 = \frac{-ik^3}{2\pi}\sum_j (m_j-1)\,V_j\,f_j(\theta,\phi)\,\cos(\theta) \tag{F.74}$$

$$f_j(\theta,\phi) = \frac{1}{V_j}\int_{V_j} e^{i\delta}\,dV\,, \tag{F.75}$$

where m_j is the relative refractive index of the jth region in a heterogeneous scatterer, V_j is the volume of the jth region, $f_j(\theta,\phi)$ is the form factor, θ is the zenith angle, ϕ is the azimuth angle, and δ is the dot product between the tangential surface vector, and the difference between the surface normal and tangential surface vector along the axis which the electric field is incident. More details of the Rayleigh-Gans theory are found in Bohren and Huffman (1983).

F.7 Geometric Optics

In geometric optics, rays are used to trace the path of the incident, scattered, and transmitted electric fields. The rays propagate through interfaces according to the Fresnel equations and Snell's law. To model an electromagnetic field, many rays may be used, with each ray generating its own incident, reflected, and transmitted angles to be used in the Fresnel equations and Snell's law. Geometric optics is often used as an approximation for exact solutions (e.g. Mie theory) due to its simplistic treatment of electromagnetic waves as a collection of rays.

As geometric optics is treated in detail in Hecht (2002), and scattering-related examples given in Bohren and Huffman (1983), further discussion in this Appendix is unnecessary.

F.8 Beckmann Distribution Function

Surface roughness is often modelled as an array of microfacets on an otherwise flat surface. The slopes and spacings of these facets are defined as a distribution function (probability density function). One simple model is the Gaussian model where roughness is altered via changes to the standard deviation of a Gaussian distribution function. In accordance with literature, this standard deviation is called the distribution factor m; a small m implies smoothness, while large m indicates roughness. Each microfacet has a unit surface normal $\mathbf{N}$; the incoming radiation with respect to $\mathbf{N}$ is unit vector $\mathbf{L}$; the viewing direction with respect to $\mathbf{N}$ is unit vector $\mathbf{V}$; the vector that bisects $\mathbf{L}$ and $\mathbf{V}$ is $\mathbf{H}$. The angle of incidence between $\mathbf{N}$ and $\mathbf{H}$ is α.

A similar but more thorough model is called the Beckmann distribution function (Beckmann and Spizzichino 1963). Its simplified form is given in Equation (F.76). To account for some facets that may be blocked from the incident radiation by other facets, a geometric attenuation factor G as given in Equation (F.77) is incorporated.

$$D = \frac{1}{m^2 \cos^4 \alpha} e^{-\left(\frac{\tan \alpha}{m}\right)^2}. \tag{F.76}$$

$$G = \min\left(1, \frac{2(\mathbf{N}\cdot\mathbf{H})(\mathbf{N}\cdot\mathbf{V})}{\mathbf{V}\cdot\mathbf{H}}, \frac{2(\mathbf{N}\cdot\mathbf{H})(\mathbf{N}\cdot\mathbf{L})}{\mathbf{V}\cdot\mathbf{H}}\right). \tag{F.77}$$

One of the issues encountered in conducting the study presented in Chapter 5 was the presence of rat hair on the skin samples. Although the skin surface was shaved prior to excision, it is not possible to remove all hair follicles. This raises the question if hair follicles interfere with the THz measurements through strong surface reflection. Figure F.1 shows the extracted optical properties from 0.3–1 THz for lyophilised rat ventral skin with and without removal of the hair through shaving. The plots of the extinction coefficients deviate by no more than 0.01 at each frequency, thus are quite similar. The plots of the refractive indices may initially appear very different but considering the small range of values in the ordinate (y-axis), their refractive indices are not dissimilar. Therefore, the reduction in hair length through shaving appears to have not altered the sample's surface reflectivity. To verify this observation, a novel study was conducted using the Beckmann distribution function to determine if hair causes surface reflections. The results of the study are presented in the next Subsection.

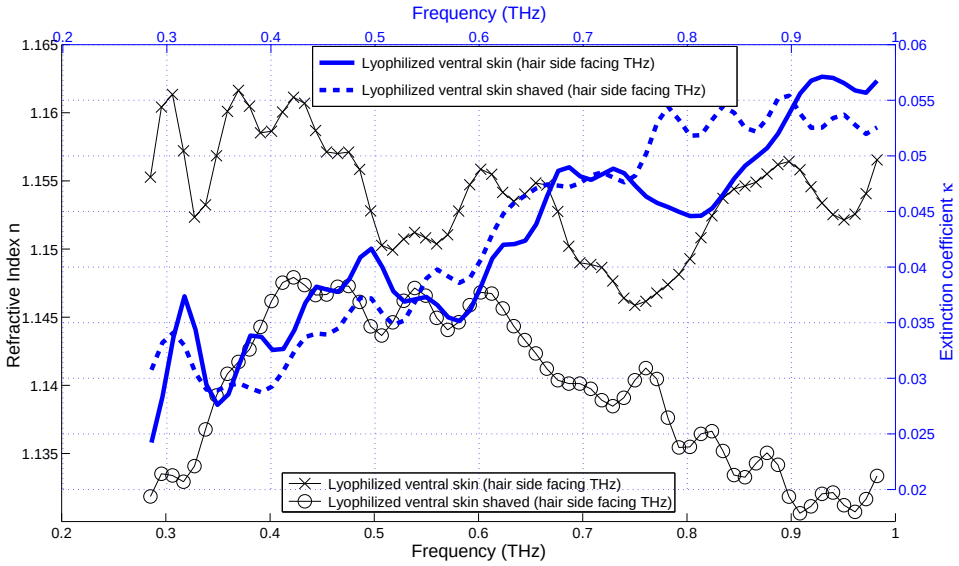

Figure F.1: Optical properties of rat ventral skin, with and without shaving. The solid and dashed lines represent the extinction coefficients, while the lines with circle and cross markers represent the refractive indices. Even with shaving, the surface of the rat skin contains hair follicles.

F.8.1 Application of the Beckmann Distribution Function

The scene size used in this simulation is 128×128 pixels. The amount of specular versus diffuse reflection can be altered using the factors s and d respectively, where $s + d = 1$. The sample simulated in this study is ideal fresh skin (no moisture) with optical properties consistent with those reported in (Fitzgerald *et al.* 2003). The Fresnel reflection coefficient $F(\theta, \lambda)$ of the sample can therefore be calculated, where λ is the wavelength and θ is the angle of incidence between $\mathbf{L}$ and $\mathbf{N}$. The skin sample is assumed to be slightly convex in the direction of the incoming THz radiation in order to mimic actual skin samples that are seldom flat. The solid angle Ω of the incident THz radiation $I_i(\lambda)$ is calculated over 2×2 pixels. The reflected THz signal $I_r(\lambda)$ in the frequency domain is therefore equal to:

$$I_r(\lambda) = I_i(\lambda)(\mathbf{N} \cdot \mathbf{L})\Omega \left(\frac{sF(\theta, \lambda)\, D\, G}{\pi(\mathbf{N} \cdot \mathbf{V})(\mathbf{N} \cdot \mathbf{L})} + \frac{dF(\theta = 0^\circ, \lambda)}{\pi} \right). \tag{F.78}$$

Figures F.2(a) and F.2(b) show the magnitude of I_r at 1.225 THz for smooth and rough skin surfaces with the same diffuse and specular reflection factors d and s respectively. The rough skin surface mimics the rat skin with hair, and the smooth surface mimics a perfect hairless surface. The signal reflected from a rough surface is one order

of magnitude less than for a smooth surface, implying that the rough surface reflects less than the smooth surface. Since d and s are similar for both models, the reduction in reflection from the rough surface cannot be attributed to stronger diffuse reflection from the rough surface. The reduction is instead consistent with the notion of more loss from repeated bounces off the facets. This observation is in agreement with Dikmelik *et al.* (2006), where reflection mode THz spectroscopy of rough surfaces result in attenuated detected signals. Therefore, the strong reflection from the smooth surface may be beneficial to reflection mode THz spectroscopy, but disadvantageous for transmission mode THz spectroscopy.

To further support the observations in Figs. F.2(a) and F.2(b), Fig. F.3 presents a comparison of the incident and reflected THz signal, where the reflected THz signal is assumed to be reflected by 180°. The magnitude of the reflected signal is more than 4 orders of magnitude weaker than the incident THz signal, again suggesting negligible loss through surface reflection. Since the measured results shown in Fig. F.1 are similar to the observations in Figs. F.2(b) and F.3, this implies that the unshaved surface has similar roughness to the shaved surface, both being poor surface reflectors of THz radiation. Based on the modelling using the Beckmann distribution function, and the THz measurements, the conclusion is that the incomplete removal of hair from rat skin samples does not contribute to surface reflections.

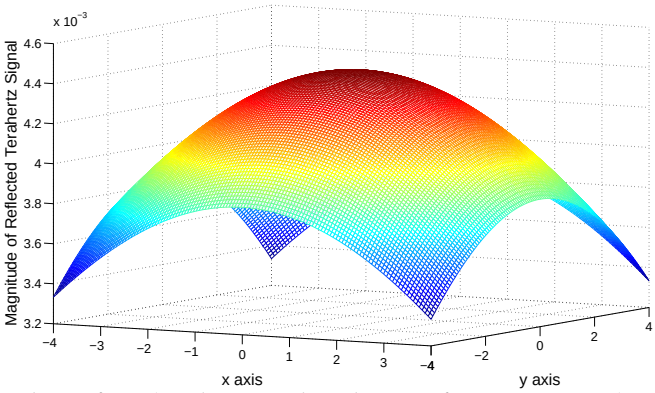

(a) Smooth surface (Beckmann distribution factor $m = 0.1$), specular reflection factor $s = 0.1$, and diffuse reflection factor $d = 0.9$

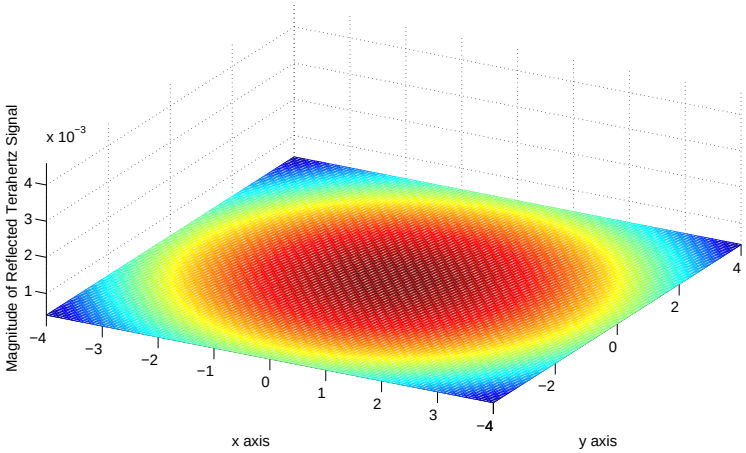

(b) Rough surface (Beckmann distribution factor $m = 1$), specular reflection factor $s = 0.1$, and diffuse reflection factor $d = 0.9$

Figure F.2: Magnitudes of the reflected THz signal at 1.225 THz. The $y-$axes of Figs. F.2(a) and F.2(b) have arbitrary units (a.u.). (a) As shown by the dark red peak, the maximum magnitude at 4.6×10^{-3} a.u. indicates maximum reflectivity from the smooth sample. (b) The maximum magnitude for the rough sample is 4.06×10^{-4} a.u., which is one order of magnitude less than for the smooth surface, implying that the rough surface reflects less than the smooth surface.

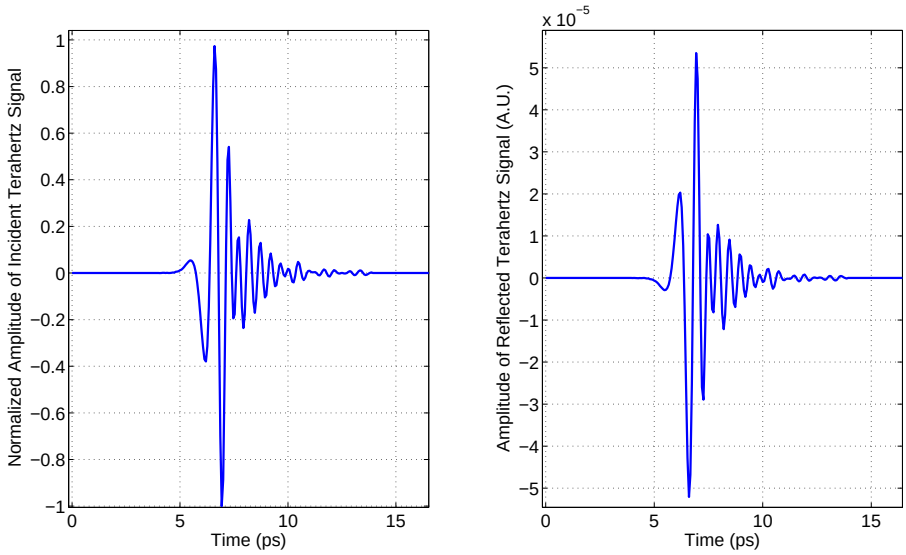

Figure F.3: Comparison between the incident THz signal and the simulated reflected signal using the Beckmann distribution function. The measured incident THz signal is more than 4 orders of magnitude stronger than the reflected THz signal simulated using the Beckmann distribution function with distribution factor $m = 1$ (rough), indicating that hair does not interfere with transmission mode THz measurements.

Appendix G

General Solution of the Helmholtz Equation

THIS Appendix presents the derivation of the general solution of the Helmholtz equation as required in Chapter 9.

G.1 General Solution of the Helmholtz Equation

This Appendix derives the general solution for the Helmholtz equation given in Equation (9.3) for the mth layer.

The differential form of Maxwell's equation can be expressed as:

$$\begin{aligned}
\nabla^2\mathbf{E} - \mu\sigma\frac{\partial\mathbf{E}}{\partial t} - \mu\epsilon\frac{\partial^2\mathbf{E}}{\partial t^2} &= \boldsymbol{\nabla}\left(\frac{\rho}{\epsilon}\right) \\
\nabla^2\mathbf{B} &= \mu\sigma\frac{\partial\mathbf{B}}{\partial t} + \mu\epsilon\frac{\partial^2\mathbf{B}}{\partial t^2} \\
\text{but } \mu\mathbf{H} &= \mathbf{B} \\
\therefore\ \mu\nabla^2\mathbf{H} &= \mu^2\sigma\frac{\partial\mathbf{H}}{\partial t} + \mu^2\epsilon\frac{\partial^2\mathbf{H}}{\partial t^2} \\
\nabla^2\mathbf{H} &= \mu\sigma\frac{\partial\mathbf{H}}{\partial t} + \mu\epsilon\frac{\partial^2\mathbf{H}}{\partial t^2}\,.
\end{aligned}$$

For an electromagnetic wave with electric field vector in the plane of incidence (xz plane), the differential form of Maxwell's equation can be written as:

$$\left[\nabla^2 H(x,z,t) = \frac{\partial^2 H(x,z,t)}{\partial x^2} + \frac{\partial^2 H(x,z,t)}{\partial z^2}\right] = \mu\sigma\frac{\partial H(x,z,t)}{\partial t} + \mu\epsilon\frac{\partial^2 H(x,z,t)}{\partial t^2}\,. \quad \text{(G.1)}$$

In the frequency domain, where the angular frequency $\omega = 2\pi\nu$ and ν is the frequency in units of Hertz, Equation (G.1) becomes:

$$\begin{aligned}
\nabla^2 H(x,z,\omega) &= i\omega\mu\sigma H(x,z,\omega) - \omega^2\mu\epsilon H(x,z,\omega) \\
\left[\nabla^2 - (i\omega\mu\sigma - \omega^2\mu\epsilon)\right] H(x,z,\omega) &= 0 \\
\left[\nabla^2 - \gamma^2\right] H(x,z,\omega) &= 0 \\
\left[\frac{\partial^2 H(x,z,\omega)}{\partial x^2} + \frac{\partial^2 H(x,z,\omega)}{\partial z^2} - \gamma^2 H(x,z,\omega)\right] &= 0\,. \quad \text{(G.2)}
\end{aligned}$$

Equation (G.2) is the Helmholtz equation, and the square of the propagation constant γ is equal to:

$$\gamma^2 = (i\omega\mu\sigma - \omega^2\mu\epsilon) = -\hat{k}^2 = -\left\{k\,\hat{n}\right\}^2 = -\left\{k(n - i\kappa)\right\}^2\,, \quad \text{(G.3)}$$

and $\hat{k}$ is the complex wavenumber, $k = 2\pi/\lambda$ is the wavenumber, $\hat{n}$ is the complex refractive index with real and imaginary components n and κ respectively. For a multilayered surface, the square of the propagation constant of the mth layer is equal to:

$$\gamma_m^2 = i\omega\mu_m\sigma - \omega^2\mu_m\epsilon_m\,. \quad \text{(G.4)}$$

To find the solution to the Helmholtz equation in Equation (G.2), separation of variables is used as follows:

$$\begin{aligned} H(x,z,\omega) &= F(x,\omega)G(z,\omega)\,, \\ \text{or more simply } H(x,z) &= F(x)G(z) \end{aligned} \tag{G.5}$$

since all terms are dependent on the angular frequency ω.

Differentiating Equation (G.5) gives:

$$\frac{\partial H}{\partial x} = \frac{\partial F(x)}{\partial x}G(z) \tag{G.6}$$

$$\frac{\partial^2 H}{\partial x^2} = \frac{\partial^2 F(x)}{\partial x^2}G(z) \tag{G.7}$$

$$\frac{\partial^2 H}{\partial z^2} = \frac{\partial^2 G(z)}{\partial z^2}F(x)\,. \tag{G.8}$$

Substitute Equations (G.7) and (G.8) into Equation (G.2) gives:

$$\begin{aligned} \frac{\partial^2 F(x)}{\partial x^2}G(z) + \frac{\partial^2 G(z)}{\partial z^2}F(x) - \gamma^2 F(x)G(z) &= 0 \\ \frac{\partial^2 F(x)}{\partial x^2}G(z) &= -\frac{\partial^2 G(z)}{\partial z^2}F(x) + \gamma^2 F(x)G(z)\,. \end{aligned} \tag{G.9}$$

Dividing both sides of Equation (G.9) by $F(x)G(z)$ results in:

$$\begin{aligned} \frac{1}{F(x)}\frac{\partial^2 F(x)}{\partial x^2} &= -\frac{1}{G(z)}\frac{\partial^2 G(z)}{\partial z^2} + \gamma^2 \\ &= \frac{1}{G(z)}\left[-\frac{\partial^2 G(z)}{\partial z^2} + \gamma^2 G(z)\right]. \end{aligned} \tag{G.10}$$

Both sides of this explicit equation must be equal to a constant. For the solutions to be unique, the constant must be a negative number. Let this negative constant be $-\beta^2$. The left side of Equation (G.10) becomes:

$$\begin{aligned} \frac{1}{F(x)}\frac{\partial^2 F(x)}{\partial x^2} &= -\beta^2 \\ \frac{\partial^2 F(x)}{\partial x^2} + \beta^2 F(x) &= 0\,. \end{aligned} \tag{G.11}$$

The right side of Equation (G.10) becomes:

$$\frac{1}{G(z)}\left[-\frac{\partial^2 G(z)}{\partial z^2} + \gamma^2 G(z)\right] = -\beta^2$$

$$\frac{\partial^2 G(z)}{\partial z^2} - \gamma^2 G(z) - \beta^2 G(z) = 0. \tag{G.12}$$

Equations (G.11) and (G.12) are now homogeneous ordinary differential equations (ODEs) with constant coefficients,therefore their general solutions can now be easily found. For $F(x)$:

$$\text{let } F(x) = e^{px} \tag{G.13}$$
$$\therefore \frac{\partial^2 F(x)}{\partial x^2} = p^2 e^{px}, \tag{G.14}$$

where p is the root of $F(x)$.

Substituting Equations (G.13) and (G.14) into Equation (G.11) gives:

$$\begin{aligned}
\frac{\partial^2 F(x)}{\partial x^2} + \beta^2 F(x) &= 0 \\
p^2 e^{px} + \beta^2 e^{px} &= 0 \\
e^{px}(p^2 + \beta^2) &= 0 \quad \text{where the characteristic equation is } p^2 + \beta^2 \\
p^2 &= -\beta^2 \\
p &= \pm i\beta \\
\therefore F(x) &= c_1 e^{-i\beta x} \quad \text{where } c_1 \text{ is a constant.}
\end{aligned}$$

For $G(z)$:

$$\text{let } G(z) = e^{hz} \tag{G.15}$$
$$\therefore \frac{\partial^2 G(z)}{\partial z^2} = h^2 e^{hz}, \tag{G.16}$$

where h is the root of $G(z)$.

Substituting Equations (G.15) and (G.16) into Equation (G.12) gives:

$$\begin{aligned}
\frac{\partial^2 G(z)}{\partial z^2} - \gamma^2 G(z) - \beta^2 G(z) &= 0 \\
h^2 e^{hz} - \gamma^2 e^{hz} - \beta^2 e^{hz} &= 0
\end{aligned}$$

$$\begin{aligned}
e^{hz}(h^2 - \gamma^2 - \beta^2) &= 0 \quad \text{where the characteristic equation is } h^2 - \gamma^2 - \beta^2 \\
h^2 &= \gamma^2 + \beta^2 \\
h &= \pm\sqrt{\gamma^2 + \beta^2} \\
\therefore G(z) &= c_2 e^{z\sqrt{\gamma^2+\beta^2}} + c_3 e^{-z\sqrt{\gamma^2+\beta^2}} \quad \text{where } c_2, c_3 \text{ are constants.}
\end{aligned}$$

Therefore, the general solution of Equation (G.5) is:

$$\begin{aligned} H(x,z) &= F(x)G(z) \\ &= c_1 e^{-i\beta x}\left(c_2 e^{-z\sqrt{\gamma^2+\beta^2}} + c_2 e^{z\sqrt{\gamma^2+\beta^2}}\right) \qquad \text{(G.17)} \\ &= c_1 c_2 e^{-z\sqrt{\gamma^2+\beta^2}-i\beta x} + c_1 c_2 e^{z\sqrt{\gamma^2+\beta^2}-i\beta x} \\ &= a e^{-z\sqrt{\gamma^2+\beta^2}-i\beta x} + b e^{z\sqrt{\gamma^2+\beta^2}-i\beta x}. \qquad \text{(G.18)} \end{aligned}$$

As function of frequency ω, Equation (G.18) becomes:

$$\begin{aligned} H(x,z,\omega) &= F(x,\omega)G(z,\omega) \\ &= a(\omega)e^{-z\sqrt{\gamma^2+\beta^2}-i\beta x} + b(\omega)e^{z\sqrt{\gamma^2+\beta^2}-i\beta x}. \qquad \text{(G.19)} \end{aligned}$$

However, recall that the square of the propagation constant γ^2 varies with frequency ω and layer depth m as highlighted in Equation (G.4). Therefore, at the mth layer:

$$H_m(x,z,\omega) = a_m(\omega)e^{-z\sqrt{\gamma_m^2+\beta^2}-i\beta x} + b_m(\omega)e^{z\sqrt{\gamma_m^2+\beta^2}-i\beta x}, \qquad \text{(G.20)}$$

where γ_m^2 is a function of frequency ω. Equation (G.20) is repeated as Equation (9.6) in Chapter 9.

Appendix H

Data Processing Algorithms

THIS Appendix provides a summary of the MATLAB source code used to generate results in Chapters 5–9 and Appendix A of this Thesis. The names of the source code files, their functions, and the related Chapters in this Thesis are listed. The full source code is available in the enclosed CD-ROM. Where applicable, extracts of the full source code are presented in this Appendix to highlight notable steps undertaken in data processing.

H.1 Data Processing Common to All Measured Datasets

As highlighted in Section 5.2, data processing of the measured THz signal is usually required before meaningful interpretation of the data can be conducted. In this Thesis, all measured THz signals are first processed using a common set of data processing techniques illustrated in Fig. H.1(a). This first set of processing fetches the raw data, strips away any header information, performs truncation of the time domain data, averages multiple sets of data if requested, and transforms the data from the time domain to the frequency domain. The illustration includes the equations referred to in Section 5.2.3.

The second set of data processing, as illustrated in Fig. H.1(b), allows the user to extract the optical (dielectric) properties of the sample under investigation. The extracted optical properties can then be written to separate files for future analysis.

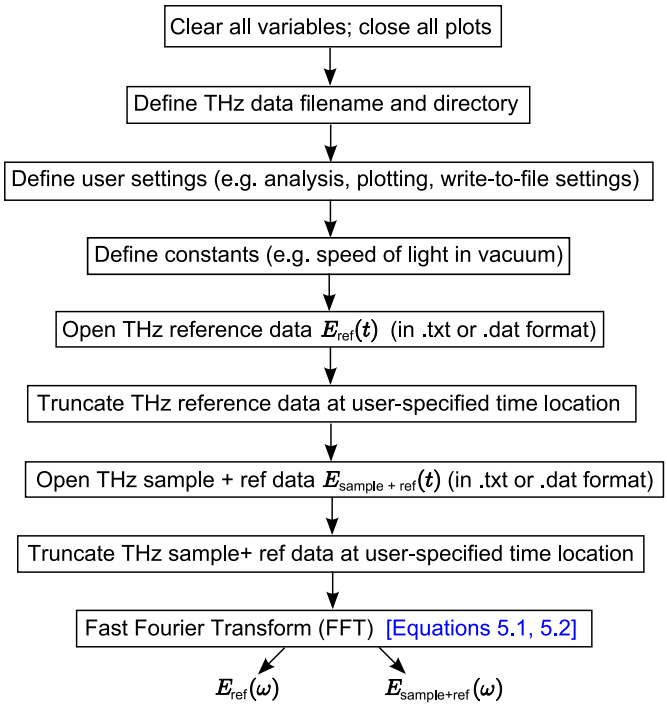

(a) First set of data processing deals mainly with the time domain THz measurement

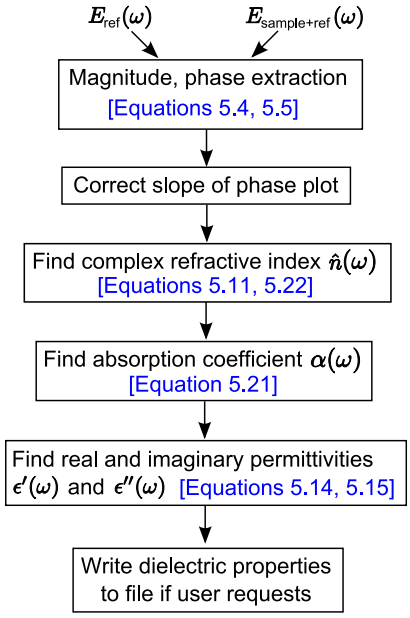

(b) Second set of data processing deals with extracting the optical (dielectric) properties

Figure H.1: Flow chart of common data processing techniques used in this Thesis. (a) The first part of the data processing involves fetching the raw THz measurement files that are recorded in the time domain in either .txt or .dat format. The built-in MATLAB Fast Fourier Transform function `fft` is used to transform the data from the time domain to the frequency domain. (b) The second part of the data processing involves extracting the optical (dielectric) properties, and writing them to separate files if requested.

Name of File (*.m)	Function	Related Chapter(s)
freqanalysis30Oct09	Main program	Chapters 4–8
origfilesPE	User chooses file related to polyethylene	Chapter 4
origfilesrattissue	User chooses file related to rat tissue	Chapter 5
origflesbrain	User chooses file related to snap-frozen brain tissue	Chapter 6
origfilesbelg	User chooses file related to protein gels/solutions	Chapter 7
origfilesfibres	User chooses file related to fibreglass array	Chapter 8
getaccessfile	Fetch storage path of chosen file, and stored information about sample (e.g. thickness)	Chapters 4–8
findrefaverage	Average reference files if this option chosen	Chapters 4–8
setplotcolours	Set plotting colours	Chapters 4–8
getdatafromfile	Fetch data for analysis	Chapters 4–8
findaverage2	Average sample files if this option chosen	Chapters 4–8
plottimewaveforms	Plot time domain waveforms without error bars	Chapters 4–8
plottimewaveformsErrorbars	Plot time domain waveforms with error bars	Chapters 4–8
plotfreqwaveforms	Plot frequency domain waveforms	Chapters 4–8
plotabsorbancecoeffwaveforms	Plot absorption (extinction) coefficient waveforms	Chapters 4–8
findrefractiveindex	Plot absorption (extinction) coefficient waveforms	Chapters 4–8
getfilestatus4	Write optical (dielectric) properties to file	Chapters 4–8

Table H.1: MATLAB source code files for performing common data processing. Apart from the main program file called freqanalysis30Oct09.m, all files listed in this Table are functions called by the main program.

H.1.1 List of Source Code Files

Table H.1 lists the name of files containing MATLAB source code that performs the operations illustrated in Fig. H.1.

By calling the last function listed in Table H.1, getfilestatus4.m, the optical (dielectric) properties are written to separate files. To open and plot these files individually or as a batch, the file called plotfromseparatefilesopprop9.m is used.

Name of File (*.m)	Function
scattercyl	Main program
getanyfile	Opens any type of file
callsscattercylcs	Adjusts radius array, then calls scattercscyl.m
scattercylcs	Finds C_{sca}, C_{ext}, Q_{sca}, and Q_{ext}
findscattercylab	Calculates the a and b scattering coefficients for a cylinder
findbessel	Calculates the Bessel functions of the first and second kinds
scattercylTscatmat	Calculates the scattering T-matrix for a cylinder
findscattercylT12	Calculates either T1 or T2 in the scattering matrix for a cylinder
findscattercylT34	Calculates either T3 or T4 in the scattering matrix for a cylinder
MieWn	Uses algorithm by Wiscombe (1980) to deal with NaNs (not-a-number) in Matlab (author: Ville Bergholm)

Table H.2: MATLAB source code files for modelling scattering. The main program scattercyl.m calls the functions listed from row 2 onwards in this Table.

H.2 Algorithms for Modelling Scattering

Table H.2 lists the name of files containing MATLAB source code that models scattering from cylinders (fibrils). These source code files implement the equations in Sections 7.5.1 and 8.3.2. Extracts of source code obtained online[82] have been included where applicable to enhance built-in tests for errors. The author, Ville Bergholm, has been acknowledged where appropriate in the source code files. The source code MieWn.m by Ville Bergholm is used verbatim as it implements the algorithm by Wiscombe (1980) for dealing with NaNs (not-a-number) generated by MATLAB.

H.2.1 Source Code

Source code for three functions for modelling scattering are provided in this Subsection. For brevity, the source code presented here have been edited in length to remove plotting commands. Plotting commands are included in the source code in the CD-ROM.

[82] From *Mie Matlab* at <http://diogenes.iwt.uni-bremen.de/vt/laser/wriedt/Mie_Type_Codes/body_mie_type_codes.html> (last accessed: 2009-01-24). Author of source code: Ville Bergholm. The 'Mie Matlab' link is not available when last checked on 2010-05-27.

Function: scattercylcs.m

```
% scattercscyl.m
%
% This program finds the scattering cross section Csa, the extinction cross section Cext,
% the scattering efficiency Qsca, and the extinction efficiency Qext.
%
% Version info: Checked against Ville Bergholm's 2001, 2002 algorithm MieCS.m
%
% Author: Gretel M. Png
% Last edited: 07 Jan 2010

function [Cext, Csca, Qext, Qsca, x, a, b, a0, b0, smalllimit] = ...
    scattercscyl(r, L, k, m, norder, efield, Eincangle, varyparamtype, n0, trueradius, s)

if nargin < 11
  % particle surface conductivity parameter
  s = 0;
end

nu = 0.5; % order of first bessel function

if Eincangle == 90
   Eincanglerad = pi/2;
   Eincanglecase = 1;
else
   Eincanglerad = Eincangle*pi/180;
   Eincanglecase = 2;
end % End if test (Eincangle == 90)

r = r.';
trueradius = trueradius.';
k = k.';     % k = 2*pi*n_medium/lambda
morig = m;
m = m.';     % m = n_sample/n_medium;
x = k.*trueradius;

nmax = norder;
xnew = x.';  % x = k*trueradius = n_medium*2*pi*trueradius/lambda;

if (max(x) < 0.4) && (max(abs(m).*x) < 0.4)
    smalllimit = 1;
    disp('Small-particle limit reached');
else
    smalllimit = 0;
end % End if test

if smalllimit == 1
    switch efield
        case 'para'
            b0 = (-i*pi*(xnew.^2).*(morig.^2 - 1))/4;
```

```
            b =  (-i*pi*(xnew.^4).*(morig.^2 - 1))/32;
            a0 = zeros(size(b0));
            a =  zeros(size(b));
        case 'perp'
            a0 = (-i*pi*(xnew.^4).*(morig.^2 - 1))/32;
            a =  (-i*pi*(xnew.^2).*(morig.^2 - 1))./(4*(morig.^2 + 1));
            b0 = zeros(size(a0));
            b =  zeros(size(a));
        otherwise
    end % End switch test (efield)
else
    [a,b,a0,b0] = findscattercylab(nmax, x, m, efield, Eincangle, n0, nu, s);

    % From Ville Bergholm: Check for NaNs. If yes, replace with zeros
    while 1 %infinite loop
        test = find(any(any(isnan([a;b]), 3),1)); % indices of faulty x's
        if isempty(test)
            break; % break out of the while loop
        end
        disp('NaN found. Replacing with zeros');
        a(:, test, :) = 0;
        b(:, test, :) = 0; % remove the NaNs
        nmax2 = MieWn(x(test)); % take a new (smaller) nmax
        if nmax2 > nmax
            error('This should never happen');
        end % end if test (nmax2 > nmax)

        [A,B,A0,B0] = findscattercylab(nmax2, x(test), m(test), efield, Eincangle, s);

        a(1:nmax2, test, :) = A;
        b(1:nmax2, test, :) = B;
    end % End while loop
end % End if test (smalllimit == 1)

switch varyparamtype
    case 'frequency'
        geoxsection = 2*trueradius*L; % geometric cross-section of a cylinder = rectangle
        switch efield
            case 'para' % E field parallel to xz plane
                if smalllimit == 1
                  Qext = (2./xnew).*real(2*b + b0);
                  Qsca = (2./xnew).*(2*((abs(a).^2) + (abs(b).^2)) + (abs(b0)).^2);
                else
                  Qext = (2./xnew).*real(2*sum(b) + b0);
                  Qsca = (2./xnew).*(2*sum((abs(a).^2) + (abs(b).^2)) + (abs(b0)).^2);
                end % End if test (smalllimit == 1)
            case 'perp' % E field perpendicular to xz plane
                 if smalllimit == 1
                  Qext = (2./xnew).*real(2*a + a0);
                  Qsca = (2./xnew).*(2*((abs(a).^2) + (abs(b).^2)) + (abs(a0)).^2);
                 else
                  Qext = (2./xnew).*real(2*sum(a) + a0);
                  Qsca = (2./xnew).*(2*sum((abs(a).^2) + (abs(b).^2)) + (abs(a0)).^2);
```

```
                end % End if test (smalllimit == 1)
            otherwise
                disp('Unknown E polarization');
                Qext1 = (2./xnew).*real(2*sum(b) + b0);
                Qsca1 = (2./xnew).*(2*sum((abs(a).^2) + (abs(b).^2)) + (abs(b0)).^2);
                Qext2 = (2./xnew).*real(2*sum(a) + a0);
                Qsca2 = (2./xnew).*(2*sum((abs(a).^2) + (abs(b).^2)) + (abs(a0)).^2);
                Qext = 0.5.*(Qext1 + Qext2);
                Qsca = 0.5.*(Qsca1 + Qsca2);
        end % End switch test (efield)
    case 'radius'
        trueradiusnew = trueradius.';
        geoxsection = 2*trueradiusnew*L; % geometric cross-section of a cylinder = rectangle
        switch efield
            case 'para' % E field parallel to xz plane
                Qext = (2./xnew).*real(2*sum(b) + b0);
                Qsca = (2./xnew).*(2*sum((abs(a).^2) + (abs(b).^2)) + (abs(b0)).^2);
            case 'perp' % E field perpendicular to xz plane
                Qext = (2./xnew).*real(2*sum(a) + a0);
                Qsca = (2./xnew).*(2*sum((abs(a).^2) + (abs(b).^2)) + (abs(a0)).^2);
            otherwise
                disp('Unknown E polarization');
                Qext1 = (2./xnew).*real(2*sum(b) + b0);
                Qsca1 = (2./xnew).*(2*sum((abs(a).^2) + (abs(b).^2)) + (abs(b0)).^2);
                Qext2 = (2./xnew).*real(2*sum(a) + a0);
                Qsca2 = (2./xnew).*(2*sum((abs(a).^2) + (abs(b).^2)) + (abs(a0)).^2);
                Qext = 0.5.*(Qext1 + Qext2);
                Qsca = 0.5.*(Qsca1 + Qsca2);
        end % End switch test (efield)
    otherwise
        disp('Please choose varyparamtype again.');
end % End switch test (varyparamtype)

Cext = geoxsection.*Qext;
Csca = geoxsection.*Qsca;
```

Function: findscattercylab.m

```
% findscattercylab.m
%
% This program calculates the a and b scattering coefficients for a cylinder.
%
% Author: Gretel M. Png
% Last edited: 25 Nov 2009

function [a,b,a0,b0] = findscattercylab(nmax, x, m, efield, Eincangle, n0, nu, s)

if nargin < 8
  s = 0; % default: no surface conductance
end
```

```
if Eincangle == 90
   Eincanglerad = pi/2;
   Eincanglecase = 1;
else
   Eincanglerad = Eincangle*pi/180;
   Eincanglecase = 2;
end % End if test (Eincangle == 90)

% open up m and x into row vectors
m = m(:).';    % m = n_sample/n_medium;
x = (x(:).')./n0;    % x = n_medium*k.*r = n_medium*2*pi*r/lambda
mx = m.*x;    % mx = n_sample*k.*r

switch Eincanglecase
    case 1 % Eincangle == 90
        [J,Y] = findbessel(nmax,x,nu);
        H = J + i*Y;

        [J_m,temp] = findbessel(nmax,mx,nu);
        clear temp;

        J0 = besselj(nu,x);
        Y0 = bessely(nu,x);
        H0 = J0 + i*Y0;
        J0_m = besselj(nu,mx);
        Y0_m = bessely(nu,mx);

        DJ0 = -J(1,:);
        DY0 = -Y(1,:);
        DJ0_m = -m.*J_m(1,:);
        DH0 = DJ0 + i*DY0;

%         temp vectors for calculating derivatives
        TJ = [sin(x) ; J(1:(nmax-1),:)];      % J_0 = sin(x)
        TJ_m = [sin(mx) ; J_m(1:(nmax-1),:)];
        TY = [-cos(x) ; Y(1:(nmax-1),:)];  % H_0 = -cos(x)

        % temp matrices to facilitate computation of derivatives
        N = ((1:nmax).')*ones(1,length(x));
        Nm = ((1:nmax).')*ones(1,length(mx));

        if length(mx) > 1
            mx2 = ones(nmax,1)*mx;
            if length(x) > 1
                x2 = ones(nmax,1)*x;
            else
                x2 = x;
            end % End if test (length(x) > 1)
        else
            mx2 = mx;
            x2 = x;
        end % End if test (length(mx) > 1)
```

```
        orginalm = m;
        clear m;
        if length(orginalm) == 1
            m = temp*ones(nmax,length(x));
        else
            m = repmat(orginalm,nmax,1);
        end % End if test (length(orginalm) == 1)
        clear temp;

        % derivatives are calculated using recursion formulae
        DJ = TJ-N.*J./x2;
        DJ_m = TJ_m-Nm.*J_m./(mx2); %
        DY = TY-N.*Y./x2;
        DH = DJ + i * DY;

        switch efield
            case 'para' % E field parallel to xz plane
                if length(m) == 1
                    b = (J_m.*DJ - m*DJ_m.*J)./(J_m.*DH - m*DJ_m.*H);
                    b0 = (J0_m.*DJ0 - orginalm*DJ0_m.*J0)./(J0_m.*DH0 - orginalm*DJ0_m.*H0);
                else
                    b = (J_m.*DJ - m.*DJ_m.*J)./(J_m.*DH - m.*DJ_m.*H);
                    b0 = (J0_m.*DJ0 - orginalm.*DJ0_m.*J0)./(J0_m.*DH0 - orginalm.*DJ0_m.*H0);
                end % End if test (length(m) == 1)
                a = zeros(nmax,length(x));
                a0 = zeros(1,length(x));
            case 'perp' % E field perpendicular to xz plane
                if length(m) == 1
                  a = (m*DJ.*J_m - J.*DJ_m)./(m*J_m.*DH - DJ_m.*H);
                  a0 = (orginalm*DJ0.*J0_m - J0.*DJ0_m)./(orginalm*J0_m.*DH0 - DJ0_m.*H0);
                else
                  a = (m.*DJ.*J_m - J.*DJ_m)./(m.*J_m.*DH - DJ_m.*H);
                  a0 = (orginalm.*DJ0.*J0_m - J0.*DJ0_m)./(orginalm.*J0_m.*DH0 - DJ0_m.*H0);
                end % End if test (length(m) == 1)
                b = zeros(nmax,length(x));
                b0 = zeros(1,length(x));
            otherwise
                disp('Unknown E polarization');
        end % End switch test (efield)

    case 2 % Eincangle < 90
        if length(m) == 1
            m = m*ones(1,length(x));
        end % End if test (length(m) == 1)

        m2 = m.^2;
        xi = x.*sin(Eincanglerad);
        eta = x.*sqrt(m2-(cos(Eincanglerad)).^2);

        [J_xi,Y_xi] = findbessel(nmax,xi,nu);
        H_xi = J_xi + i*Y_xi;

        % psi_m = RB1(nmax, mx);% size = [nmax, length(mx)]
```

```
[J_eta,temp] = findbessel(nmax,eta,nu);
clear temp;

% temp vectors for calculating derivatives
TJ_xi = [sin(x) ; J_xi(1:(nmax-1),:)];      % J_0 = sin(x)
TJ_eta = [sin(mx) ; J_eta(1:(nmax-1),:)]; %longer
TY_xi = [-cos(x) ; Y_xi(1:(nmax-1),:)];  % H_0 = -cos(x)

% temp matrices to facilitate computation of derivatives
N = ((1:nmax).')*ones(1,length(x));
Nm = ((1:nmax).')*ones(1,length(mx));

if length(mx) > 1
   mx2 = ones(nmax,1)*mx;
   if length(x) > 1
      x2 = ones(nmax,1)*x;
   else
      x2 = x;
   end
else
   mx2 = mx;
   x2 = x;
end

% derivatives are calculated using recursion formulae
DJ_xi = TJ_xi-N.*J_xi./x2; % DJ_xi
DJ_eta = TJ_eta-Nm.*J_eta./(mx2); % DJ_eta
DY_xi = TY_xi-N.*Y_xi./x2; % DY_xi
DH_xi = DJ_xi + i * DY_xi; % DH_xi

n = repmat([1:1:nmax].',1,length(x));
temp = m2; clear m2;
m2 = repmat(temp,nmax,1); clear temp;
temp = xi; clear xi;
xi = repmat(temp,nmax,1); clear temp;
temp  = eta; clear eta;
eta = repmat(temp,nmax,1); clear temp;

Cn = cos(Eincanglerad)*n.*eta.*J_eta.*J_xi.*((xi./eta).^2 - 1);
Dn = cos(Eincanglerad)*n.*eta.*J_eta.*H_xi.*((xi./eta).^2 - 1);
Vn = xi.*(m2.*xi.*DJ_eta.*H_xi - eta.*J_eta.*DH_xi);
Wn = i*xi.*(eta.*J_eta.*DH_xi - xi.*DJ_eta.*H_xi);
switch efield
    case 'para' % E field parallel to xz plane
         Bn = xi.*(m2.*xi.*DJ_eta.*J_xi - eta.*J_eta.*DJ_xi);
         a = (Cn.*Vn - Bn.*Dn) ./(Wn.*Vn + i*(Dn.^2));
         b = (Wn.*Bn + i*Dn.*Cn) ./(Wn.*Vn + i*(Dn.^2));
    case 'perp' % E field perpendicular to xz plane
         An = i*xi.*(xi.*DJ_eta.*J_xi - eta.*J_eta.*DJ_xi);
         a = -(An.*Vn - i*Cn.*Dn) ./(Wn.*Vn + i*(Dn.^2));
         b = -i*(Cn.*Wn + An.*Dn) ./(Wn.*Vn + i*(Dn.^2));
    otherwise
        disp('Unknown E polarization');
```

```
        end % End switch test (efield)
    otherwise % Eincangle > 90
        disp('E field incident at an angle exceeding 90 degrees');
end % End switch (Eincanglecase)
```

Function: scattercylTscatmat.m

```
% scattercylTscatmat.m
%
% This program calculates the scattering T-matrix for a cylinder.
%
% Author: Gretel M. Png
% Last edited: 07 January 2009

function [T1,T2,T3,T4] = scattercylTscatmat(nmax, azimuth, acoeff, acoeff0, ...
                         bcoeff, bcoeff0, efield, zenangle, flipazimuth)

T1 = findscattercylT12(nmax, azimuth, bcoeff, bcoeff0, flipazimuth);
T2 = findscattercylT12(nmax, azimuth, acoeff, acoeff0, flipazimuth);

T3 = MieT34(nmax, azimuth, acoeff, flipazimuth);
T4 = MieT34(nmax, azimuth, bcoeff, flipazimuth);
```

H.3 Data Processing for Modelling Stratified Layers

The MATLAB program impulsefunctionlayers.m implements the equations introduced in Section 9.3. The source code of impulsefunctionlayers.m is as follows.

```
% impulsefunction_layers.m
%
% Material: Quartz, Skin, Adipose, Bone, Dura; Conditions: Dry Skin;
% Literature: gabriel_1996c_pmb, fitzgerald_2003_jbp
%
% This programme simulates the transmission of THz into 1 layer of skin. Properties of
% skin (relative permittivity, conductivity) are taken from interpolated data based on
% 2 authors---1 microwave and 1 THz
%
% Author: Gretel M. Png
% Last edited: 12 October 2005

close all, clear all;

% Constants
epsilon_0 = 8.8542e-12;  % permittivity of air
mu_0 = 4e-7*pi;          % permeability of air
sigma_0 = 0;             % conductivity of air
c = 3e8;                 % Speed of light
lambda = 1;              % dummy variable for model
```

```
plotlinethickness = 1.5; % Line thickness (1 point = 1/72"), default = 0.5
plotfontsize = 16;       % Font size of axes, (1 point = 1/72"), default = 10;
textfontsize = 14;       % Font size of text, (1 point = 1/72"), default = 10;

filePath = 'C:\GPngTRayFiles\GPngModelMatlabFiles\Brad\powderData\';
getdataPath = 'C:\GPngTRayFiles\GPngModelMatlabFiles\MatlabScripts\Extrapolation\';
savePath = 'C:\GPngTRayFiles\GPngModelMatlabFiles\Figures\UsingBradData\EPSFigs\';

% Electrical Properties of M-layered Model
% ---------------------------------------
% Layer 0
nquartz = 2.1;    % refractive index of quartz
hquartz = 0.002; % Thickness of quartz plate

% Layer 1
mu_1 = 1;        % Relative permeability of layer 1 (air)
%epsilon_1 = 1;  % Relative permittivity of layer 1 (air)
%sigma_1 = 1e-3;  % conductivity of layer 1 (air)

% Layer 2
mu_2 = 1;         % Relative permeability of layer 2 (adipose tissue)
sigma_2 = 0.9;    % conductivity of layer 2 (adipose tissue)
epsilon_2 = 20-i*5;     % Relative permittivity of layer 2 (adipose tissue)
psilon_2 = 20;   % Relative permittivity of layer 2 (adipose tissue)

% Layer 3
mu_3 = 1;         % Relative permeability of layer 3 (cortical bone)
sigma_3 = 0.1;    % conductivity of layer 3 (cortical bone)
epsilon_3 = 1.5 - i*3;   % Relative permittivity of layer 3 (cortical bone)
%epsilon_3 = 1.5; % Relative permittivity of layer 3 (cortical bone)

% Layer 4
mu_4 = 1;         % Relative permeability of layer 4 (dura)
sigma_4 = 0.48;   % conductivity of layer 4 (dura)
epsilon_4 = 6 - i*6;   % Relative permittivity of layer 4 (dura)
%epsilon_4 = 6;    % Relative permittivity of layer 4 (dura)

% Layer 5
mu_5 = 1;         % Relative permeability of layer 5 (CSF)
sigma_5 = 0.765;   % conductivity of layer 5 (CSF)
epsilon_5 = 9.3 - i*13.8;   % Relative permittivity of layer 5 (CSF)
%epsilon_5 = 9.3;    % Relative permittivity of layer 5 (CSF)

% Layer 6
mu_6 = 1;         % Relative permeability of layer 6 (grey)
sigma_6 = 0.533;   % conductivity of layer 6(grey)
epsilon_6 = 7.75 - i*9.6;   % Relative permittivity of layer 6 (grey)
%epsilon_6 = 7.75;    % Relative permittivity of layer 6 (grey)

% Layer 7
mu_7 = 1;         % Relative permeability of layer 7 (white)
sigma_7 = 0.4;   % conductivity of layer 7 (white)
epsilon_7 = 6;    % Relative permittivity of layer 7 (white)
```

```
% Thickness of M-layered Model
% ------------------------------
% Values for pics in paper
h1 = 100e-6;      % thickness of layer 1 in meters
h2 = 0.001;       % thickness of layer 2 in meters
h3 = 0.01;        % thickness of layer 3 in meters
h4 = 250e-6;      % thickness of layer 4 in meters
h5 = 200e-6;      % thickness of layer 5 in meters
h6 = 0.002;       % thickness of layer 6 in meters
h7 = 0.1;         % thickness of layer 7 in meters

num_layers = 7; % Pick number of layers to observe
extensionfactor = 1.5;

% Open data file containing permittivity values
% ----------------------------------------------
fid = fopen(strcat(getdataPath,'skin_epsilon.txt'), 'r');
data_extract = fread(fid, 'double');
fclose(fid);

num_types_data = data_extract(1); % Types of data stored
% First batch = frequencies
% Second batch = \epsilon^\prime
% Third batch = \epsilon^{\prime\prime}
% Fourth batch = \sigma
end_first_batch = (max(size(data_extract))-1)/num_types_data + 1;
end_second_batch = 2*(max(size(data_extract))-1)/num_types_data + 1;
end_third_batch = 3*(max(size(data_extract))-1)/num_types_data + 1;

max_epsilonprime1 = max(data_extract(end_first_batch+1:end_second_batch));
%max_epsilonprime2 = max(real(epsilon_2));

% switches to determine which part of the script is executed:
[mFree2mm,nX,nY,nTime,nAngle,dX,dY,dTime,dAngle] = ...
                        openLIACTFile(strcat(filePath,'THzFreeSpace2mm1529'));

% Calculate the maximum amount of time required to observe plots
maxtime1 = (2*h1/(c/sqrt(real(max_epsilonprime1))))/1e-12;
maxtime = maxtime1;
sprintf('Layer 1: %3.3f', maxtime)
if num_layers >= 2
    maxtime2 = (2*h2/(c/sqrt(real(epsilon_2))))/1e-12;
    maxtime = maxtime + maxtime2;
    sprintf('Layers 1 and 2: %3.3f', maxtime)
end
if num_layers >= 3
    maxtime3 = (2*h3/(c/sqrt(real(epsilon_3))))/1e-12;
    maxtime = maxtime + maxtime3;
    sprintf('Layers 1 to 3: %3.3f', maxtime)
end
if num_layers >= 4
    maxtime4 = (2*h4/(c/sqrt(real(epsilon_4))))/1e-12;
```

```
    maxtime = maxtime + maxtime4;
    sprintf('Layers 1 to 4: %3.3f', maxtime)
end
if num_layers ≥ 5
    maxtime5 = (2*h5/(c/sqrt(real(epsilon_5)))/1e-12);
    maxtime = maxtime + maxtime5;
    sprintf('Layers 1 to 5: %3.3f', maxtime)
end
if num_layers ≥ 6
    maxtime6 = (2*h6/(c/sqrt(real(epsilon_6)))/1e-12);
    maxtime = maxtime + maxtime6;
    sprintf('Layers 1 to 6: %3.3f', maxtime)
end
if num_layers ≥ 7
    maxtime7 = (2*h7/(c/sqrt(real(epsilon_7)))/1e-12);
    maxtime = maxtime + maxtime7;
    sprintf('Layers 1 to 7: %3.3f', maxtime)
end
maxtime = maxtime*extensionfactor;
%maxtime/extensionfactor
numIntervals = ceil(maxtime/dTime);
if numIntervals ≤ nTime
    numIntervals = nTime+150;
end
timerangeFree = dTime*[0:1:numIntervals-1]; % In picoseconds

% Delay due to quartz crystal
delay_quartz = hquartz*nquartz*1e12/c; % In picoseconds
delay_quartz_units = ceil(delay_quartz/dTime);

%clear mFree2mm;
mFree2mmtemp = zeros(1,numIntervals);
mFree2mmnoquartz = zeros(1,numIntervals);
choosecol = 25;
mFree2mmnoquartz(1:10) = mFree2mm(77:86,choosecol);  % Impulse function

% Choose type of input signal (T-ray or impulse function)
% ------------------------------------------------------
inputchoice = 2;
if inputchoice == 1
    % Choice 1: T-ray
    mFree2mmtemp(1:nTime) = reshape(mFree2mm(:,choosecol),1,nTime);
elseif inputchoice == 2
    % Choice 2: Gaussian function
    if delay_quartz_units ≠ 0
        % Flip impulse function to simulate phase change after passing through
        % quartz crystal
        mFree2mmtemp(delay_quartz_units+2:delay_quartz_units+10) = -1e6*mFree2mm(78:86,choosecol);
    else
        mFree2mmtemp(delay_quartz_units+25:delay_quartz_units+33) = 1e6*mFree2mm(78:86,choosecol);
    end
elseif inputchoice == 3
    % Choice 3: Cosine
```

```
    fmax = 2/10e-12;
    delayunits = 800;
    for cosinecount = delayunits:1:nTime+delayunits
        mFree2mmtemp(cosinecount) = cos(2*pi*timerangeFree(cosinecount)*1e-12*fmax);
    end
else
    % Choice 4: Impulse (2 units wide)
    mFree2mmtemp(2) = 1;
end
clear mFree2mm;
mFree2mm = mFree2mmtemp;
clear mFree2mmtemp;

figure, stem(timerangeFree,mFree2mm);

% Frequency Domain
% ----------------
fftsize = numIntervals;
half_fftsize = ceil(fftsize/2);

X = fft(mFree2mm, fftsize);
freq = [0:(fftsize-1)]/(dTime*(fftsize-1)); % Frequencies of interest (THz)

freq_step_epsilon = (data_extract(3)-data_extract(2))*1e3; % GHz
freq_step_current = (freq(2) - freq(1))*1e3;

if freq_step_epsilon ~= freq_step_current
   if freq_step_epsilon < freq_step_current
      freq_mult = floor(freq_step_current/freq_step_epsilon);
      newfreqcount = 1;
      for freqcount = 1:freq_mult:end_first_batch-1
          epsilon_1(newfreqcount) = ...
              data_extract(end_first_batch + freqcount) - ...
              (i*data_extract(end_second_batch + freqcount));
          sigma_1(newfreqcount) = data_extract(end_third_batch + freqcount)/100;
          newfreqcount = newfreqcount + 1;
      end
      epsilon_1(newfreqcount:fftsize) = epsilon_1(newfreqcount-1);
      sigma_1(newfreqcount:fftsize) = sigma_1(newfreqcount-1);
   else
      freq_mult = floor(freq_step_epsilon/freq_step_current);
      newfreqcount = 1;
      for freqcount = 1:1:end_first_batch-2
          epsilon_1prime(newfreqcount) = data_extract(end_first_batch+freqcount);
          epsilon_1primeprime(newfreqcount) = data_extract(end_second_batch+freqcount);
          sigma_1(newfreqcount) = data_extract(end_third_batch+freqcount)/100;

          newfreqcount = newfreqcount + freq_mult;
          epsilon_1prime(newfreqcount-freq_mult+1:newfreqcount) = ...
                    (data_extract(end_first_batch+freqcount) +...
                    data_extract(end_first_batch+freqcount+1))/2;
          epsilon_1primeprime(newfreqcount-freq_mult+1:newfreqcount) = ...
                    (data_extract(end_second_batch+freqcount) +...
```

```
                    data_extract(end_second_batch+freqcount+1))/2;
            sigma_1(newfreqcount-freq_mult+1:newfreqcount) = ...
                    (data_extract(end_third_batch+freqcount) +...
                    data_extract(end_third_batch+freqcount+1))/200;
            newfreqcount = newfreqcount + 1;
        end
        epsilon_1(1:newfreqcount-1) = epsilon_1prime - i*epsilon_1primeprime;
        clear epsilon_1prime; clear epsilon_1primeprime;
        epsilon_1(newfreqcount:fftsize) = epsilon_1(newfreqcount-1);
        sigma_1(newfreqcount:fftsize) = sigma_1(newfreqcount-1);
    end
end

% James Wait (1996)
% ------------------
for freqloop = 1:1:fftsize
    u1(freqloop) = sqrt(lambda^2 + (i*sigma_1(freqloop)*mu_1*mu_0*2e12*pi*freq(freqloop))...
                   - epsilon_1(freqloop)*epsilon_0*mu_1*mu_0*((2e12*pi*freq(freqloop))^2));
    if num_layers >= 2
        u2(freqloop) = sqrt(lambda^2 + i*sigma_2*mu_2*mu_0*2e12*pi*freq(freqloop)...
                       - epsilon_2*epsilon_0*mu_2*mu_0*((2e12*pi*freq(freqloop))^2));
    end
    if num_layers >= 3
        u3(freqloop) = sqrt(lambda^2 + i*sigma_3*mu_3*mu_0*2e12*pi*freq(freqloop)...
                       - epsilon_3*epsilon_0*mu_3*mu_0*((2e12*pi*freq(freqloop))^2));
    end
    if num_layers >= 4
        u4(freqloop) = sqrt(lambda^2 + i*sigma_4*mu_4*mu_0*2e12*pi*freq(freqloop)...
                       - epsilon_4*epsilon_0*mu_4*mu_0*((2e12*pi*freq(freqloop))^2));
    end
    if num_layers >= 5
        u5(freqloop) = sqrt(lambda^2 + i*sigma_5*mu_5*mu_0*2e12*pi*freq(freqloop)...
                       - epsilon_5*epsilon_0*mu_5*mu_0*((2e12*pi*freq(freqloop))^2));
    end
    if num_layers >= 6
        u6(freqloop) = sqrt(lambda^2 + i*sigma_6*mu_6*mu_0*2e12*pi*freq(freqloop)...
                       - epsilon_6*epsilon_0*mu_6*mu_0*((2e12*pi*freq(freqloop))^2));
    end
    if num_layers >= 7
        u7(freqloop) = sqrt(lambda^2 + i*sigma_7*mu_7*mu_0*2e12*pi*freq(freqloop)...
                       - epsilon_7*epsilon_0*mu_7*mu_0*((2e12*pi*freq(freqloop))^2));
    end
    K0(freqloop) = (sqrt(lambda^2 + i*sigma_0*mu_0*2e12*pi*freq(freqloop)...
                   - epsilon_0*mu_0*((2e12*pi*freq(freqloop))^2)))/...
                   (sigma_0 + i*2e12*pi*freq(freqloop)*epsilon_0);
    if K0(freqloop) == Inf
       K0(freqloop) = (sqrt(lambda^2 + i*sigma_0*mu_0*2e12*pi*(freq(freqloop)+0.001)...
                   - epsilon_0*mu_0*((2e12*pi*(freq(freqloop)+0.001))^2)))/...
                   (sigma_0 + i*2e12*pi*(freq(freqloop)+0.001)*epsilon_0);
    end
    K1(freqloop) = (sqrt(lambda^2 + i*sigma_1(freqloop)*mu_1*mu_0*2e12*pi*freq(freqloop)...
                   - epsilon_1(freqloop)*epsilon_0*mu_1*mu_0*((2e12*pi*freq(freqloop))^2)))/...
                  (sigma_1(freqloop) + i*2e12*pi*freq(freqloop)*epsilon_1(freqloop)*epsilon_0);
```

```
if K1(freqloop) == Inf
   K1(freqloop) = (sqrt(lambda^2 + i*sigma_1(freqloop)*mu_1*mu_0*2e12*pi*...
                  (freq(freqloop)+0.001)- epsilon_1(freqloop)*epsilon_0*mu_1*mu_0*...
                  ((2e12*pi*(freq(freqloop)+0.001))^2)))/(sigma_1(freqloop) + ...
                  i*2e12*pi*(freq(freqloop)+0.001)*epsilon_1(freqloop)*epsilon_0);
end
if num_layers >= 2
    K2(freqloop) = (sqrt(lambda^2 + i*sigma_2*mu_2*mu_0*2e12*pi*freq(freqloop)...
                   - epsilon_2*epsilon_0*mu_2*mu_0*((2e12*pi*freq(freqloop))^2)))/...
                   (sigma_2 + i*2e12*pi*freq(freqloop)*epsilon_2*epsilon_0);
    if K2(freqloop) == Inf
        K2(freqloop) = (sqrt(lambda^2 + i*sigma_2*mu_2*mu_0*2e12*pi*...
                       (freq(freqloop)+0.001)- epsilon_2*epsilon_0*mu_2*mu_0*...
                       ((2e12*pi*(freq(freqloop)+0.001))^2)))/(sigma_2 + ...
                       i*2e12*pi*(freq(freqloop)+0.001)*epsilon_2*epsilon_0);
    end
end
if num_layers >= 3
    K3(freqloop) = (sqrt(lambda^2 + i*sigma_3*mu_3*mu_0*2e12*pi*freq(freqloop)...
                   - epsilon_3*epsilon_0*mu_3*mu_0*((2e12*pi*freq(freqloop))^2)))/...
                   (sigma_3 + i*2e12*pi*freq(freqloop)*epsilon_3*epsilon_0);
    if K3(freqloop) == Inf
        K3(freqloop) = (sqrt(lambda^2 + i*sigma_3*mu_3*mu_0*2e12*pi*...
                       (freq(freqloop)+0.001)- epsilon_3*epsilon_0*mu_3*mu_0*...
                       ((2e12*pi*(freq(freqloop)+0.001))^2)))/(sigma_3 + ...
                       i*2e12*pi*(freq(freqloop)+0.001)*epsilon_3*epsilon_0);
    end
end
if num_layers >= 4
    K4(freqloop) = (sqrt(lambda^2 + i*sigma_4*mu_4*mu_0*2e12*pi*freq(freqloop)...
                   - epsilon_4*epsilon_0*mu_4*mu_0*((2e12*pi*freq(freqloop))^2)))/...
                   (sigma_4 + i*2e12*pi*freq(freqloop)*epsilon_4*epsilon_0);
    if K4(freqloop) == Inf
       K4(freqloop) = (sqrt(lambda^2 + i*sigma_4*mu_4*mu_0*2e12*pi*...
                      (freq(freqloop)+0.001)- epsilon_4*epsilon_0*mu_4*mu_0*...
                      ((2e12*pi*(freq(freqloop)+0.001))^2)))/(sigma_4 + ...
                      i*2e12*pi*(freq(freqloop)+0.001)*epsilon_4*epsilon_0);
    end
end
if num_layers >= 5
    K5(freqloop) = (sqrt(lambda^2 + i*sigma_5*mu_5*mu_0*2e12*pi*freq(freqloop)...
                   - epsilon_5*epsilon_0*mu_5*mu_0*((2e12*pi*freq(freqloop))^2)))/...
                   (sigma_5 + i*2e12*pi*freq(freqloop)*epsilon_5*epsilon_0);
    if K5(freqloop) == Inf
       K5(freqloop) = (sqrt(lambda^2 + i*sigma_5*mu_5*mu_0*2e12*pi*...
                      (freq(freqloop)+0.001)- epsilon_5*epsilon_0*mu_5*mu_0*...
                      ((2e12*pi*(freq(freqloop)+0.001))^2)))/(sigma_5 + ...
                      i*2e12*pi*(freq(freqloop)+0.001)*epsilon_5*epsilon_0);
    end
end
if num_layers >= 6
    K6(freqloop) = (sqrt(lambda^2 + i*sigma_6*mu_6*mu_0*2e12*pi*freq(freqloop)...
                   - epsilon_6*epsilon_0*mu_6*mu_0*((2e12*pi*freq(freqloop))^2)))/...
```

```
                    (sigma_6 + i*2e12*pi*freq(freqloop)*epsilon_6*epsilon_0);
        if K6(freqloop) == Inf
            K6(freqloop) = (sqrt(lambda^2 + i*sigma_6*mu_6*mu_0*2e12*pi*...
                (freq(freqloop)+0.001)- epsilon_6*epsilon_0*mu_6*mu_0*...
                ((2e12*pi*(freq(freqloop)+0.001))^2)))/(sigma_6 + ...
                i*2e12*pi*(freq(freqloop)+0.001)*epsilon_6*epsilon_0);
        end
    end
    if num_layers >= 7
        K7(freqloop) = (sqrt(lambda^2 + i*sigma_7*mu_7*mu_0*2e12*pi*freq(freqloop)...
                - epsilon_7*epsilon_0*mu_7*mu_0*((2e12*pi*freq(freqloop))^2)))/...
                (sigma_7 + i*2e12*pi*freq(freqloop)*epsilon_7*epsilon_0);
        if K7(freqloop) == Inf
            K7(freqloop) = (sqrt(lambda^2 + i*sigma_7*mu_7*mu_0*2e12*pi*...
                (freq(freqloop)+0.001)- epsilon_7*epsilon_0*mu_7*mu_0*...
                ((2e12*pi*(freq(freqloop)+0.001))^2)))/(sigma_7 + ...
                i*2e12*pi*(freq(freqloop)+0.001)*epsilon_7*epsilon_0);
        end
    end
end

if num_layers == 7
    Z8 = K0;
    Z7 = K7.*(Z8 + (K7.*tanh(u7*h7)))./(K7 + (Z8.*tanh(u7*h7)));
    Z6 = K6.*(Z7 + (K6.*tanh(u6*h6)))./(K6 + (Z7.*tanh(u6*h6)));
    Z5 = K5.*(Z6 + (K5.*tanh(u5*h5)))./(K5 + (Z6.*tanh(u5*h5)));
    Z4 = K4.*(Z5 + (K4.*tanh(u4*h4)))./(K4 + (Z5.*tanh(u4*h4)));
    Z3 = K3.*(Z4 + (K3.*tanh(u3*h3)))./(K3 + (Z4.*tanh(u3*h3)));
    Z2 = K2.*(Z3 + (K2.*tanh(u2*h2)))./(K2 + (Z3.*tanh(u2*h2)));
elseif num_layers == 6
    Z7 = K0;
    Z6 = K6.*(Z7 + (K6.*tanh(u6*h6)))./(K6 + (Z7.*tanh(u6*h6)));
    Z5 = K5.*(Z6 + (K5.*tanh(u5*h5)))./(K5 + (Z6.*tanh(u5*h5)));
    Z4 = K4.*(Z5 + (K4.*tanh(u4*h4)))./(K4 + (Z5.*tanh(u4*h4)));
    Z3 = K3.*(Z4 + (K3.*tanh(u3*h3)))./(K3 + (Z4.*tanh(u3*h3)));
    Z2 = K2.*(Z3 + (K2.*tanh(u2*h2)))./(K2 + (Z3.*tanh(u2*h2)));
elseif num_layers == 5
    Z6 = K0;
    Z5 = K5.*(Z6 + (K5.*tanh(u5*h5)))./(K5 + (Z6.*tanh(u5*h5)));
    Z4 = K4.*(Z5 + (K4.*tanh(u4*h4)))./(K4 + (Z5.*tanh(u4*h4)));
    Z3 = K3.*(Z4 + (K3.*tanh(u3*h3)))./(K3 + (Z4.*tanh(u3*h3)));
    Z2 = K2.*(Z3 + (K2.*tanh(u2*h2)))./(K2 + (Z3.*tanh(u2*h2)));
elseif num_layers == 4
    Z5 = K0;
    Z4 = K4.*(Z5 + (K4.*tanh(u4*h4)))./(K4 + (Z5.*tanh(u4*h4)));
    Z3 = K3.*(Z4 + (K3.*tanh(u3*h3)))./(K3 + (Z4.*tanh(u3*h3)));
    Z2 = K2.*(Z3 + (K2.*tanh(u2*h2)))./(K2 + (Z3.*tanh(u2*h2)));
elseif num_layers == 3
    Z4 = K0;
    Z3 = K3.*(Z4 + (K3.*tanh(u3*h3)))./(K3 + (Z4.*tanh(u3*h3)));
    Z2 = K2.*(Z3 + (K2.*tanh(u2*h2)))./(K2 + (Z3.*tanh(u2*h2)));
elseif num_layers == 2
    Z3 = K0;
```

Name of File (*.m)	Function
skin_extrapolation	Interpolates between microwave and THz skin data
adipose_extrapolation	Interpolates between microwave and THz adipose tissue data
bone_extrapolation	Interpolates between microwave and THz bone data
dura_extrapolation	Extrapolates microwave dura mater data into the THz range
csf_extrapolation	Extrapolates microwave cerebrospinal fluid (CSF) data into the THz range
grey_extrapolation	Extrapolates microwave grey matter data into the THz range
white_extrapolation	Extrapolates microwave white matter data into the THz range

Table H.3: MATLAB source code files for interpolating and extrapolating. Interpolating is required for data where either the frequency interval between data points is large, or a gap exists between microwave and THz data. Extrapolation is required when only microwave data exists, and extrapolation is used to extend the data into the THz range using the 4-term Cole-Cole model.

```
    Z2 = K2.*(Z3 + (K2.*tanh(u2*h2)))./(K2 + (Z3.*tanh(u2*h2)));
elseif num_layers == 1
    Z2 = K0;
end
Z1 = K1.*(Z2 + (K1.*tanh(u1*h1)))./(K1 + (Z2.*tanh(u1*h1)));

H = (K0 - Z1)./(K0 + Z1);
Hnew = repmat(reshape(H,fftsize,1), 1, 51);
Y = H.*X;
Ynew = reshape(Y,numIntervals,1);

% Reconstruct the time signal via IFFT
yrecon = ifft(Y,numIntervals);
clear Y;
```

H.4 Algorithms for Optical (Dielectric) Properties

Table H.3 lists the MATLAB source code files used to implement the interpolation and extrapolation detailed in Section 9.4.

H.4.1 Source Code

One example of a MATLAB implementation of extrapolation between microwave and THz skin data is presented in skin_extrapolation.m as follows.

```
% skin_extrapolation.m
%
% Material: Skin; Conditions: Dry skin; Literature: gabriel_1996c_pmb, fitzgerald_2003_jbp
%
% This programme plots the relative and complex permittivities of skin using data from
% 2 authors---1 microwave and 1 THz. Plots are generated to compare if extrapoltaed
% microwave results are comparable to measured THz results.
%
% Author: Gretel M. Png
% Last edited: 12 October 2005

close all, clear all;
savePath = 'C:\GPngTRayFiles\GPngModelMatlabFiles\Figures\EPSpics\Extrapolation\Skin\';
dataSavePath = 'C:\GPngTRayFiles\GPngModelMatlabFiles\MatlabScripts\Extrapolation\';
printOpts = '-deps2c';
printOn = 0;  % Print to EPS file = 1, Don't print = 0;

% Constants
epsilon_0 = 8.8542e-12;  % Permittivity of freespace
c = 3e8;                 % Speed of light
plotlinethickness = 1.5; % Line thickness (1 point = 1/72"), default = 0.5
plotfontsize = 12;       % Font size of axes, (1 point = 1/72"), default = 10;
textfontsize = 12;       % Font size of text, (1 point = 1/72"), default = 10;

% Values from gabriel_1996c_pmb
epsilon_inf_gabriel = 4.0;            % High frequency limit of permittivity
delta_epsilon1_gabriel = 32.0;        % Low frequency limit of permittivity
tau1_gabriel = 7.23e-12;              % Relaxation Time
%f_R1_gabriel = 1/(2*pi*tau1_gabriel); % Relaxation Frequency
alpha1_gabriel = 0;                   % Distribution parameter
delta_epsilon2_gabriel = 1100;        % Low frequency limit of permittivity
tau2_gabriel = 32.48e-9;              % Relaxation Time
%f_R2_gabriel = 1/(2*pi*tau2_gabriel); % Relaxation Frequency
alpha2_gabriel = 0.20;                % Distribution parameter
delta_epsilon3_gabriel = 0;           % Low frequency limit of permittivity
delta_epsilon4_gabriel = 0;           % Low frequency limit of permittivity
sigma_i_gabriel = 0.0002;               % Ionic conductivity

count = 0;
for f = 0:5:100                % Frequency in GHz
    count = count + 1;
    frequency(count) = f*1e-3; % Convert to terahertz

    % gabriel_1996c_pmb: Cole-Cole
    epsilon_hat_gabriel(count) = epsilon_inf_gabriel + (delta_epsilon1_gabriel /...
        (1+ ((i*2*pi*f*1e9*tau1_gabriel)^(1-alpha1_gabriel)))) + (delta_epsilon2_gabriel /...
        (1+ ((i*2*pi*f*1e9*tau2_gabriel)^(1-alpha2_gabriel)))) + ...
        (sigma_i_gabriel/(i*2*pi*f*1e9*epsilon_0));
    if epsilon_hat_gabriel(count) == Inf
        epsilon_hat_gabriel(count) = epsilon_inf_gabriel + (delta_epsilon1_gabriel /...
        (1+ ((i*2*pi*(f+1)*1e9*tau1_gabriel)^(1-alpha1_gabriel)))) + (delta_epsilon2_gabriel /...
        (1+ ((i*2*pi*(f+1)*1e9*tau2_gabriel)^(1-alpha2_gabriel)))) + ...
        (sigma_i_gabriel/(i*2*pi*(f+1)*1e9*epsilon_0));
```

```
    end
    sigma_gabriel(count) = -imag(epsilon_hat_gabriel(count))*epsilon_0*2*pi*f*1e9; % Conductivity
    n_hat_gabriel(count) = sqrt(epsilon_hat_gabriel(count)); % Refractive Index
    alpha_gabriel(count) = -imag(n_hat_gabriel(count))*4*pi*frequency(count)*...
                           1e12/(c*100); % Absorption Coefficient
end

count2 = 0;
for f = 105:5:1500                  % Frequency in GHz
    count2 = count2 + 1;
    frequency2(count2) = f*1e-3; % Convert to terahertz

    % gabriel_1996c_pmb: Cole-Cole
    epsilon_hat_gabriel2(count2) = epsilon_inf_gabriel + (delta_epsilon1_gabriel /...
        (1+ ((i*2*pi*f*1e9*tau1_gabriel)^(1-alpha1_gabriel)))) + ...
        (delta_epsilon2_gabriel /(1+ ((i*2*pi*f*1e9*tau2_gabriel)^(1-alpha2_gabriel)))) + ...
        (sigma_i_gabriel/(i*2*pi*f*1e9*epsilon_0));
    sigma_gabriel2(count2) = -imag(epsilon_hat_gabriel2(count2))*...
                             epsilon_0*2*pi*f*1e9; % Conductivity (Eq 3.16 von Hippel)
    n_hat_gabriel2(count2) = sqrt(epsilon_hat_gabriel2(count2)); % Refractive Index
    alpha_gabriel2(count2) = -imag(n_hat_gabriel2(count2))*4*pi*frequency2(count2)*...
                             1e12/(c*100); % Absorption Coefficient
end

% fitzgerald_2003_jbp
% ---------------------
% Broadband pulsed terahertz imaging system
% Figure 1a: order of columns is
% Frequency (THz); \alpha (cm^{-1})
skinvals_fitzgerald = [0.5 0.55 0.6 0.65 0.7 0.75 0.8 0.85 0.9 0.95 1 1.05 1.1 1.15 ...
                       1.2 1.25 1.3 1.35 1.4 1.45 1.5; 70 70 70 73 73 75 80 85 90 95 ...
                       100 105 110 115 120 122.5 125 130 130 130 130];
n_real_fitzgerald = 1.69;
sigma_literature_fitzgerald = 0.39;
count3 = 0;
count_to_9 = 0;
spec_freq_count = 0;
for f = 500:5:1500 % Frequency in GHz
    count3 = count3 + 1;
    frequency_fitzgerald(count3) = f*1e-3; % Convert to terahertz
    if rem(f,50) == 0
        spec_freq_count = spec_freq_count + 1;
        alpha_fitzgerald(count3) = skinvals_fitzgerald(2,spec_freq_count);
        kappa_fitzgerald(count3) = alpha_fitzgerald(count3)*c*100/(4*pi*f*1e9);
        n_fitzgerald(count3) = n_real_fitzgerald;
        sigma_fitzgerald(count3) = sigma_literature_fitzgerald*100; % S/cm
    else
        count_to_9 = count_to_9 + 1;
        if count_to_9 == 9
            % Interpolate data at 5 GHz intervals
            alpha_fitzgerald(count3-8:count3) = ...
                interp1([skinvals_fitzgerald(1,spec_freq_count)...
                    skinvals_fitzgerald(1,spec_freq_count+1)],...
```

```
                    [skinvals_fitzgerald(2,spec_freq_count)...
                    skinvals_fitzgerald(2,spec_freq_count+1)], ...
                   [frequency_fitzgerald(count3-8):0.005:frequency_fitzgerald(count3)],'spline');
            sigma_fitzgerald(count3-8:count3) = sigma_literature_fitzgerald*100; % S/cm
            n_fitzgerald(count3-8:count3) = n_real_fitzgerald;
            kappa_fitzgerald(count3-8:count3) = alpha_fitzgerald(count3-8:count3)*c*100./...
              (4*pi*[frequency_fitzgerald(count3-8)*1e3:5:frequency_fitzgerald(count3)*1e3]*1e9);
            count_to_9 = 0;
        else
            alpha_fitzgerald(count3) = NaN;
            n_fitzgerald(count3) = NaN;
            sigma_fitzgerald(count3) = NaN;
            kappa_fitzgerald(count3) = NaN;
        end
    end
end
epsilon_hat_fitzgerald = (n_fitzgerald - i*kappa_fitzgerald).^2;

% Fill in the empty frequencies
%------------------------------
frequency_fillin = [105*1e-3:5*1e-3:495*1e-3]; % in THz
alpha_fillin = NaN*ones(1,((495-105)/5)+1);

% To combine Fitzgerald's \alpha values with Gabriel's \alpha values
%-------------------------------------------------------------------
frequency_total = [frequency frequency_fillin frequency_fitzgerald];
alpha_gabriel_ext = [alpha_gabriel alpha_fillin NaN*ones(1,count3)];
alpha_fitzgerald_ext = [NaN*ones(1,count) alpha_fillin alpha_fitzgerald];

% To combine Fitzgerald's \sigma values with Gabriel's \sigma values
%-------------------------------------------------------------------
sigma_gabriel_ext = [sigma_gabriel alpha_fillin NaN*ones(1,count3)];
sigma_fitzgerald_ext = [NaN*ones(1,count) alpha_fillin sigma_fitzgerald];

% To combine Fitzgerald's and Gabriel's permittivity values
%----------------------------------------------------------
epsilonprime_gabriel_ext = [real(epsilon_hat_gabriel) alpha_fillin NaN*ones(1,count3)];
epsilonprimeprime_gabriel_ext = [-imag(epsilon_hat_gabriel) alpha_fillin NaN*ones(1,count3)];
epsilonprime_fitzgerald_ext = [NaN*ones(1,count) alpha_fillin real(epsilon_hat_fitzgerald)];
epsilonprimeprime_fitzgerald_ext = [NaN*ones(1,count) alpha_fillin -imag(epsilon_hat_fitzgerald)];

% Interpolate permittivities in the region between 0.1 and 0.5 THz
%-----------------------------------------------------------------
ypoints = [5 4.5 4 3.2 2.9];
ypoints_imag = [5.7 4.5 3.3 1.8 1.3];
xpoints = [0.12 0.15 0.2 0.3 0.4];
epsilonprime_ext = real(epsilon_hat_gabriel);
epsilonprimeprime_ext = -imag(epsilon_hat_gabriel);
for intercount = 1:1:length(ypoints)+1
    if intercount == 1
        ycurrent = [real(epsilon_hat_gabriel(count)) ypoints(1)];
        ycurrent_imag = [-imag(epsilon_hat_gabriel(count)) ypoints_imag(1)];
        xcurrent = [0.1 xpoints(1)];
```

```
        xsteps = [0.105:0.005:xpoints(1)-0.005];
        ynew = interp1(xcurrent,ycurrent,xsteps,'spline');
        ynew_imag = interp1(xcurrent,ycurrent_imag,xsteps,'spline');
    elseif intercount == length(ypoints)+1
        ycurrent = [ypoints(intercount-1) real(epsilon_hat_fitzgerald(1))];
        ycurrent_imag = [ypoints_imag(intercount-1) -imag(epsilon_hat_fitzgerald(1))];
        xcurrent = [xpoints(intercount-1) 0.5];
        xsteps = [xpoints(intercount-1)+0.005:0.005:0.495];
        ynew = interp1(xcurrent,ycurrent,xsteps,'spline');
        ynew_imag = interp1(xcurrent,ycurrent_imag,xsteps,'spline');
    else
        ycurrent = [ypoints(intercount-1) ypoints(intercount)];
        ycurrent_imag = [ypoints_imag(intercount-1) ypoints_imag(intercount)];
        xcurrent = [xpoints(intercount-1) xpoints(intercount)];
        xsteps = [xpoints(intercount-1)+0.005:0.005:xpoints(intercount)-0.005];
        ynew = interp1(xcurrent,ycurrent,xsteps,'cubic');
        ynew_imag = interp1(xcurrent,ycurrent_imag,xsteps,'cubic');
    end
    if intercount == length(ypoints)+1
        epsilonprime_ext = cat(2,epsilonprime_ext,ynew,real(epsilon_hat_fitzgerald));
        epsilonprimeprime_ext = cat(2,epsilonprimeprime_ext,ynew_imag,...
                                    -imag(epsilon_hat_fitzgerald));
    else
        epsilonprime_ext = cat(2,epsilonprime_ext,ynew,ypoints(intercount));
        epsilonprimeprime_ext = cat(2,epsilonprimeprime_ext,ynew_imag,ypoints_imag(intercount));
    end
    clear ycurrent; clear ycurrent_imag; clear xcurrent; clear xsteps;
    clear ynew; clear ynew_imag;
end

% Interpolate conductivity in the region between 0.1 and 0.5 THz
%-------------------------------------------------------------------
sigma_interpolate = interp1([0.1 0.5],[sigma_gabriel(21) sigma_literature_fitzgerald*100],...
                            [0.105:0.005:0.495],'spline');
sigma_ext = [sigma_gabriel sigma_interpolate sigma_fitzgerald];
```

H.5 Algorithms for Plotting HFSS Field Overlay Patterns

Table H.4 lists the MATLAB source code files used to extract the HFSS field overlay patterns presented in Section 8.9.1.

H.6 Algorithm for Pseudo-Phase Contrast

The MATLAB program pc_viaTimeDelay6.m implements the pseudo-contrast method introduced in Appendix Section A.1. The source code of pc_viaTimeDelay6.m is as follows.

Name of File (*.m)	Function
writetoptsfile	Writes user defined x, y and z spatial points to a .pts file
openhfssfile9	Opens a HFSS field plot file (in .reg format) and displays it
fetchregfilesize	Returns the x, y and z size of a .reg file

Table H.4: MATLAB source code files for writing to and reading from HFSS. The .pts file generated by writetoptsfile.m is read by HFSS during the writing process. A .reg file containing the field overlay pattern is then created by HFSS. To display the field overlay pattern in MATLAB, the size of the .reg file needs to be fetched.

```
% pc_viaTimeDelay6.m
%
% This program performs phase contrast by displaying the time delay of each
% pixel.
%
% Author: Gretel M. Png
% Last edited: 24 Jan 2005

clear all, close all;

% The data in the file fly.raw has the following properties
XDIM = 300;
YDIM = 100;
ZDIM = 99;
timeResn = 4e-14; % Time resolution in seconds = 0.04 ps

fid = fopen('C:\GPngTRayFiles\GPngLeafFiles\fly.raw','r','ieee-le');
if (fid == -1)
    fprintf('ERROR: pc_viaTimeDelay could not open file: %s!\n',fileNameDat);
    return;
end
mDat = fread(fid,XDIM*YDIM*ZDIM,'float');
fclose(fid);

% Change the shape of the long stream of data
m3 = reshape(mDat,[XDIM,YDIM,ZDIM]);

m3(:,:,1)=(m3(:,:,2));
m3(:,:,9)=(m3(:,:,8)+m3(:,:,10))/2; % correct those lines
m3(:,:,36)=(m3(:,:,35)+m3(:,:,37))/2;
m3(:,:,40)=(m3(:,:,39)+m3(:,:,41))/2;
m3(:,:,65)=(m3(:,:,64)+m3(:,:,66))/2;
m3(:,:,96)=(m3(:,:,95)+m3(:,:,97))/2;

% FIND THE PEAKS OF EACH PIXEL IN TIME (PEAK OF EACH COLUMN)
%peakabsvals = max(abs(m3));
peakabsvals = max(m3); % Find only positive peaks
peakpos = zeros(1,YDIM, ZDIM);
```

```
for colcount = 1:1:YDIM
    for depthcount = 1:1:ZDIM
        %temp = find(abs(m3(:,colcount,depthcount)) == peakabsvals(1,colcount,depthcount));
        temp = find(m3(:,colcount,depthcount) == peakabsvals(1,colcount,depthcount));
        [temprows tempcols] = size(temp);
        peakpos(1,colcount,depthcount) = temp(temprows,1);
        peakvals(1,colcount,depthcount) = m3(peakpos(1,colcount,depthcount),colcount,depthcount);
    end
end
clear tempcols, clear temprows;

timerange = [0:0.04:XDIM*0.04-0.04];

%-------------------------------------------------------------------
% ABSORPTION INDEX
%-------------------------------------------------------------------
% INTENSITY IMAGE
peakImage = reshape(peakvals, YDIM,ZDIM); % YDIM rows, ZDIM columns

% EXTRACT PEAK POSITION OF REFERENCE PIXEL (FREESPACE DATA)
refpixIntensity = (sum(peakvals(1,1:5,ZDIM))+ sum(peakvals(1,1:5,ZDIM-1)) + ...
    sum(peakvals(1,1:5,ZDIM-2)))/15; % Top right

% ENHANCE INTENSITY IMAGE
%-------------------------
% Remove holder
peakImage(87:YDIM,:) = refpixIntensity;  % Set the pixels that show the holder

% Invert intensity so that leaf and insect are enhanced
peakImage = refpixIntensity - peakImage; % Accentuate the leaf and insect

% Denoising (First pass): Remove scattered noise pixels via 8-neighbourhood
noisemask = [1 1 1;1 1 1;1 1 1];
borderImage = zeros(YDIM+2, ZDIM+2);
borderImage(2:YDIM+1, 2:ZDIM+1) = peakImage;
denoisedImage = zeros(YDIM, ZDIM);

for rowmask = 1:1:YDIM
    for colmask = 1:1:ZDIM
        noisematrix = borderImage(rowmask:rowmask+2, colmask:colmask+2).*noisemask;
        zerocount = 0;
        for matrixloop = 1:1:9
            if matrixloop ~= 5
               if (noisematrix(matrixloop) == 0)
                  zerocount = zerocount + 1;
               end
            end
        end

        if zerocount >= 7
            denoisedImage(rowmask,colmask) = 0;
        else
            denoisedImage(rowmask,colmask) = peakImage(rowmask,colmask);
```

```
        end
    end
end

% Denoising (Second pass): Remove scattered noise pixels via weighted mask
referencetolerence = sum(sum(denoisedImage(1:5,1:5),1),2)/25;
noisemask = [1 1 1;1 1 1;1 1 1];
borderImage = zeros(YDIM+2, ZDIM+2);
borderImage(2:YDIM+1, 2:ZDIM+1) = denoisedImage;
denoisedImage2 = zeros(YDIM, ZDIM);
for rowmask = 1:1:YDIM
    for colmask = 1:1:ZDIM
        noisematrix = borderImage(rowmask:rowmask+2, colmask:colmask+2).*noisemask;
        avnoisematrix = (sum(sum(noisematrix,1),2))/sum(sum(noisemask,1),2);
        if abs(avnoisematrix - referencetolerence) <= 0.15 % Noise pixel
            denoisedImage2(rowmask,colmask) = 0;
        else
            denoisedImage2(rowmask,colmask) = denoisedImage(rowmask,colmask);
        end
    end
end

% Edge detection
laplacianmask = [-1 -1 -1;-1 8 -1;-1 -1 -1];
borderImage = zeros(YDIM+2, ZDIM+2);
borderImage(2:YDIM+1, 2:ZDIM+1) = denoisedImage2;
edgeImage = zeros(YDIM, ZDIM);

for rowmask = 1:1:YDIM
    for colmask = 1:1:ZDIM
        edgematrix = borderImage(rowmask:rowmask+2, colmask:colmask+2).*laplacianmask;
        sumedgematrix = sum(sum(edgematrix,1),2) - edgematrix(2,2);
        %edgeImage(rowmask,colmask) = sumedgematrix;
        if sumedgematrix < edgematrix(2,2)
            edgeImage(rowmask,colmask) = denoisedImage2(rowmask,colmask);
        else
            edgeImage(rowmask,colmask) = 0;
        end
    end
end

% Combine denoised and edge detected images
denoisedImage3 = peakImage.*double(edgeImage & denoisedImage2);

% Last pass: 8-neighbourhood again
noisemask = [1 1 1;1 1 1;1 1 1];
borderImage = zeros(YDIM+2, ZDIM+2);
borderImage(2:YDIM+1, 2:ZDIM+1) = denoisedImage3;
finalImage = zeros(YDIM, ZDIM);
for rowmask = 1:1:YDIM
    for colmask = 1:1:ZDIM
        noisematrix = borderImage(rowmask:rowmask+2, colmask:colmask+2).*noisemask;
        zerocount = 0;
```

```
        for matrixloop = 1:1:9
            if matrixloop ≠ 5
                if (noisematrix(matrixloop) == 0)
                    zerocount = zerocount + 1;
                end
            end
        end

        if zerocount ≥ 3
            finalImage(rowmask,colmask) = 0;
        else
            finalImage(rowmask,colmask) = denoisedImage3(rowmask,colmask);
        end
    end
end

negpos = find(finalImage < 0);
[neg_rows negtemp] = size(negpos);
for negcount = 1:1:neg_rows
   finalImage(negpos(negcount)) = 0;
end
clear neg_rows, clear negtemp;

% Make a matrix that captures the outline of finalImage
cleanmask = ones(YDIM,ZDIM) & finalImage;

% OPACITY
% ————————
maxAbsorption = max(max(finalImage));
newalphamap = finalImage/maxAbsorption;

% ————————————————————————————————————————————————————————
% REFRACTIVE INDEX
% ————————————————————————————————————————————————————————
posImage = reshape(peakpos, YDIM,ZDIM); % YDIM rows, ZDIM columns
temp2 = posImage;
% EXTRACT PEAK POSITION OF REFERENCE PIXEL (FREESPACE DATA)
%%refpix = peakpos(1,1,ZDIM); % Top right
%%refpix = peakpos(1,1,1); % Top left
%%refpix = peakpos(1,YDIM,ZDIM); % Bottom right
%%refpix = peakpos(1,YDIM,1); % Bottom left
refpos = round((sum(peakpos(1,1:5,ZDIM))+ sum(peakpos(1,1:5,ZDIM-1)) + ...
    sum(peakpos(1,1:5,ZDIM-2)))/15); % Top right

% Remove holder
posImage(87:YDIM,:) = refpos;  % Set the pixels that show the holder

% Check that there is no superluminance
badpos = find(posImage < refpos);
[numbad tempval] = size(badpos);
for badcount = 1:1:numbad
    if (abs(posImage(badpos(badcount)) - refpos) ≤ 2) % Air pixel?
        posImage(badpos(badcount)) = refpos;
```

```
    end
end
clear badpos, clear numbad, clear tempval;

% Remove air pixels
badpos = find(abs(posImage - refpos) <= 1);
[numbad tempval] = size(badpos);
for badcount = 1:1:numbad
    if (abs(peakImage(badpos(badcount))-refpixIntensity) < 0.6)
        posImage(badpos(badcount)) = refpos;
    end
end

% FIND DELAY FROM REFERENCE PIXEL
% ------------------------------------
delayImage = posImage - refpos;
finaldelayImage = cleanmask.*delayImage;

% THICKNESS
% ----------
% Get thickness based on:
% relative thickness = distance = speed of light x relative time delay
thicknessImage = (3e8 * timeResn * finaldelayImage)/1e-3; % In milimeters
%normthicknessImage = thicknessImage/max(max(thicknessImage));
normthicknessImage = thicknessImage;
figure, surface(normthicknessImage, 'FaceAlpha', 'flat','AlphaDataMapping','scaled',...
    'AlphaData', newalphamap, 'EdgeColor', 'none');
colormap([0.8  1  0.3; 0.6  0.3  0.1]);
view(-168, 60); % Figure a
whitebg([0.3 0.3 0.3]);
xlabel('z-axis','FontSize',15, 'Color','black');
ylabel('y-axis','FontSize',15,'Color','black');
zlabel('Optical path length (mm)','FontSize',15,'Color','black'), grid off;
```

Bibliography

ABDALLA-A AND TEOH-A (2006). A multi-layered model of human head irradiated by electromagnetic plane wave of 100 MHz-300 GHz, *International Journal of Scientific Research*, **16**, pp. 397–403. 9.2, 9.1

ADVANCED LIGHT SOURCE (ALS) (1996). *The Electromagnetic Spectrum*, Lawrence Berkeley National Laboratory, Berkeley, CA, USA, <http://www.lbl.gov/MicroWorlds/ALSTool/EMSpec/EMSpec2.html>, (Accessed: 2009-02-10). 1.1

ADVANCED RESEARCH TECHNOLOGIES INC. (2008). *I Want To Be Sure About My Breast Health*, Montreal, Quebec, Canada, <http://www.art.ca/docs/products/SoftScan-Brochure.pdf>, (Accessed: 2009-02-05). 4.6, 4.3.2

AFSAR-M AND HASTED-J (1977). Measurements of the optical constants of liquid H_2O and D_2O between 6 and 450 cm^{-1}, *Journal of the Optical Society of America*, **67**(7), pp. 902–904. 4

AFSAR-M, HASTED-J AND CHAMBERLAIN-J (1976). New techniques for dispersive Fourier transform spectrometry of liquids, *Infrared Physics*, **16**(1-2), pp. 301–310. 3

ALABASTER-C (2004). *The Microwave Properties of Tissue and Other Lossy Dielectrics*, PhD thesis, Cranfield University. 9.4.1

ALISON-J AND SHEPPARD-R (1990). A precision waveguide system for the measurement of complex permittivity of lossy liquids and solid tissues in the frequency range 29 GHz to 90 GHz—I. the liquid system for 29 to 45 GHz; an investigation into water, *Measurement Science and Technology*, **1**(10), pp. 1093–1098. 13

ALISON-J AND SHEPPARD-R (1991). A precision waveguide system for the measurement of complex permittivity of lossy liquids and solid tissues in the frequency range 29 GHz to 90 GHz—III. the liquid system for 57 to 82 GHz: an investigation into water and formamide, *Measurement Science and Technology*, **2**(10), pp. 975–979. 13

ALISON-J AND SHEPPARD-R (1993). Dielectric properties of human blood at microwave frequencies, *Physics in Medicine and Biology*, **38**(7), pp. 971–978. 15

ALZHEIMER-A (1907). Über eine eigenartige Erkrankung der hirnrinde (on a peculiar disease of the cerebral cortex), *Allgemeine Zeitschrift für Psychiatrie: Psychisch-Gerichtliche Medizin*, **64**, pp. 146–148. 59

ALZHEIMER'S DISEASE RESEARCH (2000). *Plaques and Tangles*, American Health Assistance Foundation, Clarksburg, MD, USA, <http://www.ahaf.org/alzheimers/about/understanding/plaques-and-tangles.html>, (Accessed: 2009-05-22). 6.2

AMERICAN INSTITUTE OF PHYSICS (2008). *Lawrence and the Cyclotron*, American Institute of Physics, College Park, MD, USA, <http://www.aip.org/history/lawrence/>, (Accessed: 2008-10-20). 17

ANBARASU-A (2008). *Characterization of Defects in Fiber Composites Using Terahertz Imaging*, PhD thesis, Georgia Institute of Technology. 2.11

ANDERSON-R AND PARRISH-J (1981). The optics of human skin, *Journal of Investigative Dermatology*, **77**(1), pp. 13–19. 4.3.2, 4.3.2

ÅNGSTRÖM-K (1900). Ueber die Bedeutung des Wasserdampfes und der Kohlensäure bei der Absorption der Erdatmosphäre, *Annalen der Physik und Chemie*, **308**(12), pp. 720–732. 1.4

ANSOFT (2010). *Ansoft: ANSYS Product Suite*, ANSYS, Inc., <http://www.ansoft.com/>, (Accessed: 2010-04-29). 7

ANTONETTI-A, MALLEY-M, MOUROU-G AND ORSZAG-A (1977a). High power switching with picosecond precision: Applications to high speed Kerr cell and Pockels cell, *Optics Communications*, **23**(3), pp. 435–439. 3.5.1, 3.5.2

ANTONETTI-A, MIGUS-A, MALLEY-M AND MOUROU-G (1977b). Optoelectronic sampling in the picosecond range, *Optics Communications*, **21**(2), pp. 211–214. 3.5.1

APPELL-D (1997). Terahertz imaging - real-time terahertz imaging captures living tissue, *Laser Focus World*, **33**(10), p. 16. 1.4.2

ARGONNE NATIONAL LABORATORY (2008). *Advanced Photon Source (APS)*, Argonne, IL, USA, <http://www.aps.anl.gov/Beamlines/>, (Accessed: 2008-10-23). 2.12

ARMSTRONG-J, BLOEMBERGEN-N, DUCUING-J AND PERSHAN-P (1962). Interactions between light waves in a nonlinear dielectric, *Physical Review*, **127**(6), pp. 1918–1939. 3.3, 3.5

ARNAUDOV-L AND DE VRIES-R (2005). Thermally induced fibrillar aggregation of hen egg white lysozyme, *Biophysical Journal*, **88**(1), pp. 515–526. 7.4.2

ARNOLD-S, HYMAN-B, FLORY-J, DAMASIO-A AND VAN HOESEN-G (1991). The topographical and neuroanatomical distribution of neurofibrillary tangles and neuritic plaques in the cerebral cortex of patients with Alzheimer's disease, *Cerebral Cortex*, **1**(1), pp. 103–116. 6.3.1

ARNONE-D, CIESLA-C, CORCHIA-A, EGUSA-S, PEPPER-M, CHAMBERLAIN-J, BEZANT-C, LINFIELD-E, CLOTHIER-R AND KHAMMO-N (1999). Applications of terahertz (THz) technology to medical imaging, *Proc. SPIE Terahertz Spectroscopy and Applications II*, **3828**, Ed: J. Chamberlain, 16–18 June 1999, Munich, Germany, pp. 209–219. 1.4.2, 1.5

ASAKI-M, REDONDO-A, ZAWODZINSKI-T AND TAYLOR-A (2002). Dielectric relaxation of electrolyte solutions using terahertz transmission spectroscopy, *Journal of Chemical Physics*, **116**(19), pp. 8469–8482. 4.5.2

ASANO-S AND SATO-M (1980). Light scattering by randomly oriented spheroidal particles, *Applied Optics*, **19**(6), pp. 962–974. 8.2

ASANO-S AND YAMAMOTO-G (1975). Light scattering by a spheroidal particle, *Applied Optics*, **14**(1), pp. 29–49. 8.2

ASHWORTH-P, PICKWELL-MACPHERSON-E, PINDER-S, PROVENZANO-E, PURUSHOTHAM-A, PEPPER-M AND WALLACE-V (2007). Terahertz spectroscopy of breast tumors, *Proc. Joint 32nd International Conference on Infrared and Millimeter Waves and 15th International Conference on Terahertz Electronics (IRMMW-THz)*, **2**, Eds: M. Griffin, P. Hargrave, T. Parker and K. Wood, 3–7 September 2007, Cardiff, UK, pp. 603–604. 4.5.4

ASHWORTH-P, PICKWELL-MACPHERSON-E, PROVENZANO-E, PINDER-S, PURUSHOTHAM-A, PEPPER-M AND WALLACE-V (2009). Terahertz pulsed spectroscopy of freshly excised human breast cancer, *Optics Express*, **17**(15), pp. 12444–12454. 4.6

ASHWORTH-P, ZEITLER-J, PEPPER-M AND WALLACE-V (2006). Terahertz spectroscopy of biologically relevant liquids at low temperatures, *Proc. Joint 31st International Conference on Infrared and Millimeter Waves and 14th International Conference on Terahertz Electronics (IRMMW-THz)*, 18–22 September 2006, Shanghai, China, p. 184. 5.5.1, 5.7, 6.1.2, 6.4.4, 7.4, 7.6.2

ASLIN-R AND MEHLER-J (2005). Near-infrared spectroscopy for functional studies of brain activity in human infants: promise, prospects, and challenges, *Journal of Biomedical Optics*, **10**(1), article number 011009. 4.3.2

ATTAS-E, POSTHUMUS-T, SCHATTKA-B, SOWA-M, MANTSCH-H AND ZHANG-S (2002a). Long-wavelength near-infrared spectroscopic imaging for in-vivo skin hydration measurements, *Vibrational Spectroscopy*, **28**(1), pp. 37–43. 4.3.2

ATTAS-E, SOWA-M, POSTHUMUS-T, SCHATTKA-B, MANTSCH-H AND ZHANG-S (2002b). Near-IR spectroscopic imaging for skin hydration: The long and the short of it, *Biopolymers*, **67**(2), pp. 96–106. 4.3.2, 4.4

AUSTON-D (1968a). Forced and spontaneous phase locking of the transverse modes of a He-Ne laser, *IEEE Journal of Quantum Electronics*, **4**(7), pp. 471–473. 3.5.1

AUSTON-D (1968b). Transverse mode locking, *IEEE Journal of Quantum Electronics*, **4**(6), pp. 420–422. 3.5.1

AUSTON-D (1971). Nonlinear spectroscopy of picosecond pulses, *Optics Communications*, **3**(4), pp. 272–276. 3.5

AUSTON-D (1975). Picosecond optoelectronic switching and gating in silicon, *Applied Physics Letters*, **26**(3), pp. 101–103. 3.5.1, 3.6

AUSTON-D (1983). Subpicosecond electro-optic shock waves, *Applied Physics Letters*, **43**(8), pp. 713–715. 3.4.2

AUSTON-D AND CHEUNG-K (1985). Coherent time-domain far-infrared spectroscopy, *Journal of the Optical Society of America B: Optical Physics*, **2**(4), pp. 606–612. 1.3.2, 1.4, 3.6

AUSTON-D AND GLASS-A (1972). Optical generation of intense picosecond electrical pulses, *Applied Physics Letters*, **20**(10), pp. 398–399. 3.5.1

AUSTON-D AND NUSS-M (1988). Electrooptic generation and detection of femtosecond electrical transients, *IEEE Journal of Quantum Electronics*, **24**(2), pp. 184–197. 3.6

AUSTON-D AND SMITH-P (1983). Generation and detection of millimeter waves by picosecond photoconductivity, *Applied Physics Letters*, **43**(7), pp. 631–633. 1.3.2, 3.6

AUSTON-D, CHEUNG-K AND SMITH-P (1984a). Picosecond photoconducting Hertzian dipoles, *Applied Physics Letters*, **45**(3), pp. 284–286. 3.6, 3.8, 3.10, 3.8, 3.8.1

AUSTON-D, CHEUNG-K, VALDMANIS-J AND KLEINMAN-D (1984b). Cherenkov radiation from femtosecond optical pulses in electro-optic media, *Physical Review Letters*, **53**(16), pp. 1555–1558. 1.3.2, 3.4.2, 3.6

AUSTON-D, JOHNSON-A, SMITH-P AND BEAN-J (1980a). Picosecond optoelectronic detection, sampling, and correlation measurements in amorphous semiconductors, *Applied Physics Letters*, **37**(4), pp. 371–373. 3.5.1, 3.8.2

AUSTON-D, LAVALLARD-P, SOL-N AND KAPLAN-D (1980b). An amorphous silicon photodetector for picosecond pulses, *Applied Physics Letters*, **36**(1), pp. 66–68. 3.5.1, 3.8

AUSTON-D, MCAFEE-S, SHANK-C, IPPEN-E AND TESCHKE-O (1978). Picosecond spectroscopy of semiconductors, *Solid-State Electronics*, **21**(1), pp. 147–150. 1.3.2

AUSTRALIAN SYNCHROTRON (2008). *Image Gallery Archive*, Australian Synchrotron, Clayton, VIC, Australia, <http://www.synchrotron.vic.gov.au/content.asp?Document_ID=5235>, (Accessed: 2008-10-27). 2.12

AVERY-O, MACLEOD-C AND MCCARTY-M (1944). Studies on the chemical nature of the substance inducing transformation of pneumococcal types: Induction of transformation by a desoxyribonucleic acid fraction isolated from pneomococcus type III, *Journal of Experimental Medicine*, **79**, pp. 137–158. 4.5.2

AXER-H, GRÄSSEL-D, STEINHAUER-M, STÖHR-P, JOHN-A, COENEN-V, JANSEN-R AND VON KEYSERLINGK-D (2002). Microwave dielectric measurements and tissue characteristics of the human brain: potential in localizing intracranial tissues, *Physics in Medicine and Biology*, **47**(10), pp. 1793–1803. 19

AZAD-A AND ZHANG-W (2005). Resonant terahertz transmission in subwavelength metallic hole arrays of sub-skin-depth thickness, *Optics Letters*, **30**(21), pp. 2945–2947. A.2

BACSKAI-B, HICKEY-G, SKOCH-J, KAJDASZ-S, WANG-Y, HUANG-G.-F, MATHIS-C, KLUNK-W AND HYMAN-B (2003). Four-dimensional multiphoton imaging of brain entry, amyloid binding, and clearance of an amyloid-β ligand in transgenic mice, *Proceedings of the National Academy of Sciences of the United States of America*, **100**(21), pp. 12462–12467. 6.2.2

BAKER-C, TRIBE-W, COLE-B AND KEMP-M (2004). Developments in people-screening using terahertz technology, *Proc. SPIE Optics and Photonics for Counterterrorism and Crime Fighting*, **5616**, Eds: T. Donaldson and C. Lewis, 2004-10-27, London, UK, pp. 61–68. 1.4.2, 1.5

BAKER-C, TRIBE-W, LO-T, COLE-B, CHANDLER-S AND KEMP-M (2005). People screening using terahertz technology, *Proc. SPIE Terahertz for Military and Security Applications III*, **5790**, Eds: R. Hwu and D. Woolard, 28–29 March 2005, Orlando, FL, USA, pp. 1–10. 1.3.2, 1.8

BAKOPOULOS-P, KARANASIOU-I, PLEROS-N, ZAKYNTHINOS-P, UZUNOGLU-N AND AVRAMOPOULOS-H (2009). A tunable continuous wave (CW) and short-pulse optical source for THz brain imaging applications, *Measurement Science & Technology*, **20**(10), article number 104001. 10.3.2

BAKOPOULOS-P, KARANASIOU-I, ZAKYNTHINOS-P, PLEROS-N, AVRAMOPOULOS-H AND UZUNOGLU-N (2008). Towards brain imaging using THz technology, *Proc. IEEE International Workshop on Imaging Systems and Techniques*, Ed: G. Giakos, 10–11 September 2008, Chania, Crete, Greece, pp. 7–10. 10.3.2

BALAKRISHNAN-J, FISCHER-B AND ABBOTT-D (2009). Fixed dual-thickness terahertz liquid spectroscopy using a spinning sample technique, *IEEE Photonics Journal*, **1**(2), pp. 88–98. 4.5.2

BALANIS-C (1989). *Advanced Engineering Electromagnetics*, John Wiley & Sons, New York, NY, USA. 71, 8.6.5, 8.7.2

BAMBERY-K, WOOD-B, QUINN-M AND MCNAUGHTON-D (2004). Fourier transform infrared imaging and unsupervised hierarchical clustering applied to cervical biopsies, *Australian Journal of Chemistry*, **57**(12), pp. 1139–1143. 4.3.2

BANDYOPADHYAY-A, SENGUPTA-A, BARAT-R, GARY-D, FEDERICI-J, CHEN-M AND TANNER-D (2007). Effects of scattering on THz spectra of granular solids, *International Journal of Infrared and Millimeter Waves*, **28**(11), pp. 969–978. 8.1, 8.6.5

BANWELL-C (1966). *Fundamental of Molecular Spectroscopy*, McGraw-Hill Publishing Company Limited, Maidenhead, Berkshire, England. 4.2, 4.3

BARABÁS-M (1987). Scattering of a plane wave by a radially stratified tilted cylinder, *Journal of the Optical Society of America A: Optics and Image Science, and Vision*, **4**(12), pp. 2240–2248. 8.2

BARTHEL-J, BACHHUBER-K, BUCHNER-R AND HETZENAUER-H (1990). Dielectric spectra of some common solvents in the microwave region: water and lower alcohols, *Chemical Physics Letters*, **165**(4), pp. 369–373. 12, 9.4.1

BASS-M, FRANKEN-P, WARD-J AND WEINREICH-G (1962). Optical rectification, *Physical Review Letters*, **9**(11), pp. 446–448. 3.3

BEARD-M, TURNER-G AND SCHMUTTENMAER-C (2002). Terahertz spectroscopy, *Journal of Physical Chemistry*, **106**(29), pp. 7146–7159. 4.5.2

BECKMANN-J, RICHTER-H, ZSCHERPEL-U, EWERT-U, WEINZIERL-J, SCHMIDT-L.-P, RUTZ-F, KOCH-M, RICHTER-H AND HÜBERS-H.-W (2006). Imaging capability of terahertz and millimeter-wave instrumentations for NDT of polymer materials, *Proc. 9th European Conference on Nondestructive Testing (NDT)*, Ed: R. Diederichs, September 2006, Berlin, Germany, article number We.2.8.1. 8.1

BECKMANN-P AND SPIZZICHINO-A (1963). *The Scattering of Electromagnetic Waves from Rough Surfaces*, , **4** of *Electromagnetic Waves*, Pergamon Press Ltd., London. 8.2, F.8

BELKEBIR-K, KLEINMAN-R AND PICHOT-C (1997). Microwave imaging—location and shape reconstruction from multifrequency scattering data, *IEEE Transactions on Microwave Theory and Techniques*, **45**(4), pp. 469–476. 8.2

BELL-B AND BICKEL-W (1981). Single fiber light scattering matrix: an experimental determination, *Applied Optics*, **20**(22), pp. 3874–3879. 8.2

BELL LABORATORIES PHYSICAL SCIENCES RESEARCH (2000). *Quantum Cascade Laser: Intro*, Lucent Technologies Bell Laboratories Research, Murray Hill, NJ, USA, <http://www.bell-labs.com/org/physicalsciences/projects/qcl/qcl.html>, (Accessed: 2009-01-02). 2.4.1

BENNETT-A, JUPNIK-H, OSTERBERG-H AND RICHARDS-O (1951). *Phase Microscopy: Principles and Applications*, John Wiley & Sons, New York, NY, USA. A.1.1

BENNETT-H (1963). Specular reflectance of aluminized ground glass and the height distribution of surface irregularities, *Journal of the Optical Society of America*, **53**(12), pp. 1389–1394. 8.2

BENTHAM INSTRUMENTS LTD. (2008). Model 225 lock-in amplifier, *Technical report*. 3.10.5

BERGNER-A, HEUGEN-U, BRÜNDERMANN-E, SCHWAAB-G, HAVENITH-M, CHAMBERLIN-D AND HALLER-E (2005). New p-Ge THz laser spectrometer for the study of solutions: THz absorption spectroscopy of water, *Review of Scientific Instruments*, **76**(6), article number 063110. 2.4.1, 4.5.1

BERRY-E, FITZGERALD-A, ZINOV'EV-N, WALKER-G, HOMER-VANNIASINKAM-S, SUDWORTH-C, MILES-R, CHAMBERLAIN-J AND SMITH-M (2003a). Optical properties of tissue measured using terahertz-pulsed imaging, *Proc. SPIE Medical Imaging 2003: Physics of Medical Imaging*, **5030**, Eds: M. Yaffe and L. Antonuk, June 2003, San Diego, CA, USA, pp. 459–470. 1.4.2, 4.5.4, 9.3, 9.2

BERRY-E, WALKER-G, FITZGERALD-A, ZINOV'EV-N, CHAMBERLAIN-M, SMYE-S, MILES-R AND SMITH-M (2003b). Do *in vivo* terahertz imaging systems comply with safety guidelines?, *Journal of Laser Applications*, **15**(3), pp. 192–198. 4.5.4, 51

BIBER-S, BOZZI-M, GÜNTHER-O, PERREGRINI-L AND SCHMIDT-L.-P (2006). Design and testing of frequency-selective surfaces on silicon substrates for submillimeter-wave applications, *IEEE Transactions on Antennas and Propagation*, **54**(9), pp. 2638–2645. A.2, A.3

BIBER-S, GÜNTHER-O, BOZZI-M, PERREGRINI-L, FISCHER-B, HOFMANN-A, JEPSEN-P, HELM-H AND SCHMIDT-L.-P (2004a). A frequency selective surface for harmonic suppression in THz-Multipliers, *Proc. Joint 29th International Conference on Infrared and Millimeter Waves and 12th International Conference on Terahertz Electronics (IRMMW-THz)*, Eds: M. Thumm and W. Wiesbeck, October 2004, Karlsruhe, Germany, pp. 132–135. A.2

BIBER-S, SCHNEIDERBANGER-D, SCHMIDT-L.-P, WALTHER-M, FISCHER-B, SCHWARZER-M AND JEPSEN-P (2004b). Low loss silicon window material for submillimeter waves using micromachined artificial dielectrics for anti-reflection coating, *Proc. Joint 29th International Conference on Infrared and Millimeter Waves and 12th International Conference on Terahertz Electronics*, Eds: M. Thumm and W. Wiesbeck, 27 September–1 October 2004, Karlsruhe, Germany, pp. 105–106. A.2

BICKEL-W, DAVIDSON-J, HUFFMAN-D AND KILKSON-R (1976). Application of polarization effects in light scattering: A new biophysical tool, *Proceedings of the National Academy of Sciences of the United States of America*, **73**(2), pp. 486–490. 8.2

BICKEL-W, GILLIAR-W AND BELL-B (1980). Light scattering from fibers: a closer look with a new twist, *Applied Optics*, **19**(21), pp. 3671–3675. 8.2

BJARNASON-J, CHAN-T, LEE-A, CELIS-M AND BROWN-E (2004). Millimeter-wave, terahertz, and mid-infrared transmission through common clothing, *Applied Physics Letters*, **85**(4), pp. 519–521. 8.1

BLOEMBERGEN-N (1965). *Nonlinear Optics*, World Scientific, Reading, MA, USA. 3.5

BLOEMBERGEN-N AND PERSHAN-P (1962). Light waves at the boundary of nonlinear media, *Physical Review*, **128**(2), pp. 606–622. 3.5

BOHREN-C AND HUFFMAN-D (1983). *Absorption and Scattering of Light by Small Particles*, Wiley Science Paperback Series, John Wiley & Sons, New York, NY, USA. 7.5.1, 7.5.1, 8.3, 8.3.1, 8.1, 8.3.2, 8.3.2, F.1, F.6, F.7

BOOTH-D, SUNDE-M, BELLOTTI-V, ROBINSON-C, HUTCHINSON-W, FRASER-P, HAWKINS-P, DOBSON-C, RADFORD-S, BLAKE-C AND PEPYS-M (1997). Instability, unfolding and aggregation of human lysozyme variants underlying amyloid fibrillogenesis, *Nature*, **385**(6619), pp. 787–793. 6.2, 6.3

BORN-M AND WOLF-E (1999). *Principles of Optics: Electromagnetic Theory of Propagation, Interference and Diffraction of Light*, 7th edn, Cambridge University Press, Cambridge, UK. 5.5.1, D.1, D.1.1

BOSQ-T. D, PEALE-R, WEEKS-A, GRANTHAM-J, DILLERY-D, LEE-D, MUH-D AND BOREMAN-G (2005). Terahertz/millimeter wave characterizations of soils for mine detection: transmission and scattering, *Proc. SPIE Terahertz for Military and Security Applications III*, **5790**, Eds: R. Hwu and D. Woolard, 28–29 March 2005, Orlando, FL, USA, pp. 66–73. 1.3.2, A.4

BOSTAK-J, VAN DER WEIDE-D, BLOOM-D, AULD-B AND ÖZBAY-E (1994). All-electronic terahertz spectroscopy system with terahertz free-space pulses, *Journal of the Optical Society of America B: Optical Physics*, **11**(12), pp. 2561–2565. 3.8.3

BOYD-R (2003). *Nonlinear Optics*, 2nd edn, Academic Press, San Diego, CA, USA. 2.5, 3.2, 3.3, B.1, B.1.1, B.1

BOYE-J, MA-C, ISMAIL-A, HARWALKAR-V AND KALAB-M (1997). Molecular and microstructural studies of thermal denaturation and gelation of β-lactoglobulins A and B, *Journal of Agricultural and Food Chemistry*, **45**(5), pp. 1608–1618. 7.3.2

BRAAK-H AND BRAAK-E (1990). Neurofibrillary changes confined to the entorhinal region and an abundance of cortical amyloid in cases of presenile and senile dementia, *Acta Neuropathologica*, **80**(5), pp. 479–486. 6.1.1

BRAAK-H AND BRAAK-E (1991). Neuropathological stageing of Alzheimer-related changes, *Acta Neuropathologica*, **82**(4), pp. 239–259. 6.3.1

BRAINTREE SCIENTIFIC INC. (2000). *Brain Matrices*, Braintree, MA, USA, <http://www.braintreesci.com/Products/matrice.asp>, (Accessed: 2009-02-20). 5.5

BRERETON-R (2003). *Chemometrics: Data Analysis for the Laboratory and Chemical Plant*, John Wiley & Sons, Chichester, England. 4.3.1

BRIDGES-W AND CHESTER-A (1971). *Ionized Gas Lasers*, Handbook of Lasers with Selected Data on Optical Technology, CRC Press, Cleveland, OH, USA, pp. 242–297. 2.3

BRIGHAM YOUNG UNIVERSITY (2009). *Crystal Planes in Semiconductors*, Brigham Young University, Provo, UT, USA, <http://cleanroom.byu.edu/EW_orientation.phtml>, (Accessed: 2010-04-09). B.3

BROMBERG-J (1991). *The Laser in America, 1950–1970*, MIT Press, Cambridge, MA, USA. 1

BROMLEY-E, KREBS-M AND DONALD-A (2005). Aggregation across the length-scales in β-lactoglobulin, *Faraday Discussions*, **128**, pp. 13–27. 7.2, 7.3.2

BROMLEY-E, KREBS-M AND DONALD-A (2006). Mechanisms of structure formation in particulate gels of β-lactoglobulin formed near the isoelectric point, *European Physical Journal E*, **21**(2), pp. 145–152. 7.3.2, 7.2

BROWN-E, BJARNASON-J, CHAN-T, LEE-A AND CELIS-M (2004). Optical attenuation signatures of Bacillus subtillis in the THz region, *Applied Physics Letters*, **84**(18), pp. 3438–3440. 4.5.3

BROWN-W (2000). *Introduction to Organic Chemistry*, 2nd edn, Saunders College Publishing, Orlando, FL, USA. 4.2, 4.3, 4.5.2, 4.5.2

BRUCHERSEIFER-M, NAGEL-M, BOLÍVAR-P, KURZ-H, BOSSERHOFF-A AND BÜTTNER-R (2000). Label-free probing of the binding state of DNA by time-domain terahertz sensing, *Applied Physics Letters*, **77**(24), pp. 4049–4051. 1.4.1, 4.5.2

BRÜNDERMANN-E, CHAMBERLIN-D AND HALLER-E (1999). Novel design concepts of widely tunable germanium terahertz lasers, *Infrared Physics & Technology*, **40**(3), pp. 141–151. 2.4.1

BRÜNDERMANN-E, CHAMBERLIN-D AND HALLER-E (2000). High duty cycle and continuous terahertz emission from germanium, *Applied Physics Letters*, **76**(21), pp. 2991–2993. 2.4.1

BRÜNDERMANN-E, HAVENITH-M, SCALARI-G, GIOVANNINI-M, FAIST-J, KUNSCH-J, MECHOLD-L AND ABRAHAM-M (2006). Turn-key compact high temperature terahertz quantum cascade lasers: imaging and room temperature detection, *Optics Express*, **15**(5), pp. 1829–1841. 2.4.1, 2.6

BRYANT-C AND MCCLEMENTS-D (1998). Molecular basis of protein functionality with special consideration of cold-set gels derived from heat-denatured whey, *Trends in Food Science & Technology*, **9**(4), pp. 143–151. 7.3.2

BUCCIANTINI-M, GIANNONI-E, CHITI-F, BARONI-F, FORMIGLI-L, ZURDO-J, TADDEI-N, RAMPONI-G, DOBSON-C AND STEFANI-M (2002). Inherent toxicity of aggregates implies a common mechanism for protein misfolding diseases, *Nature*, **416**(6880), pp. 507–511. 7.2, 7.7.1

BUDKO-N AND VAN DER BERG-P (1999). Characterization of a two-dimensional subsurface object with an effective scattering model, *IEEE Transactions on Geoscience and Remote Sensing*, **37**(5), pp. 2585–2596. 8.2

BUKHGEIM-A (2000). *Introduction to the Theory of Inverse Problems*, Inverse and Ill-Posed Problems Series, VSP, Utrecht. A.4

BULYSHEV-A, SEMENOV-S, SOUVOROV-A, SVENSON-R, NAZAROV-A, SIZOV-Y AND TATSIS-G (2001). Computational modeling of three-dimensional microwave tomography of breast cancer, *IEEE Transactions on Biomedical Engineering*, **48**(9), pp. 1053–1056. 4.4.2

BURSULAYA-B AND KIM-H (1998). Spectroscopic and dielectric properties of liquid water: A molecular dynamics simulation study, *Journal of Chemical Physics*, **109**(12), pp. 4911–4919. 9.4.1

BURTON-E, BARBER-R, MUKAETOVA-LADINSKA-E, ROBSON-J, PERRY-R, JAROS-E, KALARIA-R AND OBRIEN-J (2009). Medial temporal lobe atrophy on MRI differentiates Alzheimers disease from dementia with Lewy bodies and vascular cognitive impairment: a prospective study with pathological verification of diagnosis, *Brain*, **132**(1), pp. 195–203. 6.2.3

CAMPBELL-A AND LAND-D (1992). Dielectric properties of female human breast tissue measured in vitro at 3.2 GHz, *Physics in Medicine and Biology*, **37**(1), pp. 193–210. 14

CAMPBELL-M AND HEILWEIL-E (2003). Noninvasive detection of weapons of mass destruction using terahertz radiation, *Proc. SPIE Terahertz for Military and Security Applications*, **5070**, Eds: R. Hwu and D. Woolard, 21 April 2003, Orlando, FL, USA, pp. 38–43. 1.3.2

CARR-G (1999). High-resolution microspectroscopy and sub-nanosecond time-resolved spectroscopy with the synchrotron infrared source, *Vibrational Spectroscopy*, **19**(1), pp. 53–60. 2.7.1

CARR-G, MARTIN-M, MCKINNEY-W, JORDAN-K, NEIL-G AND WILLIAMS-G (2002). Very high power THz radiation at Jefferson Lab, *Physics in Medicine and Biology*, **47**, pp. 3761–3764. 3.11

CASTAGNE-R, LAVAL-S AND LAVAL-R (1976). Picosecond 1-wavelength optoelectronic gate, *Electronics Letters*, **12**(17), pp. 438–439. 3.8

CASTRO-CAMUS-E AND JOHNSTON-M (2008). Conformational changes of photoactive yellow protein monitored by terahertz spectroscopy, *Chemical Physics Letters*, **455**(4-6), pp. 289–292. 1.4.1, 4.5.2

CHAN-D, FOX-N, SCAHILL-R, CRUM-W, WHITWELL-J, LESCHZINER-G, ROSSOR-A, STEVENS-J, CIPOLOTTI-L AND ROSSOR-M (2001). Patterns of temporal lobe atrophy in semantic dementia and Alzheimers disease, *Annals of Neurology*, **49**(4), pp. 433–442. 6.2.3

CHANDRASEKHAR-S (1960). *Radiative Transfer*, Dover Publications, New York, NY, USA. 8.2

CHAN-T, BJARNASON-J, LEE-A, CELIS-M AND BROWN-E (2004). Attenuation contrast between biomolecular and inorganic materials at terahertz frequencies, *Applied Physics Letters*, **85**(13), pp. 2523–2525. 4.5.2, 4.5.3

CHATTOPADHYAY-G, GLENN-J, BOCK-J, ROWND-B, CALDWELL-M AND GRIFFIN-M (2003). Feed horn coupled bolometer arrays for SPIRE—design, simulations, and measurements, *IEEE Transactions on Microwave Theory and Techniques*, **51**(10), pp. 2139–2146. 8.7

CHEN-H, WANG-L, QU-Y, KUANG-T, LI-L AND PENG-W (2007a). Investigation of guanidine hydrochloride induced chlorophyll protein 43 and 47 denaturation in the terahertz frequency range, *Journal of Applied Physics*, **102**(7), article number 074701. 4.5.2

CHEN-J.-Y, KNAB-J, CERNE-J AND MARKELZ-A (2005). Large oxidation dependence observed in terahertz dielectric response for cytochrome c, *Physical Review E*, **72**(4), article number 040901. 4.5.2

CHEN-J.-Y, KNAB-J, YE-S, HE-Y AND MARKELZ-A (2007b). Terahertz dielectric assay of solution phase protein binding, *Applied Physics Letters*, **90**(24), article number 243901. 1.4.1, 4.5.2

CHEN-Q, JIANG-Z AND ZHANG-X.-C (1999). All-optical THz imaging, *Proc. Terahertz Spectroscopy and Applications*, **3617**, Ed: M. Sherwin, 1999-01-25, San Jose, CA, USA, pp. 98–105. 1.4.2

CHEUNG-K AND AUSTON-D (1986). A novel technique for measuring far-infrared absorption and dispersion, *Infrared Physics*, **26**(1), pp. 23–27. 1.3.2, 3.6

CHEVILLE-R (2008). *Terahertz Time-Domain Spectroscopy with Photoconductive Antennas*, Terahertz Spectroscopy: Principles and Applications, CRC Press, Boca Raton, FL, USA, pp. 1–39. 3.8.1, 3.12, 3.8.2

CHEVILLE-R, REITEN-M, MCGOWAN-R AND GRISCHKOWSKY-D (2003). *Applications of Optically Generated Terahertz Pulses to Time Domain Ranging and Scattering*, Springer Series in Optical Sciences, Springer-Verlag, Berlin, Germany, pp. 237–293. 8.1

CHOI-M, BETTERMANN-A AND VAN DER WEIDE-D (2004). Potential for detection of explosive and biological hazards with electronic terahertz systems, *Philosophical Transactions of the Royal Society A: Mathematical, Physical and Engineering Sciences*, **362**(1815), pp. 337–349. 1.3.2

CIESLA-C, ARNONE-D, CORCHIA-A, CRAWLEY-D, LONGBOTTOM-C, LINFIELD-E AND PEPPER-M (2000). Biomedical applications of terahertz pulse imaging, *Proc. SPIE Commercial and Biomedical Applications of Ultrafast Lasers II*, **3934**, Eds: J. Neev and M. Reed, 24–25 January 2000, San Jose, CA, USA, pp. 73–81. 1.3.2

CLARKE-A (1971). *Ocular Hazards*, Handbook of Lasers with Selected Data on Optical Technology, CRC Press, Cleveland, OH, USA, pp. 3–10. 3.7.1

CLEETON-C AND WILLIAMS-N (1933). A magnetostatic oscillator for the generation of 1 to 3 cm waves, *Physical Review*, **44**(5), p. 421. 1.3.1

CLEETON-C AND WILLIAMS-N (1934). Electromagnetic waves of 1.1 cm wave-length and the absorption spectrum of ammonia, *Physical Review*, **45**(4), pp. 234–237. 1.3.1

COLAK-S, VAN DER MARK-M, HOOFT-G, HOOGENRAAD-J. H, VAN DER LINDEN-E AND KUIJPERS-F (1999). Clinical optical tomography and NIR spectroscopy for breast cancer detection, *IEEE J. of Selected Topics in Quantum Electronics*, **5**(4), pp. 1143–1158. 4.3.2

COLE-B, WOODWARD-R, CRAWLEY-D, WALLACE-V, ARNONE-D AND PEPPER-M (2001). Terahertz imaging and spectroscopy of human skin, *In-vivo*, *Proc. SPIE Commercial and Biomedical Applications of Ultrashort Pulse Lasers; Laser Plasma Generation and Diagnostics*, **4276**, Eds: R. Haglund Jr., J. Neev and R. Wood, 23 January 2001, San Jose, CA, USA, pp. 1–10. 1.4.2

COLE-K AND COLE-R (1941). Dispersion and absorption in dielectrics I. alternating current characteristics, *Journal of Chemical Physics*, **9**, pp. 341–351. 9.4.2

COLOMBELLI-R, SRINIVASAN-K, TROCCOLI-M, PAINTER-O, GMACHL-C, TENNANT-D, SERGENT-A, SIVCO-D, CHO-A AND CAPASSO-F (2008). Quantum cascade surface-emitting photonic crystal laser, *Science*, **302**, pp. 1374–1377. 2.4.1, 2.6

COLTHUP-N, DALY-L AND WIBERLEY-S (1964). *Introduction to Infrared and Raman Spectroscopy*, Academic Press Inc., New York, NY, USA. 4.3

CORRIDON-P, ASCÁZUBI-R, KREST-C AND WILKE-I (2006). Time-domain terahertz spectroscopy of artificial skin, *Proc. SPIE Advanced Biomedical and Clinical Diagnostic Systems IV*, **6080**, Eds: G. Cohn, W. Grundfest, D. Benaron and T. Vo-Dinh, 21–26 January 2006, San Jose, CA, USA, pp. 23–34. 1.5.1

CRAWLEY-D, LONGBOTTOM-C, COLE-B, CIESLA-C, ARNONE-D, WALLACE-V AND PEPPER-M (2003a). Terahertz pulse imaging: A pilot study of potential applications in dentistry, *Caries Research*, **37**(5), pp. 352–359. 1.3.2

CRAWLEY-D, LONGBOTTOM-C, WALLACE-V, COLE-B, ARNONE-D AND PEPPER-M (2003b). Three-dimensional terahertz pulse imaging of dental tissue, *Biomedical Optics*, **8**(2), pp. 303–307. 1.3.2

CRICK-F (1970). Central dogma of molecular biology, *Nature*, **227**, pp. 561–563. 4.5.2

CROWE-T, GLOBUS-T, WOOLARD-D AND HESLER-J (2004). Terahertz sources and detectors and their application to biological sensing, *Philosophical Transactions of the Royal Society A: Mathematical, Physical and Engineering Sciences*, **362**(1815), pp. 365–377. 2.4

CUMMINGS-J (2003). *The Neuropsychiatry of Alzheimer's Disease and Related Dementias*, Martin Dunitz Ltd., London, England. 6.2, 6.2

CUNNINGTON JR.-G, TONG-T AND SWATHI-P (1992). Angular scattering of radiation from coated cylindrical fibers, *Journal of Quantitative Spectroscopy and Radiative Transfer*, **48**(4), pp. 353–362. 8.2

CYCLOTEK (2009). *Production Offerings - F*, Bundoora, VIC, Australia, <http://www.cyclotek.com/capability_production_f.html>, (Accessed: 2009-06-09). 6.2.2

CZERNY-M (1930). Messungen am Steinsalz im Ultraroten zur Prüfung der Dispersionstheorie, *Zeitschrift für Physik A: Hadrons and Nuclei*, **65**(9-10), pp. 600–631. 1.4, 3

DARMO-J, TAMOSIUNAS-V, FASCHING-G, KRÖLL-J, UNTERRAINER-K, BECK-M, GIOVANNINI-M, FAIST-J, KREMSER-C AND DEBBAGE-P (2004). Imaging with a terahertz quantum cascade laser, *Optics Express*, **12**(9), pp. 1879–1884. 2.4.1

DARROW-J, HU-B, ZHANG-X.-C AND AUSTON-D (1990). Subpicosecond electromagnetic pulses from large-aperture photoconducting antennas, *Optics Letters*, **15**(6), pp. 323–325. 3.8.3

DAWKINS-A, SHEPPARD-R AND GRANT-E (1979). An on-line computer-based system for performing time domain spectroscopy: I. main features of the basic system, *Journal of Physics E (Scientific Instruments)*, **12**(11), pp. 1091–1099. 4.4.1

DAWSON-T, CAPUTA-K, STUCHLY-M AND KAVET-R (2001). Electric fields in the human body resulting from 60-Hz contact currents, *IEEE Transactions on Biomedical Engineering*, **48**(9), pp. 1020–1026. 9.2

DEBYE-P (1929). *Polar Molecules*, Dover Publications, New York, NY, USA. 76

DEIBEL-J AND MITTLEMAN-D (2006). Designing and simulating THz wire waveguides using FEM modeling, *RF Design*, pp. 36–43. 9.2

DE KRUIF-K, HOFFMANN-M, VAN MARLE-M, VAN MIL-P, ROEFS-S, VERHEUL-M AND ZOON-N (1995). Gelation of proteins from milk, *Faraday Discussions*, **101**(101), pp. 185–200. 7.1, 7.3.1

DE LA FUENTE-M, SINGH-H AND HEMAR-Y (2002). Recent advances in the characterisation of heat-induced aggregates and intermediates of whey proteins, *Trends in Food Science & Technology*, **13**(8), pp. 262–274. 7.4.2

DE LUCIA-F, HELMINGER-P, COOK-R AND GORDY-W (1972). Submillimeter microwave spectrum of $H_2^{16}O$, *Physical Review A: General Physics*, **5**(2), pp. 487–490. 1, 4.2

DEMETER-S, ROSENE-D AND HOESEN-G. V (1989). Commissural connections and symmetry of degeneration in Alzheimer's disease, *Archives in Neurology*, **46**(7), pp. 723–724. 6.3.1

DEUTSCH-T (1971). *Dye Lasers*, Handbook of Lasers with Selected Data on Optical Technology, CRC Press, Cleveland, OH, USA, pp. 350–354. 3.7.1

DICK-B, GIERULSKI-A, MAROWSKY-G AND REIDER-G (1985). Determination of the nonlinear optical susceptibility $\chi^{(2)}$ of surface layers by sum and difference frequency generation in reflection and transmission, *Applied Physics B (Photophysics and Laser Chemistry)*, **38**(2), pp. 107–116. 2.5

DIKMELIK-Y, SPICER-J, FITCH-M AND OSIANDER-R (2006). Effects of surface roughness on reflection spectra obtained by terahertz time-domain spectroscopy, *Optics Letters*, **31**(24), pp. 3653–3655. 8.1, F.8.1

DIMBYLOW-P (1997). FDTD calculations of the whole-body averaged SAR in an anatomically realistic voxel model of the human body from 1 MHz to 1 GHz, *Physics in Medicine and Biology*, **42**(3), pp. 479–490. 4.4.2

DIMBYLOW-P (2002). Fine resolution calculations of SAR in the human body for frequencies up to 3 GHz, *Physics in Medicine and Biology*, **47**(16), pp. 2835–2846. 4.1, 4.4.2

DINGLE-R, WIEGMANN-W AND HENRY-C (1974). Quantum states of confined carriers in very thin $Al_xGa_{1-x}As$-GaAs-$Al_xGa_{1-x}As$ heterostructures, *Physical Review Letters*, **33**(14), pp. 827–830. 2.4.1

DMITRIEV-V, GURZADYAN-G AND NIKOGOSYAN-D (1999). *Handbook of Nonlinear Optical Crystals*, Springer Series in Optical Sciences, 3rd edn, Springer-Verlag, Berlin, Germany. 3.4, B.2

DODSON-C, FITCH-M, OSIANDER-R AND SPICER-J (2005). Terahertz imaging for anti-personnel mine detection, *Proc. SPIE Terahertz for Military and Security Applications III*, **5790**, Eds: R. Hwu and D. Woolard, 28–29 March 2005, Orlando, FL, USA, pp. 85–93. 1.3.2

DORIA-A, GALLERANO-G, GIOVENALE-E, MESSINA-G, LAI-A, RAMUNDO-ORLANDO-A, SPOSATO-V, D'ARIENZO-M, PERROTTA-A, ROMANÓ-M, SARTI-M, SCARFÍ-M, SPASSOVSKY-I AND ZENI-O (2004). THz radiation studies on biological systems at the ENEA FEL facility, *Infrared Physics & Technology*, **45**(5-6), pp. 339–347. 2.16, 2.7.2, 4.5.2

DORNEY-T, BARANIUK-R AND MITTLEMAN-D (2001). Material parameter estimation with terahertz time-domain spectroscopy, *Journal of the Optical Society of America A: Optics and Image Science, and Vision*, **18**(7), pp. 1562–1571. A.3.1

DORNEY-T, JOHNSON-J, MITTLEMAN-D AND BARANIUK-R (2000). Imaging with terahertz pulses, *Proc. SPIE Applications of Digital Image Processing XXIII*, Ed: A. Tescher, 31 July–3 August 2000, San Diego, CA, USA, pp. 688–699. 1.5.1

DOWNEY-P AND SCHWARTZ-B (1984). Picosecond photoresponse in $^{3}He^{+}$ bombarded in InP photoconductors, *Applied Physics Letters*, **44**(2), pp. 207–209. 3.8.3

DREZEK-R, DUNN-A AND RICHARDS-KORTUM-R (1999). Light scattering from cells: finite-difference time-domain simulations and goniometric measurements, *Applied Optics*, **38**(16), pp. 3651–3661. 8.2

DRYSDALE-T, BLAIKIE-R AND CUMMING-D (2003). Tunable photonic crystal filter for terahertz frequency applications, *Proc. SPIE Terahertz for Military and Security Applications*, **5070**, Eds: R. Hwu and D. Woolard, Orlando, FL, USA, pp. 89–97. A.2

DUHAMEL-F, HUYNEN-I AND VORST-A. V (1997). Measurements of complex permittivity of biological and organic liquids up to 110 GHz, *Proc. Microwave Symposium Digest*, 8–13 June 1997, pp. 107–110. 17

DULING III-I AND ZIMDARS-D (2007). Terahertz imaging: Compact TD-THz systems offer flexible, turnkey imaging solutions, *Laser Focus World*, **43**(4), pp. 63–69. 3.4

DUVERNOY-H, DELON-S AND VANNSON-J (1981). Cortical blood vessels of the human brain, *Brain Research Bulletin*, **7**(5), pp. 519–579. 6.18

DUVILLARET-L, GARET-F AND COUTAZ-J.-L (1996). A reliable method for extraction of material parameters in terahertz time-domain spectroscopy, *IEEE Journal of Selected Topics in Quantum Electronics*, **2**(3), pp. 739–746. 1.5.1, A.3, A.3.2, A.8, D.2.2

DUVILLARET-L, GARET-F AND COUTAZ-J.-L (1999). Highly precise determination of optical constants and sample thickness in terahertz time-domain spectroscopy, *Applied Optics*, **38**(2), pp. 409–415. D.2.2

DUVILLARET-L, GARET-F, ROUX-J.-F AND COUTAZ-J.-L (2001). Analytic modeling and optimization of terahertz time-domain spectroscopy experiments using photoswitches as antennas, *IEEE Journal of Selected Topics in Quantum Electronics*, **7**(4), pp. 615–623. 1.5.1

DYKAAR-D, GREENE-B, FEDERICI-J, LEVI-A, PFEIFFER-L AND KOPF-R (1991). Log-periodic antennas for pulsed terahertz radiation, *Applied Physics Letters*, **59**(3), pp. 262–264. 3.8.3

EBBINGHAUS-S, KIM-S, HEYDEN-M, YU-X, GRUEBELE-M, LEITNER-D AND HAVENITH-M (2008). Protein sequence- and pH-dependent hydration probed by terahertz spectroscopy, *Journal of the American Chemical Society*, **130**(8), pp. 2374–2375. 1.4.1, 7.1

EL-TAWIL-S, ADNAN-R, MUHAMED-Z AND OTHMAN-N (2008). Comparative study between pap smear cytology and ftir spectroscopy: a new tool for screening for cervical cancer, *Pathology*, **40**(6), pp. 600–603. 4.3.2

EMCORE CORPORATION (2008). *PB7100 Frequency Domain Terahertz Spectrometer Datasheet*, Warminster, PA, USA, <http://www.emcore.com/assets/fiber/PB7100_Data_Sheet_R100807.pdf>, (Accessed: 2008-11-24). 3.2

EPSZTEIN-B (1952). *Backward Flow Travelling Wave Oscillator*, US patent number 2,880,355, date issued: 1959-03-31. 23

EUROPEAN FUSION DEVELOPMENT AGREEMENT (EFDA) (2008). *Joint European Torus (JET)*, Abingdon, Oxfordshire, UK, <www.jet.efda.org>, (Accessed: 2008-10-22). 2.10

EUROPEAN ORGANISATION FOR ASTRONOMICAL RESEARCH IN THE SOUTHERN HEMISPHERE (ESO) (2008a). *ALMA Simulations: ALMA Site*, Las Condes, Chile, <http://www.alma.cl/alma_board/>, (Accessed: 2008-10-28). 1.3

EUROPEAN ORGANISATION FOR ASTRONOMICAL RESEARCH IN THE SOUTHERN HEMISPHERE (ESO) (2008b). *Atacama Large Millimeter Array (ALMA)*, Las Condes, Chile, <http://www.eso.org/public/astronomy/projects/alma.html>, (Accessed: 2008-07-30). 1.3.1

EUROPEAN ORGANISATION FOR ASTRONOMICAL RESEARCH IN THE SOUTHERN HEMISPHERE (ESO) (2008c). *First Move of an Antenna with the Transporter*, Las Condes, Chile, <http://www.alma.cl/ta/index.php>, (Accessed: 2008-10-28). 1.3

EUROPEAN SPACE AGENCY (ESA) (2004). *Artist's Impression of the Herschel Spacecraft*, <http://sci.esa.int/science-e/www/object/index.cfm?fobjectid=34681>, (Accessed: 2008-10-28). 1.2

EUROPEAN SPACE AGENCY (ESA) (2007). *Herschel Cryostat*, ESA/AOES Medialab, <http://sci.esa.int/science-e/www/object/index.cfm?fobjectid=41310>, (Accessed: 2008-10-28). 1.2

EUROPEAN SPACE AGENCY (ESA) AND THE HIFI CONSORTIUM (2009a). *HIFI Spectrum of Comet Garradd*, European Space Agency, <http://sci.esa.int/science-e/www/object/index.cfm?fobjectid=45987>, (Accessed: 2010-01-27). 1.2

EUROPEAN SPACE AGENCY (ESA) AND THE SPIRE CONSORTIUM (2009b). *SPIRE Spectrum of the Orion Bar*, European Space Agency, <http://sci.esa.int/science-e/www/object/index.cfm?fobjectid=45976>, (Accessed: 2010-01-27). 1.2

EVANS-G, EVANS-M, MINGUZZI-P, SALVETTI-G, REID-C AND VIJ-J (1987). The dynamics of liquid water: Simulation and submillimeter spectroscopy, *Journal of Molecular Liquids*, **34**(4), pp. 285–306. 8

FAIST-J, AJILI-L, SCALARI-G, GIOVANNINI-M, BECK-M, ROCHAT-M, BEERE-H, DAVIES-A, LINFIELD-E AND RITCHIE-D (2004). Terahertz quantum cascade lasers, *Philosophical Transactions of the Royal Society of London: Mathematical, Physical and Engineering Sciences*, **362**(1815), pp. 215–229. 2.4.1

FAIST-J, CAPASSO-F, SIVCO-D, SIRTORI-C, HUTCHINSON-A AND CHO-A (1994). Quantum cascade laser, *Science*, **264**(5158), pp. 553–556. 2.4.1

FALCONER-R, ABBOTT-D, FISCHER-B, JONE-I, MIDDELBERG-A AND ZAKARIA-H (2009). Far-infrared spectrometry of proteins and their higher order structures, *Proc. 5th International Conference on Advanced Vibrational Spectroscopy (ICAVS5)*, 12-17 July 2009, Melbourne, Australia, p. 24. 2.7.1

FÄNDRICH-M, FLETCHER-M AND DOBSON-C (2001). Amyloid fibrils from muscle myoglobin - even an ordinary globular protein can assume a rogue guise if conditions are right, *Nature*, **410**(6825), pp. 165–166. 6.2.1

FARIES-D, GEHRING-K, RICHARDS-P AND SHEN-Y (1969). Tunable far-infrared radiation generated from the difference frequency between two ruby lasers, *Physical Review*, **180**(2), pp. 363–365. 3.5

FATTERPEKAR-G, NAIDICH-T, DELMAN-B, AGUINALDO-J, GULTEKIN-S, SHERWOOD-C, HOF-P, DRAYER-B AND FAYAD-Z (2002). Cytoarchitecture of the human cerebral cortex: MR microscopy of excised specimens at 9.4 Tesla, *American Journal of Neuroradiology*, **23**(8), pp. 1313–1321. 6.4.2

FATTINGER-C AND GRISCHKOWSKY-D (1988). Point source terahertz optics, *Applied Physics Letters*, **53**(16), pp. 1480–1482. 1.3.2, 3.8, 3.11

FATTINGER-C AND GRISCHKOWSKY-D (1989a). A Cherenkov source for freely-propagating terahertz beams, *IEEE Journal of Quantum Electronics*, **25**(12), pp. 2608–2610. 3.6

FATTINGER-C AND GRISCHKOWSKY-D (1989b). Terahertz beams, *Applied Physics Letters*, **54**(6), pp. 490–492. 3.11

FEAR-E AND STUCHLY-M (2000). Microwave detection of breast cancer, *IEEE Transactions on Microwave Theory and Techniques*, **48**(11), pp. 1854–1863. 20, 4.10

FEAR-E, LI-X, HAGNESS-S AND STUCHLY-M (2002). Confocal microwave imaging for breast cancer detection: Localization of tumors in three dimensions, *IEEE Transactions on Microwave Theory and Techniques*, **49**(8), pp. 812–822. 20

FEDERICI-J, GARY-D, BARAT-R AND MICHALOPOULOU-Z.-H (2008). *T-Rays vs. Terrorists*, IEEE Spectrum, <www.spectrum.ieee.org/print/5278>, (Accessed: 2008-11-25). 3.4

FEDERICI-J, GARY-D, BARAT-R AND ZIMDARS-D (2005). Thz standoff detection and imaging of explosives and weapons, *Proc. SPIE Optics and Photonics in Global Homeland Security*, **5781**, Ed: T. Saito, 29 March–1 April 2005, Orlando, FL, USA, pp. 75–84. 1.3.2

FELCH-K, BLANK-M, BORCHARD-P, CAHALAN-P, CAUFFMAN-S AND JORY-H (2008). Recent test results on a 95 GHz, 2 MW gyrotron, *Proc. 33rd International Conference on Infrared, Millimeter, and Terahertz Waves*, 15–19 September 2008, Pasadena, CA, USA, article number 1608. 2.9

FERGUSON-B AND ABBOTT-D (2001). De-noising techniques for terahertz responses of biological samples, *Microelectronics Journal*, **32**(12), pp. 943–953. 1.4.2

FERGUSON-B, LIU-H, HAY-S, FINDLAY-D, ZHANG-X.-C AND ABBOTT-D (2004). In vitro osteosarcoma biosensing using THz time domain spectroscopy, *Proc. SPIE BioMEMS and Nanotechnology*, **5275**, Eds: D. Nicolau, U. Muller and J. Dell, March 2004, pp. 304–316. 4.5.4

FERGUSON-B, WANG-S, GRAY-D, ABBOTT-D AND ZHANG-X.-C (2002a). Identification of biological tissue using chirped probe THz imaging, *Microelectronics Journal*, **33**(12), pp. 1043–1051. 1.3.2, 1.4.2, 4.3.1, 4.5.4

FERGUSON-B, WANG-S, GRAY-D, ABBOTT-D AND ZHANG-X.-C (2002b). Towards functional 3D T-ray imaging, *Physics in Medicine and Biology*, pp. 3735–3742. 1.3.2, 1.5

FISCHER-B, HELM-H AND JEPSEN-P (2007). Chemical recognition with broadband THz spectroscopy, *Proceedings IEEE*, **95**(8), pp. 1592–1604. 4.5.3

FISCHER-B, HOFFMANN-M, HELM-H, MODJESCH-G AND JEPSEN-P (2005a). Chemical recognition in terahertz time-domain spectroscopy and imaging, *Semiconductor Science and Technology*, **20**(7), pp. S246–S253. 1.2, 4.5.3

FISCHER-B, HOFFMANN-M, HELM-H, WILK-R, RUTZ-F, KLEINE-OSTMANN-T, KOCH-M AND JEPSEN-P (2005b). Terahertz time-domain spectroscopy and imaging of artificial RNA, *Optics Express*, **13**(14), pp. 5205–5215. 1.4.1, 4.5.2

FISCHER-B, WALTHER-M AND JEPSEN-P (2002). Far-infrared vibrational modes of DNA components studied by terahertz time-domain spectroscopy, *Physics in Medicine and Biology*, **47**(21), pp. 3807–3814. 1.4.1, 4.5.2, 7.1

FISCHER-J, HANNAY-H, LORING-D AND LEZAK-M (2004). *Observational Methods, Rating Scales, and Inventories*, Neuropsychological Assessment, 4th edn, Oxford University Press, New York, NY, USA, pp. 698–737. 6.2.2

FISCHL-B AND DALE-A (2000). Measuring the thickness of the human cerebral cortex from magnetic resonance images, *Proceedings of the National Academy of Sciences of the United States of America*, **97**(20), pp. 11050–11055. 6.4.2

FITZGERALD-A, BERRY-E, ZINOV'EV-N, HOMER-VANNIASINKAM-S, MILES-R, CHAMBERLAIN-J AND SMITH-M (2003). Catalogue of human tissue optical properties at terahertz frequencies, *Journal of Biological Physics*, **129**(2-3), pp. 123–128. 1.4.2, 4.5.4, 4.16, 7.5, 9.3, 9.4.3, 9.4.3, 77, 9.2, 9.3, 9.2, F.8.1

FITZGERALD-A, BERRY-E, ZINOV'EV-N, WALKER-G, SMITH-M AND CHAMBERLAIN-J (2002). An introduction to medical imaging with coherent terahertz frequency radiation, *Physics in Medicine and Biology*, **47**, pp. R67–R84. 1.4.2

FITZGERALD-A, COLE-B AND TADAY-P (2005). Nondestructive analysis of tablet coating thicknesses using terahertz pulsed imaging, *Journal of Pharmaceutical Sciences*, **94**(1), pp. 177–183. 1.3.2

FIZEAU-A (1862). Recherches sur les modifications que subit la vitesse de la lumiére dans le verre sous l'influence de la chaleur, *Annales des Chimie et des Physique*, **66**, pp. 429–482. 4

FLETCHER-J, SWIFT-G, DAI-D, LEVITT-J AND CHAMBERLAIN-J (2007). Propagation of terahertz radiation through random structures: An alternative theoretical approach and experimental validation, *Journal of Applied Physics*, **101**(1), article number 013102. 8.1, 8.1.1

FOEGEDING-E, KUHN-P AND HARDIN-C (1992). Specific divalent cation-induced changes during gelation of β-lactoglobulin, *Journal of Agricultural and Food Chemistry*, **40**(11), pp. 2092–2097. 7.3.1

FOLSTEIN-M, FOLSTEIN-S AND MCHUGH-P (1975). mini-mental state: A practical method for grading the cognitive state of patients for the clinician, *Journal of Psychiatric Research*, **12**(3), pp. 189–198. 6.2.2

FOSTER-K, SCHEPPS-J AND SCHWAN-H (1980). Microwave dielectric relaxation in muscle: A second look, *Biophysical Journal*, **29**(2), pp. 271–281. 2

FOSTER-K, SCHEPPS-J, STOY-R AND SCHWAN-H (1979). Dielectric properties of brain tissue between 0.01 and 10 GHz, *Physics in Medicine and Biology*, **24**(6), pp. 1177–1187. 1

FOYT-A, LEONBERGER-F AND WILLIAMSON-R (1982). Picosecond InP optoelectronic switches, *Applied Physics Letters*, **40**(6), pp. 447–449. 3.8.3

FRANKEN-P AND WARD-J (1963). Optical harmonics and nonlinear phenomena, *Reviews of Modern Physics*, **35**(1), pp. 23–39. 3.5

FRANKEN-P, HILL-A, PETERS-C AND WEINREICH-G (1961). Generation of optical harmonics, *Physical Review Letters*, **7**(4), pp. 118–119. 1.3.1, 3.2, 3.2, 3.3, 3.5

FRANZ-M, FISCHER-B, ABBOTT-D AND HELM-H (2006). Terahertz study of chiral and racemic crystals, *Proc. Joint 31st International Conference on Infrared and Millimeter Waves and 14th International Conference on Terahertz Electronics (IRMMW-THz)*, 18-22 September 2006, Shanghai, China, p. 230. 1.4.1, 4.5.3

FRANZ-M, FISCHER-B AND WALTHER-M (2008). The Christiansen effect in terahertz of coarse-grained powders, *Applied Physics Letters*, **92**(2), article number 021107. 8.1

FRATIGLIONI-L, DE RONCHI-D AND AGÜERO-TORRES-H (1999). Worldwide prevalence and incidence of dementia, *Drugs & Aging*, **15**(5), pp. 365–375. 6.2

FREUND-D, MCCALLY-R AND FARRELL-R (1986). Direct summation of fields for light scattering by fibrils with applications to normal corneas, *Applied Optics*, **25**(16), pp. 2739–2746. 8.2

FUKUNAGA-K, WATANABE-S AND YAMANAKA-Y (2004). Dielectric properties of tissue-equivalent liquids and their effects on specific absorption rate, *IEEE Transactions on Electromagnetic Compatibility*, **46**(1), pp. 126–129. 4.4.2

GABRIEL-C AND GABRIEL-S (1997a). *Compilation of the Dielectric Properties of Body Tissues at RF and Microwave Frequencies*, <http://niremf.ifac.cnr.it/docs/DIELECTRIC/Report.html>, (Accessed: 2005-10-14). 4.4.2, 9.4.1, 9.4.2, 9.4.3

GABRIEL-C AND GABRIEL-S (1997b). *Modelling the Frequency Dependence of the Dielectric Properties to a 4 Dispersions Spectrum*, <http://niremf.ifac.cnr.it/docs/DIELECTRIC/AppendixC.html>, (Accessed: 2005-10-14). 9.4.2, 9.1, 9.2

GABRIEL-C AND GRANT-E (1985). Dielectric properties of ocular tissues in the supercooled and frozen states, *Physics in Medicine and Biology*, **30**(9), pp. 975–983. 7

GABRIEL-C, CHAN-T AND GRANT-E (1994). Admittance models for open ended coaxial probes and their place in dielectric spectroscopy, *Physics in Medicine and Biology*, **39**(12), pp. 2183–2200. 9.4.2

GABRIEL-C, GABRIEL-S AND CORTHOUT-E (1996a). The dielectric properties of biological tissues: I. literature survey, *Physics in Medicine and Biology*, **41**(11), pp. 2231–2249. 4.4.2, 9.4.2

GABRIEL-C, SHEPPARD-R AND GRANT-E (1983). Dielectric properties of ocular tissues at 37°C, *Physics in Medicine and Biology*, **28**(1), pp. 43–49. 5

GABRIEL-S, LAU-R AND GABRIEL-C (1996b). The dielectric properties of biological tissues: II. measurements in the frequency range 10 Hz to 20 GHz, *Physics in Medicine and Biology*, **41**(11), pp. 2251–2269. 4.4.2, 9.4.2, 9.4.3, 9.2, 9.2

GABRIEL-S, LAU-R AND GABRIEL-C (1996c). The dielectric properties of biological tissues: III. parametric models for the dielectric spectrum of tissues, *Physics in Medicine and Biology*, **41**(11), pp. 2271–2293. 4.4.2, 9.4.2, 9.4.3, 9.4.3, 77, 9.2, 9.3, 9.1, 9.2

GAGE-A AND BAUST-J (1998). Mechanisms of tissue injury in cryosurgery, *Cryobiology*, **37**(3), pp. 171–186. 5.5.1

GAJŠEK-P, HURT-W, ZIRIAX-J AND MASON-P (2001). Parametric dependence of SAR on permittivity values in a man model, *IEEE Transactions on Biomedical Engineering*, **48**(10), pp. 1169–1177. 4.4.2

GALLAGHER-W, CHI-C.-C, DULING III-I, GRISCHKOWSKY-D, HALAS-N, KETCHEN-M AND KLEINSASSER-A (1987). Subpicosecond optoelectronic study of resistive and superconductive transmission lines, *Applied Physics Letters*, **50**(6), pp. 350–352. 3.8.3

GALLANT-A, KALITEEVSKI-M, BRAND-S, WOOD-D, PETTY-M, ABRAM-R AND CHAMBERLAIN-J (2007a). Terahertz frequency bandpass filters, *Journal of Applied Physics*, **102**(2), article number 023102. A.2.1

GALLANT-A, KALITEEVSKI-M, WOOD-D, PETTY-M, ABRAM-R, BRAND-S, SWIFT-G, ZEZE-D AND CHAMBERLAIN-J (2007b). Passband filters for terahertz radiation based on dual metallic photonic structures, *Applied Physics Letters*, **91**(16), article number 161115. A.2.1

GAZI-E, DWYER-J, LOCKYER-N, MIYAN-J, GARDNER-P, HART-C, BROWN-M AND CLARKE-N (2005). A study of cytokinetic and motile prostate cancer cells using synchrotron-based FTIR microspectroscopic imaging, *Vibrational Spectroscopy*, **38**(1-2), pp. 193–201. 4.3.1

GEORGE-P, HUI-W, RANA-F, HAWKINS-B, SMITH-A AND KIRBY-B (2008). Microfluidic devices for terahertz spectroscopy of biomolecules, *Optics Express*, **16**(3), pp. 1577–1582. 4.5.2

GIOVENALE-E, D'ARIENZO-M, DORIA-A, GALLERANO-G, LAI-A, MESSINA-G AND PICCINELLI-D (2003). Absorption and diffusion measurements of biological samples using a THz free electron laser, *Journal of Biological Physics*, **29**(2-3), pp. 159–170. 2.7.2, 4.5.2

GJONAJ-E, BARTSCH-M, CLEMENS-M, SCHUPP-S AND WEILAND-T (2002). High-resolution human anatomy models for advanced electromagnetic field computations, *IEEE Transactions on Magnetics*, **38**(2), pp. 357–360. 4.4.2

GLASS-A AND AUSTON-D (1972). Excited state dipole moments of impurities in polar crystals, *Optics Communications*, **5**(1), pp. 45–49. 1.3.2

GLOBUS-T, WOOLARD-D, CROWE-T, KHROMOVA-T, GELMONT-B AND HESLER-J (2006). Terahertz Fourier transform characterization of biological materials in a liquid phase, *Journal of Physics D: Applied Physics*, **39**(15), pp. 3405–3414. 1.4.1, 4.5.2

GLOBUS-T, WOOLARD-D, KHROMOVA-T, CROWE-T, BYKHOVSKAIA-M, GELMONT-B, HESLER-J AND SAMUELS-A (2003). THz-spectroscopy of biological molecules, *Journal of Biological Physics*, **29**(2-3), pp. 89–100. 1.4.1, 4.5.2

GLYAVIN-M, LUCHININ-A AND GOLUBIATNIKOV-G (2008). Generation of 1.5-kW, 1-THz coherent radiation from a gyrotron with a pulsed magnetic field, *Physical Review Letters*, **100**(1), article number 015101. 2.9, 2.6.1

GOLAY-M (1949). Multi-slit spectrometry, *Journal of the Optical Society of America*, **39**(6), pp. 437–444. 1.3.1

GORODNICHEV-E, KUZOVLEV-A AND ROGOZKIN-D (2006). Depolarization of multiply scattered light in transmission through a turbid medium with large particles, *Optics Communications*, **260**(1), pp. 30–45. 8.2

GOSAL-W, CLARK-A AND ROSS-MURPHY-S (2004a). Fibrillar β-Lactoglobulin gels: Part 1. fibril formation and structure, *Biomacromolecules*, **5**(6), pp. 2408–2419. 7.1.1, 7.2, 7.3, 7.3, 7.4, 7.4.2

GOSAL-W, CLARK-A AND ROSS-MURPHY-S (2004b). Fibrillar β-Lactoglobulin gels: Part 2. dynamic mechanical characterization of heat-set systems, *Biomacromolecules*, **5**(6), pp. 2420–2429. 7.4

GOSAL-W, CLARK-A AND ROSS-MURPHY-S (2004c). Fibrillar β-lactoglobulin gels: Part 3. dynamic mechanical characterization of solvent-induced systems, *Biomacromolecules*, **5**(6), pp. 2430–2438. 7.4

GOSAL-W, CLARK-A, PUDNEY-P AND ROSS-MURPHY-S (2002). Novel amyloid fibrillar networks derived from a globular protein: β-lactoglobulin, *Langmuir*, **18**(19), pp. 7174–7181. 7.2

GOURAUD-H (1971). Continuous shading of curved surfaces, *IEEE Transactions on Computers*, **C-20**(6), pp. 623–629. 8.2

GOUSEV-Y, ALTUKHOV-I, KOROLEV-K, SINIS-V, KAGAN-M, HALLER-E, ODNOBLYUDOV-M, YASSIEVICH-I AND CHAO-K.-A (1999). Widely tunable continuous-wave THz laser, *Applied Physics Letters*, **75**(6), pp. 757–759. 2.4.1

GRANT-E, SHEPPARD-R AND SOUTH-G (1978). *Dielectric Behaviour of Biological Molecules in Solution*, Monographs on Physical Biochemistry, Oxford University Press, Oxford, England. 4.5.2, 9.4.3

GREENE-B, FEDERICI-J, DYKAAR-D, LEVI-A AND PFEIFFER-L (1991). Picosecond pump and probe spectroscopy utilizing freely propagating terahertz radiation, *Optics Letters*, **16**(1), pp. 48–49. 3.8.3

GRISCHKOWSKY-D (1980a). Angular and velocity distribution of desorbed sodium atoms, *Applied Physics Letters*, **36**(8), pp. 711–713. 1.3.2

GRISCHKOWSKY-D (1980b). Doppler-free backward-fluorescence spectroscopy in vapors, *Optics Letters*, **5**(12), pp. 534–536. 1.3.2

GRISCHKOWSKY-D, DULING III-I, CHEN-J AND CHI-C.-C (1987). Electromagnetic shock waves from transmission lines, *Physical Review Letters*, **59**(15), pp. 1663–1666. 1.3.2

GROSSE-E (2002). THz radiation from free electron lasers and its potential for cell and tissue studies, *Physics in Medicine and Biology*, **47**(21), pp. 3755–3760. 2.7.2

GUO-B, WANG-Y, PENG-C, ZHANG-H, LUO-G, LE-H, GMACHL-C, SIVCO-D, PEABODY-M AND CHO-A (2004). Laser-based mid-infrared reflectance imaging of biological tissues, *Optics Express*, **12**(1), pp. 208–219. 4.3.2, 4.8

GYROTRON TEHCNOLOGY INC. (2008). *What is Gyrotron Technology?*, Bensalem, PA, USA, <http://www.gyrotrontech.com/>, (Accessed: 2008-10-21). 2.6.1

HADAMARD-J (1923). *Lectures on Cauchys Problem in Linear Partial Differential Equations*, Oxford University Press, Oxford, UK. A.4

HADJILOUCAS-S, KARATZAS-L AND BOWEN-J (1999). Measurements of leaf water content using terahertz radiation, *IEEE Transactions on Microwave Theory and Techniques*, **47**(2), pp. 142–149. 5.1

HAFNER-C (1995). Multiple multipole program computation of periodic structures, *Journal of the Optical Society of America A: Optics and Image Science, and Vision*, **12**(5), pp. 1057–1067. 8.10

HAFNER-C (1999). *The Multiple Multipole Program (MMP) and the Generalized Multipole Technique (GMT), Generalized Multipole Techniques for Electromagnetic and Light Scattering*, Elsevier Science B.V., Amsterdam, The Netherlands, pp. 21–38. 8.10

HALL-R, FENNER-G, KINGSLEY-J, SOLTYS-T AND CARLSON-R (1962). Coherent light emission from GaAs junctions, *Physical Review Letters*, **9**(9), pp. 366–368. 2.4.1

HALL-W (1998). The safety and efficacy of stereotactic biopsy for intracranial lesions, *Cancer*, **82**(9), pp. 1749–1755. 75

HAMPEL-H AND BUERGER-K (2006). *Biomarkers in Blood and Cerebrospinal Fluid*, The Dementias: Early Diagnosis and Evaluation, Taylor & Francis Group, New York, NY, USA, pp. 73–107. 6.2.2

HANDLEY-J, FITZGERALD-A, BERRY-E AND BOYLE-R (2002). Wavelet compression in medical terahertz pulsed imaging, *Physics in Medicine and Biology*, **47**(21), pp. 3885–3892. 1.4.2

HANGYO-M, TOMOZAWA-S, MURAKAMI-Y, TONOUCHI-M, TANI-M, WANG-Z, SAKAI-K AND NAKASHIMA-S (1996). Terahertz radiation from superconducting $YBa_2Cu_3O_{7-\delta}$ thin films excited by femtosecond optical pulses, *Applied Physics Letters*, **69**(14), pp. 2122–2124. 3.8.3

HANNAY-H, HOWIESON-D, LORING-D, FISCHER-J AND LEZAK-M (2004). *Neuropathology for Neuropsychologists*, Neuropsychological Assessment, 4th edn, Oxford University Press, New York, NY, USA, pp. 157–285. E.2

HAN-P AND ZHANG-X.-C (1998). Coherent, broadband midinfrared terahertz beam sensors, *Applied Physics Letters*, **73**(21), pp. 3049–3051. 3.10

HAN-P, CHO-G AND ZHANG-X.-C (2000). Time-domain transillumination of biological tissues with terahertz pulses, *Optics Letters*, **25**(4), pp. 242–244. 8.1

HARWOOD-L, MOODY-C AND PERCY-J (1999). *Experimental Organic Chemistry: Standard and Microscale*, Blackwell Science Ltd., Oxford, UK. 4.3, 4.3, 4.1

HASTED-J, HUSAIN-S, FRESCURA-F AND BIRCH-J (1985). Far-infrared absorption in liquid water, *Chemical Physics Letters*, **118**(6), pp. 622–625. 6

HASTED-J, HUSAIN-S, FRESCURA-F AND BIRCH-J (1987). The temperature variation of the near millimetre wavelength optical constants of water, *Infrared Physics*, **27**(1), pp. 11–15. 7, 9.4.1

HAWRYSZ-D AND SEVICK-MURACA-E (2000). Developments toward diagnostic breast cancer imaging using near-infrared optical measurements and fluorescent contrast agents, *Neoplasia*, **2**(5), pp. 388–417. 4.3.2

HAYASHI-I, PANISH-M, FOY-P AND SUMSKI-S (1970). Junction lasers which operate continuously at room temperature, *Applied Physics Letters*, **17**(3), pp. 109–111. 2.4.1

HEBDEN-J (2003). Advances in optical imaging of the newborn infant brain, *Psychophysiology*, **40**(4), pp. 201–510. 4.3.2, 4.7

HEBDEN-J, GIBSON-A, YUSOF-R, EVERDELL-N, HILLMAN-E, DELPY-D, ARRIDGE-S, AUSTIN-T, MEEK-J AND WYATT-J (2002). Three-dimensional optical tomography of the premature infant brain, *Physics in Medicine and Biology*, **47**(23), pp. 4155–4166. 4.3.2, 4.7

HEBEL-R AND STROMBERG-M (1986). *Anatomy and Embryology of the Laboratory Rat*, BioMed Verlag, Wörthsee, Germany. 5.5.5

HECHT-E (2002). *Optics*, 4th edn, Addison-Wesley Publishing Company, San Francisco, CA, USA. 30, 3.4, 3.7.4, 8.5.2, 9.3, 79, A.3.1, D.1, F.7

HE-G AND LIU-S (1999). *Physics of Nonlinear Optics*, World Scientific, Singapore. 3.3.1

HE-M, AZAD-A, YE-S AND ZHANG-W (2006). Far-infrared signature of animal tissues characterized by terahertz time-domain spectroscopy, *Optics Communications*, **259**(1), pp. 389–392. 4.5.4

HERAUD-P, CAINE-S, SANSON-G, GLEADOW-R, WOOD-B AND MCNAUGHTON-D (2007). Focal plane array infrared imaging: a new way to analyse leaf tissue, *New Phytologist*, **173**(1), pp. 216–225. 4.3.2

HERSCHEL-W (1800a). Experiments on the solar, and on the terrestrial rays that occasion heat; with a comparative view of the laws to which light and heat, or rather the rays which occasion them, are subject, in order to determine whether they are the same, or different. Part I, *Philosophical Transactions of the Royal Society of London*, **90**, pp. 293–326. 1.3.1

HERSCHEL-W (1800b). Experiments on the solar, and on the terrestrial rays that occasion heat; with a comparative view of the laws to which light and heat, or rather the rays which occasion them, are subject, in order to determine whether they are the same, or different. Part II, *Philosophical Transactions of the Royal Society of London*, **90**, pp. 437–538. 1.3.1

HERSCHEL-W (1800c). Investigation of the powers of the prismatic colours to heat and illuminate objects; with remarks, that prove the different refrangibility of radiant heat. to which is added, an inquiry into the method of viewing the sun advantageously, with telescopes of large apertures and high magnifying powers, *Philosophical Transactions of the Royal Society of London*, **90**, pp. 255–283. 1.3.1

HERTZ-H (1893). *On Very Rapid Electric Oscillations*, Electric Waves, Macmillan & Co., London, UK, pp. 29–53. 3.10

HINES-M AND FOEGEDING-E (1993). Interactions of α-lactalbumin and bovine serum-albumin with β-lactoglobulin in thermally induced gelation, *Journal of Agricultural and Food Chemistry*, **41**(3), pp. 341–346. 7.3.1

HO-L, MÜLLER-R, GORDON-K, KLEINEBUDDE-P, PEPPER-M, RADES-T, SHEN-Y, TADAY-P AND ZEITLER-A (2008). Applications of terahertz pulsed imaging to sustained-release tablet film coating quality assessment and dissolution performance, *Journal of Controlled Release*, **127**(1), pp. 79–87. 1.3.2

HOLOGIC INC. (2008). *The ThinPrep Pap Test*, Marlborough, MA, USA, <http://www.thinprep.com/>, (Accessed: 2009-02-03). 4.3.2

HOLONYAK JR.-N AND BEVACQUA-S (1962). Coherent (visible) light emission from $Ga(As_{1-x}P_x)$ junctions, *Applied Physics Letters*, **1**(4), pp. 82–83. 2.4.1

HORE-P (1995). *Nuclear Magnetic Resonance*, Oxford Chemistry Primers, Oxford University Press, Oxford, England. 1.1, 4.3

HOR-Y, FEDERICI-J AND WAMPLE-R (2008). Nondestructive evaluation of cork enclosures using terahertz/millimeter wave spectroscopy and imaging, *Applied Optics*, **47**(1), pp. 72–78. 1.3.2, 8.1

HOSHINA-H, HAYASHI-A, MIYOSHI-N, MIYAMARU-F AND OTANI-C (2009). Terahertz pulsed imaging of frozen biological tissues, *Applied Physics Letters*, **94**(12), article number 123901. 6.1.2

HSIANG-T, WHITAKER-J, SOBOLEWSKI-R, DYKAAR-D AND MOUROU-G (1987). Propagation characteristics of picosecond electrical transients on coplanar striplines, *Applied Physics Letters*, **51**(19), pp. 1551–1553. 3.8.3

HUANG-F, SCHULKIN-B, ALTAN-H, FEDERICI-J, GARY-D, BARAT-R, ZIMDARS-D, CHEN-M AND TANNER-D (2004). Terahertz study of 1,3,5-trinitro-s-triazine by time-domain and Fourier transform infrared spectroscopy, *Applied Physics Letters*, **85**(23), pp. 5535–5537. 4.5.3

HUANG-J.-Y, GONG-S.-H AND WANG-F (2005). *Optimal Scattering Polarization Characteristic for Cylinder Target in Rain at Millimeter Wave Band*, EMW Publishing. 8.2

HU-B AND NUSS-M (1995). Imaging with terahertz waves, *Optics Letters*, **20**(16), pp. 1716–1718. 1.3.2, 1.4.2, 7, 1.4, 1.5, 5.1

HU-B, DARROW-J, ZHANG-X.-C, AUSTON-D AND SMITH-P (1990a). Optically steerable photoconducting antennas, *Applied Physics Letters*, **56**(10), pp. 886–888. 3.8.3

HU-B, ZHANG-X.-C, AUSTON-D AND SMITH-P (1990b). Free-space radiation from electro-optic crystals, *Applied Physics Letters*, **56**(6), pp. 506–508. 3.6

HUDSON-H, DAUBERT-C AND FOEGEDING-E (2000). Rheological and physical properties of derivitized whey protein isolate powders, *Journal of Agricultural and Food Chemistry*, **48**(8), pp. 3112–3119. 7.3.1, 7.4

HUNSCHE-S, KOCH-M, BRENER-I AND NUSS-M (1998). THz near-field imaging, *Optics Communications*, **150**(1-6), pp. 22–26. 4.5.2

HURT-W (1985). Multiterm debye dispersion-relations for permittivity of muscle, *IEEE Transactions on Biomedical Engineering*, **32**(1), pp. 60–64. 9.4.2

HUSAIN-S, HASTED-J, ROSEN-D, NICOL-E AND BIRCH-J (1984a). FIR spectra of amino acids and related molecules, *Infrared Physics*, **24**(2-3), pp. 201–208. 4.5.2

HUSAIN-S, HASTED-J, ROSEN-D, NICOL-E AND BIRCH-J (1984b). FIR spectra of saccharides and polysaccharides, *Infrared Physics*, **24**(2-3), pp. 209–213. 4.5.2

HYMAS-W, STEVENSON-J, TAGGART-E AND HILLYARD-D (2005). Use of lyophilized standards for the calibration of a newly developed real time PCR assay for human herpes type six (HHV6) variants A and B, *Journal of Virological Methods*, **128**(1-2), pp. 143–150. 5.5.2

IDEHARA-T, TSUCHIYA-H, AGUSU-L, MITSUDO-S, MURASE-H, MORI-H, KANEMAKI-T AND SAITO-T (2006). Development of a THz gyrotron with 20 T pulsed magnet, *Proc. Yamada Conference LX on Research in High Magnetic Fields*, 16–19 August 2006, Sendai Civic Auditorium, Sendai, Japan, pp. 553–556. 2.6.1

INGRAM-D (1967). *Spectroscopy at Radio and Microwave Frequencies*, 2nd edn, Butterworth & Co., London, UK. 4.2, 4.4

ISHIHARA-K, OHASHI-K, IKARI-T, MINAMIDE-H, YOKOYAMA-H, I. SHIKATA-J AND ITO-H (2006). Terahertz-wave near-field imaging with subwavelength resolution using surface-wave-assisted bow-tie aperture, *Applied Physics Letters*, **89**(20), article number 201120. 3.8.3

JACK JR.-C, WENGENACK-T, REYES-D, GARWOOD-M, CURRAN-G, BOROWSKI-B, LIN-J, PREBOSKE-G, HOLASEK-S, ADRIANY-G AND PODUSLO-J (2005). *In Vivo* magnetic resonance microimaging of individual amyloid plaques in Alzheimer's transgenic mice, *The Journal of Neuroscience*, **25**(43), pp. 10041–10048. 6.2.2

JACKSON-J (1975). *Classical Electrodynamics*, 2nd edn, John Wiley & Sons, New York, NY, USA. 3.8.1, 5.2.3, 53, D.1

JACKSON-J, MOUROU-M, WHITAKER-J, DULING III-I, WILLIAMSON-S, MENU-M AND MOUROU-G (2008). Terahertz imaging for non-destructive evaluation of mural paintings, *Optics Communications*, **281**(4), pp. 527–532. 1.3.2

JAVAN-A (1959). Possibility of production of negative temperature in gas discharges, *Physical Review Letters*, **3**(2), pp. 87–89. 2.3

JAVAN-A, BENNETT JR.-W AND HERRIOTT-D (1961). Population inversion and continuous optical maser oscillation in a gas discharge containing a He-Ne mixture, *Physical Review Letters*, **6**(3), pp. 106–110. 2.3

JEFFERSON LAB (2008). *Bright Light/Dark Matter*, Newport News, VA, USA, <http://www.jlab.org/news/articles/homepics_2008.html>, (Accessed: 2008-10-27). 2.15

JEPSEN-P AND FISCHER-B (2005). Dynamic range in terahertz time-domain transmission and reflection spectroscopy, *Optics Letters*, **30**(1), pp. 29–31. 4.5.2, 5.4.1

JEPSEN-P AND KEIDING-S (1995). Radiation patterns from lens-coupled terahertz antennas, *Optics Letters*, **20**(8), pp. 807–809. 3.8.1, 3.8.3

JEPSEN-P, JACOBSEN-R AND KEIDING-S (1996). Generation and detection of terahertz pulses from biased semiconductor antennas, *Journal of the Optical Society of America B: Optical Physics*, **13**(11), pp. 2424–2436. 3.8.1, 3.8.3

JIANG-J AND WU-D (2004). Ice and water permittivities for millimeter and sub-millimeter remote sensing applications, *Atmospheric Science Letters*, **5**(7), pp. 146–151. 9.4.1

JIANG-Z, LI-M AND ZHANG-X.-C (2000). Dielectric constant measurement of thin films by differential time-domain spectroscopy, *Applied Physics Letters*, **76**(22), pp. 3221–3223. 4.5.2

JIAN-Z, PEARCE-J AND MITTLEMAN-D (2003). Characterizing individual scattering events by measuring the amplitude and phase of the electric field diffusing through a random medium, *Physical Review Letters*, **91**(3), article number 033903. 8.1

JÖBSIS-F (1977). Noninvasive, infrared monitoring of cerebral and myocardial oxygen sufficiency and circulatory parameters, *Science*, **198**(4323), pp. 1264–1267. 4.3.2, 4.3.2

JOHNSON-A AND AUSTON-D (1975). Microwave switching by picosecond photoconductivity, *IEEE Journal of Quantum Electronics*, **11**(6), pp. 283–287. 1.3.2, 33

JOHNSON-J, DORNEY-T AND MITTLEMAN-D (2001). Interferometric imaging with terahertz pulses, *IEEE Journal of Selected Topics in Quantum Electronics*, **7**(4), pp. 592–599. 1.3.2

JOHNSTON-M, WHITTAKER-D, DOWD-A, DAVIES-A, LINFIELD-E, LI-X AND RITCHIE-D (2002). Generation of high-power terahertz pulses in a prism, *Optics Letters*, **27**(21), pp. 1935–1937. 3.11

JONES-B (1998). A reappraisal of the use of infrared thermal image analysis in medicine, *IEEE Transactions on Medical Imaging*, **17**(6), pp. 1019–1027. 4.3.2

JUDENHOFER-M, WEHRL-H, NEWPORT-D, CATANA-C, SIEGEL-S, BECKER-M, THIELSCHER-A, KNEILLING-M, LICHY-M, EICHNER-M, KLINGEL-K, REISCHL-G, WIDMAIER-S, RÖCKEN-M, NUTT-R, MACHULLA-H.-J, ULUDAG-K, CHERRY-S, CLAUSSEN-C AND PICHLER-B (2008). Simultaneous PET-MRI: a new approach for functional and morphological imaging, *Nature Medicine*, **14**(4), pp. 459–465. 61

KALITEEVSKI-M, BEGGS-D, BRAND-S, ABRAM-R, FLETCHER-J, SWIFT-G AND CHAMBERLAIN-J (2006). Propagation of electromagnetic waves through a system of randomly placed cylinders: the partial scattering wave resonance, *Journal of Modern Optics*, **53**(14), pp. 2089–2097. 8.1

KAMINOW-I (1974). *An Introduction to Electrooptic Devices*, Academic Press, New York, NY, USA. 3.4.1, B.1.1, B.3, B.4

KAMINOW-I AND TURNER-E (1971). *Linear Electrooptical Materials*, Handbook of Lasers with Selected Data on Optical Technology, CRC Press, Cleveland, OH, USA, pp. 447–459. 3.4.1, 3.4.1

KARIN-J, DOWNEY-P AND MARTIN-R (1986). Radiation from picosecond photoconductors in microstrip transmission lines, *IEEE Journal of Quantum Electronics*, **22**(5), pp. 677–681. 3.8

KAŠALYNAS-I, SELIUTA-D, TAMOŠIŪNAS-V, MACUTKEVIČ-J, BALAKAUSKAS-S, VALUŠIS-G AND KÖHLER-K (2009). Terahertz GaAs/AlGaAs- and InGaAs-based bow-tie diodes: spectral features and applications for imaging, *Journal of Physics: Conference Series*, **193**, article number 012077. 3.13

KATZENELLENBOGEN-N AND GRISCHKOWSKY-D (1991). Efficient generation of 380 fs pulses of THz radiation by ultrafast laser pulse excitation of a biased metal-semiconductor interface, *Applied Physics Letters*, **58**(3), pp. 222–224. 3.8.3

KAVANAGH-G, CLARK-A AND ROSS-MURPHY-S (2000). Heat-induced gelation of globular proteins: part 3. molecular studies on low pH β-lactoglobulin gels, *International Journal of Biological Macromolecules*, **28**(1), pp. 41–50. 7.3.2

KAWASE-K, OGAWA-Y AND WATANABE-Y (2003). Non-destructive terahertz imaging of illicit drugs using spectral fingerprints, *Optics Express*, **11**(20), pp. 2549–2554. 1.3.2, 4.5.3

KEMP-M, TADAY-P, COLE-B, CLUFF-J, FITZGERALD-A AND TRIBE-W (2003). Security applications of terahertz technology, *Proc. SPIE Terahertz for Military and Security Applications*, **5070**, Eds: R. Hwu and D. Woolard, 21 April 2003, Orlando, FL, USA, pp. 44–52. 1.3.2

KERKER-M (1969). *Scattering of Light and Other Electromagnetic Radiation*, Physical Chemistry, Academic Press, New York, USA. 8.3.2, 8.3.2

KETCHEN-M, GRISCHKOWSKY-D, CHEN-T, CHI-C.-C, DULING III-I, HALAS-N, HALBOUT-J.-M, KASH-J AND LI-G (1986). Generation of subpicosecond electrical pulses on coplanar transmission lines, *Applied Physics Letters*, **48**(12), pp. 751–753. 3.8.1, 3.12

KHAZAN-M (2002). *Time-Domain Terahertz Spectroscopy and its Application to the Study of High-T_c Superconductor Thin Films*, PhD thesis, University of Hamburg. 3.7.4

KIM-J, XIA-M AND LIU-H (2005). Extinction coefficients of hemoglobin for near-infrared spectroscopy of tissue, *IEEE Engineering in Medicine and Biology*, **24**(2), pp. 118–121. 4.3.2

KIMMIT-M (2003). Restrahlen to T-Rays—100 years of terahertz radiation, *Journal of Biological Physics*, **29**(2-3), pp. 77–85. 1.3.1

KIM-S, HATAMI-F, HARRIS-J, KURIAN-A, FORD-J, SCALARI-G, GIOVANNINI-M, HOYLER-N, FAIST-J AND HARRIS-G (2006). Biomedical terahertz imaging with a quantum cascade laser, *Applied Physics Letters*, **88**(15), article number 153903. 2.4.1, 2.8

KINCADE-K (2000). Terahertz technology may improve medical imaging, *Laser Focus World*, **36**(5), pp. 123–125. 4.5.4

KINDT-J AND SCHMUTTENMAER-C (1996). Far-infrared dielectric properties of polar liquids probed by femtosecond terahertz pulse spectroscopy, *Journal of Physical Chemistry*, **100**, pp. 10373–10379. 4.5.1, 9.4.1, 9.4.2

KINDT-J AND SCHMUTTENMAER-C (1997). Far-infrared absorption spectra of water, ammonia, and chloroform calculated from instantaneous normal mode theory, *Journal of Chemical Physics*, **106**(11), pp. 4389–4400. 4.5.1

KINDT-J AND SCHMUTTENMAER-C (1999). Theory for determination of the low-frequency time-dependent response function in liquids using time-resolved terahertz pulse spectroscopy, *Journal of Chemical Physics*, **110**(17), pp. 8589–8596. 4.5.1

KIRSCH-A (1996). *An Introduction to the Mathematical Theory of Inverse Problems*, Applied Mathematical Sciences, Springer-Verlag, New York, USA. A.4, A.4

KISTNER-C, ANDRE-A, FISCHER-T, THOMA-A, JANKE-C, BARTELS-A, GISLER-T, MARET-G AND DEKORSY-T (2007). Hydration dynamics of oriented DNA films investigated by time-domain terahertz spectroscopy, *Applied Physics Letters*, **90**(23), article number 233902. 7.1

KLEINE-OSTMANN-T, JANSEN-C, PIESIEWICZ-R, MITTLEMAN-D, KOCH-M AND KÜRNER-T (2007). Propagation modeling based on measurements and simulations of surface scattering in specular direction, *Proc. Joint 32nd International Conference on Infrared and Millimetre Waves, and 15th International Conference on Terahertz Electronics (IRMMW-THz)*, **1**, Eds: M. Griffin, P. Hargrave, T. Parker and K. Wood, 3–7 September 2007, Cardiff, UK, pp. 408–410. 8.1

KLEINMAN-D (1962). Nonlinear dielectric polarization in optical media, *Physical Review*, **126**(6), pp. 1977–1979. 3.5

KLEINMAN-D AND AUSTON-D (1984). Theory of electrooptic shock radiation in nonlinear optical media, *IEEE Journal of Quantum Electronics*, **20**(8), pp. 964–970. 3.4.2, 3.6

KLUNK-W, ENGLER-H, NORDBERG-A, WANG-Y, BLOMQVIST-G, HOLT-D, BERGSTROM-M, SAVITCHEVA-I, F. HUANG-G, ESTRADA-S, AUSÈN-B, DEBNATH-M, BARLETTA-J, PRICE-J, SANDELL-J, LOPRESTI-B, WALL-A, KOIVISTO-P, ANTONI-G, MATHIS-C AND LÅNGSTRÖM-B (2004). Imaging brain amyloid in Alzheimer's disease with Pittsburgh compound-B, *Annals of Neurology*, **55**(3), pp. 306–319. 6.2.2, 6.4

KNAB-J, CHEN-J.-Y AND MARKELZ-A (2006). Hydration dependence of conformational dielectric relaxation of lysozyme, *Biophysical Journal*, **90**(7), pp. 2576–2581. 4.5.2, 7.1

KNAB-J, CHEN-J.-Y, HE-Y AND MARKELZ-A (2007). Terahertz measurements of protein relaxational dynamics, *Proceedings IEEE*, **95**(8), pp. 1605–1610. 1.4.1, 4.5.2

KNAB-J, SHAH-B, CHEN-J.-Y AND MARKELZ-A (2005). Critical hydration and temperature effects on terahertz biomolecular sensing, *Proc. Chemical and Biological Standoff Detection III*, **5995**, Eds: J. Jensen and J.-M. Thériault, 2005-11-04, Boston, MA, USA, article number 59950P. 7.1

KNOBLOCH-P, SCHILDKNECHT-C, KLEINE-OSTMANN-T, KOCH-M, HOFFMANN-S, HOFMANN-M, REHBERG-E, SPERLING-M, DONHUIJSEN-K, HEIN-G AND PIERZ-K (2002). Medical THz imaging: an investigation of histo-pathological samples, *Physics in Medicine and Biology*, **47**(21), pp. 3875–3884. 1.4.2, 4.5.4, 4.6

KNOBLOCH-P, SCHMALSTIEG-K, KOCH-M, REHBERG-E, VAUTI-F AND DONHUIJSEN-K (2001). THz imaging of histo-pathological samples, *Proc. SPIE Hybrid and Novel Imaging and New Optical Instrumentation for Biomedical Applications*, **4434**, Eds: A.-C. Boccara and A. Oraevsky, 18–21 June 2001, Munich, Germany, pp. 239–245. 1.4.2, 1.6, 4.5.4, 4.6

KNOPMAN-D AND JANKOWIAK-J (2005). Recovery from dementia: An interesting case, *Neurology*, **64**(4), pp. E18–E19. 6.2.2

KNOTT-E, SHAEFFER-J AND TULEY-M (2004). *Radar Cross Section*, The SciTech Radar and Defense Series, 2nd edn, SciTech Publishing Inc., Rayleigh, NC, USA. 7.5.1, 8.3.2

KÖHLER-R, TREDICUCCI-A, BELTRAM-F, BEERE-H, LINFIELD-E, DAVIES-A, RITCHIE-D, IOTTI-R AND ROSSI-F (2002). Terahertz semiconductor-heterostructure laser, *Nature*, **417**, pp. 156–159. 2.4.1

KOHNO-T, KOBAYASHI-K, MAEDA-T, SATO-K AND TAKASHIMA-A (1996). Three-dimensional structures of the amyloid beta peptide (25-35) in membrane-mimicking environment, *Biochemistry*, **35**(50), pp. 16094–16104. 4.14

KOJIMA-S, KITAHARA-H, NISHIZAWA-S, YANG-Y AND TAKEDA-M (2005). Terahertz time-domain spectroscopy of low-energy excitations in glasses, *Journal of Molecular Structure*, **744-747**, pp. 243–246. 8.6.1

KOLNER-B AND BLOOM-D (1986). Electrooptic sampling in GaAs integrated circuits, *IEEE Journal of Quantum Electronics*, **22**(1), pp. 79–93. 3.8.3

KOMPFNER-R (1952). *Backward Wave Tube*, US patent number 2,985,790, date issued: 1961-05-23. 23

KOSMAS-P, RAPPAPORT-C AND BISHOP-E (2004). Modeling with the FDTD method for microwave breast cancer detection, *IEEE Transactions on Antennas and Propagation*, **52**(8), pp. 1890–1897. 4.4.2

KRAMERS-H (1927). La diffusion de la Lumiere par les Atomes, *Atti del Congresso Internazionale dei Fisici (Transactions of Volta Centenary Congress at Como)*, **2**, pp. 545–557. 54

KREBS-M, DEVLIN-G AND DONALD-A (2007). Protein particulates: Another generic form of protein aggregation?, *Biophysical Journal*, **92**(4), pp. 1336–1342. 7.2, 7.3.2, 7.3, 7.4.2

KRESSEL-H AND NELSON-H (1969). Close-confinement gallium arsenide pn junction lasers with reduced optical loss at room temperature, *RCA Review*, **30**(1), pp. 106–114. 2.4.1

KRISTENSEN-T, WITHAYACHUMNANKUL-W, JEPSEN-P AND ABBOTT-D (2010). Modeling terahertz heating effects on water, *Optics Express*, **18**(5), pp. 4727–4739. 9.6

KRÖKEL-D, GRISCHKOWSKY-D AND KETCHEN-M (1989). Subpicosecond electrical pulse generation using photoconductive switches with long carrier lifetimes, *Applied Physics Letters*, **54**(11), pp. 1046–1047. 3.8.3

KRONIG-R (1926). On the theory of dispersion of X-rays, *Optical Society of America*, **12**(6), pp. 547–558. 54

KURTH-C, LIU-H, THAYER-W AND CHANCE-B (1995). A dynamic phantom brain model for near-infrared spectroscopy, *Physics in Medicine and Biology*, **40**(12), pp. 2079–2092. 4.3.2

LAMAN-N, HARSHA-S, GRISCHKOWSKY-D AND MELINGER-J (2008). High-resolution waveguide THz spectroscopy of biological molecules, *Biophysical Journal*, **94**(3), pp. 1010–1020. 4.5.2

LAND-D AND CAMPBELL-A (1992). A quick accurate method for measuring the microwave dielectric properties of small tissue samples, *Physics in Medicine and Biology*, **37**(1), pp. 183–192. 4.4.1

LAWRENCE-E AND LIVINGSTON-M (1932). Production of high speed light ions without use of high voltages, *Physical Review*, **40**(1), pp. 19–35. 17

LE BON-C, NICOLAI-T AND DURAND-D (1999). Kinetics of aggregation and gelation of globular proteins after heat-induced denaturation, *Macromolecules*, **32**(19), pp. 6120–6127. 7.2

LEE-B, BELKIN-M AND CAPASSO-F (2008). Array of tiny quantum cascade lasers provides tunable mid-IR output, *Photonics Spectra*, **42**(5), p. 70. 2.6, 2.4.1

LEE-C (1977). Picosecond optoelectronic switching in GaAs, *Applied Physics Letters*, **30**(2), pp. 84–86. 3.8.3

LEE-C, ANTONETTI-A AND MOUROU-G (1977). Measurements on the photoconductive lifetime of carriers in GaAs by optoelectronic gating technique, *Optics Communications*, **21**(1), pp. 158–161. 3.5.1, 3.8.3

LEE-T.-W AND HAGNESS-S (2004). Pseudospectral time-domain methods for modeling optical wave propagation in second-order nonlinear materials, *Journal of the Optical Society of America B*, **21**(2), pp. 330–342. 9.7.1

LEFÈVRE-T AND SUBIRADE-M (2000). Molecular differences in the formation and structure of fine-stranded and particulate β-lactoglobulin gels, *Biopolymers*, **54**(7), pp. 578–586. 7.1, 7.3.2

LEONBERGER-F AND MOULTON-P (1979). High-speed InP optoelectronic switch, *Applied Physics Letters*, **35**(9), pp. 712–714. 3.5.1

LITCHFIELD-S AND NAGY-Z (2001). New temperature modification makes the Bielschowsky silver stain reproducible, *Acta Neuropathologica*, **101**(1), pp. 17–21. 6.3.1

LITVAK-A (2008). High power gyrotrons: development and applications, *Proc. 33rd International Conference on Infrared, Millimeter, and Terahertz Waves*, 15–19 September 2008, Pasadena, CA, USA, article number 1734. 2.6.1

LIU-H, PLOPPER-G, EARLEY-S, CHEN-Y, FERGUSON-B AND ZHANG-X.-C (2007). Sensing minute changes in biological cell monolayers with THz differential time-domain spectroscopy, *Biosensors & Bioelectronics*, **22**(6), pp. 1075–1080. 4.5.4

LIU-K, KANG-H.-S, KIM-T.-K AND ZHANG-X.-C (2002). Study of ZnCdTe crystals as terahertz wave emitters and detectors, *Applied Physics Letters*, **81**(22), pp. 4115–4117. B.2

LIU-K, XU-J AND ZHANG-X.-C (2004). GaSe crystals for broadband terahertz wave detection, *Applied Physics Letters*, **85**(6), pp. 863–865. B.2

LIU-L, MATITSINE-S, GAN-Y AND ROZANOV-K (2005). Effective permittivity of planar composites with randomly or periodically distributed conducting fibers, *Journal of Applied Physics*, **98**, article number 063512. 8.7

LIU-Q (1997). The PSTD algorithm: A time-domain method requiring only two cells per wavelength, *Microwave and Optical Technology Letters*, **15**(3), pp. 158–165. 9.7.1

LIU-Q (1999a). A frequency-dependent PSTD algorithm for general dispersive media, *IEEE Microwave and Guided Wave Letters*, **9**(2), pp. 51–53. 9.7.1

LIU-Q (1999b). Large-scale simulations of electromagnetic and acoustic measurements using the pseudospectral time-domain (PSTD) algorithm, *IEEE Transactions on Geoscience and Remote Sensing*, **37**(2), pp. 917–926. 9.7.1

LIU-Q (1999c). PML and PSTD algorithm for arbitrary lossy anisotropic media, *IEEE Microwave and Guided Wave Letters*, **9**(2), pp. 48–50. 9.7.1

LIU-Q AND FAN-G.-X (1999). Simulations of GPR in dispersive media using a frequency-dependent PSTD algorithm, *IEEE Transactions on Geoscience and Remote Sensing*, **37**(5), pp. 2317–2324. 9.7.1

LI-X AND HAGNESS-S (2001). A confocal microwave imaging algorithm for breast cancer detection, *IEEE Microwave and Wireless Components Letters*, **11**(3), pp. 130–132. 20

LI-X, DAVIS-S, HAGNESS-S, VAN DER WEIDE-D AND VEEN-B. V (2004). Microwave imaging via space-time beamforming: Experimental investigation of tumor detection in multilayer breast phantoms, *IEEE Transactions on Microwave Theory and Techniques*, **52**(8), pp. 1856–1865. 20

LO-C, HSIEH-C.-F, PAN-R.-P AND PAN-C.-L (2005). Effects of hole material on enhanced terahertz transmission through metallic hole arrays, *Proc. LEOS*, Eds: D. Mittleman, A. Braun, J. Feldmann, D. Kim, D. Leaird, M. Mielke and J. Shan, Sydney, NSW, Australia, pp. 983–984. A.2, A.2

LOEFFLER TECHNOLOGY GMBH (2008). *SynViewScan 300*, Glashütten, Germany, <http://www.loeffler-technology.de/mediapool/54/542811/data/SynViewScan_300_final.pdf>, (Accessed: 2008-11-24). 2.1

LOEWENSTEIN-E (1966). The history and current status of fourier transform spectroscopy, *Applied Optics*, **5**(5), pp. 845–854. 1.4

LÖFFLER-T, BAUER-T, SIEBERT-K, ROSKOS-H, FITZGERALD-A AND CZASCH-S (2001). Terahertz dark-field imaging of biomedical tissue, *Optics Express*, **9**(12), pp. 616–621. 1.4.2

LÖFFLER-T, SIEBERT-K, CZASCH-S, BAUER-T AND ROSKOS-H (2002). Visualization and classification in biomedical terahertz pulsed imaging, *Physics in Medicine and Biology*, **47**, pp. 3847–3852. 1.4.2

LÖFFLER-T, SIEBERT-K, QUAST-H, HASEGAWA-N, LOATA-G, WIPF-R, HAHN-T, THOMSON-M, LEONHARDT-R AND ROSKOS-H (2004). All-optoelectronic continuous-wave terahertz systems, *Philosophical Transactions of the Royal Society A: Mathematical, Physical and Engineering Sciences*, **362**(1815), pp. 263–279. 1.4.2

LÜHRS-T, RITTER-C, ADRIAN-M, RIEK-LOHER-D, BOHRMANN-B, DÖBELI-H, SCHUBERT-D AND RIEK-R (2005). 3D structure of Alzheimers amyloid-β(1-42) fibrils, *Proceedings of the National Academy of Sciences of the United States of America*, **102**(48), pp. 17342–17347. 6.3

LU-J, HU-X.-H AND DONG-K (2000). Modeling of the rough-interface effect on a converging light beam propagating in a skin tissue phantom, *Applied Optics*, **39**(31), pp. 5890–5897. 4.3.2, 9.2

LU-J.-Y, KUO-C.-C, CHIU-C.-M, CHEN-H.-W, HWANG-Y.-J, PAN-C.-L AND SUN-C.-K (2008). THz interferometric imaging using subwavelength plastic fiber based THz endoscopes, *Optics Express*, **16**(4), pp. 2494–2501. 4.5.4

LUTZ-C AND DEFONZO-A (1989). Far-field characteristics of optically pulsed millimeter wave antennas, *Applied Physics Letters*, **54**(22), pp. 2186–2188. 3.8.3

MACDONALD-D, KABANI-N, AVIS-D AND EVANS-A (2000). Automated 3-D extraction of inner and outer surfaces of cerebral cortex from MRI, *NeuroImage*, **12**(3), pp. 340–356. 6.4.2

MACKENZIE-I (2007). *Neuropathology of Alzheimer's disease*, Atlas of Alzheimer's Disease, Informa UK Ltd, London, UK, pp. 71–81. 57, 6.2

MAIMAN-T (1960a). Optical and microwave-optical experiments in ruby, *Physical Review Letters*, **4**(11), pp. 564–566. 1.3.1

MAIMAN-T (1960b). Stimulated optical radiation in ruby, *Nature*, **187**(4736), pp. 493–494. 1.3.1

MAIR-S, GOMPF-B AND DRESSEL-M (2002). Microspectroscopy and imaging in the THz range using coherent CW radiation, *Physics in Medicine and Biology*, **47**(21), pp. 3719–3725. 4.5.2

MAKAROV-S AND PUZELLA-A (2007). Scan impedance for an infinite dipole array: Hansen's formulas compared with Ansoft HFSS simulations, *IEEE Antennas and Propagation Magazine*, **49**(4), pp. 143–156. 8.7

MALLOZZI-J (2003). Harnessing THz for medical applications, *R & D*, **45**(10), p. 28. 4.5.4

MARKELZ-A (2008). Terahertz dielectric sensitivity to biomolecular structure and function, *IEEE Journal of Selected Topics in Quantum Electronics*, **14**(1), pp. 180–190. 4.5.2, 7.1

MARKELZ-A, KNAB-J, CHEN-J AND HE-Y (2007). Protein dynamical transition in terahertz dielectric response, *Chemical Physics Letters*, **442**(4-6), pp. 413–417. 1.4.1, 4.5.2, 7.1

MARKELZ-A, ROITBERG-A AND HEILWEIL-E (2000). Pulsed terahertz spectroscopy of DNA, bovine serum albumin and collagen between 0.1 and 2.0 THz, *Chemical Physics Letters*, **320**(2000), pp. 42–48. 1.4.1, 4.5.2, 7.1

MARKELZ-A, WHITMIRE-S, HILLEBRECHT-J AND BIRGE-R (2002). THz time domain spectroscopy of biomolecular conformational modes, *Physics in Medicine and Biology*, **47**(21), pp. 3797–3805. 4.5.2

MARX-B (2002). Terahertz imaging - CW imager targets medicine, *Laser Focus World*, **38**(3), p. 32. 4.5.4

MASTERS-J (2002). HeLa cells 50 years on: the good, the bad and the ugly, *Nature Reviews Cancer*, **2**, pp. 315–319. 46

MATCHER-S, KIRKPATRICK-P, NAHID-K, COPE-M AND DELPY-D (1995). Absolute quantification methods in tissue near-infrared spectroscopy, *Proc. SPIE Optical Tomography, Photon Migration, and Spectroscopy of Tissue and Model Media: Theory, Human Studies, and Instrumentation*, **2389**, Eds: B. Chance and R. Alfano, May 1995, pp. 486–495. 4.3.2

MATEI-A AND DRESSEL-M (2003). Experimental determination of the far-infrared optical properties of biological matter in aqueous solution, *Journal of Biological Physics*, **29**(2-3), pp. 101–108. 4.5.2, 4.5.2

MATHIS-C, BACSKAI-B, KAJDASZ-S, MCLELLAN-M, FROSCH-M, HYMAN-B, HOLT-D, WANG-Y, HUANG-G.-F, DEBNATH-M AND KLUNK-W (2002). A lipophilic thioflavin-T derivative for positron emission tomography (PET) imaging of amyloid in brain, *Bioorganic & Medicinal Chemistry Letters*, **12**(3), pp. 295–298. 6.2.2

MATHIS-C, WANG-Y, HOLT-D, HUANG-G.-F, DEBNATH-M AND KLUNK-W (2003). Synthesis and evaluation of ^{11}C-labeled 6-substituted 2-arylbenzothiazoles as amyloid imaging agents, *Journal of Medicinal Chemistry*, **46**(13), pp. 2740–2754. 6.2.2

MATHWORKS, INC. (2010). *The MathWorks, Inc.*, The MathWorks, Inc., Natick, MA, USA, <http://www.mathworks.com/>, (Accessed: 2010-04-29). 7, 5.2.3

MATOUSEK-P, CLARK-I AND DRAPER-E (2005a). Subsurface probing in diffusely scattering media using spatially offset Raman spectroscopy, *Applied Spectroscopy*, **59**(4), pp. 393–400. 4.3

MATOUSEK-P, DRAPER-E AND GOODSHIP-A (2006). Noninvasive Raman spectroscopy of human tissue *in vivo*, *Applied Spectroscopy*, **60**(7), pp. 758–763. 4.3

MATOUSEK-P, MORRIS-M AND EVERALL-N (2005b). Numerical simulations of subsurface probing in diffusely scattering media using spatially offset Raman spectroscopy, *Applied Spectroscopy*, **59**(12), pp. 1485–1492. 4.3

MAXIMOV-A, CAPJACK-C, ROZMUS-W AND SHAO-Y (2001). Three-dimensional modelling of light scattering in biological tissue by the spectral method, *Proc. Optical Diagnostics of Living Cells IV*, **4260**, Eds: D. Farkas and R. Leif, 24–25 Jan 2001, San Jose, CA, USA, pp. 59–67. 9.2

MAZZURANA-M, SANDRINI-L, VACCARI-A, MALACARNE-C, CRISTOFORETTI-L AND PONTALTI-R (2003). A semi-automatic method for developing an anthropomorphic numerical model of dielectric anatomy by MRI, *Physics in Medicine and Biology*, **48**(19), pp. 3157–3170. 4.4.2

MCCUBBIN JR.-T AND SINTON-W (1950). Recent investigations in the far infrared, *Journal of the Optical Society of America*, **40**(8), pp. 537–539. 1.3.1, 1.4

MEEK-J (2002). Basic principles of optical imaging and application to the study of infant development, *Developmental Science*, **5**(3), pp. 371–380. 4.3.2

MELLES GRIOT (2007a). *Polarization Components*, Melles Griot, <http://www.mellesgriot.com/pdf/0012.-12.1.pdf>, (Accessed: 2008-11-05). 3.17

MELLES GRIOT (2007b). *Wollaston Prisms*, <http://www.mellesgriot.com/pdf/CatalogX/X_12_12.pdf>, (Accessed: 2008-11-05). 3.17

MENDAŠ-I AND CVIJIN-P. V (1983). Waveform of the amplitude modulated laser light by means of a mechanical chopper, *Applied Physics B (Photophysics and Laser Chemistry)*, **32**(3), pp. 119–122. 3.7.2

MENDIS-R (2006a). Guided-wave THz time-domain spectroscopy of highly doped silicon using parallel-plate waveguides, *Electronics Letters*, **42**(1), pp. 19–20. 3.11

MENDIS-R (2006b). Nature of subpicosecond terahertz pulse propagation in practical dielectric-filled parallel-plate waveguides, *Optics Letters*, **31**(17), pp. 2643–2645. 3.11

MENDIS-R (2007). THz transmission characteristics of dielectric-filled parallel-plate waveguides, *Journal of Applied Physics*, **101**(8), article number 083115. 3.11

MENDIS-R AND GRISCHKOWSKY-D (2000). Plastic ribbon THz waveguides, *Applied Physics B (Lasers and Optics)*, **88**(7), pp. 4449–4451. 3.11

MENDIS-R AND GRISCHKOWSKY-D (2001). Undistorted guided-wave propagation of subpicosecond terahertz pulses, *Optics Letters*, **26**(11), pp. 846–848. 3.11

MENDIS-R, SMITH-M, BIGNELL-L, VICKERS-R AND LEWIS-R (2005a). Strong terahertz emission from (100) *p*-type InAs, *Journal of Applied Physics*, **98**(12), article number 126104. 3.11

MENDIS-R, SYDLO-C, SIGMUND-J, FEIGINOV-M, MEISSNER-P AND HARTNAGEL-H (2004). Tunable CW-THz system with a log-periodic photoconductive emitter, *Solid-State Electronics*, **48**(10-11), pp. 2041–2045. 2.4

MENDIS-R, SYDLO-C, SIGMUND-J, FEIGINOV-M, MEISSNER-P AND HARTNAGEL-H (2005b). Coherent generation and detection of continuous terahertz waves using two photomixers driven by laser diodes, *International Journal of Infrared and Millimeter Waves*, **26**(2), pp. 201–207. 3.11

MENIKH-A, MICKAN-S, LIU-H, MACCOLL-R AND ZHANG-X.-C (2004). Label-free amplified bioaffinity detection using terahertz wave technology, *Biosensors & Bioelectronics*, **20**(3), pp. 658–662. 4.5.2

MERCADÉ-PRIETO-R AND CHEN-X (2006). Dissolution of whey protein concentrate gels in alkali, *American Institute of Chemical Engineers (AIChE) Journal*, **52**(2), pp. 792–803. 7.1

MERRIAM-WEBSTER DICTIONARY (2010). *Merriam-Webster Dictionary*, Merriam-Webster, Inc., Springfield. MA, USA, <http://www.merriam-webster.com/>, (Accessed: 2010-04-29). 4

MERYMAN-H (1956). Mechanics of freezing in living cells and tissues, *Science*, **124**(3221), pp. 515–521. 7.6.2

MESSER-J, DE LUCIA-F AND HELMINGER-P (1983). The pure rotational spectrum of water vapor-a millimeter, submillimeter, and far infrared analysis, *International Journal of Infrared and Millimeter Waves*, **4**(4), pp. 505–539. 5, 4.2

MEYER-J, ROYCHOWDHURY-S, RUSSELL-E, CALLAHAN-C, GITELMAN-D AND MESULAM-M (1996). Location of the central sulcus via cortical thickness of the precentral and postcentral gyri on MR, *American Journal of Neuroradiology*, **17**(9), pp. 1699–1706. 6.4.2

MICKAN-S, ABBOTT-D, MUNCH-J AND ZHANG-X.-C (2002a). Noise reduction in terahertz thin film measurements using a double modulated differential technique, *Fluctuation and Noise Letters*, **2**(1), pp. R13–R28. 4.5.2

MICKAN-S, DORDICK-J, MUNCH-J, ABBOTT-D AND ZHANG-X.-C (2002b). Terahertz spectroscopy of bound water in nano suspensions, *Proc. SPIE Biomedical Applications of Micro- and Nanoengineering*, **4937**, Eds: D. Nicolau and A. Lee, Melbourne, VIC, Australia, pp. 49–61. 4.15, 4.5.2

MICKAN-S, LEE-K.-S, LU-T.-M, MUNCH-J, ABBOTT-D AND ZHANG-X.-C (2002c). Double modulated differential THz-TDS for thin film dielectric characterization, *Microelectronics Journal*, **33**(12), pp. 1033–1042. 4.5.2

MICKAN-S, MENIKH-A, LIU-H, MANNELLA-C, MACCOLL-R, ABBOTT-D, MUNCH-J AND ZHANG-X.-C (2002d). Label-free bioaffinity detection using terahertz technology, *Physics in Medicine and Biology*, **47**(21), pp. 3789–3795. 4.5.2

MICKAN-S, SHVARTSMAN-R, MUNCH-J, ZHANG-X.-C AND ABBOTT-D (2004). Low noise laser-based T-ray spectroscopy of liquids using double-modulated differential time-domain spectroscopy, *Journal of Optics B: Quantum and Semiclassical Optics*, **6**(8), pp. S786–S795. 4.5.2, 4.5.2

MICROTECH INSTRUMENTS INC. (2008). *Compact THz Spectrometer*, Eugene, OR, USA, <http://www.mtinstruments.com/downloads/Compact%20THz%20Spectrometers%20Datasheet.pdf>, (Accessed: 2008-11-24). 3.2

MILLER-L, SMITH-G AND CARR-G (2003). Synchrotron-based biological microspectroscopy: From the mid-infrared through the far-infrared regimes, *Journal of Biological Physics*, **29**(2-3), pp. 219–230. 2.7.1

MIN-K, BETTERMANN-A AND VAN DER WEIDE-D (2004). Potential for detection of explosive and biological hazards with electronic terahertz systems, *Philosophical Transactions of the Royal Society, London*, **362**(1815), pp. 337–349. 1.3.2

MIRRA-S AND HYMAN-B (2002). *Ageing and Dementia, Greenfield's Neuropathology*, 7th edn, Arnold, London, UK, pp. 195–271. 6.2, 6.5, 6.5

MIRRA-S, HEYMAN-A, MCKEEL-D, SUMI-S, CRAIN-B, BROWNLEE-L, VOGEL-F, HUGHES-J, VANBELLE-G AND BERG-L (1991). The Consortium to Establish a Registry for Alzheimer's Disease (CERAD). Part II. standardization of the neuropathologic assessment of Alzheimer's disease, *Neurology*, **41**(4), pp. 479–486. 6.3.1

MITSUDO-S, HOSHIZUKI-H, IDEHARA-T AND SAITO-T (2006). Development of material processing system by using a 300 GHz CW gyrotron, *Proc. Yamada Conference LX on Research in High Magnetic Fields*, 16–19 August 2006, Sendai Civic Auditorium, Sendai, Japan, p. 549–552. 2.6.1

MITTLEMAN-D, GUPTA-M, NEELAMANI-R, BARANIUK-R, RUDD-J AND KOCH-M (1999). Recent advances in terahertz imaging, *Applied Physics B (Lasers and Optics)*, pp. 1085–1094. 1.3.2, 1.4.2, 1.5, 4.6, 5.1.1

MITTLEMAN-D, HUNSCHE-S, BOIVIN-L AND NUSS-M (1997). T-ray tomography, *Optics Letters*, **22**(12), pp. 904–906. 1.3.2, 1.4.2

MITTLEMAN-D, JACOBSEN-R AND NUSS-M (1996). T-Ray imaging, *IEEE Journal of Selected Topics in Quantum Electronics*, **2**(3), pp. 679–692. 1.3.2, 1.4.2

MIYAMARU-F AND HANGYO-M (2004). Finite size effect of transmission property for metal hole arrays in subterahertz region, *Applied Physics Letters*, **84**(15), pp. 2742–2744. A.2

MOOSSY-J, ZUBENKO-G, MARTINEZ-A, RAO-G, KOPP-U AND HANIN-I (1989). Lateralization of brain morphologic and cholinergic abnormalities in Alzheimer's disease, *Archives in Neurology*, **46**(6), pp. 639–642. 6.3.1

MORRIS-J, STORANDT-M, MCKEEL JR.-D, RUBIN-E, PRICE-J, GRANT-E AND BERG-L (1996). Cerebral amyloid deposition and diffuse plaques in "normal" aging: Evidence for presymptomatic and very mild Alzheimer's disease, *Neurology*, **46**(3), pp. 707–719. 6.1.1

MOSER-E, HOLZMUELLER-P AND KRSSAK-M (1996). Improved estimation of tissue hydration and bound water fraction in rat liver tissue, *Magnetic Resonance Materials in Physics, Biology and Medicine (MAGMA)*, **4**(1), pp. 55–59. 16

MOURANT-J, GALLAGHER-S, MATANOCK-A, TAYLOR-A AND TREWHELLA-J (2001). THz spectroscopy to measure low-frequency protein motions, *Proc. Biophysical Journal*, January 2001, p. 396A. 1.4.1, 4.5.2

MOURIK-J, VAN VELDEN-F, LUBBERINK-M, KLOET-R, VAN BERCKEL-B, LAMMERTSMA-A AND BOELLAARD-R (2008). Image derived input functions for dynamic high resolution research tomograph PET brain studies, *Neuroimage*, **43**(4), pp. 676–686. 61

MOUROU-G, STANCAMPIANO-C AND BLUMENTHAL-D (1981a). Picosecond microwave pulse generation, *Applied Physics Letters*, **38**(6), pp. 470–472. 3.5.2, 3.6, 3.8

MOUROU-G, STANCAMPIANO-C, ANTONETTI-A AND ORSZAG-A (1981b). Picosecond microwave pulses generated with a subpicosecond laser-driven semiconductor switch, *Applied Physics Letters*, **39**(4), pp. 295–296. 3.6

MUELLER-E (2003). *Terahertz Radiation: Applications and Sources*, American Institute of Physics, <www.tipmagazine.com>, (Accessed: 2008-08-27). 1.5, 2.3

MUELLER-E (2008). *Optically-Pumped THz Laser Technology*, Coherent Inc., Santa Clara, CA, USA, <http://www.coherent.com/downloads/OpticallyPumpedLaser.pdf>, (Accessed: 2008-12-31). 2.3

MULLINS-R (2001). *Fluid, Electrolytes, and Shock*, Sabiston Textbook of Surgery: The Biological Basis of Modern Surgical Practices, 16th edn, W.B. Saunders Company, Philadelphia, PA, USA, pp. 45–67. 4.5.4

MURAKI-M, HARATA-K, SUGITA-N AND I.C. SATO-K (1996). Origin of carbohydrate recognition specificity of human lysozyme revealed by affinity labeling, *Biochemistry*, **35**(42), pp. 13562–13567. 6.3

NAFTALY-M AND MILES-R (2005). Terahertz time-domain spectroscopy: A new tool for the study of glasses in the far infrared, *Journal of Non-Crystalline Solids*, **351**(40-42), pp. 3341–3346. 8.6.1

NAFTALY-M AND MILES-R (2007a). A method for removing etalon oscillations from THz time-domain spectra, *Optics Communications*, **280**(2), pp. 291–295. A.3

NAFTALY-M AND MILES-R (2007b). Terahertz time-domain spectroscopy of silicate glasses and the relationship to material properties, *Journal of Applied Physics*, **102**(4), article number 043517. 8.6.1

NAGAI-M, YADA-H, ARIKAWA-T AND TANAKA-K (2006). Terahertz time-domain attenuated total reflection spectroscopy in water and biological solution, *International Journal of Infrared and Millimeter Waves*, **27**(4), pp. 505–515. 4.5.2

NAGEL-M, RICHTER-F, HARING-BOLÍVAR-P AND KURZ-H (2003). A functional THz sensor for marker-free DNA analysis, *Physics in Medicine and Biology*, **48**(22), pp. 3625–3636. 1.4.1, 4.5.2

NAHATA-A, YARDLEY-J AND HEINZ-T (2002). Two-dimensional imaging of continuous-wave terahertz radiation using electro-optic detection, *Applied Physics Letters*, **81**(6), pp. 963–965. 2.4

NAITO-K, KAGAWA-Y, UTSUNO-S, NAGANUMA-T AND KURIHARA-K (2009a). Dielectric properties of eight-harness-stain fabric glass fiber reinforced polyimide matrix composite in the THz frequency range, *NDT & E International*, **42**(5), pp. 441–445. 8.1, 8.6.2, 8.6.3

NAITO-K, KAGAWA-Y, UTSUNO-S, NAGANUMA-T AND KURIHARA-K (2009b). Dielectric properties of woven fabric glass fiber reinforced polymer matrix composites in the THz frequency range, *Composites Science and Technology*, **69**(11-12), pp. 2027–2029. 8.1

NARR-K, BILDER-R, TOGA-A, WOODS-R, REX-D, SZESZKO-P, ROBINSON-D, SEVY-S, GUNDUZ-BRUCE-H, WANG-Y.-P, DELUCA-H AND THOMPSON-P (2005). Mapping cortical thickness and gray matter concentration in first episode schizophrenia, *Cerebral Cortex*, **15**(6), pp. 708–719. 6.4.2

NÄSLUND-J, HAROUTUNIAN-V, MOHS-R, DAVIS-K, DAVIES-P, GREENGARD-P AND BUXBAUM-J (2000). Correlation between elevated levels of amyloid β-peptide in the brain and cognitive decline, *Journal of the American Medical Association*, **283**(12), pp. 1571–1577. 6.2, 7.1

NATHAN-M, DUMKE-W, GERALD-B, DILL JR.-F AND LASHER-G (1962). Stimulated emission of radiation from GaAs *p-n* junctions, *Applied Physics Letters*, **1**(3), pp. 62–64. 2.4.1

NATIONAL INSTITUTE OF ADVANCED INDUSTRIAL SCIENCE AND TECHNOLOGY (AIST) (2009). *Spectral Database for Organic Compounds (SDBS)*, <http://riodb01.ibase.aist.go.jp/sdbs/cgi-bin/cre_index.cgi?lang=eng>, (Accessed: 2009-01-28). 4.1, 4.2

NGUYEN-K, JOHNS-M, GLADDEN-L, WORRALL-C, ALEXANDER-P, BEERE-H, PEPPER-M, RITCHIE-D, ALTON-J, BARBIERI-S AND LINFIELD-E (2006). Three-dimensional imaging with a terahertz quantum cascade laser, *Optics Express*, **14**(6), pp. 2123–2129. 1.3.2, 2.4.1, 2.8

NISHIZAWA-J.-I, SASAKI-T AND TANNO-T (2008). Coherent terahertz-wave generation from semiconductors and its applications in biological sciences, *Journal of Physics and Chemistry of Solids*, **69**(2-3), pp. 693–701. 2.5, 4.5.2, 4.5.4

NISHIZAWA-J.-I., SASAKI-T, SUTO-K, YAMADA-T, TANABE-T, TANNO-T, SAWAI-T AND MIURA-Y (2005). THz imaging of nucleobases and cancerous tissue using a GaP THz-wave generator, *Optics Communications*, **244**(1-6), pp. 469–474. 2.5, 4.5.2

NISHIZAWA-J.-I, SUTO-K, SASAKI-T, TANABE-T AND KIMURA-T (2003). Spectral measurement of terahertz vibrations of biomolecules using a GaP terahertz-wave generator with automatic scanning control, *Journal of Physics D: Applied Physics*, **36**(23), pp. 2958–2961. 2.5, 4.5.2

NISHIZAWA-J.-I, SUTO-K, TANABE-T, SAITO-K, KIMURA-T AND OYAMA-Y (2007). THz generation from GaP rod-type waveguides, *IEEE Photonics Technology Letters*, **19**(3), pp. 143–145. 2.5

NISHIZAWA-J, SASAKI-T, SUTO-K, TANABE-T, YOSHIDA-T, KIMURA-T AND SAITO-K (2006). Frequency-tunable terahertz-wave generation from GaP using Cr:forsterite lasers, *International Journal of Infrared and Millimeter Waves*, **27**(7), pp. 923–929. 2.5

NOLTE-J (2002). *The Human Brain: An Introduction to Its Functional Anatomy*, 5th edn, Mosby Inc., St. Louis, MO, USA. 6.2, 58, 6.4.2, 6.4.2, 6.18, 62, 9.1

NOLTE-J AND ANGEVINE JR.-J (2000). *The Human Brain in Photographs and Diagrams*, 2nd edn, Mosby Inc., St. Louis, MI, USA. 6.7, 6.8

NORDBERG-A (2004). PET imaging of amyloid in Alzheimer's disease, *The Lancet Neurology*, **3**(9), pp. 519–527. 6.2.2

O'CONNELL-M, TUOKKO-H, GRAVES-R AND KADLEC-H (2004). Correcting the 3MS for bias does not improve accuracy when screening for cognitive impairment or dementia, *Clinical and Experimental Neuropsychology*, **26**(7), pp. 970–980. 6.2.2

OGILVIE-J (1989). lnfrared spectroscopy of diatomic molecules-the first century, *Chinese Journal of Physics*, **27**(4), pp. 281–296. 1.4

OGILVY-J (1991). *Theory of Wave Scattering from Random Rough Surfaces*, IOP Publishing Ltd, Bristol, England. A.4

O'HARA-J AND GRISCHKOWSKY-D (2002). Synthetic phased-array terahertz imaging, *Optics Letters*, **27**(12), pp. 1070–1072. 1.3.2, 1.5

OHISHI-T, HAJI-Y AND TOKUMARU-S (2002). Incident angle characteristics of SAR in two-dimensional three-layered ellipse human model exposed to EM plane waves, *Electronics and Communications in Japan, Part 1*, **85**(12), pp. 1–14. 4.4.2

OHL-R, BUDENSTEIN-P AND BURRUS-C (1959). Improved diode for harmonic generation of millimeter and submillimeter waves, *Review of Scientific Instruments*, **30**(9), pp. 765–774. 1.4

OLIVEIRA-F, BARAT-R, SCHULKIN-B, HUANG-F, FEDERICI-J, GARY-D AND ZIMDARS-D (2004). Analysis of terahertz spectral images of explosives and bioagents using trained neural networks, *Proc. SPIE Terahertz for Military and Security Applications II*, **5411**, Eds: R. Hwu and D. Woolard, September 2004, Orlando, FL, USA, pp. 45–50. A.4

OLIVEIRA-F, BARAT-R, SHULKIN-B, FEDERICI-J, GARY-D AND ZIMDARS-D (2003). Neural network analysis of terahertz spectra of explosives and bio-agents, *Proc. SPIE Terahertz for Military and Security Applications*, **5070**, Eds: R. Hwu and D. Woolard, July 2003, Orlando, FL, USA, pp. 60–70. A.4

ORFANIDIS-S. J (2008). *Electromagnetic Waves and Antennas*, Rutgers University, Piscataway, NJ, USA, <http://www.ece.rutgers.edu/~orfanidi/ewa/>, (Accessed: 2010-05-25). 8.7.2

OSIANDER-R, MIRAGLIOTTA-J, JIANG-Z, XU-J AND ZHANG-X.-C (2003). Mine field detection and identification using terahertz spectroscopic imaging, *Proc. SPIE Terahertz for Military and Security Applications*, **5070**, Eds: R. Hwu and D. Woolard, Orlando, FL, USA, pp. 1–6. 1.3.2, A.4

OTT-A, BRETELER-M, VAN HARSKAMP-F, CLAUS-J, VAN DER CAMMEN-T, GROBBEE-D AND HOFMAN-A (1995). Prevalence of Alzheimer's disease and vascular dementia: association with education. the Rotterdam study, *British Medical Journal*, **310**, pp. 970–973. 6.1

OXFORD ENGLISH DICTIONARY (2010). *Oxford English Dictionary*, Oxford University Press, Oxford, UK, <http://dictionary.oed.com/>, (Accessed: 2010-04-29). 4

PARRISH-J (1981). Phototherapy and photochemotheraphy of skin diseases, *Journal of Investigative Dermatology*, **77**(1), pp. 167–171. 4.3.2, 4.3.2

PARTHASARATHY-R, GLOBUS-T, KHROMOVA-T, SWAMI-N AND WOOLARD-D (2005). Dielectric properties of biological molecules in the Terahertz gap, *Applied Physics Letters*, **87**(11), article number 113901. 1.4.1, 4.5.2

PATEL-C (1964). Continuous-wave laser action on vibrational-rotational transitions of CO_2, *Physical Review*, **136**(5A), pp. A1187–A1193. 11

PAUL SCHERRER INSTITUT (2008). *Microtomography of Blood Vessels in a Mouse Brain*, <http://www.lightsources.org/imagebank/>, (Accessed: 2008-10-27). 2.14

PAULSSON-M, HEGG-P.-O AND CASTBERG-H (1986). Heat-induced gelation of individual whey proteins a dynamic rheological study, *Journal of Food Science*, **51**(1), pp. 87–90. 7.3.1

PEARCE-J AND MITTLEMAN-D (2003). Using terahertz pulses to study light scattering, *Physica B: Condensed Matter*, **338**(1-4), pp. 92–96. 8.1

PEARCE-J, JIAN-Z AND MITTLEMAN-D (2003). Statistics of multiply scattered broadband terahertz pulses, *Physical Review Letters*, **91**(4), article number 043903. 8.1

PEPPER-M (2003). Medical applications of terahertz imaging and spectroscopy, *Medical Physics*, **30**(6), p. 1540. 4.5.4

PERANI-D (2006). *Neuropsychological Screening and Advanced Neuropsychological Tests*, The Dementias, Taylor & Francis Group, New York NY, USA, pp. 33–71. 6.2.2

PERKIN ELMER INC. (2008). *IR Specular Reflection Set for Spectrum FT-IR Instruments*, Waltham, MA, USA, <http://las.perkinelmer.com/Content/RelatedMaterials/SpecificationSheets/SPC_IRSpecularReflectionSet.pdf>, (Accessed: 2009-06-23). 1.4

PFEIFER-T, HEILIGER-H.-M, VON KAMIENSKI-E, ROSKOS-H AND KURZ-H (1994). Fabrication and characterization of freely positionable silicon-on-sapphire photoconductive probes, *Journal of the Optical Society of America B: Optical Physics*, **11**(12), pp. 2547–2552. 3.8.3

PHONG-B (1975). Illumination for computer generated pictures, *Communications of the ACM*, **18**(6), pp. 311–317. 8.2

PICKETT-H, POYNTER-R, COHEN-E, DELITSKY-M, PEARSON-J AND MÜLLER-H (1998). Submillimeter, millimeter, and microwave spectral line catalog, *Journal of Quantitative Spectroscopy and Radiative Transfer*, **60**(5), pp. 883–890. 4.4

PICKWELL-E, COLE-B, FITZGERALD-A, PEPPER-M AND WALLACE-V (2004a). *In vivo* study of human skin using pulsed terahertz radiation, *Physics in Medicine and Biology*, **49**(9), pp. 1595–1607. 1.5.1, 9.2, 9.5, 9.5.1, 9.4, 9.5.1, 9.5.2, 9.6

PICKWELL-E, COLE-B, FITZGERALD-A, WALLACE-V AND PEPPER-M (2004b). Simulation of terahertz pulse propagation in biological system, *Applied Physics Letters*, **84**(12), pp. 2190–2192. 1.5.1, 9.2

PICKWELL-E, FITZGERALD-A, COLE-B, TADAY-P, PYE-R, HA-T, PEPPER-M AND WALLACE-V (2005). Simulating the response of terahertz radiation to basal cell carcinoma using *ex vivo* spectroscopy measurements, *Journal of Biomedical Optics*, **10**(6), article number 064021. 1.5, 1.5.1

PIESIEWICZ-R, JANSEN-C, MITTLEMAN-D, KLEINE-OSTMANN-T, KOCH-M AND KÜRNER-T (2007). Scattering analysis for the modeling of THz communication systems, *IEEE Transactions on Antennas and Propagation*, **55**(11), pp. 3002–3009. 8.1

PIESIEWICZ-R, KLEINE-OSTMANN-T, KRUMBHOLZ-N, MITTLEMAN-D, KOCH-M AND KÜRNER-T (2005). Terahertz characterisation of building materials, *Electronics Letters*, **41**(18), pp. 1002–1004. 8.6.1

PIETROVITO-A AND DAVIES-P (2007). *Solid State Chemistry*, University of Pennsylvania, <http://www.seas.upenn.edu/~chem101/sschem/solidstatechem.html>, (Accessed: 2010-04-12). B.4

PIKE-K, SAVAGE-G, VILLEMAGNE-V, NG-S, MOSS-S, MARUFF-P, MATHIS-C, KLUNK-W, MASTERS-C AND ROWE-C (2007). β-amyloid imaging and memory in non-demented individuals: evidence for preclinical Alzheimers disease, *Brain*, **130**(11), pp. 2837–2844. 6.2.2

PLANCK-M (1901). Distribution of energy in the spectrum, *Annalen der Physik und Chemie*, **4**(3), pp. 553–563. 4.2

PLATTE-W (1976). High-speed optoelectronic switching in silicon gap-shunt microstrip structures, *Electronics Letters*, **12**(17), pp. 437–438. 3.8

PLUSQUELLIC-D, KORTER-T, FRASER-G, LAVRICH-R, BENCK-E, BUCHER-C, WALKER-A. H AND DOMENECH-J (2003). Continuous-wave terahertz spectroscopy of plasmas and biomolecules, *International Journal of High Speed Electronics and Systems*, **13**(4), pp. 1287–1306. 2.4, 4.5.2

PNG-G, CHOI-J.-W, NG-B. W.-H, MICKAN-S, ABBOTT-D AND ZHANG-X.-C (2008a). The impact of hydration changes in fresh bio-tissue on THz spectroscopic measurements, *Physics in Medicine and Biology*, **53**(13), pp. 3501–3517. 1.7, 7.5, 1

PNG-G, FALCONER-R, FISCHER-B, ZAKARIA-H, MICKAN-S, MIDDELBERG-A AND ABBOTT-D (2009a). Terahertz spectroscopic differentiation of microstructures in protein gels, *Optics Express*, **17**(15), pp. 13102–13115. 1.7, 8.6.5, 3

PNG-G, FLOOK-R, NG-B. W.-H AND ABBOTT-D (2009b). Terahertz spectroscopy of misfolded proteins in bio-tissue, *Proc. 34th International Conference on Infrared, Millimeter, and Terahertz Waves (IRMMW-THz)*, 21–25 September 2009, Busan, South Korea, article number 0506. 1.7, 2

PNG-G, FLOOK-R, NG-B. W.-H AND ABBOTT-D (2009c). Terahertz spectroscopy of snap-frozen human brain tissue: an initial study, *Electronics Letters*, **45**(7), pp. 343–345. 1.7, 2

PNG-G, MICKAN-S AND ABBOTT-D (2005a). The potential use of T-rays in diagnosing the head and brain, *Proc. International Workshop on Terahertz Technology*, Ed: M. Tonouchi, 16–18 November 2005, Osaka, Japan, pp. 99–100. 1.7, 5

PNG-G, MICKAN-S AND ABBOTT-D (2005b). Simulation of terahertz radiation in stratified media, *Proc. SPIE Photonics: Design Technology, and Packaging II*, **6038**, Ed: D. Abbott, 11–14 December 2005, Brisbane, Australia, article number 60380M. 1.7, 5

PNG-G, MICKAN-S, RAINSFORD-T AND ABBOTT-D (2004). Terahertz phase contrast imaging, *Proc. SPIE Smart Structures, Devices, and Systems II*, **5649**, Ed: S. Al-Sarawi, February 2005, Sydney, Australia, pp. 768–777. 1.7, 6

PNG-G, NG-B. W.-H, CHOI-J.-W, ZHANG-X.-C AND ABBOTT-D (2007). Influence of surface clutter on THz spectroscopy of skin, *Proc. Joint 32nd International Conference on Infrared and Millimetre Waves, and 15th International Conference on Terahertz Electronics (IRMMW-THz)*, **1**, Eds: M. Griffin, P. Hargrave, T. Parker and K. Wood, 3–7 September 2007, Cardiff, UK, pp. 565–566. F.1

PNG-G, STRINGER-M, NG-B. W.-H, ABBOTT-D AND MILES-R (2008b). Orientation dependence of THz scattering from cylindrical strands, *Proc. 33rd International Conference on Infrared, Millimeter, and Terahertz Waves (IRMMW-THz)*, Pasadena, CA, USA, article number 1380. 1.7, 4

POLLACK-M (1971). *Molecular Gas Lasers*, Handbook of Lasers with Selected Data on Optical Technology, CRC Press, Cleveland, OH, USA, pp. 298–349. 2.3

POPOVIĆ-M AND TAFLOVE-A (2004). Two-dimensional FDTD inverse-scattering scheme for determination of near-surface material properties at microwave frequencies, *IEEE Transactions on Antennas and Propagation*, **52**(9), pp. 2366–2373. A.4

POPOV-L, DENISOV-G, LITVAK-A, AGAPOVA-M, GNEDENKOV-A, KOSTYNA-A, NICHIPORENKO-V, MYASNIKOV-V, TAI-E, USACHEV-S, ZAPEVALOV-V, CHIRKOV-A, ILIN-V, ILIN-V, KUFTIN-A,

MALYGIN-S, MALYGIN-V, PARSHIN-V, PAVELEV-A, RUKAVISHNIKOVA-V, ROSCHIN-Y, SOKOLOV-E, SOLUYANOVA-E AND VIKHAREV-A (2008). Development in Russia of 170 GHz gyrotron for ITER, *Proc. 33rd International Conference on Infrared, Millimeter, and Terahertz Waves*, Pasadena, CA, USA, article number 1472. 2.6.1

POWER-J, ASAD-S, CHATAWAY-T, CHEGINI-F, MANAVIS-J, TEMLETT-J, JENSEN-P, BLUMBERGS-P AND GAI-W.-P (2008). Peroxiredoxin 6 in human brain: molecular forms, cellular distribution and association with Alzheimer's disease pathology, *Acta Neuropathologica*, **115**(6), pp. 611–622. 6.6.1

POYNTER-R AND PICKETT-H (1985). Submillimeter, millimeter, and microwave spectral line catalog, *Applied Optics*, **24**(14), pp. 2235–2240. 4.4

PRAHL-S, KEIJZER-M, JACQUES-S AND WELCH-A (1989). A Monte Carlo model of light propagation in tissue, *SPIE Institute Series*, **IS 5**, pp. 102–111. 4.3.2

QADI-N AND FELDMAN-H (2007). *The diagnosis of Alzheimer's disease and dementia*, Atlas of Alzheimer's Disease, Informa UK Ltd, London, UK, pp. 59–69. 6.2.2

QIN-B, BEWLEY-M, CREAMER-L, BAKER-H, BAKER-E AND JAMESON-G (1998). Structural basis of the Tanford transition of bovine β-lactoglobulin, *Biochemistry*, **37**(40), pp. 14014–14023. 7.1

QU-D AND GRISCHKOWSKY-D (2004). Observation of a new type of THz resonance of surface plasmons propagating on metal-film hole arrays, *Physical Review Letters*, **93**(19), article number 196804. A.2

QU-D, GRISCHKOWSKY-D AND ZHANG-W (2004). Terahertz transmission properties of thin, subwavelength metallic hole arrays, *Optics Letters*, **29**(8), pp. 896–898. A.2

QUIST-T, REDIKER-R, KEYES-R, KRAG-W, LAX-B, MCWHORTER-A AND ZEIGLER-H (1962). Semiconductor maser of GaAs, *Applied Physics Letters*, **1**(4), pp. 91–92. 2.4.1

RAHMIM-A AND ZAIDI-H (2008). PET versus SPECT: strengths, limitations and challenges, *Nuclear Medicine Communications*, **29**(3), pp. 193–207. 61

RAICU-V, KITAGAWA-N AND IRIMAJIRI-A (2000). A quantitative approach to the dielectric properties of the skin, *Physics in Medicine and Biology*, **45**(2), pp. L1–L4. 9.4.2

RANDALL-H (1954). Infrared spectroscopy at the University of Michigan, *Journal of the Optical Society of America*, **44**(2), pp. 97–103. 1.4

RAY-P (1972). Broadband complex refractive indices of ice and water, *Applied Optics*, **11**(8), pp. 1836–1844. 2

REID-M AND FEDOSEJEVS-R (2006). Terahertz birefringence and attenuation properties of wood and paper, *Applied Optics*, **45**(12), pp. 2766–2772. 8.1

RESCH-J, DAUBERT-C AND FOEGEDING-E (2005). β-Lactoglobulin gelation and modification: Effect of selected acidulants and heating conditions, *Journal of Food Science*, **70**(1), pp. C79–C86. 7.1.1, 7.3.2, 7.4, 7.4.2

RICHARDS-M AND SHEPPARD-R (1991). A precision waveguide system for the measurement of complex permittivity of lossy liquids and solid tissues in the frequency range 29 GHz to 90 GHz—II. the liquid system for 90 GHz; high-frequency cell design, *Measurement Science and Technology*, **2**(7), pp. 663–667. 4.4.1

RICHARDS-P (1964). High-resolution fourier transform spectroscopy in the far-infrared, *Journal of the Optical Society of America*, **54**(12), pp. 1474–1484. 1.4

RICHMOND-J (1965a). Digital computer solutions of the rigorous equations for scattering problems, *Proceedings IEEE*, **53**(8), pp. 796–804. 8.2

RICHMOND-J (1965b). Scattering by a dielectric cylinder of arbitrary cross section shape, *IEEE Transactions on Antennas and Propagation*, **13**(3), pp. 334–341. 8.2

RICHMOND-J (1965c). Scattering by an arbitrary array of parallel wires, *IEEE Transactions on Microwave Theory and Techniques*, **13**(4), pp. 408–412. 8.2

RICHMOND-J (1966a). TE-wave scattering by a dielectric cylinder of arbitrary cross-section shape, *IEEE Transactions on Antennas and Propagation*, **14**(4), pp. 460–464. 8.2

RICHMOND-J (1966b). A wire-grid model for scattering by conducting bodies, *IEEE Transactions on Antennas and Propagation*, **14**(6), pp. 782–786. 8.2

ROBERTS-S AND VON HIPPEL-A (1946). A new method for measuring dielectric constant and loss in the range of centimeter waves, *Journal of Applied Physics*, **17**(7), pp. 610–616. 4.4.1

ROBINSON-M, RICHARDSON-M, GREEN-J AND PREECE-A (1991). New materials for dielectric simulation of tissues, *Physics in Medicine and Biology*, **36**(12), pp. 1565–1571. 9.4.2

ROMEO-M, WOOD-B, QUINN-M AND MCNAUGHTON-D (2003). Removal of blood components from cervical smears: Implications for cancer diagnosis using FTIR spectroscopy, *Biopolymers*, **72**(1), pp. 69–76. 4.3.2

RØNNE-C AND KEIDING-S (2002). Low frequency spectroscopy of liquid water using THz-time domain spectroscopy, *Journal of Molecular Liquids*, **101**(1-3), pp. 199–218. 4.5.1

RØNNE-C, ÅSTRAND-P.-O AND KEIDING-S (1999). THz spectroscopy of liquid H_2O and D_2O, *Physical Review Letters*, **82**(14), pp. 2888–2891. 4.5.1, 9.4.2

RØNNE-C, THRANE-L, ÅSTRAND-P.-O, WALLQVIST-A, MIKKELSEN-K AND KEIDING-S (1997). Investigation of the temperature dependency of dielectric relaxation in liquid water by thz reflection spectroscopy and molecular dynamics simulation, *Journal of Chemical Physics*, **107**(14), pp. 5319–5330. 4.5.1

ROSENBLUM-W (2002). Structure and location of amyloid beta peptide chains and arrays in Alzheimer's disease: new findings require reevaluation of the amyloid hypothesis and of tests of the hypothesis, *Neurobiology of Aging*, **23**(2), pp. 225–230. 7.8

ROWE-C, ACKERMAN-U, BROWNE-W, MULLIGAN-R, PIKE-K, O'KEEFE-G, TOCHON-DANGUY-H, CHAN-G, BERLANGIERI-S, JONES-G, DICKINSON-ROWE-K, KUNG-H, ZHANG-W, KUNG-M, SKOVRONSKY-D, DYRKS-T, HALL-G, KRAUSE-S, FRIEBE-M, LEHMAN-L, LINDEMANN-S, DINKELBORG-L, MASTERS-C AND VILLEMAGNE-V (2008). Imaging of amyloid β in Alzheimer's disease with ^{18}F-BAY94-9172, a novel PET tracer: proof of mechanism, *Lancet Neurology*, **7**(2), pp. 129–135. 6.2.2

ROWE-C, NG-S, ACKERMANN-U, GONG-S, PIKE-K, SAVAGE-G, COWIE-T, DICKINSON-K, MARUFF-P, DARBY-D, SMITH-C, WOODWARD-M, MERORY-J, TOCHON-DANGUY-H, O'KEEFE-G, KLUNK-W, MATHIS-C, PRICE-J, MASTERS-C AND VILLEMAGNE-V (2007). Imaging β-amyloid burden in aging and dementia, *Neurology*, **68**(20), pp. 1718–1725. 6.2.2

ROYAL ADELAIDE HOSPITAL (2008). *PET*, Department of Nuclear Medicine, PET & Bone Densitometry, Adelaide, Australia, <http://www.rah.sa.gov.au/nucmed/images/brochures/PET_brochure.pdf>, (Accessed: 2009-06-08). 6.2.2

RUBENS-H AND NICHOLS-E (1897a). Certain optical and electro-magnetic properties of heat waves of great wave-length I., *Physical Review*, **5**(2), pp. 98–112. 1.3.1

RUBENS-H AND NICHOLS-E (1897b). Certain properties of heat waves of great wave-length II., *Physical Review*, **5**(3), pp. 152–169. 1.3.1

RUIZ-B, JAZBINSEK-M AND GÜNTER-P (2008). Crystal growth of DAST, *Crystal Growth & Design*, **8**(11), pp. 4173–4184. B.2

RUPPIN-R (1990). Electromagnetic scattering from finite dielectric cylinders, *Journal of Physics D: Applied Physics*, **23**(7), pp. 757–763. 8.2

RUTZ-F, KOCH-M, KHARE-S, MONEKE-M, RICHTER-H AND EWERT-U (2006a). Terahertz quality control of polymeric products, *International Journal of Infrared and Millimeter Waves*, **27**(4), pp. 547–556. 1.3.2

RUTZ-F, WIETZKE-S, KOCH-M, RICHTER-H, HICKMANN-S, TRAPPE-V AND EWERT-U (2006b). Nondestructive testing of glass-fibre reinforced polymers using terahertz spectroscopy, *Proc. 9th European Conference on Nondestructive Testing (NDT)*, Ed: R. Diederichs, September 2006, Berlin, Germany, article number We.2.8.2. 1.3.2

RZESNICKI-T, PIOSCZYK-B, FLAMM-J, JIN-J, KERN-S, PRINZ-O AND THUMM-M (2008). Recent experimental results on the 170 GHz, 2 MW coaxial cavity pre-prototype gyrotron for ITER, *Proc. 33rd International Conference on Infrared, Millimeter, and Terahertz Waves*, Pasadena, CA, USA, article number 1521. 2.6.1

SALEH-B AND TEICH-M (1991). *Fundamentals of Photonics*, John Wiley & Sons. 3.2, 3.2, 3.4.1, 3.5, 3.4.1, B.1

SCARFÍ-M, ROMANÓ-M, PIETRO-R. D, ZENI-O, DORIA-A, GALLERANO-G, GIOVENALE-E, MESSINA-G, LAI-A, CAMPURRA-G, CONIGLIO-D AND D'ARIENZO-M (2003). THz exposure of whole blood for the study of biological effects on human lymphocytes, *Journal of Biological Physics*, **29**(2-3), pp. 171–177. 2.7.2, 4.5.2

SCHÄFER-A AND KAUFMANN-J (1999). What happens in freezing bodies? Experimental study of histological tissue change caused by freezing injuries, *Forensic Science International*, **102**(2-3), pp. 149–158. 5.5.1

SCHEPPS-J AND FOSTER-K (1980). The UHF and microwave dielectric properties of normal and tumour tissues: variation in dielectric properties with tissue water content, *Physics in Medicine and Biology*, **25**(6), pp. 1149–1159. 3

SCHNEIDER-A, NEIS-M, STILLHART-M, RUIZ-B, KHAN-R AND GÜNTER-P (2006). Generation of terahertz pulses through optical rectification in organic DAST crystals: theory and experiment, *Journal of the Optical Society of America B-Optical Physics*, **23**(9), pp. 1822–1835. B.2

SCHWAN-H AND CARSTENSEN-E (1953). Heating of fat-muscle layers by electromagnetic and ultrasonic diathermy, *Transactions of the American Institute of Electrical Engineers, Part I (Communications and Electronics)*, **72**(8), pp. 483–488. 4.4.1, 4.4.2

SCHWAN-H AND LI-K (1953). Capacity and conductivity of body tissues at ultrahigh frequencies, *Proceedings of the Institute of Radio Engineers*, **41**(12), pp. 1735–1740. 4.4.2

SCHWAN-H AND LI-K (1956). Hazards due to total body irradiation by radar, *Proceedings of the Institute of Radio Engineers*, **44**(11), pp. 1572–1581. 4.4.2

SCIENCE EDUCATION RESOURCE CENTER (2007). *Other Phase Diagrams*, Carleton College, Northfield, MN, USA, <http://serc.carleton.edu/research_education/equilibria/other_diagrams.html>, (Accessed: 2009-03-05). 5.15

SELIUTA-D, KAŠALYNAS-I, TAMOŠIŪNAS-V, BALAKAUSKAS-S, MARTŪNAS-Z, AŠMONTAS-S, VALUŠIS-G, LISAUSKAS-A, ROSKOS-H AND KÖHLER-K (2006). Silicon lens-coupled bow-tie InGaAs-based broadband terahertz sensor operating at room temperature, *Electronics Letters*, **42**(14), pp. 825–827. 3.8.3

SELKOE-D (2001). Alzheimers Disease: Genes, proteins, and therapy, *Physiological Reviews*, **81**(2), pp. 741–766. 6.5

SELKOE-D (2003). Folding proteins in fatal ways, *Nature*, **426**(6968), pp. 900–904. 6.1, 6.3, 7.1

SENITZKY-B AND OLINER-A (1970). Introduction: Submillimeter waves—a transition region, *Proc. Symposium on Submillimeter Waves*, **XX** of *Microwave Research Institute Symposia Series*, Ed: J. Fox, New York, NY, USA, pp. xxvii–xlvii. 1.3.1

SHEN-Y.-C, DAVIES-A, LINFIELD-E, TADAY-P, ARNONE-D AND ELSEY-T (2003). Determination of glucose concentration in whole blood using fourier-transform infrared spectroscopy, *Journal of Biological Physics*, **29**(2-3), pp. 129–133. 4.3.2

SHEN-Y.-C, LO-T, TADAY-P, COLE-B, TRIBE-W AND KEMP-M (2005a). Detection and identification of explosives using terahertz pulsed spectroscopic imaging, *Applied Physics Letters*, **86**(24), article number 241116. 1.3.2

SHEN-Y.-C, TADAY-P AND PEPPER-M (2008). Elimination of scattering effects in spectral measurement of granulated materials using terahertz pulsed spectroscopy, *Applied Physics Letters*, **92**(5), article number 051103. 8.1

SHEN-Y.-C, TADAY-P, NEWNHAM-D, KEMP-M AND PEPPER-M (2005b). 3D chemical mapping using terahertz pulsed imaging, *Proc. SPIE Terahertz and Gigahertz Electronics and Photonics IV*, **5727**, Eds: R. Hwu and K. Linden, 23–25 January 2005, San Jose, CA, USA, pp. 24–31. 4.5.3

SHEN-Y, TADAY-P, NEWNHAM-D AND PEPPER-M (2005c). Chemical mapping using reflection terahertz pulsed imaging, *Semiconductor Science and Technology*, **20**(7), pp. S254–S257. 4.5.3

SIEBERT-K, LÖFFLER-T, QUAST-H, THOMSON-M, BAUER-T, LEONHARDT-R, CZASCH-S AND ROSKOS-H (2002a). All-optoelectronic continuous wave THz imaging for biomedical applications, *Physics in Medicine and Biology*, **47**(21), pp. 3743–3748. 1.4.2, 2.4

SIEBERT-K, QUAST-H, LEONHARDT-R, LÖFFLER-T, THOMSON-M, BAUER-T, ROSKOS-H AND CZASCH-S (2002b). Continuous-wave all-optoelectronic terahertz imaging, *Applied Physics Letters*, **80**(16), pp. 3003–3005. 1.4.2, 2.4

SIEGEL-P (2004). Terahertz technology in biology and medicine, *IEEE Transactions on Microwave Theory and Techniques*, **52**(10), pp. 2438–2447. 1.2

SIEGEL-P (2007). THz instruments for space, *IEEE Transactions on Antennas and Propagation*, **55**(11), pp. 2957–2965. 1.3.1

SIEGRIST-K, BUCHER-C, MANDELBAUM-I, WALKER-A. H, BALU-R, GREGURICK-S AND PLUSQUELLIC-D (2006). High-resolution terahertz spectroscopy of crystalline trialanine: Extreme sensitivity to β-sheet structure and cocrystallized water, *Journal of the American Chemical Society*, **128**(17), pp. 5764–5775. 4.5.2, 7.1

SIPE-J AND COHEN-A (2000). Review: History of the amyloid fibril, *Journal of Structural Biology*, **130**(2-3), pp. 88–98. 7.8

SMITH-A (1961). *Biological Effects of Freezing and Supercooling*, Arnold, London, UK. 6.5.1

SMITH-F, LE-H, DIADIUK-V, HOLLIS-M, CALAWA-A, GUPTA-S, FRANKEL-M, DYKAAR-D, MOUROU-G AND HSIANG-T (1989). Picosecond GaAs-based photoconductive optoelectronic detectors, *Applied Physics Letters*, **54**(10), pp. 890–892. 3.8.3

SMITH-P, AUSTON-D AND NUSS-M (1988). Subpicosecond photoconducting dipole antennas, *IEEE Journal of Quantum Electronics*, **24**(2), pp. 255–260. 3.10, 3.8, 3.8.1

SMITH-P, AUSTON-D, JOHNSON-A AND AUGUSTYNIAK-W (1981). Picosecond photoconductivity in radiation-damaged silicon-on-sapphire films, *Applied Physics Letters*, **38**(1), pp. 47–50. 3.6, 3.8.2, 3.8.3

SMYE-S, CHAMBERLAIN-J, FITZGERALD-A AND BERRY-E (2001). The interaction between Terahertz radiation and biological tissue, *Physics in Medicine and Biology*, **46**, pp. R101–R112. 4.5.4

SONG-Z, DONG-K, HU-X.-H AND LU-J (1999). Monte Carlo simulation of converging laser beams propagating in biological materials, *Applied Optics*, **38**(13), pp. 2944–2949. 4.3.2

SPENCER-J, GAO-Z, MOORE-T, BUHSE-L, TADAY-P, NEWNHAM-D, SHEN-Y, PORTIERI-A AND HUSAIN-A (2008). Delayed release tablet dissolution related to coating thickness by terahertz pulsed image mapping, *Journal of Pharmaceutical Sciences*, **97**(4), pp. 1543–1550. 1.3.2

SPIRE CONSORTIUM (2007). *SPIRE Photometer Bolometer*, European Space Agency, <http://sci.esa.int/science-e/www/object/index.cfm?fobjectid=41337>, (Accessed: 2008-10-28). 1.2

STANDRING-S, ELLIS-H, HEALY-J, JOHNSON-D, WILLIAMS-A, COLLINS-P, WIGLEY-C, BERKOVITZ-B, BORLEY-N, CROSSMAN-A, DAVIES-M, FITZGERALD-M, GLASS-J, HACKNEY-C, IND-T, MUNDY-A, NEWELL-R, RUSKELL-G AND SHAH-P (2005). *Gray's Anatomy: The Anatomical Basis of Clinical Practice*, Elsevier Churchill Livingstone. 5.5.5

STEEL-M AND SHEPPARD-R (1985). Dielectric properties of mammalian brain tissue between 1 and 18 GHz, *Physics in Medicine and Biology*, **30**(7), pp. 621–630. 8

STEEL-M AND SHEPPARD-R (1988). The dielectric properties of rabbit tissue, pure water and various liquids suitable for tissue phantoms at 35 GHz, *Physics in Medicine and Biology*, **33**(4), pp. 467–472. 10

STEEL-M, SHEPPARD-R AND COLLINS-R (1987). Precision waveguide cells for the measurement of complex permittivity of lossy liquids and biological tissue at 35 GHz, *Journal of Physics E (Scientific Instruments)*, **20**(7), pp. 872–877. 4.4.1, 9

STEEL-M, SHEPPARD-R AND GRANT-E (1984). A precision method for measuring the complex permittivity of solid tissue in the frequency domain 2 and 18 GHz, *Journal of Physics E: Scientific Instruments*, **17**(1), pp. 30–34. 6

STEEVES-G, ELEZZABI-A AND FREEMAN-M (1997). Advances in picosecond scanning tunneling microscopy via junction mixing, *Applied Physics Letters*, **70**(14), pp. 1909–1911. 31

STRACHAN-C, TADAY-P, NEWNHAM-D, GORDON-K, ZEITLER-J, PEPPER-M AND RADES-T (2005). Using terahertz pulsed spectroscopy to quantify pharmaceutical polymorphism and crystallinity, *Journal of Pharmaceutical Sciences*, **94**(4), pp. 837–846. 4.5.3

STRINGER-M, LUND-D, FAULDS-A, BERRY-E, DAVIES-A AND MILES-R (2004). A THz time-domain study of human cortical bone, *Proc. Joint 29th International Conference on Infrared and Millimeter Waves and 12th International Conference on Terahertz Electronics (IRMMW-THz)*, Karlsruhe, Germany, pp. 735–736. 4.5.4

STRINGER-M, LUND-D, FOULDS-A, UDDIN-A, BERRY-E, MILES-R AND DAVIES-A (2005). The analysis of human cortical bone by terahertz time-domain spectroscopy, *Physics in Medicine and Biology*, **50**(14), pp. 3211–3219. 4.5.4

STRONG-J (1957). Interferometry for the far infrared, *Journal of the Optical Society of America*, **47**(5), pp. 354–357. 1.3.1, 1.4

STUCHLY-M (1994). Wireless communications and the safety of the user, *International Journal of Wireless Information Networks*, **1**(4), pp. 223–228. 4.4.2

STUCHLY-M AND DAWSON-T (2000). Interaction of low-frequency electric and magnetic fields with the human body, *Proceedings of the IEEE*, **88**(5), pp. 643–664. 4.4.2

STUCHLY-M, KRASZEWSKI-A, STUCHLY-S AND SMITH-A (1982). Dielectric properties of animal tissues *in vivo* at radio and microwave frequencies: comparison between species, *Physics in Medicine and Biology*, **27**(7), pp. 927–936. 4

SUBRAMANIAM-S AND HENDERSON-R (2000). Molecular mechanism of vectorial proton translocation by bacteriorhodopsin, *Nature*, **406**(6796), pp. 653–657. 4.14

SUNAGA-T, IKEHIRA-H, FURUKAWA-S, SHINKAI-H, KOBAYASHI-H, MATSUMOTO-Y, YOSHITOME-E, OBATA-T, TANADA-S, MURATA-H AND SASAKI-Y (2002). Measurement of the electrical properties of human skin and the variation among subjects with certain skin conditions, *Physics in Medicine and Biology*, **47**(1), pp. N11–N15. 9.4.2

SUZUKI-K AND TERRY-R (1967). Fine structural localization of acid phosphatase in senile plaques in Alzheimer's presenile dementia, *Acta Neuropathologica*, **8**(3), pp. 276–284. 6.5

SWATHI-P, TONG-T AND CUNNINGTON JR.-G (1991). Scattering of electromagnetic waves by cylinders coated with a radially-inhomogeneous layer, *Journal of Quantitative Spectroscopy and Radiative Transfer*, **46**(4), pp. 281–292. 8.2

SWISS LIGHT SOURCE (2008). *3D Reconstruction of the Brain of a Transgenic Mouse*, <http://www.lightsources.org/imagebank/>, (Accessed: 2008-10-27). 2.14

TADAY-P (2004). Applications of terahertz spectroscopy to pharmaceutical sciences, *Philosophical Transactions of the Royal Society: Mathematical, Physical and Engineering Sciences*, **362**(1815), pp. 351–364. 4.5.3

TADAY-P, BRADLEY-I AND ARNONE-D (2003a). Terahertz pulse spectroscopy of biological materials: L-Glutamic acid, *Journal of Biological Physics*, **29**(2-3), pp. 109–115. 4.5.2

TADAY-P, BRADLEY-I, ARNONE-D AND PEPPER-M (2003b). Using terahertz pulse spectroscopy to study the crystalline structure of a drug: A case study of the polymorphs of ranitidine hydrochloride, *Journal of Pharmaceutical Sciences*, **92**(4), pp. 831–838. 4.5.3

TAKATA-S-I, NORISUYE-T, TANAKA-N AND SHIBAYAMA-M (2000). Heat-induced gelation of β-lactoglobulin. 1. time-resolved dynamic light scattering, *Macromolecules*, **33**(15), pp. 5470–5475. 7.3.2, 7.2

TAMURA-T, TENHUNEN-M, LAHTINEN-T, REPO-T AND SCHWAN-H (1994). Modelling of the dielectric properties of normal and irradiated skin, *Physics in Medicine and Biology*, **39**(6), pp. 927–936. 9.2

TANABE-T, SUTO-K, I. NISHIZAWA-J, SAITO-K AND KIMURA-T (2003a). Frequency-tunable terahertz wave generation via excitation of phonon-polaritons in GaP, *Journal of Physics D: Applied Physics*, **36**(8), pp. 953–957. 2.5

TANABE-T, SUTO-K, NISHIZAWA-J, KIMURA-T AND SAITO-K (2003b). Frequency-tunable high-power terahertz wave generation from GaP, *Journal of Applied Physics*, **93**(8), pp. 4610–4615. 2.5

TANABE-T, SUTO-K, NISHIZAWA-J, SAITO-K AND KIMURA-T (2003c). Tunable terahertz wave generation in the 3- to 7-THz region from GaP, *Applied Physics Letters*, **83**(2), pp. 237–239. 2.5

TANAKA-M, MIYAMARU-F AND HANGYO-M (2005). Effect of a thin dielectric layer on terahertz transmission characteristics for metal hole arrays, *Optics Letters*, **30**(10), pp. 1210–1212. A.2

TANG-M, WOLKERS-W, CROWE-J AND TABLIN-F (2006). Freeze-dried rehydrated human blood platelets regulate intracellular pH, *Transfusion*, **46**(6), pp. 1029–1037. 5.5.2

TANG-X.-L, SHI-Y.-W, MATSUURA-Y, IWAI-K AND MIYAGI-M (2009). Transmission characteristics of terahertz hollow fiber with an absorptive dielectric inner-coating film, *Optics Letters*, **34**(14), pp. 2231–2233. 8.1

TAN-S AND PEPYS-M (1994). Amyloidosis, *Histopathology*, **25**(5), pp. 403–414. 6.1.1, 7.1

TE-C, FERGUSON-B AND ABBOTT-D (2002). Investigation of biomaterial classification using T-rays, *Proc. SPIE Biomedical Applications of Micro- and Nanoengineering*, **4937**, Ed: D. Nicolau, 16–18 December 2002, Melbourne, VIC, Australia, pp. 294–306. 4.3.1

TEMKIN-R, KREISCHER-K, MULLIGAN-W, MACCABE-S AND FETTERMAN-H (1982). A 100 kW, 140 GHz pulsed gyrotron, *International Journal of Infrared and Millimeter Waves*, **3**(4), pp. 427–437. 2.6.1

TENG-E AND CHUI-H (1987). The modified mini-mental state (3MS) examination, *Journal of Clinical Psychiatry*, **48**(8), pp. 314–318. 6.2.2, E.1, E.1, E.1

TERAPHYSICS INC. (2008). *The Teraphysics Micro Backward Wave Oscillator (Micro-BWO)*, Cleveland, OH, USA, <http://www.teraphysics.com/products.php3>, (Accessed: 2008-10-22). 2.11

TERAVIEW LTD (2008). *TPS Spectra 3000*, Cambridge, UK, <http://www.teraview.com/terahertz/id/19>, (Accessed: 2008-11-25). 3.3

TERRY-R AND KATZMAN-R (1983). *Senile Dementia of the Alzheimer Type: Defining a Disease, The Neurology of Aging*, F.A. Davis Company, Philadelphia, USA, pp. 51–84. 6.2.3

THERMO FISHER SCIENTIFIC INC. (2009). *Guided Microwave Spectrometer (GMS)*, <http://www.thermo.com/com/cda/product/detail/1,1055,13903,00.html>, (Accessed: 2009-02-10). 4.9

THORPE-S, FOX-B AND SANDS-D (2002). A stable lyophilized reagent for use in a potential reference assay for quantitation of anti-D in immunoglobulin products, *Biologicals*, **30**(4), pp. 315–321. 5.5.2

THRANE-L, JACOBSEN-R, JEPSEN-P AND KEIDING-S (1995). THz reflection spectroscopy of liquid water, *Chemical Physics Letters*, **240**(4), pp. 330–333. 4.5.1, 4.13

THZ SCIENCE AND TECHNOLOGY NETWORK (2008). *Goodrich Chemical Detection Technology Selected by Department of Homeland Security*, <http://www.thznetwork.org/wordpress/index.php/archives/636>, (Accessed: 2008-08-01). 1.3.2

TIERNEY-M, HERRMANN-N, GESLANI-D AND SZALAI-J (2003). Contributions of informant and patient ratings to the accuracy of the Mini-Mental State Examination in predicting probable Alzheimer's Disease, *American Geriatrics Society*, **51**(6), pp. 813–818. 6.2.2

TIJHUIS-A (1987). *Electromagnetic Inverse Profiling: Theory and Numerical Implementation*, VNU Science Press, Utrecht, The Netherlands. A.4

TIKHONOV-A AND SAMARSKII-A (1963). *Equations of Mathematical Physics*, Pergamon Press, Oxford, England. A.4

TOFIGHI-M.-R AND DARYOUSH-A (2002a). Characterization of the complex permittivity of brain tissues up to 50 GHz utilizing a two-port microstrip test fixture, *IEEE Transactions on Microwave Theory and Techniques*, **50**(10), pp. 2217–2225. 18

TOFIGHI-M.-R AND DARYOUSH-A (2002b). Comparison of two post-calibration correction methods for complex permittivity measurement of biological tissues up to 50 GHz, *IEEE Transactions on Instrumentation and Measurement*, **51**(6), pp. 1170–1176. 18

TONOUCHI-M, TANI-M, WANG-Z, SAKAI-K, HANGYO-M, WADA-N AND MURAKAMI-Y (1997). Enhanced THz radiation from YBCO thin film bow-tie antennas with hyper-hemispherical MgO lens, *IEEE Transactions on Applied Superconductivity*, **7**(2), pp. 2913–2916. 3.8.3

TORRANCE-K AND SPARROW-E (1967). Theory for off-specular reflection from roughened surfaces, *Journal of the Optical Society of America*, **57**(9), pp. 1105–1114. 8.2

TOWNES-C AND SCHAWLOW-A (1955). *Microwave Spectroscopy*, International Series in Pure and Applied Physics, McGraw-Hill Book Company, Inc., New York, NY, USA. 36, 4.4, 4.4.1

TRANG-A (1996). Simulation of mine detection over dry soil, snow, ice, and water, *Proc. SPIE Detection and Remediation Technologies for Mines and Minelike Targets*, **2765**, Eds: A. Dubey, R. Barnard, C. Lowe and J. McFee, May 1996, Orlando, FL, USA, pp. 430–440. 9.2

T-RAY SCIENCE (2008a). *THz PCA Fact Sheet*, Waterloo, ON, Canada, <http://www.t-rayscience.com/_resources/T-Ray_PCAChip.pdf>, (Accessed: 2008-12-18). 3.13

T-RAY SCIENCE (2008b). *THz Spectrometer Fact Sheet*, Waterloo, ON, Canada, <http://www.t-rayscience.com/_resources/T-Ray_Spectrometer.pdf>, (Accessed: 2008-11-24). 3.3

TRIBE-W, NEWNHAM-D, TADAY-P AND KEMP-M (2004). Hidden object detection: security applications of terahertz technology, *Proc. SPIE Terahertz and Gigahertz Electronics and Photonics III*, **5354**, Ed: R. Hwu, April 2004, San Jose, CA, USA, pp. 168–176. 1.3.2

TROY-T AND THENNADIL-S (2001). Optical properties of human skin in the near infrared wavelength range of 1000 to 2200 nm, *Journal of Biomedical Optics*, **6**(2), pp. 167–176. 9.4.1

TUCHIN-V (2000). *Tissue Optics: Light Scattering Methods and Instruments for Medical Diagnosis*, Tutorial Texts in Optical Engineering, SPIE Press, Bellingham, WA, USA. 8.2

UNIVERSITY COLLEGE LONDON (2005). *Tissue-Equivalent Phantoms*, Biomedical Optics Research Laboratory, Department of Medical Physics and Bioengineering, London, UK, <http://www.medphys.ucl.ac.uk/research/borl/research/NIR_topics/phantoms.htm>, (Accessed: 2009-02-05). 4.5

VALDMANIS-J AND MOUROU-G (1986). Subpicosecond electrooptic sampling: Principles and applications, *IEEE Journal of Quantum Electronics*, **22**(1), pp. 69–78. 3.5.2

VALDMANIS-J, MOUROU-G AND GABEL-C (1982). Picosecond electro-optic sampling system, *Applied Physics Letters*, **41**(3), pp. 211–212. 3.5.2, 3.7

VALDMANIS-J, MOUROU-G AND GABEL-C (1983). Subpicosecond electrical sampling, *IEEE Journal of Quantum Electronics*, **19**(4), pp. 664–667. 3.5.2

VAN DE HULST-H (1957). *Light Scattering by Small Particles*, John Wiley & Sons, Inc., New York, USA. 7.5.1, 8.3, 8.3.2, 8.3.2

VAN DE HULST-H (1980a). *Multiple Light Scattering : Tables, Formulas, and Applications*, **1**, Academic Press, New York, USA. 8.2

VAN DE HULST-H (1980b). *Multiple Light Scattering : Tables, Formulas, and Applications*, **2**, Academic Press, New York, USA. 8.2

VAN DER VALK-N AND PLANKEN-P (2004). Towards terahertz near-field microscopy, *Philosophical Transactions of the Royal Society A: Mathematical, Physical and Engineering Sciences*, **362**(1815), pp. 315–321. 1.3.2, 1.5, 4.5.2

VAN DER WEIDE-D (1994). Planar antennas for all-electronic terahertz systems, *Journal of the Optical Society of America B: Optical Physics*, **11**(12), pp. 2553–2560. 3.8.3

VAN EXTER-M AND GRISCHKOWSKY-D (1990). Characterization of an optoelectronic terahertz beam system, *IEEE Transactions on Microwave Theory and Techniques*, **38**(11), pp. 1684–1691. 3.8.3

VAN EXTER-M, FATTINGER-C AND GRISCHKOWSKY-D (1989a). High-brightness terahertz beams characterized with an ultrafast detector, *Applied Physics Letters*, **55**(4), pp. 337–339. 3.8.3, 3.13

VAN EXTER-M, FATTINGER-C AND GRISCHKOWSKY-D (1989b). Terahertz time-domain spectroscopy of water-vapor, *Optics Letters*, **14**(20), pp. 1128–1130. 1.3.2, 4.5.1, 4.2

VAN STAVEREN-H, MOES-C, VAN MARIE-J, PRAHL-S AND VAN GEMERT-M (1991). Light scattering in Intralipid-10% in the wavelength range of 400-1100 nm, *Applied Optics*, **30**(31), pp. 4507–4514. 8.2

VARIAN INC. (2008). *Varian FT-IR Spectrometers*, Palo Alto, CA, USA, <http://www.varianinc.com/image/vimage/docs/applications/apps/si-1368.pdf>, (Accessed: 2009-06-23). 1.4

VASIN-V AND AGEEV-A (1995). *Ill-Posed Problems with a priori Information*, VSP, Utrecht. A.4

VENABLES-D AND SCHMUTTENMAER-C (1998). Far-infrared spectra and associated dynamics in acetonitrilewater mixtures measured with femtosecond THz pulse spectroscopy, *Journal of Chemical Physics*, **108**(12), pp. 4935–4944. 4.5.2, 4.15

VERHEUL-M, PEDERSEN-J, ROEFS-S AND DE KRUIF-K (1999). Association behavior of native β-lactoglobulin, *Biopolymers*, **49**(1), pp. 11–20. 7.3.1, 7.3.2

VIANT-M, CRUZAN-J, LUCAS-D, BROWN-M, LIU-K AND SAYKALLY-R (1997). Pseudorotation in water trimer isotopomers using terahertz laser spectroscopy, *Journal of Physical Chemistry A*, **101**(48), pp. 9032–9041. 4.5.1

VIATOR-J, CHOI-B, PEAVY-G, KIMEL-S AND NELSON-J (2003). Spectra from 2.5-15 μm of tissue phantom materials, optical clearing agents and *ex vivo* human skin: implications for depth profiling of human skin, *Physics in Medicine and Biology*, **48**(2), pp. N15–N24. 4.3.2, 4.4, 4.3.2, 9.4.1

VIDEEN-G AND NGO-D (1997). Light scattering from a cylinder near a plane interface: theory and comparison with experimental data, *Journal of the Optical Society of America A: Optics and Image Science, and Vision*, **14**(1), pp. 70–78. 8.2

VINCENT-D (1986). Amplitude modulation with a mechanical chopper, *Applied Optics*, **25**(7), pp. 1035–1036. 3.7.2

VON RIBBECK-H.-G, BREHM-M, VAN DER WEIDE-D, WINNERL-S, DRACHENKO-O, HELM-M AND KEILMANN-F (2008). Spectroscopic THz near-field microscope, *Optics Express*, **16**(5), pp. 3430–3438. 1.3.2, 1.5

WAIT-J (1955). Reflection at arbitrary incidence from a parallel wire grid, *Applied Scientific Research*, **4**(1), pp. 393–400. 8.2

WAIT-J (1996). *Electromagnetic Waves in Stratified Media*, IEEE/OUP Series on Electromagnetic Theory, IEEE, New York, NY, USA. 9.2, 9.1

WALKER-G, BERRY-E, SMYE-S, ZINOV'EV-N, FITZGERALD-A, MILES-R, CHAMBERLAIN-M AND SMITH-M (2003). Two methods for modelling the propagation of terahertz radiation in a layered structure, *Journal of Biological Physics*, **29**, pp. 141–148. 1.5.1, 9.2

WALKER-G, BERRY-E, SMYE-S, ZINOV'EV-N, FITZGERALD-A, MILES-R, CHAMBERLAIN-M AND SMITH-M (2004). Modelling the propagation of terahertz radiation through a tissue simulating phantom, *Physics in Medicine and Biology*, **49**, pp. 1853–1864. 1.5.1, 9.2, 9.4.2

WALKER-G, BERRY-E, ZINOV'EV-N, FITZGERALD-A, MILES-R, CHAMBERLAIN-M AND SMITH-M (2002). Terahertz imaging and international safety guidelines, *Proc. SPIE Medical Imaging 2002: Physics of Medical Imaging*, **4682**, Eds: L. Antonuk and M. Yaffe, pp. 683–690. 9.6

WALLACE-V, FITZGERALD-A, PICKWELL-E, PYE-R, TADAY-P, FLANAGAN-N AND HA-T (2006). Terahertz pulsed spectroscopy of human Basal Cell Carcinoma, *Applied Spectroscopy*, **60**(10), pp. 1127–1133. 1.5, 5.4.2, 5.5.5, 6.1

WALLACE-V, FITZGERALD-A, SHANKAR-S, FLANAGAN-N, PYE-R, CLUFF-J AND ARNONE-D (2004). Terahertz pulsed imaging of basal cell carcinoma *ex vivo* and *in vivo*, *British Journal of Dermatology*, **151**(2), pp. 424–432. 1.5

WALSH-K, SCHULKIN-B, GARY-D, FEDERICI-J, BARAT-R AND ZIMDARS-D (2004). Terahertz near-field interferometric and synthetic aperture imaging, *Proc. SPIE Terahertz for Military and Security Applications II*, **5411**, Eds: R. Hwu and D. Woolard, Orlando, FL, USA, pp. 9–17. 4.5.2

WALTHER-M, FISCHER-B AND JEPSEN-P (2003). Noncovalent intermolecular forces in polycrystalline and amorphous saccharides in the far infrared, *Chemical Physics*, **288**(2-3), pp. 261–268. 4.5.2

WALTHER-M, FISCHER-B, SCHALL-M, HELM-H AND JEPSEN-P (2000). Far-infrared vibrational spectra of all-*trans*, 9-*cis* and 13-*cis* retinal measured by THz time-domain spectroscopy, *Chemical Physics Letters*, **332**, pp. 389–395. 4.5.2

WALTHER-M, PLOCHOCKA-P, FISCHER-B, HELM-H AND JEPSEN-P (2002). Collective vibrational modes in biological molecules investigated by terahertz time-domain spectroscopy, *Biopolymers*, **67**, pp. 310–313. 1.4.1, 4.5.3

WANG-J AND FUJIWARA-O (1999). FDTD computation of temperature rise in the human head for portable telephones, *IEEE Transactions on Microwave Theory and Techniques*, **47**(8), pp. 1528–1534. 4.4.2

WANG-S, FERGUSON-B, MANNELLA-C, ABBOTT-D AND ZHANG-X.-C (2002). Powder detection using THz imaging, *Proc. Optical Society of America Conference on Lasers and Electro-Optics (CLEO)*, 2002-05-19, Long Beach, CA, USA, p. 131. 1.3.2

WANG-X, POGUE-B, JIANG-S, DEHGHANI-H, SONG-X, SRINIVASAN-S, BROOKSBY-B, PAULSEN-K, KOGEL-C, POPLACK-S AND WELLS-W (2006). Image reconstruction of effective Mie scattering parameters of breast tissue *in vivo* with near-infrared tomography, *Journal of Biomedical Optics*, **11**(4), article number 041106. 4.3.2, 8.2

WANG-X, POGUE-B, JIANG-S, SONG-X, PAULSEN-K, KOGEL-C, POPLACK-S AND WELLS-W (2005). Approximation of Mie scattering parameters in near-infrared tomography of normal breast tissue *in vivo*, *Journal of Biomedical Optics*, **10**(5), article number 051704. 4.3.2, 8.2

WEBER-M (1971). *Insulating Crystal Lasers*, Handbook of Lasers with Selected Data on Optical Technology, CRC Press, Cleveland, OH, USA, pp. 371–417. 3.7.1

WEI-Y.-Z AND SRIDHAR-S (1989). Technique for measuring the frequency-dependent complex dielectric constants of liquids up to 20 GHz, *Review of Scientific Instruments*, **60**(9), pp. 3041–3046. 11

WESTRA-M (2008). *ITER*, ITER, <http://www.iter.org/index.htm>, (Accessed: 2008-10-21). 2.6.1

WHITMIRE-S, WOLPERT-D, MARKELZ-A, HILLEBRECHT-J, GALAN-J AND BIRGE-R (2003). Protein flexibility and conformational state: A comparison of collective vibrational modes of wild-type and D96N bacteriorhodopsin, *Biophysical Journal*, **85**(2), pp. 1269–1277. 4.5.2, 7.1

WIESENFELD-J, TUCKER-R, ANTREASYAN-A, BURRUS-C, TAYLOR-A, MATTERA JR.-V AND GARBINSKI-P (1987). Electro-optic sampling measurements of high-speed InP integrated circuits, *Applied Physics Letters*, **50**(19), pp. 1310–1312. 3.8.3

WIETZKE-S, JANSEN-C, RUTZ-F, MITTLEMAN-D AND KOCH-M (2007). Determination of additive content in polymeric compounds with terahertz time-domain spectroscopy, *Polymer Testing*, **26**(5), pp. 614–618. 1.3.2

WIKIPEDIA (2008a). *A Diagram of the EM Spectrum*, Wikipedia, <http://en.wikipedia.org/wiki/Electromagnetic_spectrum>, (Accessed: 2009-01-02). 1.1

WIKIPEDIA (2008b). *Wollaston Prism*, Wikipedia, <http://en.wikipedia.org/wiki/File:Wollaston-prism.svg>, (Accessed: 2008-12-17). 3.17

WIKIPEDIA (2009). *Miller Indices Cubes*, Wikipedia, <http://en.wikipedia.org/wiki/File:Miller_Indices_Cubes.svg>, (Accessed: 2010-04-09). B.2

WILKE-I AND SENGUPTA-S (2008). *Nonlinear Optical Techniques for Terahertz Pulse Generation and Detection—Optical Rectification and Electrooptic Sampling*, Terahertz Spectroscopy: Principles and Applications, CRC Press, Boca Raton, FL, USA, pp. 41–72. B.2, B.3.4

WILLAERT-D AND VERHASSELT-Y (1998). *World Atlas of Ageing*, World Health Organization WHO Centre for Health Development, Kobe, Japan. 6.2

WILLETT-C (1971). *Neutral Gas Lasers*, Handbook of Lasers with Selected Data on Optical Technology, CRC Press, Cleveland, OH, USA, pp. 183–241. 2.3

WILLIAMS-B, KUMAR-S, HU-Q AND RENO-J (2005). Operation of terahertz quantum-cascade lasers at 164 K in pulsed mode and at 117 K in continuous-wave mode, *Optics Express*, **13**(9), pp. 3331–3339. 2.4.1

WILLIAMS-G (2007a). *Free-Electron Laser Description: General Introduction*, Jefferson Lab, Newport News, VA, USA, <http://www.jlab.org/FEL/feldescrip.html>, (Accessed: 2008-10-27). 2.15

WILLIAMS-G (2007b). *Free-Electron Laser Description: Specifications of the JLab FEL*, Jefferson Lab, Newport News, VA, USA, <http://www.jlab.org/FEL/felspecs.html>, (Accessed: 2008-10-27). 2.7.2

WILSON-B AND ADAM-G (1983). A Monte Carlo model for the absorption and flux distributions of light in tissue, *Medical Physics*, **10**(6), pp. 824–830. 4.3.2

WILTSE-J (1984). History of millimeter and submillimeter waves, *IEEE Transactions on Microwave Theory and Techniques*, **32**(9), pp. 1118–1127. 1.3.1

WISCOMBE-W (1980). Improved Mie scattering algorithms, *Applied Optics*, **19**(9), pp. 1505–1509. H.2

WITHAYACHUMNANKUL-W, PNG-G, YIN-X.-X, ATAKARAMIANS-S, JONES-I, LIN-H, UNG-B, BALAKRISHNAN-J, NG-B.-H, FERGUSON-B, MICKAN-S, FISCHER-B AND ABBOTT-D (2007). T-ray sensing and imaging, *Proceedings IEEE*, **95**(8), pp. 1528–1558. 1.7, 5

WOLKERS-W, WALKER-N, TABLIN-F AND CROWE-J (2001). Human platelets loaded with trehalose survive freeze-drying, *Cryobiology*, **42**(2), pp. 79–87. 5.5.2

WONG-P, WONG-R, CAPUTO-T, GODWIN-T AND RIGAS-B (1991). Infrared spectroscopy of exfoliated human cervical cells: Evidence of extensive structural changes during carcinogenesis, *Proceedings of the National Academy of Sciences of the United States of America*, **88**(24), pp. 10988–10992. 4.3.2

WOOD-B, CHIRIBOGA-L, YEE-H, QUINN-M, MCNAUGHTON-D AND DIEM-M (2004). Fourier transform infrared (FTIR) spectral mapping of the cervical transformation zone, and dysplastic squamous epithelium, *Gynecologic Oncology*, **93**(1), pp. 59–68. 4.3.2, 4.3

WOOD-B, QUINN-M, BURDEN-F AND MCNAUGHTON-D (1996). An investigation into FTIR spectroscopy as a biodiagnostic tool for cervical cancer, *Biospectroscopy*, **2**(3), pp. 143–153. 4.3.2

WOOD-B, QUINN-M, TAIT-B, ASHDOWN-M, HISLOP-T, ROMEO-M AND MCNAUGHTON-D (1998). FTIR microspectroscopic study of cell types and potential confounding variables in screening for cervical malignancies, *Biospectroscopy*, **4**(2), pp. 75–91. 4.3.2, 4.3

WOODCOCK-R (1971). *Commercial Laser Glasses*, Handbook of Lasers with Selected Data on Optical Technology, CRC Press, Cleveland, OH, USA, pp. 360–364. 3.7.1

WOODWARD-R, COLE-B, WALLACE-V, PYE-R, ARNONE-D, LINFIELD-E AND PEPPER-M (2002). Terahertz pulse imaging in reflection geometry of human skin cancer and skin tissue, *Physics in Medicine and Biology*, **47**(21), pp. 3853–3863. 1.4.2, 4.6

WOODWARD-R, WALLACE-V, ARNONE-D, LINFIELD-E AND PEPPER-M (2003a). Terahertz pulsed imaging of skin cancer in the time and frequency domain, *Journal of Biological Physics*, **29**(2-3), pp. 257–261. 1.4.2

WOODWARD-R, WALLACE-V, PYE-R, COLE-B, ARNONE-D, LINFIELD-E AND PEPPER-M (2003b). Terahertz pulse imaging of *ex-vivo* Basal Cell Carcinoma, *Journal of Investigative Dermatology*, **120**(1), pp. 72–78. 1.4.2, 1.7

WOOLARD-D, LUO-Y, GELMONT-B, GLOBUS-T AND JENSEN-J (2005). A bio-molecular inspired electronic architecture: Bio-based device concepts for enhanced sensing, *Proc. SPIE Terahertz for Military and Security Applications III*, **5790**, Eds: R. Hwu and D. Woolard, 28–29 March 2005, Orlando, FL, USA, pp. 180–194. 4.5.3

WORRALL-C, ALTON-J, HOUGHTON-M, BARBIERI-S, BEERE-H, RITCHIE-D AND SIRTORI-C (2006). Continuous wave operation of a superlattice quantum cascade laser emitting at 2 THz, *Optics Express*, **14**(1), pp. 171–181. 2.4.1

WU-Q AND ZHANG-X.-C (1995). Free-space electro-optic sampling of terahertz beams, *Applied Physics Letters*, **67**(24), pp. 3523–3525. 1.3.2, 3.9

WU-Q AND ZHANG-X.-C (1996a). Design and characterization of traveling-wave electrooptic terahertz sensors, *IEEE Journal of Selected Topics in Quantum Electronics*, **2**(3), pp. 693–700. 3.10

WU-Q AND ZHANG-X.-C (1996b). Ultrafast electro-optic field sensors, *Applied Physics Letters*, **68**(12), pp. 1604–1606. 3.10, B.2

WU-Q AND ZHANG-X.-C (1997). 7 terahertz broadband GaP electro-optic sensor, *Applied Physics Letters*, **70**(14), pp. 1784–1786. 3.10

WU-Q, LITZ-M AND ZHANG-X.-C (1996). Broadband detection capability of ZnTe electro-optic field detectors, *Applied Physics Letters*, **68**(21), pp. 2924–2926. 3.10

XU-J, PLAXCO-K AND ALLEN-S (2006a). Absorption spectra of liquid water and aqueous buffers between 0.3 and 3.72 THz, *Journal of Chemical Physics*, **124**(3), article number 036101. 2.7.2, 4.5.1, 4.5.2

XU-J, PLAXCO-K AND ALLEN-S (2006b). Collective dynamics of lysozyme in water: Terahertz absorption spectroscopy and comparison with theory, *Journal of Physical Chemistry B*, **110**, pp. 24255–24259. 2.7.2, 4.5.2, 9.6

XU-J, PLAXCO-K AND ALLEN-S (2006c). Probing the collective vibrational dynamics of a protein in liquid water by terahertz absorption spectroscopy, *Protein Science*, **15**, pp. 1175–1181. 2.7.2, 4.5.2

XU-L, ZHANG-X.-C AND AUSTON-D (1992). Terahertz beam generation by femtosecond optical pulses in electro-optic materials, *Applied Physics Letters*, **61**(15), pp. 1784–1786. 3.9

XU-L, ZHANG-X.-C, AUSTON-D AND JALALI-B (1991). Terahertz radiation from large aperture Si p-M diodes, *Applied Physics Letters*, **59**(26), pp. 3357–3359. 3.8.3

YAMAGUCHI-M, YAMAMOTO-K, TANI-M AND HANGYO-M (2007). Low-frequency dynamics of proteins studied by terahertz time-domain spectroscopy, *Proc. 51st Annual Meeting of the Biophysical Society*, 3–7 March 2007, Baltimore, MD, USA, pp. 160A–161A. 1.4.1, 4.5.2

YANG-K, RICHARDS-P AND SHEN-Y (1971). Generation of far-infrared radiation by picosecond light pulses in $LiNbO_3$, *Applied Physics Letters*, **19**(9), pp. 320–323. 3.5

YARBOROUGH-J, SUSSMAN-S, PURHOFF-H, PANTELL-R AND JOHNSON-B (1969). Efficient, tunable optical emission from $LiNbO_3$ without a resonator, *Applied Physics Letters*, **15**(3), pp. 102–105. 3.5

YARIV-A (1989). *Quantum Electronics*, 3rd edn, Wiley. 3.2, 3.4.1, B.1

YARIV-A (1991). *Optical Electronics*, The Holt, Rinehart and Winston Series in Electrical Engineering, 4th edn, Saunders College Publishing. 3.4.1

YOSHIDA-H, OGAWA-Y, KAWAI-Y, HAYASHI-S, HAYASHI-A, OTANI-C, KATO-E, MIYAMARU-F AND KAWASE-K (2007). Terahertz sensing method for protein detection using a thin metallic mesh, *Applied Physics Letters*, **91**(25), article number 253901. 4.5.2, A.2

YOSHINAGA-H, FUJITA-S, MINAMI-S, MITSUISHI-A, OETJEN-R AND YAMADA-Y (1958). Far infrared spectrograph for use from the prism spectral region to about 1-mm wavelength, *Journal of the Optical Society of America*, **48**(5), pp. 315–322. 1.4

YUAN-T, PARK-H, XU-J, HAN-H AND ZHANG-X.-C (2005). Field induced THz wave emission with nanometer resolution, *Proc. Smart Structures, Devices, and Systems II*, **5649**, Ed: S. Al-Sarawi, Brisbane, Australia, pp. 1–8. 4.5.2

YU-B, ZENG-F, YANG-Y, XING-Q, CHECHIN-A, XIN-X, ZEYLIKOVICH-I AND ALFANO-R (2004). Torsional vibrational modes of tryptophan studied by terahertz time-domain spectroscopy, *Biophysical Journal*, **86**(3), pp. 1649–1654. 4.5.2

ZEITLER-J, SHEN-Y, BAKER-C, TADAY-P, PEPPER-M AND RADES-T (2007). Analysis of coating structures and interfaces in solid oral dosage forms by three dimensional terahertz pulsed imaging, *Journal of Pharmaceutical Sciences*, **96**(2), pp. 330–340. 1.3.2, 4.5.3

ZERNIKE-F (1969). Temperature-dependent phase matching for far-infrared difference- frequency generation in InSb, *Physical Review Letters*, **22**(18), pp. 931–933. 3.5

ZERNIKE JR.-F AND BERMAN-P (1965). Generation of far infrared as a difference frequency, *Physical Review Letters*, **15**(26), pp. 999–1001. 3.5

ZHANG-C, TARHAN-E, RAMDAS-A, WEINER-A AND DURBIN-S (2004). Broadened far-infrared absorption spectra for hydrated and dehydrated myoglobin, *Journal of Physical Chemistry B*, **108**(28), pp. 10077–10082. 7.1

ZHANG-J AND GRISCHKOWSKY-D (2004). Terahertz time-domain spectroscopy of submonolayer water adsorption in hydrophilic silica aerogel, *Optics Letters*, **29**(9), pp. 1031–1033. 4.5.2

ZHANG-X.-C (2002). Terahertz wave imaging: horizons and hurdles, *Physics in Medicine and Biology*, **47**(21), pp. 3667–3677. 5.4.2

ZHANG-X.-C AND XU-J (2010). *Introduction to THz Wave Photonics*, Springer, New York, USA. 1.3.1

ZHANG-X.-C, DARROW-J, HU-B, AUSTON-D, SCHMIDT-M, THAM-P AND YANG-E (1990a). Optically induced electromagnetic radiation from semiconductor surfaces, *Applied Physics Letters*, **56**(22), pp. 2228–2230. 3.8.3

ZHANG-X.-C, HU-B, DARROW-J AND AUSTON-D (1990b). Generation of femtosecond electromagnetic pulses from semiconductor surfaces, *Applied Physics Letters*, **56**(11), pp. 1011–1013. 3.9

ZHANG-X.-C, JIN-Y AND MA-X (1992a). Coherent measurement of THz optical rectification from electro-optic crystals, *Applied Physics Letters*, **61**(23), pp. 2764–2766. 3.9, B.3.4

ZHANG-X.-C, JIN-Y, WARE-K, MA-X, RICE-A, BLISS-D, LARKIN-J AND ALEXANDER-M (1994). Difference-frequency generation and sum-frequency generation near the band gap of zincblende crystals, *Applied Physics Letters*, **64**(5), pp. 622–624. 2.5

ZHANG-X.-C, MA-X, JIN-Y, LU-T, BODEN-E, PHELPS-P, STEWART-K AND YAKYMSHYN-C (1992b). Terahertz optical rectification from a nonlinear organic crystal, *Applied Physics Letters*, **61**(26), pp. 3080–3082. 3.9

ZHONG-X, CUI-T, LI-Z, TAO-Y AND LIN-H (2007). Terahertz-wave scattering by perfectly electrical conducting objects, *Journal of Electromagnetic Waves and Applications*, **21**(15), pp. 2331–2340. 8.1

ZHOU-Q AND KNIGHTON-R (1995). Numerical approximation of light scattering from tenuous cylindrical membranes at normal incidence, *Applied Optics*, **34**(13), pp. 2354–2361. 8.2

ZHOU-Q AND KNIGHTON-R (1997). Light scattering and form birefringence of parallel cylindrical arrays that represent cellular organelles of the retinal nerve fiber layer, *Applied Optics*, **36**(10), pp. 2273–2285. 8.2

ZURK-L, ORLOWSKI-B, WINEBRENNER-D, THORSOS-E, LEAHY-HOPPA-M AND HAYDEN-L (2007). Terahertz scattering from granular material, *Journal of the Optical Society of America B: Optical Physics*, **24**(9), pp. 2238–2243. 8.1

Index

Résumé

Gretel Markris Png graduated in 1997 from the University of Edinburgh, UK with a Bachelor of Engineering degree (Electrical and Electronics) with first class honours. Between 1997 and 2001, she worked as a systems engineer in Sweden and Israel. In late 2001, she commenced her Master of Science (MSc) degree by coursework in Electrical Engineering and Computer Science at the University of California at Irvine (UCI), USA. She was accepted into the PhD program at UCI after completing her MSc degree, but due to changes in family circumstances, chose to emigrate to Australia in early 2004. She commenced her PhD candidature at the University of Adelaide in mid 2004 under the supervision of Dr Brian W.-H. Ng, Prof. Derek Abbott and Dr Sam Mickan.

Gretel has consistently won a number awards during her undergraduate and postgraduate studies. At the University of Edinburgh, she won the Harold Dickinson Memorial Prize for the best undergraduate dissertation. At UCI, she won the Excellence in Teaching and Mentoring Award. At the University of Adelaide, she won the Australian Postgraduate Award, and thirteen other national and international competitive awards and grants. These prizes have enabled her to travel to Rensselaer Polytechnic Institute in the USA to conduct collaborative THz research with Prof. Xi-Cheng Zhang, and to the University of Leeds in the UK to work with Prof. Robert E. Miles.

Gretel has authored and co-authored four peer-reviewed journal papers, and eight refereed conference papers. She has given four conference presentations, including an invited talk at the International Conference on Infrared, Millimeter, and Terahertz Waves (IRMMW-THz) in 2009. She has delivered technical talks to the South Australian chapter of the Institute of Electrical and Electronics Engineers (IEEE). Gretel was also the 2006/2007 President of the IEEE student branch at the University of Adelaide.

During her PhD candidature, Gretel took two semesters off to teach full-time at the University of Adelaide, and was involved in revamping the first-year undergraduate electronics laboratory course. In addition to her scientific research interest in medical spectroscopy and computational modelling, she is currently researching the use of *edutainment* and animation in undergraduate engineering and science education.

Academic Genealogy